TOP-DOWN CONTROL OF SENSORY FOCUS IN BURSTY PYRAMIDAL CELL POPULATIONS

By
Stephen E. Clarke
October 2017

Thesis submitted to the
Faculty of Graduate and Postdoctoral Studies
in partial fulfillment of the requirements
for Doctor of Philosophy in Neuroscience

Department of Cellular and Molecular Medicine
Faculty of Medicine

uOttawa

Abstract

Through a series of original research articles, this thesis describes the role of neural network feedback in top-down control of bursty ON and OFF type electrosensory neurons while processing motion toward (looming) and away (receding) from the body. Neural codes for motion reversal in weakly electric fish are not simply evoked by bottom-up sensory input and amplified by feedback; instead, positive feedback loops must synthesize a directionally invariant representation of motion reversal that is distributed across both the ON and OFF pyramidal cell populations. Through balanced excitatory and inhibitory feedback, the system establishes an optimal distance for motion estimation (a sensory focus) that is maintained by the animal during a motion tracking behaviour. Remarkably, this sensory focus is size, direction and speed-invariant. The speed invariance likely derives from the speed-invariance of the electrosensory afferent response, a consequence of timescale-free spike frequency adaptation. Since natural swimming movements are associated with tail-bending that cause spatially diffuse sensory noise, we demonstrate that spatially localized motion processing of the ON and OFF neurons co-occurs with cancellation of the distraction; this supports the circuit's role as a robust 'sensory searchlight' mechanism for spatial attention. A simple algorithm for motion tracking is discussed, as well as potential generalizations of the described coding principles to more complex mammalian circuits.

Acknowledgements

I would like to thank my supervisor, Dr. Leonard Maler and co-supervisor Dr. André Longtin, my advisory committee members Dr. Jean-Claude Béïque and Dr. John Lewis, our lab technician William Ellis, as well as other Maler lab members for their dedication to me over the course of my studies.

I would like to thank my family and friends for their unwavering support.

Finally, I would like to thank the University of Ottawa and the province of Ontario for financial support through the Excellence Scholarship, Ontario Graduate Scholarship and Queen Elizabeth II - GSST awards; the National Sciences and Engineering Reseach Council for financial support through the Alexander Graham Bell CGS Award and the Canadian Institutes of Health Research for the Frederick Banting and Charles Best Canada Graduate Scholarship.

Dedication

I dedicate this work to Dr. Leonard Maler whose superb vision and nearly four decades of research made all of this possible. Working with Len was a sincere pleasure and an opportunity for which I am very grateful.

Abbreviations

Electric Organ Discharge	**EOD**
Amplitude Modulation	**AM**
Random Amplitude Modulation	**RAM**
Sinusoidal Amplitude Modulation	**SAM**
Receptive Field	**RF**
Electrosensory Afferent(s)	**EA**
Electrosensory Lateral Line Lobe	**ELL**
Centrolateral Segment	**CLS**
Dorsal Molecular Layer	**DML**
Ventral Molecular Layer	**VML**
Nucleus Preminentialis	**nP**
Eminentia Granularis Posterior	**EGp**
Torus Semicircularis	**TS**
Spike Frequency Adaptation	**SFA**
Inter-Spike Interval	**ISI**
Firing Rate	**FR**

Contents

List of Figures

Chapter 1

Introduction

1.1 Motion coding, ON and OFF cells and brain evolution

500 million years. Although it is hard to pinpoint the exact origin of neurons that selectively encode increases and decreases in sensory input relative to background levels (ON and OFF cells respectively), the development of the vertebrate retina dates back to an early chordate ancestor in the Cambrian period, at least 400-500 million years ago [1]. The differentiation of the ON and OFF visual pathway of flies dates back to the same period [2]. C. elegans, which diverged from our common ancestor around 500-600 million years ago, also possess ON and OFF cell types [3, 4]. During this era of intense speciation, chordate expansion saw our own ancestral line diverge from that of weakly electric fish, whose electrosense is built upon ON and OFF cells [5]. These electrosensory ON and OFF cells appear to have evolved from cells of the lateral line, an evolutionarily basal sense found in teleost fish [6], which also gave rise to ON and OFF cells in the passive (ampullary) electrosense of catfish [7, 8]. With the rapid proliferation of new species and successful innovations in sensorimotor control began a new era of strong selective pressure for high-acuity spatiotemporal coding. Given the diversity of species and sensory modalities that exploit this ON and OFF cell organization, as well as their diverse biophysical implementations, it can be argued that algorithmic selectivity for increases and decreases in sensory signal contrast has driven both conserved and convergent evolution

through improved motion processing and the resulting behavioural success [5] (printed in Appendix, A.1).

The classical mechanics that dictate natural motion required many early neural systems to accurately represent signal intensity and its spatiotemporal derivatives. As species transitioned from water to land during the Cambrian period, the reduced attenuation of light by air led to huge increases in visual sensory volume that are posited to have enabled the development of higher cognitive traits, through the need to plan and forecast more complex trajectories in space and time [9]. When abstracted away from the sensory domain, these coding mechanisms could be used by the brain to describe dynamic quantities other than spatial relationships. This view is consistent with the hypothesis that the emergence of abstract cognition and language in humans was achieved by coopting faculties that originally evolved for more tangible physical problem-solving and social coordination [10]. The brain is said to be a kludge; in other words, it builds new systems on top of old ones simply selecting, retaining and repurposing successful innovations [11, 12]. From this point of view, it is likely that many early and advantageous computations related to motion processing were carried forward and incorporated into the higher level cognitive domain, profoundly shaping the development of more complex neural systems over the next few hundred million years. In my opinion, reverse engineering high level intelligence necessitates a computational 'toolbox' of micro- and meso-circuits compiled from simple, easy-to-characterize biological systems.

1.2 Why study the electrosense?

The electrosense provides a unique opportunity for understanding neural dynamics in vivo: simple sensory signals drive suitably complex vertebrate feedback circuits at the earliest stages of sensation [13]. By avoiding the complicated effect of signal relay through multiple stages of processing, the role of 'bottom-up' sensory input and 'top-down' feedback can be readily interpreted in the electrosensory ON and OFF cells. The electrosensory circuitry offers distilled

insight into common cellular mechanisms and network organization of the mammalian sensory cortex; these include topographic columns of bursty pyramidal cells with active dendrites, regulation by local classes of inhibitory interneurons, as well as the dendritic compartmentalization of both bottom-up input and distinct sources of feedback inputs characterized by various forms of synaptic plasticity [13–16]. Given the above considerations, one would expect the ancient but sufficiently advanced vertebrate lineage of weakly electric fish to contain conserved ancestral circuit principles that led to the proliferation of more advanced neural systems.

1.3 Electrolocation

An essential function of our senses is to determine the 3D location of objects. This is achieved by interpreting patterns of sensory contrast, that is, relative differences in the level of a physical signal (such as light, pressure or electric field strength) across space and time. In the case of the gymnotiform electrosense, object motion causes amplitude modulations (AMs) of a self-generated electric field, the electric organ discharge (EOD; Figure I). These spatially localized increases or decreases in the electric potential relative to the background water allow the animal to detect the presence and identity of objects in its environment [5]. Aquatic organisms and foliage, whose electrical conductivity is higher than the surrounding water, create local increases in the electric potential sensed across the skin by cutaneous electroreceptors, evoking ON cell spiking, while suppressing OFF cell spiking. Ligneous plant tissues, sand and rock are all less conductive than the surrounding water and create local decreases in the electric potential, evoking OFF cell spiking and suppressing ON cell spiking. Through a combination of object motion, tail bending, social interactions and communication signals, electrosensory contrast can vary locally and/or diffusely across the surface of the animal's body under natural conditions (Figure I c, d). The natural scale-free statistics of electrosensory contrast are similar to those of light-dark contrast patterns in the visual system [5, 17, 18]. The electrosense has been extensively reviewed; for further information see [5, 13, 19–21].

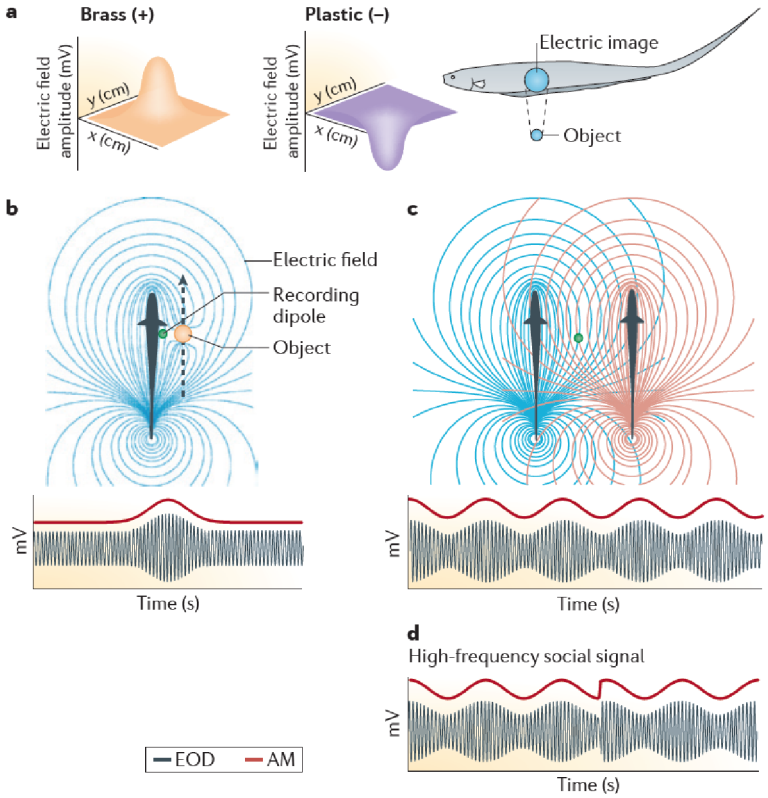

Figure I **Natural electrosensory signals** a) The formation of static electric images. Conductive objects, such as those made of brass, cause a localized increase in the amplitude of the electric field relative to its background levels (driven by the electric organ discharge (EOD)). By contrast, non-conductive objects, such as plastic, cause a localized decrease in the amplitude of the electric field. Thus, these two object classes create either positive or negative local to background, or spatial, contrast. The green dot indicates the location of a small recording dipole, which measures the amplitude of the electric potential experienced across the skin. As the fish swims by an object (a conductive sphere in this illustration), the EOD is locally increased above its baseline amplitude. The movement of the sphere through the electric field causes a low-frequency amplitude modulation (AM) that stimulates cutaneous electroreceptors. c) The effects of EOD summation when two fish are in close proximity. The summation of the EODs of the two fish results in a global, or diffuse sinusoidal AM; this beat frequency equals the difference of the two EOD frequencies. d) A communication signal that results from a frequency modulation of the EOD. This creates another type of spatially diffuse AM, which occurs on timescales shorter than the typical beat period shown in part c. Additional features such as relative motion between fish and an animal's own body-movements, occuring during tail bending for example, create further spatially diffuse perturbations to the transdermal potential (not shown). Much like the common radio, changes in amplitude and frequency of the EOD carrier wave can communicate rich information to the animal. This thesis focuses primarily on object motion, generating spatially localized first-order EOD AMs. Figure reprinted from [5] (see Appendix).

Translating sensory contrast patterns into veridical motion perception is a serious problem for neural systems. For example, characteristics of a visual object, such as its size, shape, orientation and distance from the observer, create spatial contrast patterns on the retina, a

two-dimensional sheet of photoreceptors. Many possible combinations of spatiotemporal features in the environment can cause the same pattern of contrast. Unequivocally identifying the state of the stimulus that caused a specific contrast pattern is challenging as there is no unique solution, especially as one or more of these stimulus features change over time [22] in a noisy environment. The exact same problem exists for electric fish, which must deduce object location and identity based on the electric image cast over their planar body surface. The majority of motion studies for both visual and electrosensory systems have stimulated parallel to the receptor surface, giving rise to a familiar picture of early visual and electrosensory processing; a topographic representation of visual space, where an object's location is signalled by the activation of the associated receptors on the sensory surface. However, movement perpendicular to the sensory plane is also important and it's not obvious how such 3D signals are encoded. Although motion toward the animal (looming) has been studied in the visual system with respect to collision avoidance [23, 24], far less attention has been devoted to the neural representations of motion away from the body (receding), which is fundamental to purposeful interactions with an object as opposed to simply avoiding it. Since adaptive sensory processing generates directional selectivity to moving objects in both invertebrate motion sensitive neurons and vertebrate ON and OFF retinal ganglion cells [5], it is unclear whether symmetric representations of object distance can be generated by a topographic coding scheme built upon adapting ON and OFF cell types in the electrosense. This important question addresses how adaptive, yet symmetrical neural tuning curves can be generated under conditions of dynamic stimulation and during natural behaviours.

Weakly electric fish are an important model system for studies of active sensing, a combined sensory and motor system strategy where animals direct their own sensors to extract task-relevant information in a closed loop fashion [25, 26]. For example, when tracking a moving object, the relative distance between the fish and the object is reflected by the AM of EOD intensity (Figure I); relative speed and acceleration are reflected in its first and second order temporal derivatives. Subsequently, this information is used by the motor system to position

the body; however, changing the position of the body further influences the sensory input and closes the sensorimotor loop. The spatiotemporal derivatives of the resulting signal contrast are central to localization behaviours such as the gradient-based behavioural search methods employed by bats [27], as well as the chemotaxis behaviour of C. elegans [28], the latter of which is known to rely on ON and OFF cell types [4]. Although our results are obtained from immobilized animals, they have interesting implications for feedback and sensorimotor control during active sensing behaviours.

1.4 Electrosensory circuitry

Bottom-up circuitry: Cutaneous electroreceptors detect AMs through changes in the transdermal electric potential and relay this sensory input via electrosensory afferent fibers (EAs) to two main classes of ON and OFF pyramidal cells, the non-bursty deep cells and the bursty intermediate and superficial cells (bursting described below). Pairs of ON and OFF pyramidal cells are found in topographic columns and share a spatial receptive field (RF) with the typical center-surround structure. These ON and OFF cells are further arranged within three topographic maps of the electrosensory lobe (ELL): the centromedial (CMS), centrolateral (CLS) and lateral (LS) segments [19]. The CMS and CLS are responsive to the spatially localized low-frequency signals associated with motion, while the LS is further specialized for processing high frequency communication signals [19]. In all maps the EAs drive two classes of output pyramidal neurons [5, 19, 29, 30] as illustrated for CLS in Figure II. This thesis centers on the CLS map, rather than CMS, as the RFs are medium in size, easy to access and their centers correspond best to the size of the stimulus used in our experiments. The EAs converge directly onto the AMPA and NMDA receptor-rich basal dendrites of ON pyramidal cells and local GABAergic interneurons [31–34]. OFF pyramidal cells receive indirect EA input via the local inhibitory interneurons that invert the sign of the afferent input and are driven electrotonically via gap junction input issuing from descending excitatory feedback projections [31–34]. The ON and OFF pyramidal cell populations form an information bottle-neck in the ascending

electrosensory pathway, projecting to an important midbrain nucleus, the Torus Semicircularis (TS). The TS occupies the same stage in electrosensory processing as the inferior colliculus does in auditory processing, projecting to homologues of superior colliculus and thalamus.

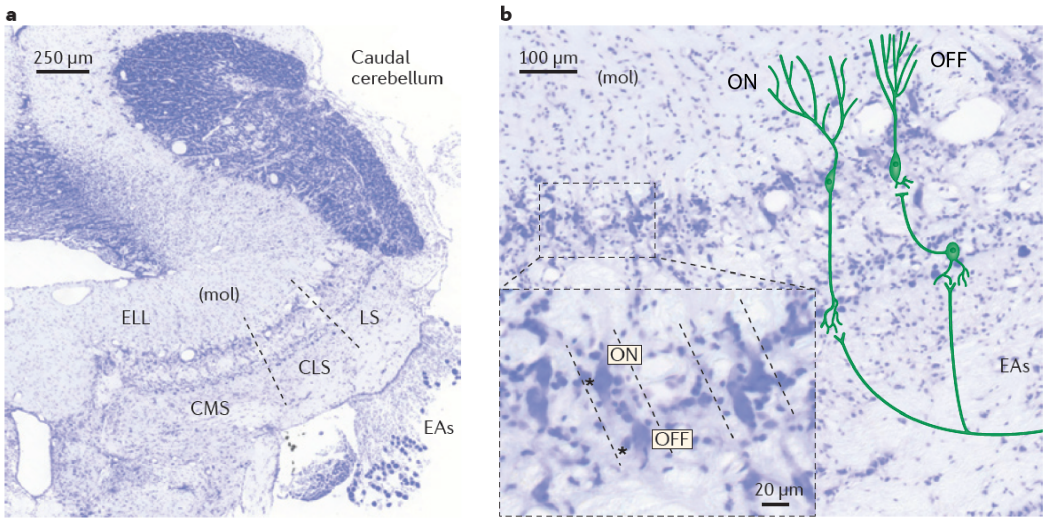

Figure II **Electrosensory lobe circuitry** a) A coronal section of the electrosensory lobe (ELL) and the overlying caudal cerebellum, Nissl stained to show cell bodies of the ON and OFF ELL pyramidal neurons and local interneurons. The ELL contains three topographic maps: the central-medial segment (CMS) and central-lateral segment (CLS) are primarily concerned with processing electrolocation information, whereas the lateral segment (LS) specializes in processing communication signals. Electroreceptor afferent (EAs) ganglion cell bodies are seen near the entry of the EAs into the ELL. The ELL molecular layer (mol) receives feedback input from the caudal cerebellum that is not discussed in this Review (see [19]). b) Each map, including the CLS, shown here at higher magnification, contains two classes of nonlinear output pyramidal neurons [90]: the ON and OFF cells. ON cells receive direct glutamatergic input from EAs, whereas OFF cells receive disynaptic input via GABAergic interneurons. The insert shows the ON cell (with basal dendrite) adjacent to the OFF cell (no basal dendrite), both marked by asterisks. The ON and OFF cells are found in pairs and organized into topographic columns (marked with dashed lines). The large apical dendrites of the ON and OFF cells extend into the molecular layer (mol) and receive inputs from distinct brain regions. Figure reprinted from [5] (see Appendix).

The distinction between superficial and intermediate pyramidal cells (< 30 Hz) is based on a correlation between firing rate, coefficient of variation, recording depth and the size of their extensive dendritic arbors; these highly nonlinear bursty neuron types are distinct from the non-bursty deep ON and OFF cells which have stunted dendrites, receive very little feedback and are nearly linear encoders of signal intensity (> 30 Hz) [35]. Consistent with the findings presented in this thesis, recent work has thoroughly characterized a continuum of properties, suggesting the classic pyramidal cell categories of deep, intermediate and superficial are rather

arbitrary [36]. However, deeps receive only static feedback [16], whereas intermediate and superficial cells receive strong plastic feedback [13,37]. Based on the distinct projection patterns of the deep cells (efferent fibers project to nP and TS) versus intermediate/superficial cells (efferent fibers project to TS only), as well as the qualitative differences in responses to low frequency motion, we effectively consider two distinct groups: non-bursty deep pyramidal cells and bursty intermediate/superficial pyramidal cells. Further anatomical and physiological details, as well as references are provided within each article.

Lateral connectivity: There is no known lateral connectivity among the pyramidal cell populations, whose only significant correlated activity arises through shared electrosensory input; no significant cross-correlation exists for cells sharing less than 20% RF overlap [38]. Although unusual, this is a useful feature of the electrosense as it helps distinguish true top-down activity (i.e. from a higher brain region) from local recurrent network activity.

Top-down circuitry: Top-down modulation of the intermediate/superficial ON and OFF pyramidal cell response is mediated through the proximal and distal compartments of their large apical dendrites. This top-down control originates from the hindbrain nucleus (nP), the cerebellum and the key midbrain nucleus, TS, which is a first stage of sparse electrosensory coding [20]. The anatomy and physiology of these feedback pathways are described in Section 2.5, when they are first manipulated experimentally.

1.5 Bursting in electrosensory ON and OFF cells

High frequency discharge of action potientials, or burst spiking, is an important feature of sensory processing and neural coding [39]. Although each neuron may define the burst differently, this high frequency activity is typically near 100 Hz and can be determined from the inter-spike interval (ISI) histogram or return map in response to stimulation, often Gaussian noise. The physiological mechanism and dynamics of bursting in electrosnesory ON and OFF cells are

briefly summarized here since it is a central theme of the thesis.

When a pyramidal cell fires an action potential, back-propagating spikes issuing from the soma spread at least 200 μm into the proximal apical dendrites of pyramidal cells, activating voltage dependent sodium channels and leading to the generation of a dendritic spike [40,41]. The dendritic spike current diffuses passively back to the soma creating a depolarizing after potential (DAP) [42]. With each somatic spike that back propagates into the dendritic arbor, the slow inactivation of sodium channels becomes more and more pronounced. This has two important effects: first, sodium channel conductance decreases, which reduces both the rate of rise and the amplitude of the dendritic spike. Secondly, due to the slower rate of rise, the activation of the re-polarizing potassium current does not occur as quickly, which causes the dendritic spike to become broader. This slows the rise of the DAP and lengthens the delay of the dendritic current's arrival at the soma [41]. In [42], a phase response curve was generated for a model pyramidal neuron which indicated that excitatory pulses arriving immediately after the peak of the spike can barely advance the phase, that is, accelerate the occurrence of the next spike. On the other hand, excitatory pulses arriving sometime after the spike peak can advance the phase significantly. This demonstrates that the timing of the DAP is crucial in a transition from somatic spike trains to bursting. Anatomical work suggests that topographic midbrain feedback will strongly activate ON and OFF cells through their active dendrites [43]. As such, the electrosensory feedback circuitry likely amplifies the response to spatially localized motion signals, enhancing the neural code by generating burst spikes.

It has become common practice (e.g. [44, 45]) to use an ISI of 10 ms or less as a burst threshold, based on the responses of a biophysically detailed in vitro model neuron [44], a criterion for deviations of in vivo spike trains from a Poisson point process (yielding an average threshold estimate of 12 ± 4 ms) [35] and the fact that, generally, ISIs $<$10 ms are in agreement with backpropagation dependent burst ISIs reported in vitro [46]. The dynamics of the burst mechanism have been thoroughly characterized (e.g. [47, 48]); as input intensity increases, a

sharp transition (i.e. bifurcation) between tonic and burst modes of spiking will occur. Detailed studies have elucidated the pyramidal cell burst mechanism [41, 47, 49] and identified numerous potential modulators of bursting [45, 50].

Chapter 2

Original Research Articles

The published research presented here was performed over the course of my doctoral studies at the University of Ottawa. Each manuscript is formatted according to the standards of their individual journals with respect to trivial matters such as section ordering and reference formatting. As per University of Ottawa guidelines for thesis preparation and organization, figures and figure legends are positioned at appropriate locations within the body of text for each section. All references have been condensed into a single section at the end of the document. Each article is prefaced by a contribution statement and a brief description of the importance, which is intended to provide rationale for the study and to frame the results in the broader perspective presented in this thesis. Figures are numbered within each manuscript as 1 through N, for easy reference and compatibility with the text.

2.1 Speed-invariant encoding of looming object distance requires power law spike rate adaptation

Clarke SE*, Naud R, Longtin A, Maler L (2013). PNAS 110(33): 13624-13629.

Contributions: Author contributions: S.E.C. and L.M. designed research; S.E.C. performed all experiments and model simulations. S.E.C., R.N., and A.L. performed the analysis of speed and acceleration dependency for the models of exponential and power law adaptation; S.E.C. analyzed data; S.E.C., R.N., A.L., and L.M. provided input on the design of the figures, which were made by S.E.C.; S.E.C., A.L., and L.M. wrote the paper. *S.E.C. is the corresponding author.

Significance: In response to sustained stimulation, virtually all neurons adapt the frequency of their action potential discharge, which occurs on timescales ranging from milliseconds to seconds. One obvious explanation is energetics, the cost of an action potential is high and sustaining a large firing rate to an unoriginal stimulus is a waste of resource. Additionally, spike-frequency adaptation and its behaviour over time can have profound effects on neural coding: one of the most important features of adaptation is its ability to match stimulus statistics and maintain a dynamic coding rage in the face of different signal intensities. Yet adaptation is inherently a temporal filtering process and, in many neurons, it is selective for a specific stimulus timescale. A neuron with only one matching timescale of adaptation generates different responses to the same stimulus intensity depending on its rate of change over time. This creates ambiguity in the readout of the instantaneous firing rate and spike counts. For example, did an object move just a bit closer (small change in firing rate), rapidly (large change), or, did it move much closer (large change) but slowly (small change)? The ambiguity of mapping time-dependent stimulus features into a scalar firing rate is yet another sensory inverse problem (described for signal contrast above). Under the constraints of spike-frequency adaptation, we show that neurons with a unique functional form of power law adaptation can

flexibly match the timescale of the stimulus and encode the changing signal intensity (distance) in real-time with high fidelity, invariant to its rate of change (speed and accelaration).

Reprint Permission: "PNAS authors need not obtain permission for the following cases: 1) to use their original figures or tables in their future works; 2) to make copies of their papers for their own personal use, including classroom use, or for the personal use of colleagues, provided those copies are not for sale and are not distributed in a systematic way; 3) to include their papers as part of their dissertations; or 4) to use all or part of their articles in printed compilations of their own works."

Abstract

Neural representations of a moving object's distance and approach speed are essential for determining appropriate orienting responses, such as those observed in the localization behaviours of the weakly electric fish, A. leptorhynchus. We demonstrate that a power law form of spike rate adaptation transforms an electroreceptor afferent's response to looming object motion, effectively parsing information about distance and approach speed into distinct measures of the firing rate. Neurons with dynamics characterized by fixed timescales are shown to confound estimates of object distance and speed. Conversely, power law adaptation modifies an electroreceptor afferent's response according to the timescales present in the stimulus, generating a rate code for looming object distance which is invariant to speed and acceleration. Consequently, estimates of both object distance and approach speed can be uniquely determined from an electroreceptor afferent's firing rate, a multiplexed neural code operating over the extended timescales associated with behaviourally relevant stimuli.

Introduction

Determining how nervous systems maintain perceptual invariance in the face of multi-featured sensory input is a general problem when attempting to connect sensory physiology to high level perception. For instance, spatial parameters such as an object's size, distance, and orientation are inextricably confounded in sensory images projected onto the retina [22]. This becomes an even more acute problem for the encoding of dynamic stimuli [22]; when presented with a temporally modulated visual stimulus, retinal ganglion cells are sensitive to as many as six different features of the input [51]. In its most reduced form, a generic neuron's conversion of input current into membrane potential is characterized by a membrane time constant (SI Appendix). A single response time constant endows a neuron with the ability to faithfully encode variations in stimulus intensity over one specific timescale. Since naturalistic stimuli can vary over a wide range of timescales, there will be inevitable mismatches between the rate at which the stimulus intensity changes and the temporal dynamics that define a neuron's response. Therefore, during sensation, neurons may be highly sensitive to

both stimulus intensity and the time course over which it evolves. This introduces ambiguity into the estimation of stimulus features from a neuron's firing rate, and presents a further challenge for understanding how neural systems maintain perceptual invariance.

An object moving towards an animal provides a concrete example of such a problem, since two variables of interest, the object's distance and approach speed, are both expected to influence the firing rate of a primary sensory neuron. These 'looming' stimuli arise commonly in many sensory systems, including the electrosense, and appear to pose the same rate-coding dilemma for the electroreceptor afferents, whose firing rate has previously been described as sensitive to both stimulus intensity and its temporal derivative [52]. By studying responses of the electroreceptor afferents to this natural problem of distance perception, we identify a mechanism for the temporal disambiguation of stimulus intensity from a neuron's firing rate.

Looming stimuli are obviously important for survival and are processed by central nervous system networks of both invertebrates [23] and vertebrates [24]. During environmental navigation, looming motion forms a basic component of the electrosensory signals experienced by A. leptorhynchus, particularly during prey capture [53, 54]. As an object draws near the body, its presence is sensed by the fish as a perturbation to a self-generated electric field, whose amplitude drives the activity of approximately 16, 000 cutaneous electroreceptors [29].
An approaching object, whose electrical conductivity is greater than that of the surrounding water, causes the electric potential to rise locally (Fig. 1A) and evokes increases in the discharge rate of the electroreceptor afferents. Previous work has carefully detailed the change in transdermal electric potential as a function of object distance [55]. Following this protocol, we implanted a transdermal recording dipole on an immobilized fish and moved a brass sphere at constant speeds along the lateral axis, towards the dipole center. Figure 1B shows data obtained from the recording dipole with an overlay of the expected change in electric potential according to an empirically derived relationship [55]. Using this model, we generated mimic looming signals corresponding to object approach for 6 cm along the lateral axis, at speeds ranging from 0.5 to 5 cm/s. These signals were used as input for spike rate adaptation models, and as looming stimuli while recording in vivo from electroreceptor afferents.

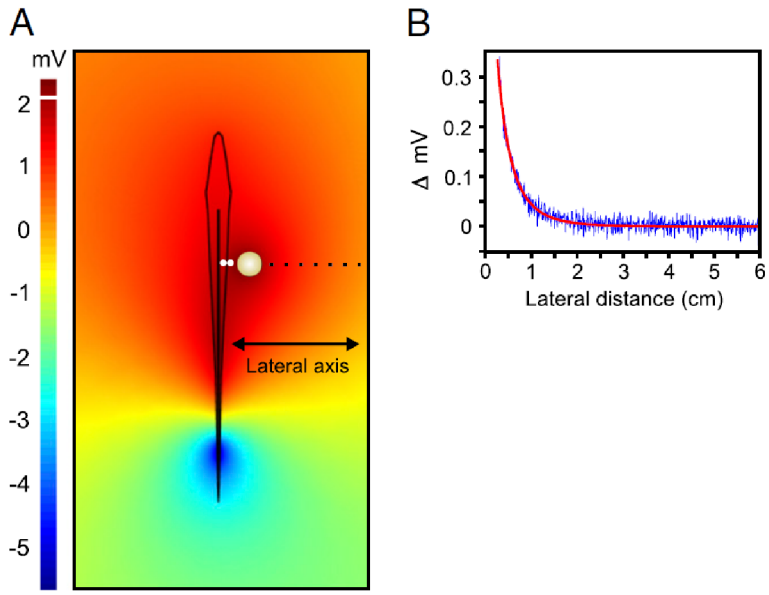

Figure 1 **Object distance and the electrosense**. A) A model plot of the electric potential (mV) produced by the self-generated electric field of A. leptorhynchus. The presence of conducting objects, such as this brass sphere ($r = 0.635$ cm), cause a local increase in the electric potential as measured by a transdermal recording dipole (white dots). Natural examples of relative conductors include aquatic plants, predators and prey. B) The recorded stimulus-induced change in transdermal potential (blue) is plotted as a function of the brass sphere's lateral distance. The overlying red curve is the change in potential predicted by a previously existing model [55]. Signals of this form are considered in the following.

Results

Speed invariant coding of object distance. We recorded from 24 electroreceptor afferents (7 fish) whose range of spontaneous firing rates (100 to 400 Hz) was similar to that previously reported [52]. Although a function of object distance as expected, Fig. 2A demonstrates the remarkable fact that the firing rate of an electroreceptor afferent is practically independent of approach speed (regardless of object size - SI Appendix). In the absence of stimulation, fluctuations in electroreceptor afferent firing rate are normally distributed and thought to represent intrinsic noise [56, 57]. Illustrated in the context of this variability, Fig. 2B shows the largest difference in firing rate between the looming speed responses of Fig. 2A, plotted as a function of distance. These small discrepancies in rate are clearly insignificant as they are masked by the inherent fluctuations in spiking activity. Furthermore, speed induced variations to a distance-rate code are negligible when compared to the high firing rates over which the electrosensory afferents operate [52].

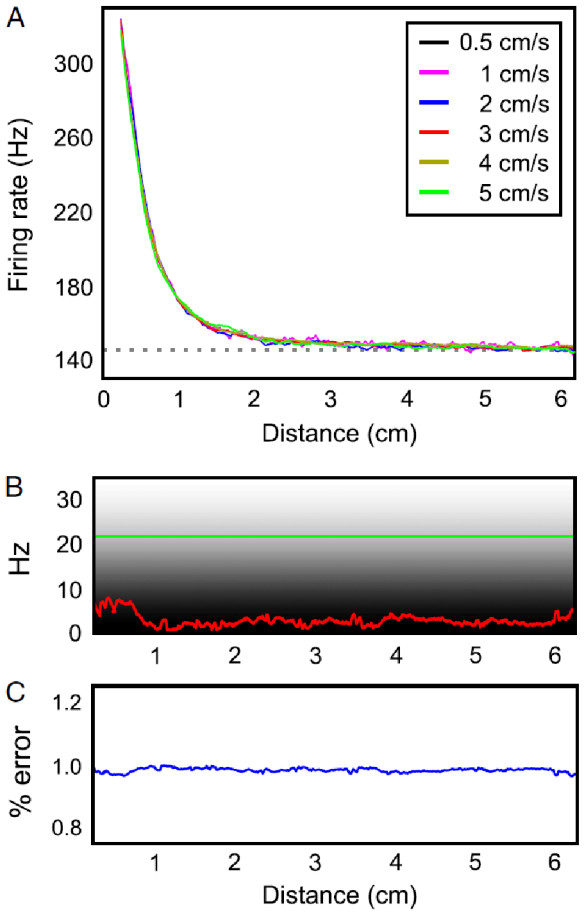

Figure 2 **Electroreceptor afferents encode object distance, invariant to approach speed.** A) The averaged responses of a single electroreceptor afferent to looming stimuli with approach speeds spanning an order of magnitude (0.5 to 5 cm/s). Remarkably, the firing rate is a function of object distance only and is invariant to approach speed. B) The maximum difference in firing rate for the approach speeds of Fig. 2A is plotted as a function of distance. The distribution of fluctuations in spontaneous firing rate, centered about the mean, is shaded and the value of one standard deviation is marked by the green line. This value (21.33 $\pm$ 5.5 Hz) was previously determined as an average over many electroreceptor units [52] for a bin-width of 32 ms. Note that our comparison with this data is justified since our firing rates were computed using a smoothing kernel of comparable duration (methods). C) At each point along the lateral axis, the differences from Fig. 2B are weighted as a percent error of the average firing rate at that distance. The error is small and essentially constant, highlighting the insignificance of any speed-related differences in firing rate.

At each point along the lateral axis, Fig. 2C shows the maximum differences from Fig. 2B plotted as a percent error of the averaged firing rate for that given distance. This measure of rate-code corruption was determined for all 24 cells in response to the looming stimuli, and an average error was computed. This global error measure showed no significant trend as a function of distance (SI Appendix), therefore we calculated a total average of 0.98%. At a distance of 6.25 cm from the fish's skin, the brass sphere from Fig. 1 causes a change in

transdermal potential of 0.15 μV, a signal weaker than the limit of behavioral detection [58]. The percent error measured at this point is not significantly different from when the sphere is 0.25 cm away, causing a change in transdermal potential of 350 μV. This confirms that minute discrepancies in firing rate, introduced by approach speed, are no more deleterious for a distance-rate code than endogenous noise acting in the absence of stimulation.

Speed invariance arises from power law adaptation. The electroreceptor afferents are not passive rate coders and show strong spike rate adaptation in response to sustained stimulation [59,60]. Spike rate, or spike frequency adaptation (SFA), is a ubiquitous and conserved feature of neural processing, which has been well-documented in systems ranging from invertebrate sensory neurons to mammalian cortex [61, 62]. A generic model of SFA consists of cellular- or circuit-level mechanisms that integrate the response of a neuron and exert negative feedback to control its output firing rate [63,64]. The different types of SFA observed experimentally are dictated by the specific form of the integrator, which is often described as a single exponential process [61, 65]. As an example, exponential SFA permits the electroreceptor afferents of A. leptorhynchus to act as selective filters for communication signals [60]. However, many neurons display multiple adaptive timescales, indicative of multi-exponential or power law adaptation [64, 66–71]. A wide range of adaptive timescales has also been identified in the electroreceptor afferents [59], prompting a demonstration that power law dynamics can account for the experimentally observed SFA [64]. Therefore, we investigated two existing SFA models of the electroreceptor afferents in an attempt to understand the observed looming speed-invariance.

Figure 3A shows the looming responses of an existing model of electroreceptor afferent activity which incorporates an exponential form of adaptation [56]. Previous experiments and modeling studies have shown that the time constant of exponential adaptation is very short ($\approx$ 10 ms) and can successfully account for spontaneous inter-spike-interval correlations, as well as responses to constant intensity stimuli and high frequency communication signals [56, 60, 72]. However, when processing looming signals, such rapid adaptation is not well suited for accurate distance estimation (SI Appendix). In fact, regardless of the choice of time constant, the

exponential adaptation model's firing rate is a function of both object distance and approach speed, confounding estimates of these values (SI Appendix). In this case, a decoder of firing rate must extract information about both the spatial and temporal features of a moving object from a scalar value, a problem for which no invertible mapping exists. Since the firing rate is a non-separable function of speed and distance (SI Appendix), it is not immediately clear how this response could be decoded so as to enable the accurate electrolocation observed in behavioral experiments [53, 54]. Therefore, we tried a model of SFA that incorporates a power law [64], in order to account for the weak SFA observed over longer time scales [59]. Figure 3B shows that the model responses, like the data, only encode distance information and are nearly invariant to approach speed. Power law adaptation is able to transform a neuron's response to non-stationary looming signals, and permits the formation of a well-defined map between changes in firing rate and the distance of a looming object. As shown in Fig. 3C, the firing rate of the electroreceptor afferents is also a linear function of looming stimulus intensity, until the signal becomes very strong and the response saturates. The power law adaptation model does not incorporate a saturating component and maintains a linear encoding for all intensity values (Fig. 3C). This adaptation model is based on a power law function with an exponent of negative one [64]. Below, we demonstrate analytically that this is the only form of adaptation able to modify a neuron's response to looming stimuli such that the firing rate is independent of speed. Using the same formalism, we show why the outputs of exponential adaptation models depend on speed, explaining the divergent responses seen in Fig. 3A (SI Appendix). The exponential adaptation model is not capable of rescaling the firing rate in response to a looming stimulus and cannot linearly encode stimulus intensity (Fig. 3D).

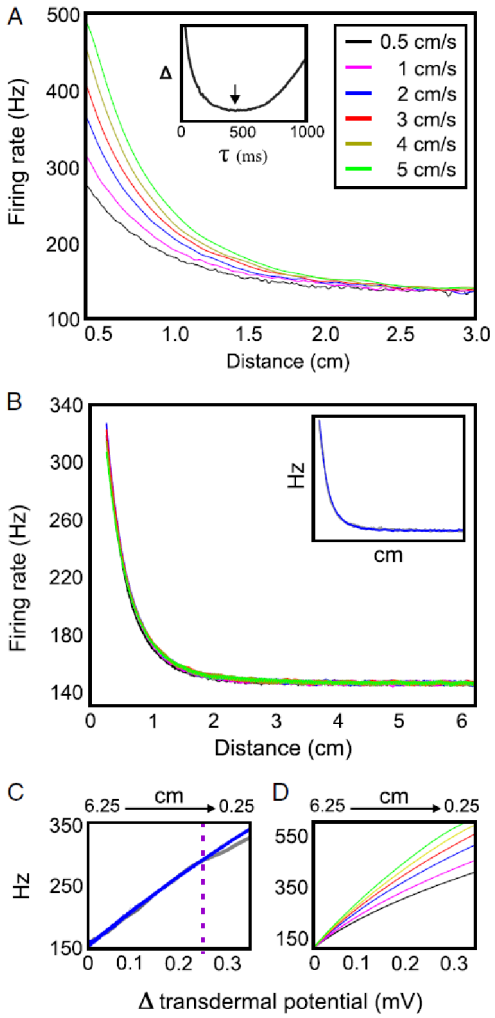

Figure 3 **Power law adaptation generates speed invariant responses**. A) Responses of an electroreceptor model with exponential adaptation [56] to our looming stimuli. Significant speed-induced discrepancies in firing rate occur for distances less than 2 cm, a range important to the fish during hunting and tracking behaviors [53] [54]. Since the estimated time constant derived from exponential models of adaptation (≈10 ms) performed poorly (SI Appendix), the model responses illustrated here were obtained using the best possible time constant of adaptation for our range of speeds (420 ms; inset), which was chosen to yield the smallest possible differences in firing rate (see also Fig. S3). B) The firing rates of an established power law adaptation model [64] to the same stimuli. In this case, firing rate is essentially a function of looming object distance only. The figure inset shows a model response (blue) overlaid onto the data of Fig. 2A (grey) with superb agreement. C) The electroreceptor responses (grey) and the power law model response (blue) are plotted against the intensity of the looming stimulus, displaying a linear relationship. Consistent with previous results [52], we see the data begins to saturate and deviates from the linear coding regime for high signal intensities. D) The exponential adaptation model responses are plotted as a function of stimulus intensity, clearly demonstrating the failure of exponential adaptation to produce linear coding.

Many studies describe the role of SFA as a means to filter out static and low frequency components of a stimulus [60] or to regulate a neuron's response to prolonged stimulation at various intensities [70, 71, 73]. With a few notable exceptions [68, 74, 75], little has been done to

investigate the role of SFA in processing natural, non-stationary signals. Our results show that power law adaptation implements a real-time sensory transformation, which shapes a neuron's transfer function to achieve a systems level coding goal. By removing the effects of speed, this transformation permits a primary afferent's firing rate to serve as a foundation for dynamic distance perception. Furthermore, although its effects on the response are neutralized, the approach speed can still be uniquely determined from the firing rate as described below.

Estimating approach speed from firing rate. The derivative of the electroreceptor afferent firing rate (λ), with respect to time, is given by $\dot{\lambda} = v \cdot d\lambda/dx$, where $v = dx/dt$ is the speed of the looming stimulus. Since λ is independent of speed, so is its spatial derivative. Therefore, at a fixed distance, the temporal derivative of firing rate is directly proportional to speed. For illustrative purposes, three different looming responses are plotted as a function of time in Fig. 4A. For each curve, a linear approximation to the tangent was evaluated at a distance of 1.5 cm: faster approach speeds produce steeper slopes. When evaluated at one particular distance, the firing rate's temporal derivative ($\dot{\lambda}$) provides a simple, linear encoding of the object's speed (Fig. 4A inset). Figure 4B shows $\dot{\lambda}$ as a function of lateral distance for all the looming speeds considered. Since $\dot{\lambda}$ is a function of both distance and speed, it can achieve the same value for different combinations of these two variables. Therefore, unambiguously extracting looming speed from $\dot{\lambda}$ relies on a downstream computation: a decoder must use the distance information contained in the firing rate in order to calibrate the speed estimate. Provided this occurs, an invertible mapping from $\dot{\lambda}(t)$ to the object's approach speed can be constructed. Physiological mechanisms exist that are well suited to decode temporal derivatives, such as synapses endowed with short-term depression and a variety of feed forward- and recurrent neural networks [76].

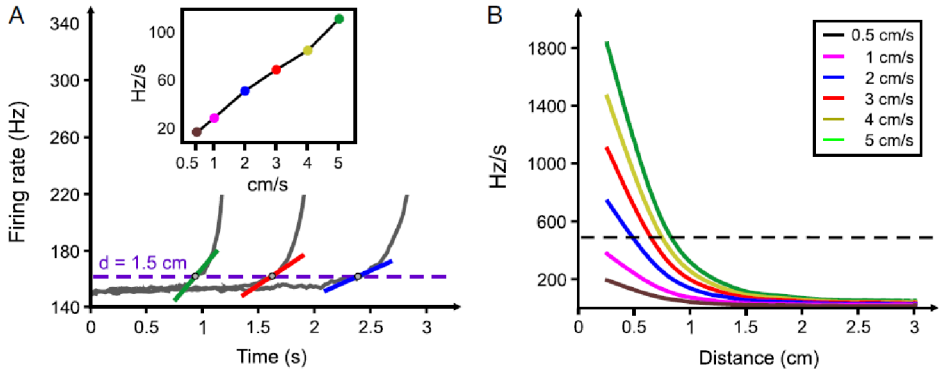

Figure 4 **Estimating approach speed from firing rate**. A) Electroreceptor responses from Fig. 2A, for 2, 3 and 5 cm/s looming stimuli, are plotted as a function of time (truncated for > 220 Hz to accommodate the inset). Linear approximations to the tangents of these three curves, evaluated at a distance of 1.5 cm, clearly demonstrate that a faster moving object causes a proportionally larger temporal derivative of firing rate. The figure inset shows a plot of the tangent slopes, evaluated at 1.5 cm, for the six speeds considered. At each fixed distance, there exists a linear relationship between firing rate and speed. B) The temporal derivative of all responses from Fig. 2A, plotted as a function of distance. The temporal derivative of firing rate is strongly influenced by the speed of motion as well as object distance. As illustrated by the grey dashed line, a given value of the rate of change in firing rate intersects curves generated by multiple approach speeds, and thus requires distance information to avoid ambiguity when decoding looming object speed.

Analysis of speed invariance. To further investigate the role of adaptation in speed invariance, we sought to formally understand the importance of the power-law in the model proposed by Drew and Abbott [64]. The neuron's membrane potential (V) is described by a leaky-integrate-and-fire neuron as follows,

$$\tau_m \frac{dV}{dt} = -V + I_0 + s(t) - [\eta * \lambda](t) \tag{1}$$

where τ_m is the membrane time constant, I_0 is the bias current, $s(t)$ is the stimulus-induced current, λ is the firing rate of the neuron, and η is the adaptation kernel which is convolved with the firing rate response. This neuron spikes when the membrane potential reaches a fixed threshold and then resets to zero. Consistent with Equation 1, it has been shown that the electroreceptor afferents express SFA through the action of a subtractive, hyperpolarizing current [60]. In any case, the following result pertains to the adaptation current, $[\eta * \lambda](t)$, whose dependence on speed does not rely on whether adaptation is subtractive or divisive.

We show that there exists a unique adaptation kernel which enables the output of a generic neuron to encode looming distance (x), regardless of the approach speed (v). From our experimental data and model simulations, it is clear that power law adaptation removes the dependency of λ on approach speed. We have seen that the firing rate is a linear function of stimulus intensity (i.e. object distance), so let $\lambda = c \cdot s(x)$. Above, looming distance was implicitly defined as $x(t) = x_0 - v \cdot t$. Through a simple change of variable, we reduce the problem to studying the net current as a function of the distance travelled ($x = vt$). As such, the temporal dynamics of (1) are determined by

$$\begin{aligned} I_{net} &= s(x(t)) - [\eta * \lambda](t) \\ &= s(x(t)) - \int_{-\infty}^{t} \eta(t - t^*)\lambda(t^*)dt^* \\ &= s(x) - \frac{c}{v}\int_{-\infty}^{x} \eta\Big(\frac{x - x^*}{v}\Big)s(x^*)dx^* \end{aligned}$$

This illustrates that there is only one suitable form of adaptation kernel that can be used to achieve the observed speed invariance: $\eta \equiv t^{-1}$, which yields,

$$I_{net} = s(x(t)) - c\int_{-\infty}^{x} \frac{s(x^*)}{x - x^*}dx^*$$

The reader can verify that the choice of $\eta \equiv t^{-1}$ results in a subtractive current that is simply a Hilbert transform of the stimulus, a common technique in signal processing to extract the envelope of a signal [77,78]. Interestingly, it has been shown that multiple adaptive timescales contribute to the encoding of low frequency envelopes generated by whisker motion in the rat vibrissae pathway [68]. It is worth noting that power law adaptation has been observed with exponents other than negative one [66]. Since the temporal disambiguation of stimulus intensity requires a unique adaptation kernel, it seems likely that different forms of power law adaptation correspond to different system-specific processing goals.

Realistically, looming motion may not always occur at a constant speed, an assumption the above argument relies on. The simple dependence of the net current on the stimulus suggests that invariance may arise more generally, i.e. for non-constant speeds. Therefore, we tested looming stimuli which accelerated or decelerated during approach. Under these conditions, we demonstrate that neurons displaying power law adaptation can still maintain invariant representations of object distance (see SI Appendix for data, simulations and theory).

The biophysics of adaptation. The success of adaptation in the above sensory transformation depends on its ability to act over different stimulus timescales. In general, adaptive processes can operate over many timescales, from tens of milliseconds to minutes [59, 79]. This capacity may arise from the action of numerous biophysical mechanisms such as voltage- and ion-gated channels [61, 63, 65, 80, 81], ion depletion and the action of electrogenic pumps [74, 82], synaptic transmission and short-term synaptic plasticity [74, 83], as well as the inactivation kinetics of ion channels [84–87]. Power law adaptation in spider mechanoreceptor afferents has been simulated with Hodgkin-Huxley (HH) neurons suggesting that the voltage-dependent gating of sodium and potassium channels form the biophysical basis of the power law transformation [66]. We confirmed that a HH neuron with standard parameters is capable of producing the observed speed invariance for the looming signals tested in our experiments (SI Appendix). All of these processes are common features of neural transmission, suggesting that power law dynamics may exist as an emergent property of interacting biophysical sources, encompassing a wide range of characteristic time constants. On the other hand, the fast exponential adaptation present in the electroreceptor afferents is likely controlled by a single source; the action of a voltage- or calcium sensitive potassium channel [60]. Although technical issues prevent us from conclusively demonstrating the subcellular mechanisms responsible for the different forms of adaptation, one thing is clear: the exponential and power law forms function cooperatively. While the fish navigates its environment, the amplitude modulations caused by electrolocation targets will not recruit fast exponential adaptation, whose cut-off frequency of 23 Hz exceeds their low frequency content (SI Appendix) [60]. However, when a conspecific emits a transient

communication signal, fast exponential adaptation ensures its selective encoding over electrolocation targets, setting a momentary precedence for social information. In this manner, the two forms of adaptation have effectively partitioned a stimulus frequency space, each operating in its own regime.

Discussion

Power laws appear at many levels of biological description, from single channel kinetics to human psychophysics [64]. The scale-invariance property of the power law likely explains its ubiquity, as it can easily conform to a large range of stimulus timescales present in an animal's environment [70, 71, 88]. By permitting the timescales of the stimulus to determine the dynamics of the response, power law adaptation can actively rescale a neuron's transfer function, imparting flexibility to a rate coding system. In the case of the electroreceptor afferents, adaptive rescaling allows a rate code to reliably transmit distance information about a looming stimulus, regardless of its approach speed. Where exponential adaptation fails, a power law transformation provides an elegant solution to an otherwise conflated sensory estimation problem. This is similar to the notion of a multiplexed neural code [89], in that it enables disambiguation of stimulus features that cannot be discriminated on a single response timescale. However, instead of different stimulus features being encoded into different timescales of the spiking response, distance and speed are simultaneously encoded through the action of adaptive processes that operate over extended timescales.

When an animal selects a behaviorally appropriate response to an approaching object, accurate estimates of speed and distance are fundamentally important. This has been made particularly clear in the looming responses of the locust, where representations of distance and approach speed form the substrates of a time-to-collision computation [23]. Different target cells in the electrosensory lateral line lobe (ELL) appear well suited to begin extraction of the distance and speed information present in the output of the electroreceptor afferents. ELL pyramidal cells can be divided into two broad classes: those which respond in a near linear manner to the electroreceptor afferent firing rate [90], and highly nonlinear cells that are very

sensitive to changes in firing rate [90, 91]. Therefore, we propose the linear class of pyramidal cells relay information about an object's distance from the skin, while the nonlinear class initiates extraction of approach speed from the temporal derivative of the firing rate. The midbrain target of the ELL pyramidal cells is the torus semicircularis, a structural analog of the mammalian inferior colliculus. In turn, the torus provides massive input to the optic tectum [20], an analog of the mammalian superior colliculus. Collision-sensitive neurons have been discovered in the optic tectum of frogs [92], suggesting that the differential responses of ELL pyramidal cells initiate distinct streams of information, which serve as the basis for tectal neurons to compute and initiate appropriate motor commands in response to looming stimuli.

It was recently demonstrated that a class of retinal ganglion cells can register the location of longitudinally moving objects independent of their speed [93], achieving the same effect that we have described for the electroreceptor afferents. It would be interesting to determine whether the biophysical mechanisms described in this paper also exploit the scale-free nature of power law dynamics, or whether another sort of computation can result in speed invariant localization.

Neural implementation of efficient coding strategies has been the subject of intense investigation. Unfortunately, it is not always easy to recognize or confirm that a particular coding strategy has been achieved. In the work presented here, understanding the advantage for neural coding was facilitated by a well understood context: precise knowledge about the nature of the inputs [55], the corresponding behavioural goals of the animal [53, 54] and the suggested encoding scheme [52]. The role of power law adaptation should be further explored in response to realistic, non-stationary inputs, including the envelope signals generated in the visual [94], auditory [95] and somatosensory systems [68]. The range of frequency content in these envelopes will draw out different timescales of adaptation at the cellular and circuit level that may support power law transformations. Can scale-free dynamics also optimize coding strategies in these sensory systems? How about higher levels of the central nervous system? Answers to such questions should enhance our understanding of the different functional purposes that adaptation and power law relationships serve for efficient neural coding.

Materials and Methods

A standard surgical protocol was performed to expose the hindbrain of A. leptorhynchus and all procedures were approved by the Animal Care Committee at the University of Ottawa (see SI Appendix for full experimental details). The fish were immobilized and mounted into a large tank of 27°C water with the electrical conductivity kept between 120-150 μS/cm. Glass micropipettes (filled with 3M potassium acetate; resistance 90-120 MΩ) were advanced through the cerebellum to take extracellular recordings from electroreceptor nerve afferents in the deepest layer of the ELL [29]. Firing rates for both electrophysiological data, as well as the models, were computed by convolving binary spike trains with a causal, 50 ms exponential kernel. Averaged firing rates were then computed from repeated presentations of the looming signal (10-20). All analysis was performed using custom scripts and available functions in MATLAB (Mathworks). We recorded the change in transdermal potential resulting from a looming brass sphere moving towards the recording dipole center. The brass sphere was attached to a thin plastic rod and mounted to the mobile platform of a Parker LP28 linear actuator, controlled by a Parker ViX 250 IM micro-stepping drive. The looming sphere saturates the tiny receptive fields of the electroreceptors directly in front of it [29]. During in vivo recordings, finding the exact center of the tiny electroreceptor receptive field center can be challenging. Furthermore, recordings from the fine electroreceptor afferents are difficult to maintain while trying to manually align the motor and position it within a given electroreceptor's receptive field. Therefore, using the stimulus shown in Fig. 1B, we directly modulated the amplitude of a fish's electric field in order to simulate electrosensory looming stimuli. This guaranteed that looming approach was simulated exactly over the receptive field center of the particular electroreceptor afferent whose activity was being recorded.

2.2 A neural code for looming and receding motion is distributed over a population of electrosensory ON and OFF contrast cells

Clarke SE*, Longtin A, Maler L. (2014). Journal of Neuroscience 34: 5583-5594.

Contributions: S.E.C., A.L., and L.M. designed research; S.E.C. performed research; S.E.C. analyzed data; S.E.C., A.L., and L.M. wrote the paper. *S.E.C is corresponding author.

Significance: The electrosensory ON and OFF cells, like their retinal counterparts, are known to selectively encode increases and decreases in sensory contrast relayed by the EAs. However, in both systems the definition of these fundamental cell types has always been somewhat ambiguous. Are these cells seletive for signal intensity, or are they sensitive to the signal's rate of change? Typically ON and OFF cells are identified by simple step-up and step-down inputs, which gives little insight into their natural coding properties over time. Conversely studying the response to random signal intensity leads to activation of both cell types and highly variable, non-repeating responses. Smooth motion toward the body followed by reversal and motion away from the body provide the perfect test of ON and OFF cell selectively. Using a positive contrast stimulus (brass) and a negative contrast stimulus (plastic) for looming and receding motion generates four scenarios: positive contrast and positive temporal derivative (looming brass); positive contrast and negative derivative (receding brass); negative contrast and negative derivative (looming plastic); negative contrast, positive derivative (receding plastic). We show that ON and OFF cells are not bound strictly to the sign of the signal contrast and are instead highly selective for its temporal derivative. As a result, motion reversal leads to dramatic switches between the ON and OFF cell populations, creating a distributed representation of motion that adds context to a neural code built upon scalar firing rates.

the place of original publication and, for the first six months after publication, refrain from making the work publicly available. Authors are automatically granted permission to use an article in a thesis and/or dissertation."

Abstract

Object saliency is based on the relative local-to-background contrast in the physical signals that underlie perceptual experience. As such, contrast detecting neurons (ON/OFF cells) are found in many sensory systems, responding respectively to increased or decreased intensity within their receptive field centers. This differential sensitivity suggests that ON and OFF cells initiate segregated streams of information for positive and negative sensory contrast. However, while recording in vivo from the ON and OFF cells of Apteronotus leptorhynchus, we report that stimulus motion reversal triggers paradoxical responses to electrosensory contrast. By considering the instantaneous firing rates of both ON and OFF cell populations, a bidirectionally symmetric representation of motion is achieved for both positive and negative contrast stimuli. Whereas the firing rates of the individual contrast detecting neurons convey scalar information, such as object distance, it is their sequential activation over longer timescales that track changes in the direction of movement.

Introduction

The ability to measure sensory contrast is a cornerstone of perceptual experience: by encoding coherent patterns of contrast, nervous systems can assemble spatiotemporal representations of distinct stimuli in their environment. In order to detect relative differences in these physical signals, many diverse sensory systems possess two subsets of modality-specific neurons that are selective for either increased or decreased intensity within their receptive field (RF) centers. Traditionally termed ON and OFF cells in the vertebrate [121] and invertebrate [110] visual systems, these distinct classes have been documented in other sensory modalities including audition [125] and chemoreception [114]. Under static conditions, ON retinal ganglion cells

(RGCs) are excited by increased illumination at their RF centers (positive contrast), whereas OFF RGCs are excited by decreased illumination (negative contrast). Conversely, ON RGCs are notably supressed by negative contrast at their RF centers, and OFF RGCs are supressed by positive contrast. These classic observations suggest that ON/OFF cells act as labeled lines, which initiate parallel pathways for positive and negative visual contrast information [121]. However, Geffen et al. [107] provide preliminary evidence that ON/OFF cell contrast coding is not as simple as it seems.

A population of ON/OFF neurons also operate in the electrosense of gymnotiform fish, such as A. leptorhynchus [91]. During electrolocation, these fish sense objects as local amplitude modulations to a self-generated electric field: the electric organ discharge (EOD) [20]. These changes in EOD amplitude are encoded by cutaneous electroreceptors, whose afferents project topographically to pyramidal cells in the electrosensory lateral line lobe (ELL) [19]. E (ON) type pyramidal cells receive direct excitatory input from the electroreceptor afferents [32] and respond to increased EOD amplitude at their RF centers [91]. The same electroreceptor afferents also project indirectly to I (OFF) cells via local inhibitory interneurons [32]. Disynaptic inhibition implements a sign inversion on the input, creating electrosensory contrast neurons that are selective for decreases in EOD amplitude [91]. E and I cell pairs are arranged in columns and share joint receptive fields, which display the same center-surround organization as the iconic ON/OFF retinal ganglion cells [19, 121]. The functional analogy between the electrosensory and visual system ON/OFF cells has been previously emphasized [20, 34] and, until now, E and I pyramidal cells have been thought to act as strict labeled lines for positive and negative contrast intensity.

By presenting motion stimuli that reverse direction within their RF, we analyzed the role of the electrosensory ON/OFF cells as the neural basis of sensorimotor behaviours, such as the electromotor response [109] and prey capture [54]. We show that 'labeled lines' are too rigid a coding scheme for electrolocation and the perception of motion.

Materials and Methods

As previously described [96], surgery was performed on adult fish (male and female) to expose the caudal cerebellum overlying the ELL. All surgical procedures were reviewed and approved by the Animal Care Committee at the University of Ottawa. Fish were mounted into a large tank of water (27°C; 100-120 μS/cm) and a custom holder was used to stabilize the head during recordings. Their tails were tethered in position with thread to avoid any significant displacement of the body due to the hydro-mechanical effects caused by looming/receding motion. The fish were monitored for signs of stress and allowed time to acclimatize before commencing our stimulus protocols.

Extracellular recordings were obtained from pyramidal cells of the centrolateral map of the ELL [19]. This map was chosen because its neurons respond well to object movement [19] and have large RFs that are easy to locate [29]. After locating a cell's RF center using a local stimulus dipole, we classified it as E or I based on its response to EOD amplitude increases and decreases respectively [91]. We then mapped out the RF center, which yielded spatial spreads consistent with anatomical estimates previously generated for the centrolateral map [29]. The baseline firing rates of the recorded E and I pyramidal cells (9.3-20.2 Hz; $N_E = 15$, $N_I = 10$) demonstrate they are the superficial and intermediate types [19, 100]. Next, according to cell type, a plastic or brass sphere was mounted to an electromechanical positioner, controlled by outputs from our recording software. The selected sphere was aligned with the cell's RF center along the lateral body axis, and stimulation consisted of ten repetitions of a continuous loom/recede sequence at a speed of 2 cm/s, chosen as an intermediate value from locomotion studies [53, 54] and prey escape behaviors [118]. This stimulation protocol was then repeated with the other sphere. In some cases, we were able to simultaneously record from E/I cell pairs and directly compare their differential responses to object motion. For 23 of the 25 pyramidal cells used in this study, the same looming/receding sequence was repeated with a 7 second pause at the skin before reversing and returning to the initial position.

We also studied the responses of E and I cells to reversal of motion within their RFs for stimuli moving parallel with the longitudinal body axis. For these experiments, the spheres were positioned at a fixed lateral axis distance of 0.5 cm, and, starting caudal of the RF,

travelled 3 cm into the RF centre followed by reversal back to the initial position ($N_E = 3$, $N_I = 2$).

Estimation of stimulus-induced firing rates is not a trivial problem, since our dynamic stimuli drive nonstationary inter-spike-interval (ISI) statistics in the ELL pyramidal cells. To estimate the underlying rate responses, we initially applied a smoothing algorithm that selects an optimal and variable kernel bandwidth, determined locally in time over the course of our looming/receding stimulus [97]. This method produced response trends that are readily grasped, making effective visual aids. Although partially due to averaging variable responses to the repeated stimulus, the peak firing rates experienced during bursting are underestimated by the algorithm, which cannot fully capture the abrupt transitions between different modes of spiking (e.g. burst spiking to quiescence). This is not entirely surprising since the algorithm relies on the premise that the ISIs are Poisson distributed; although ELL pyramidal cell spiking can be modeled as a renewal process, burst spiking significantly alters the ISI distributions. Therefore, we used a fixed 30 ms Gaussian kernel that produced peak firing rate responses consistent with previous studies on burst spiking in ELL pyramidal cells [44,96]. Responses to ten consecutive loom/recede sequences were averaged together to obtain the firing rate (FR), which was normalized as a proportional change in baseline firing rate (μ_{FR}):

$$\Delta FR = \frac{FR - \mu_{FR}}{\mu_{FR}}$$

These values were then converted to a stimulus-induced, percent increase or decrease in firing rate ($\%\Delta FR$).

For recordings from the primary electroreceptor afferents, glass micropipettes (filled with 3M potassium acetate; resistance 90-120 MΩ) were advanced through the cerebellum to take extracellular recordings from the electroreceptor nerve in the deepest layer of the ELL's centrolateral map (N = 25, 7 fish). While recording in vivo, we directly modulated the EOD amplitude with custom-made stimulus dipoles, in order to recreate the electrosensory signals generated at a pyramidal cell's RF center by the looming/receding spheres [104]. For the sake

of consistency with the pyramidal cell analysis, firing rates were computed by convolving the spike train data with a 30 ms Gaussian kernel. Averaged firing rates were then computed from repeated presentations of a looming signal and were taken over 10-15 repetitions.

The large range of baseline firing rates of the electroreceptor afferents produce noticeable bias in the $\%\Delta FR$ measure used for the ELL pyramidal cells. Consequently, for each afferent, we use a measure of change that is normalized to the largest stimulus-induced difference between the cell's response and it baseline firing rate. When the firing rate increases (brass stimulus) we implicitly use the maximum definition of our gain measure and, when the firing rate decreases (plastic stimulus), the minimum definition is used:

$$\Delta FR_{norm} = \frac{FR - \mu_{FR}}{max[FR] - \mu_{FR}}$$

or

$$\Delta FR_{norm} = \frac{FR - \mu_{FR}}{min[FR] - \mu_{FR}}$$

The analysis in Fig. 4 is the only time the ΔFR_{norm} measure is applied to the looming/receding pyramidal cell data, since it allows for direct gain comparison with the electroreceptor afferent data. It should be noted that electroreceptor afferents with extreme firing rates (< 150 Hz and > 400 Hz) were excluded from the analysis due to firing rate saturation effects in the near-field. We modified a pre-existing E cell model [46], in order to determine whether it could explain the results observed in response to motion reversal. The model was designed to capture the nonlinear interactions between a pyramidal cell's soma and its proximal dendrites, which generates burst spiking, like that observed in vitro. The parameters used in the model were left unchanged; only gain and bias current were manipulated to generate baseline and peak firing rates, comparable to those observed in vivo. In addition, we added a source of exponential spike frequency adaptation to this model, which was calibrated at the physiological adaptation time constant of 0.2 s obtained for the CLS map [113].

Given a single output spike train from the model, convolution with the 30 ms Gaussian

kernel results in choppy estimation of the firing rate when the motion stimuli are weak and the ISIs are long. To obtain smooth firing rates from the deterministic spiking model, different realizations of Gaussian noise ($\rho(t) = 4 \cdot e^{-t^2}$) were added to the subthreshold membrane potential dynamics. The resulting jitter in the model spike times better resembles the noisy responses of E cells and also allows us to average over many individual trials to obtain a smooth firing rate estimate after convolution with the Gaussian kernel. We did not perform any simulations for I cells because their local circuitry is far more complex [34] and has not been adequately modeled.

Results

Consistent with contrast coding definitions, when non-conducting objects (e.g. rocks) move across the sensory surface of A. leptorhynchus and into the RF of an E/I pair, the I cell responds to the negative contrast with an increase in firing rate, while the E cell is suppressed. Likewise, positive contrast caused by conducting objects (e.g. plants and prey) moving into the RF of an E/I pair, evokes an increased firing rate from the E cell, while the I cell's activity is depressed [31, 103]. During navigation, objects in the environment moving towards the body (looming) are a common occurrence. We have shown that a looming, positive-contrast inducing stimulus causes the firing rate of the electroreceptor afferents to increase, which encodes changes in object distance [104]. In agreement with known physiology, the positive contrast is expected to evoke a strong response in the E cells, while inhibiting I cell activity. Likewise, a looming, negative-contrast inducing stimulus will cause decreases in electroreceptor afferent firing rates, which lead to strong I cell responses and a decreased firing rate in the E cells. Therefore, it appears that looming object motion generates responses that adhere to the conventional definitions of contrast coding.

Looming stimuli are of obvious importance in the visual system and have been extensively studied [105]. Interestingly, far less attention has been devoted to how the visual system might encode receding movements, even though such stimuli occur naturally. In the electrosense, both looming and receding signals are readily processed by gymnotiform fish, as evidenced by the

electromotor response designed by Heiligenberg [53, 109]. In this sensorimotor task, a fish actively tracks the motion of swinging plastic rods (non-conductive objects) that loom and recede relative to its body. Like the visual system's optomotor response, the electromotor response relies on the system's ability to discriminate features of the moving stimulus such as distance, speed and the direction of movement, in order to initiate appropriate motor commands [53,109]. This experiment was inspired by the tendency of gymnotiform fish to track plants (conducting objects) swaying in water currents. Therefore, we designed our looming/receding stimulus protocols with both negative- and positive-contrast inducing stimuli (plastic spheres and brass spheres) to mimic conditions of Heiligenberg's experiments and the natural behaviours that inspired them (Fig. 1A).

Responses of I and E cells to looming/receding trajectories I cells respond with an increased firing rate as the plastic object looms towards their RF centers (Fig. 1B, top). On average, the peak firing rate of I cells increased by 770.44 ± 112.66% from baseline levels and was marked by strong bursting. ELL pyramidal cells have an intrinsic burst generating mechanism that is activated by low frequency signals [39], such as those induced by looming motion [104], and which generates ISIs < 10 ms [44, 96]. Using this criterion, we sorted burst spikes from tonic spikes, allowing us to calculate the fraction of all action potentials contributed by the burst mechanism [44]. The burst fraction (BF) of I cells increased dramatically when the plastic sphere drew close to the fish's skin, from 0.21 ± 0.09 to 0.78 ± 0.13.

I cells were not excited by the negative contrast created by the receding plastic sphere. Instead, upon direction reversal, I cells immediately stopped bursting (BF: 0.026 ± 0.12) and their firing rates dropped significantly to -91.05 ± 15.28% of baseline (Fig. 1B, top), calculated as an average rate over the first 0.5 cm of withdrawal. In many cases, the I cells were reduced to complete silence, followed by a slow recovery to baseline as the spheres moved beyond detectable limits (3-4 cm; [55]). Since E cells are the only other ELL projection neurons

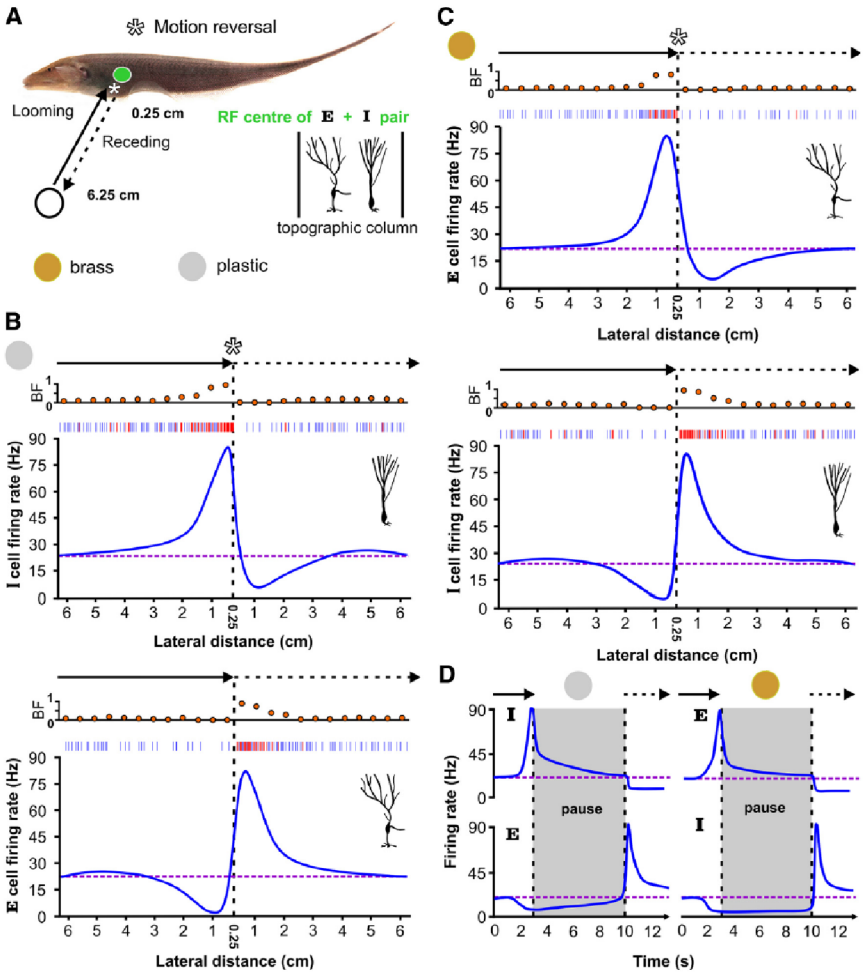

Figure 1 **E (ON) and I (OFF) cells cooperatively encode object movement along the lateral body axis.** A) Starting from an initial position of 6.25 cm from the skin, plastic or brass spheres loom towards the RF center of an E and I cell pair, stopping at 0.25 cm. The sphere then immediately recedes back to the initial position (velocity ± 2 cm/s and acceleration ± 150 cm/s^2 during reversal periods). This sequence was repeated to mimic the swinging of plastic rods during a behavioural tracking experiment [53], while we recorded in vivo from E and I cells. B) Upper panel: As expected from static conditions and labeled line coding, the firing rate of an I cell increases as the plastic object approaches the cell's RF center. Although there are increases in both tonic (blue) and burst spiking (ISI < 10 ms; red), the top raster plot shows that burst spikes dominate at closer range as reflected by the dramatic increase in burst fraction (BF). However, as the sphere reverses direction, and begins to recede from the body, the strong bursting is immediately silenced and the I cell firing rate decreases sharply, dropping below baseline levels (purple dashed line). Note that the smoothing algorithm underestimates the peak firing rates; nevertheless, it is an effective aid for visualizing the trends. Lower panel: As the plastic sphere looms towards an E cell's RF center, the firing rate is suppressed due to the local decrease in electrical contrast. As the plastic sphere withdraws, the E cell suddenly explodes into action with increased bursting and tonic spiking, despite the fact that the local sensory contrast is still negative. The E cell firing rate gradually returns to baseline as the sphere recedes, effectively mirroring the response of the I cell during the plastic sphere approach. C) For a conducting object, like the brass sphere, we see that the E and I cells (upper and lower panels) switch motion coding roles. D) An object may come to rest near the fish, and then, at some future point, recede. To ensure E and I cell switches still occurred, we tested the same motion sequence, but delayed receding by 7 seconds after looming. Despite the changing state of adaptation in the system, the switch responses are still observed.

responding to EOD amplitude modulations, we recorded their activity in response to the same stimulus (Fig. 1B, bottom). As anticipated, a looming plastic sphere strongly inhibited E cells (-90.24 ± 16.28%) due to the locally decreased EOD amplitude. However, when the plastic sphere suddenly reversed its motion, strong burst responses were immediately evoked in E cells (BF: 0.18 ± 0.09 to 0.76 ± 0.14). Tonic spiking also contributes to the observed peak firing rates (768.65 ± 106.28%), which were followed by a smooth decline back to baseline levels. The increased E cell firing rates to the receding plastic sphere occur under negative electrosensory contrast conditions - a strong violation of contrast coding definitions.

As anticipated, E cells encoded the looming brass sphere with an increase in firing rate, reaching a peak of 770.82 ± 115.13%, marked by increased burst discharge (Fig. 1C top; BF: 0.18 ± 0.09 to 0.78 ± 0.15). However, immediately upon direction reversal, E cells cease to discharge (-90.85 ± 14.01%), and their firing rates gradually climbed back to baseline levels. As shown in Fig. 1C (bottom), the baseline firing rate of I cells was almost completely suppressed by the looming brass sphere (-91.97 ± 15.50%), with an associated decrease in burst fraction (0.025 ± 0.14). As was the case with E cell responses to the receding plastic sphere, I cells show a switch in their preferred contrast and encode the withdrawal of the brass sphere by massively increasing their firing rate (781.41 ± 106.23%) and burst fraction (0.21 ± 0.09 to 0.83 ± 0.11). As the brass sphere withdrew, the I cell firing rates gradually relaxed back to baseline levels.

Although all receding motion in the environment is technically preceded by looming, an object may come to rest near the fish, and then recede at some future point. Detailed studies of electrosensory images from free-swimming A. leptorhynchus confirm their natural tendency to hover near an object and then move on [17]. To test if the E and I cell switches would still occur, we repeated the same motion sequence, with the exception of a pause of 7 seconds after looming, before beginning to recede. The E and I cell firing rates clearly adapted during the pause period but the switch response upon motion reversal was still observed, despite the delay (N = 25; Fig. 1D). Although not acquired systematically for all cells, hold times of 1, 2, 3, 5 and 10 seconds were also tested, yielding no change in switch behaviour (data not shown).

The peak firing rates experienced during looming and receding motion strongly correlate with the baseline firing rate of the cell (Fig. 2A, left). The cellular and/or network mechanisms that control the baseline firing rates of ELL pyramidal neurons are not well understood and we are presently unable to explain this correlation. In the following, this trend is significantly

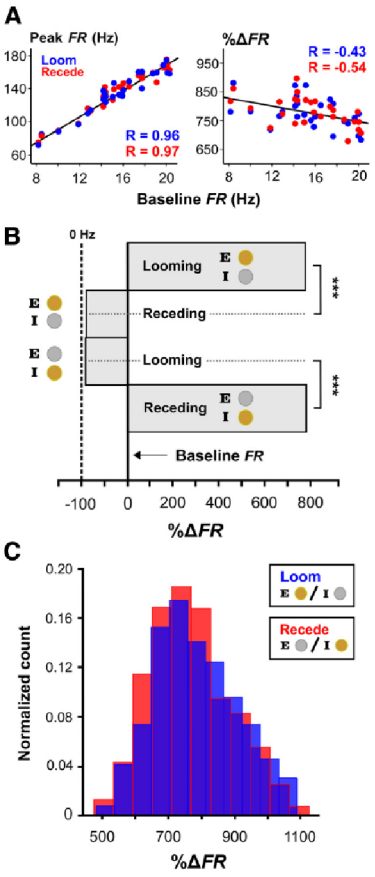

Figure 2 **E and I cell responses to non-preferred receding stimuli match E and I cell responses to preferred looming stimuli** A) The averaged peak firing rates in the presence of the stimulus are plotted against baseline firing rates for each pyramidal cell (left), showing the linear relationship between these variables (correlation coefficients shown in blue and red). By considering these responses as proportional changes in firing rate relative to baseline values, we see the trend is significantly weakened (right). B) The normalized responses of E/I cells to looming brass/plastic spheres are significantly different from their responses to receding brass/plastic spheres. Similarly, E/I cell responses to the looming plastic/brass spheres are significantly different from their responses to the receding plastic/brass spheres. Error bars (standard error of the mean) were omitted in these graphs since the averages were done for hundreds of individual responses, with relatively small standard deviations compared to the mean, resulting in barely visible lines. C) Histogram distributions of the peak firing rates, which were measured as a normalized percent change from baseline spiking rates. The null hypothesis that, the looming responses under conventional contrast conditions are the same as the receding responses under non-conventional contrast conditions, could not be rejected (two sample KS test, $\alpha = 0.05$, p = 0.34). These results suggest that the receding responses are a mirror of the looming responses, and that combined E/I cell activity form the basis for a bidirectional representation of motion.

reduced by considering proportional changes in firing rate relative to baseline (Fig. 2A, right). The distributions of peak discharge rates for the E cells in response to looming brass and the I cells in response to looming plastic, were not significantly different (two-sample KS test, $\alpha = 0.05$, $p = 0.84$). Likewise, the distribution of peak discharge rates of the E cells in response to receding plastic and the I cells in response to receding brass, were not significantly different either (two-sample KS test, $\alpha = 0.05$, $p = 0.32$). Therefore, we grouped E and I cell responses together to form two categories: pyramidal cell responses to a preferred looming object and pyramidal cell responses to a conventionally, non-preferred receding object (Fig. 2B, C). The distributions of peak firing rates for these two categories were not significantly different (two-sample KS test, $\alpha = 0.05$, $p = 0.34$). Effectively, the pyramidal cell responses to a non-preferred receding object mimics the firing rate produced by that same pyramidal cell in response to the approach of a preferred object. By utilizing both electrosensory contrast channels, a bidirectional representation of a moving object's distance is achieved. This more complex code requires switching between E and I cell activity in a controlled manner, precisely at the time of direction reversal.

Responses of electroreceptor afferents to looming/receding trajectories. Although we have shown that conventional contrast coding is not sufficient for electrolocation, we still do not have a satisfying account of why this coding paradigm fails. After all, the EOD amplitude modulations are symmetric and unambiguously reflect object distance, regardless of whether it is looming or receding (Fig. 3A, B top). If the electrical contrast still has the correct sign and the physical signal is bidirectionally symmetric to begin with, why does the system abandon well-defined contrast labels?

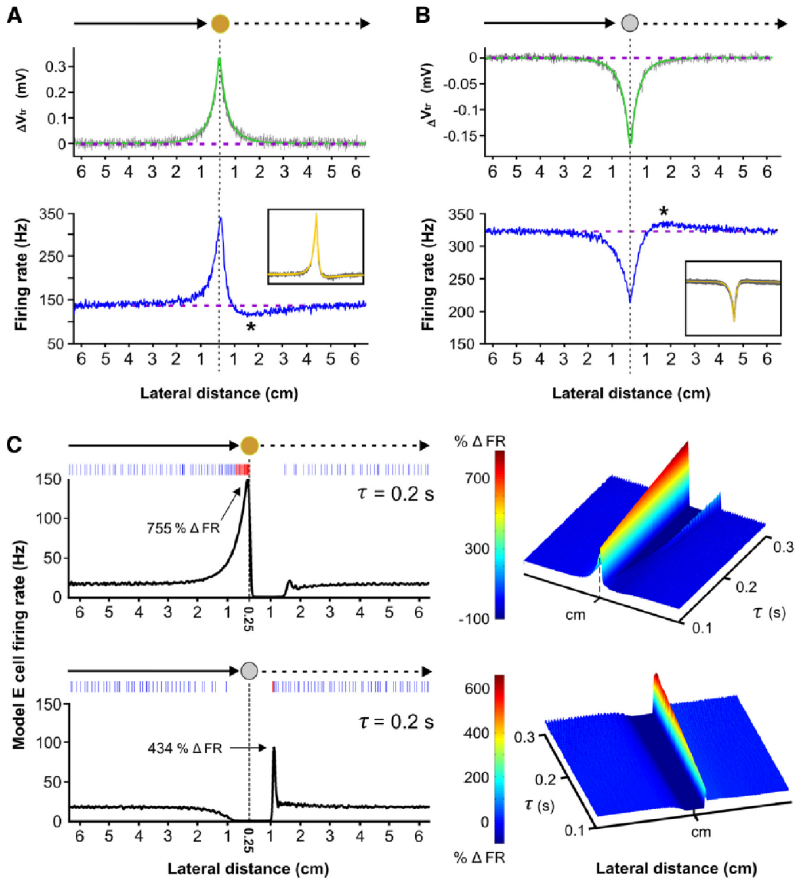

Figure 3 **Computation at a cost: adaptation introduces ambiguity into a simple intensity-rate code for object distance** A) Top: Averaged stimulus-induced change in transdermal potential (ΔV_{tr}) recorded for the looming/receding brass sphere. The modeled physical signal (green) is symmetric with respect to distance [55], which we confirmed experimentally (grey). Bottom: Conversely, the averaged response of an electroreceptor afferent to the same loom/recede sequence is strongly skewed for brass withdrawal. The asterisk marks the average distance where the firing rate dropped below baseline and reached a minimum (1.75 ± 0.11 cm). As shown in the boxed inset, this asymmetry is predicted by a model of power law spike frequency adaptation (yellow) which is superimposed onto many realizations of electroreceptor afferent responses (grey). Despite being essential for looming distance estimation [104], the presence of SFA in the electroreceptor afferents prevents a well-defined distance-rate code under motion reversal conditions. B) Top: Averaged stimulus-induced change in transdermal potential recorded for the looming/receding plastic sphere. Bottom: The electroreceptor afferent data and the power law adaptation model show that a directional skew is also introduced for receding non-conducting objects, where the averaged position of the overshoot maximum was determined to be 1.77 ± 0.09 cm. C) Using our electroreceptor afferent spike train data as input, we tested whether adaptation at the level of the ELL pyramidal cells could explain the looming/receding responses observed in vivo. Simulations were performed using a previously developed bursting model [46], to which we added a single-timescale (τ) adaptation current ([113]; Methods). The model response to the looming brass resembles the *in vivo* data, producing strong burst discharge (see raster). Upon brass withdrawal, there is a complete suppression of the model E cell responses (only observed when adaptation is added to the model). At low values of τ the model E cell fails to produce a sharp cessation in firing rate upon brass reversal and continues to discharge into the receding response, reminiscent of the skewed electroreceptor afferent firing rates (right surface plot). In response to the looming plastic sphere, the model E cell shows an expected decrease in firing rate for all values of τ. Upon plastic withdrawal, adaptation generates a single rebound burst (see raster) but it is delayed and fails to match the prolonged bursting and increased tonic spiking observed in our experiments for any value of τ (right surface plot). Adaptive effects are clearly an important component of E and I cell switches but are not the whole explanation. Note that adaptation introduces a slight rebound response upon recovery from brass withdrawal that is not observed in vivo.

Spike frequency adaptation (SFA) is present in many neuron types. There are two different forms present in the electroreceptor afferents, exponential and power law [64]. We have demonstrated that the power law form of SFA is essential for precisely encoding the changes in distance of a looming brass sphere into the firing rates of the electroreceptor afferents [104]. Since spike frequency adaptation has been shown to introduce directional selectivity in locust visual neurons [61], we suspected that adaptive processes in the electroreceptor afferents would cause asymmetrical firing rates for looming versus receding motion. We tested and confirmed this conjecture by stimulating the electroreceptors with the same loom/recede motion profile (see Methods). Electroreceptor afferent firing rates increased dramatically in response to the looming brass spheres, driving strong adaption (Fig. 3A, bottom). Upon sudden withdrawal, the signal intensity diminishes; yet strong adaptation is expected to persist, suppressing the already decaying firing rate below baseline levels, reaching a minimum at 1.75 ± 0.11 cm. Due to the decreased spiking activity, adaptation strength subsides and the electroreceptor afferent firing rates return to baseline values. An equivalent response pattern is seen in the electroreceptor afferent responses to the looming/receding plastic sphere (Fig. 3B, bottom). The rate of afferent discharge decreases in response to the looming plastic sphere and adaptation strength decreases accordingly. During plastic withdrawal, the local contrast becomes less negative and the firing rate of the electroreceptor afferents increase, which is expected to momentarily overpower the reduced adaptation strength. This results in an overshoot of the baseline firing rate, which reaches a maximum at 1.77 ± 0.09 cm. As adaptation strength recovers, the electroreceptor afferent spiking is brought back to baseline levels. We confirmed that these skewed responses arise in a generic model of power law adaptation [64], which successfully captures the looming responses of the electroreceptor afferents (Fig. 3A, B bottom; insets). Although power law adaptation is essential for the formation of a well-defined temporal code between firing rate and the change in looming object distance [104], it comes at a cost - a directional asymmetry that distorts a simple distance-rate code for receding stimuli at the primary stage of sensation. This appears to be remedied in the ELL, where a symmetrical representation is assembled through the cooperative activity of ON and OFF cells.

It is difficult to envision the neural basis of the strong, nonlinear gain displayed by E and I cells to motion reversal. The simplest possibilities are the intrinsic bursting dynamics of ELL pyramidal cells and/or the dynamics associated with their afferent inputs (excitatory and inhibitory). Since adaptive gain control has been implicated in the anticipatory responses of ON/OFF RGCs cells to moving stimuli [101], we tested whether adaptation could explain the counter-intuitive contrast coding displayed by the electrosensory ON and OFF cells. It has been shown that E and I cells exhibit spike frequency adaptation in response to step increases or decreases in EOD amplitude respectively [100,113]. Detailed cellular analyses of this inhibition are not available but estimates of the adaptation time constants exist for the cell types used in our study [113]. From the peak, stimulus-evoked response, it was found that E cells adapted exponentially with an estimated average time constant of 200 ms. We incorporated adaptation into an established dynamical model of a bursting E cell [46] and used our electroreceptor afferent data as input for looming/receding simulations (see Methods). A physiological range of adaptation time constants (τ) was considered in order to assess the types of responses that could be expected in the population. In response to the looming brass sphere, the model shows increases in tonic and burst spiking (Fig. 3C, top), consistent with the in vivo data and the fact that the electroreceptor afferents strongly drive E cell activity in vivo and in vitro [32,91]. For almost all of the adaptation values, there is a sharp cessation in the model response as the brass sphere recedes. This also resembles our in vivo data and demonstrates that the adaptive skew in afferent firing rate, coupled with adaptation in the ELL, effectively suppress E cell output upon motion reversal.

In response to the looming plastic sphere, the model E cell firing rate decreases, as expected from our experiments. However, as the sphere recedes, the sharp recovery of the electroreceptor afferent firing rate only generates a single, delayed burst doublet or triplet (Fig. 3C, bottom). This model response is very distinct from the receding responses seen in vivo, where higher peak firing rates are achieved, marked by immediate and prolonged burst spiking. Therefore, in vivo, the observed receding plastic response of an E cell cannot be solely attributed to the electroreceptor afferent input, sources of pyramidal cell adaptation or the dynamics of the

intrinsic burst mechanism. Additional studies are required to identify and isolate the source of the strong excitatory drive on E cells while the plastic sphere recedes.

During motion reversal, there exist an obvious contrast coding discrepancy between the stimulus-induced electrosensory contrast, the skewed electroreceptor afferent firing rates and the bidirectionally symmetric looming/receding responses displayed by the ELL pyramidal cells (Fig. 4A). For example, the electroreceptor afferents still discharge above baseline for the first 0.5 cm of brass sphere withdrawal, reflecting the strong positive contrast. Based on the electroreceptor afferent firing rates in response to the looming brass sphere, this should evoke strong discharge in E cells and inhibit I cells. However, the opposite occurs, E cell discharge is suppressed, while I cells discharge vigorously, deviating from the activity of the afferent inputs. For the remainder of withdrawal, adaptive skew causes the electroreceptor afferent firing rates to drop below baseline, producing an erroneous representation of negative contrast. Interestingly, this is expected to contribute to the sustained receding response in the I (OFF) channel, since, by the time the receding sphere is approximately 1.75 cm away from the fish, the pyramidal cell firing rates are not significantly different from the looming case (Fig. 4B). This suggests that the system returns to relying mainly on the input from the electroreceptor afferents to generate the remainder of the receding responses. Similarly, a temporary and paradoxical 'relabeling' of contrast is also observed for the first 0.5 cm of plastic sphere withdrawal, and, for distances greater than 1.75 cm, the pyramidal cell responses once again appear to depend on the feedforward drive of the electroreceptor afferents.

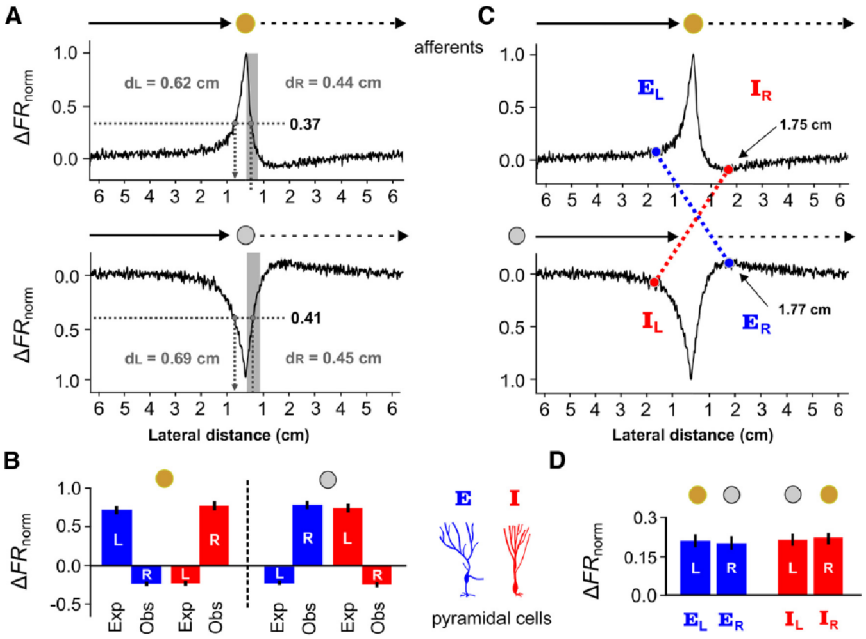

Figure 4 **Electroreceptor afferent firing rates cannot fully explain E and I cell responses to receding motion** A) Normalized firing rates of the electroreceptor afferents (ΔFR_{norm}, Methods) were averaged across the first 0.5 cm of withdrawal, in order to obtain a representative value of the response to the positive contrast created by the receding brass sphere. Due to the adaptive skew in firing rate, the distances (d_L and d_R) at which this value occurred were different for the looming and receding responses. The same procedure was repeated to obtain d_L and d_R for the looming/receding plastic sphere. B) Next, the average responses for E cells (blue) and I cells (red) were measured at d_L and d_R and plotted in a bar graph (± SEM) for the brass and plastic spheres. Left of dashed line: If the response of an E or I cell to a receding object was driven by the electroreceptor input, then the response to a brass sphere at $d_R = 0.44$ cm should be the same as their response at $d_L = 0.62$ cm. For an E cell (blue), the response expected from looming motion (Exp) is a substantial increase in firing rate, whereas the observed response during receding motion (Obs) is a decrease in firing rate. For an I (red) cell the expected response to the looming brass sphere is a decrease in firing rate, but its observed response to the receding brass sphere is a strong increase in firing rate. Right of dashed line: For the looming/receding plastic sphere, we compared the expected responses at $d_L = 0.69$ cm to the observed receding responses at $d_R = 0.45$ cm, obtaining similar results. The observed E/I responses to the receding plastic/brass spheres are as if the local contrast was the exact opposite for the first 0.5 cm of receding motion, despite the fact that the electroreceptors still signal the correct sign. C) The skewed adaptive responses displayed by the electroreceptor afferents likely contribute to the sustained receding responses of E and I cells. In response to the receding plastic sphere, the afferents produce a maximal rebound increase in firing rate at 1.77 cm from the skin (E_R). We found the distance (E_L) at which the looming brass sphere evokes the same increase in electroreceptor afferent firing rate. The crossed dashed blue line indicates the points at which the afferents provide the same increased drive to an E cell. If the E cell were principally driven by afferent input, then its receding response at 1.77 cm (E_R) should be equal to its looming response at E_L. Similarly, in response to a receding brass sphere, the afferents produce an under shoot in firing rate, achieving a minimum at 1.75 cm (I_R). We found the distance (I_L) at which the looming plastic sphere evokes the same decrease in afferent firing rate. The crossed dashed red line indicates the points at which the afferents would be giving the same decreased drive to an I cell. If the I cell were mainly driven by afferent input, then its receding response at 1.75 cm (I_R) should equal to its looming response at I_L. D) These averaged pyramidal cell response values are plotted in the bar graph (±SEM). The responses of an E cell at E_R and E_L are nearly equal, as are the I cell responses at I_R an I_L. This suggests that the skewed I_R electroreceptor afferent firing rates may once again contribute to the receding response in a manner consistent with the looming response.

Responses of E and I cells to reversing longitudinal trajectories While foraging, A. leptorhynchus often reverses its direction of motion when encountering prey [54, 117] or inanimate objects [102]. This sharp reversal will inevitably occur over the RF of some pyramidal cells. As an object approaches a RF along the longitudinal axis, the electroreceptor afferents will undergo spike rate adaptation as the signal intensity increases, such that, right after motion reversal, there is a skew in their response as the signal intensity decreases. We hypothesized that the asymmetries introduced by the electroreceptor afferents would also induce ON/OFF switches for objects that reverse direction when moving across the sensory surface. To test this idea, we moved brass and plastic spheres longitudinally into the RF center of a cell, reversed direction and then immediately moved back out, mimicking the relative motion experienced during natural scanning behaviors (Fig. 5A). As expected, E and I cells ($N_E = 3$, $N_I = 2$) responded respectively to the movement of brass and plastic spheres into their RFs with a peak firing rate of 498.14 ± 96.04%, and an associated increase in burst fraction to 0.47 ± 0.19. Upon direction reversal, the firing rate and the BF of the conventional detector immediately collapses (-81.56 ± 21.79%; BF: 0.041 ± 0.067), recovering to baseline as the object moves away (Fig. 5B). As usual, E and I cell firing rates are suppressed by approaching plastic and brass objects respectively (-84.77 ± 20.70%; BF: 0.012 ± 0.069). However, like the lateral axis, a moving object's reversal of direction along the longitudinal axis evoked strong responses in the opposing contrast detectors (487.49 ± 87.02%, BF: 0.50 ± 0.20) and an abandonment of conventional contrast coding.

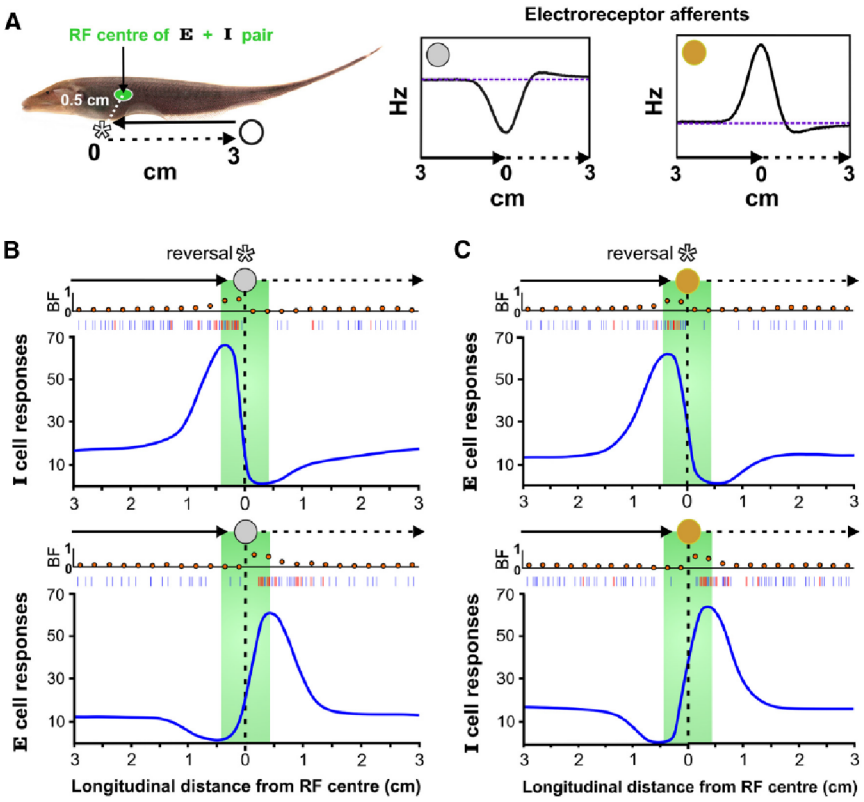

Figure 5 **E and I cells cooperatively encode object movement along trajectories parallel to the longitudinal body axis** A) Starting from an initial position of 3 cm caudal of the RF center and with the lateral axis distance fixed at 0.5 cm, the plastic or brass sphere (not shown to scale) moves into the RF center of an E or I cell, whose spatial spread is delineated by the green shading. It then immediately moves back to the initial position (velocity = ± 2 cm/s and acceleration = ± 150 cm/s^2 during reversal). This sequence was repeated to mimic a scanning behavior [54] while we recorded in vivo from E and I cells. The inserts show the predicted electroreceptor afferent model responses to the same stimulus sequences. As shown for the lateral axis, the electroreceptor firing rate is skewed after direction reversal. B) As expected, the firing rate and burst fraction of I cells increased as the plastic object approached the RF center. When the plastic sphere reversed direction and withdrew from the RF center, the bursting ceased and I cell firing rates decreased rapidly, dropping well below baseline levels. As the plastic sphere approached the RF center, E cell firing rates were suppressed below spontaneous levels and the BF decreased. However, as the plastic sphere withdrew, the E cells showed marked increases in burst and tonic spiking despite the fact that, under static conditions, the cell's firing rate would be depressed. The E cell firing rate gradually returns to baseline as the sphere recedes. C) The firing rate and BF of E cells increased as the brass object approached their RF center. When the brass sphere reversed direction and withdrew from the RF, bursting was silenced. As the brass sphere approached the RF center, I cell firing rates were suppressed below baseline levels and there was a marked decrease in BF. However, as the brass sphere withdrew, I cells showed large increases in spiking despite the fact that, under these contrast conditions, the firing rate should be depressed. I cell firing rates gradually return to baseline as the brass sphere recedes. We see that E/I cell coding switches and the patterning of burst discharge upon motion reversal, generalize to both principal axes of motion.

We summarize the E/I cell responses to looming/receding and longitudinal movements (Fig. 6A, B). We have shown that E and I cells respond with strong burst discharge to looming brass

and plastic spheres respectively, as well as to longitudinal movement of these spheres into their RFs, which is entirely expected based on extensive anatomical data [33, 34, 173], in vitro electrophysiology [32], in vivo responses to receptive field stimulation [91] and longitudinal motion signals [31, 103]. Despite the fact that the local electrical contrast has the wrong sign according to conventional ON/OFF cell definitions, both E and I cells respond vigorously to motion reversal of the plastic and brass spheres respectively (Fig. 6A, B). A likely implication of these E/I cell switches for natural predatory behavior is illustrated in Fig. 6C. While scanning past a Daphnia (water flea and staple prey), it can suddenly jump away, requiring the fish to perform an adaptive strike [54]. As the fish initially swims alongside a Daphnia, the relative longitudinal motion creates a positive contrast pattern that activates a topographic sequence of E cells and supresses I cells. However, if a Daphnia suddenly jerks back to avoid capture, its receding motion will recruit I cells, whose activity signal a sudden withdrawal and presumably guide an appropriate prey capture response. The fish's rapid recalibration of movement to capture its target suggests an important neuroethological role for E/I pyramidal cell switches, both as a salient cue and as a means to estimate stimulus motion parameters.

Discussion

We have shown that E and I cells cooperatively produce a firing rate representation of a moving object's position that is symmetric under reversal of motion direction; this was observed for two principal electrolocation axes (Fig1 and 5). Simulations with our E cell model demonstrate that the electroreceptor afferent firing rates and intrinsic burst dynamics principally determine the responses of E cells to looming movement into their RFs. Yet, these mechanisms were unable to account for the receding responses that effectively mirror the encoding of distance information observed during looming, despite the clear departure from the afferent firing rates and expected physiology (Fig. 3C, 4). We hypothesize that a central mechanism recreates the looming distance rate code in order to accurately estimate the location of the receding sphere for lateral distances < 1.75 cm. Therefore, the receding responses of the pyramidal cells may be a form of predictive coding, similar in purpose to the anticipatory responses seen in retinal

ganglion cells to moving stimuli [101,116]. The critical question becomes: what are the neural mechanisms that generate these surprising departures from conventional contrast coding?

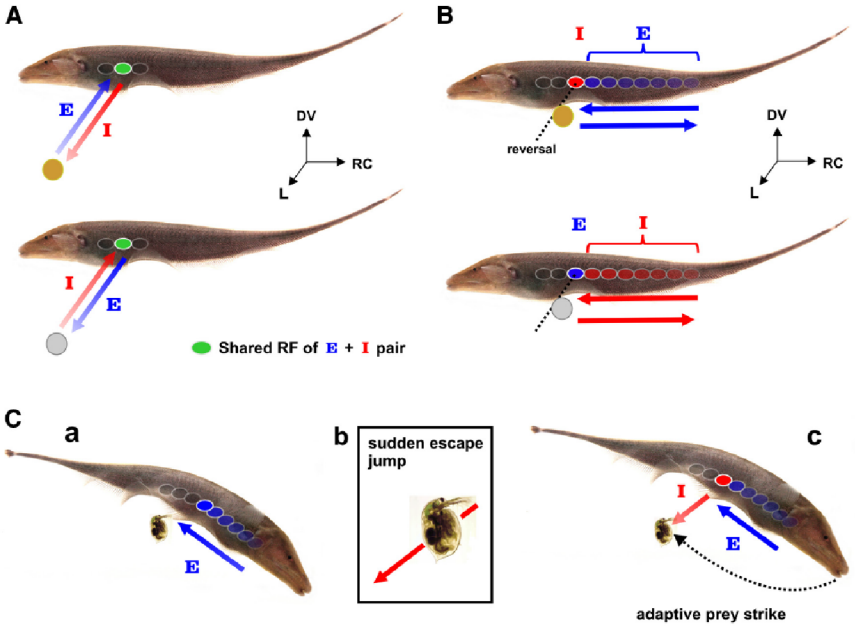

Figure 6 **Synergistic E and I cell coding paradigms for electrolocation** A) Top: An E cell encodes the relative distance of a looming conductive object by an increase in its firing rate and burst spiking (indicated by the shaded arrow). Upon object withdrawal along the lateral axis, E cell activity is suppressed while the I cell encodes the motion of the brass sphere. Bottom: An I cell encodes the looming non-conductive object by increasing its firing rate and burst spiking. However, as the non-conducting object recedes, I cells are suppressed and E cells encode the receding brass sphere. B) Top: As these fish scan past conducting objects in their environment, their relative motion causes local positive contrast to move across the body surface (rostro-caudal and dorso-ventral plane). This will evoke discharge in a topographic sequence of sequentially activated E cells (RF shading represents the sequence of activation). At the point of direction reversal, the firing rate of the E cell is suppressed and strong bursting is evoked in the I cells within that same topographic column. As the object moves in the reverse direction, an E cell representation may progressively return. Bottom: As a non-conducting object moves into the RF of an I cell there is an increase in firing rate and BF. If the object's trajectory suddenly reverses, then the suppressed E cell responds to the withdrawal, while the I cell goes silent. C) We illustrate the expected responses of E and I cells during a documented prey capture sequence ([54]; Fig.13 within). (a) While scanning its environment, a fish swims forward, past a Daphnia (water flea). This conductive organism will evoke discharge in a topographic sequence of E cells as indicated by the arrow. (b) Between the time of prey detection and capture, the Daphnia will sometimes make an escape jump [118]. (c) The conductive organism is now receding from the fish's body and is expected to evoke a response in the I cells, whose activity represents the body location from where the Daphnia is receding and whose decreasing firing rate measures its displacement. Meanwhile E cell discharge in the same ELL column will be suppressed. In this instance, gymnotiform fish often perform an adaptive strike to capture the prey, where estimation of the prey's location now appears to be predictably encoded by the firing rate of the OFF channel.

Physiological mechanisms of the receding response. We have shown that empirically motivated spike frequency adaptation (SFA) is enough to suppress the E cell model response to the receding brass sphere when coupled with the adaptive skew present in the electroreceptor afferent firing rates (Fig. 3C). The source of this pyramidal cell adaptation is currently unknown. Afferent synaptic depression is unlikely because it recovers far too rapidly (< 8 ms; [111]). Instead, we expect that the source is disynaptic inhibition, mediated by GABAergic interneurons activating GABA-A receptors [32, 33]. Shumway and Maler [123] have directly shown that pyramidal cell SFA is greatly reduced after blockade of GABA-transmission and there is a strong correlation between the extent of GABAergic innervation of pyramidal cells and the extent of SFA [31, 33]. Furthermore, brief stimulation of the electroreceptor afferents can induce strong GABA-A mediated shunting inhibition that outlasts the stimulus by 100s of ms and is due to sustained interneuron discharge [32]. Therefore, we suspect that the afferent-driven discharge of GABAergic interneurons evoked by the looming brass sphere will persist after motion reversal, accounting for the observed suppression.

In the case of the receding plastic sphere, the dynamics of the electroreceptor afferents, the intrinsic bursting mechanism and the adaptation of ELL pyramidal cells are all incapable of reproducing the in vivo responses of E cells. The physiological mechanisms that generate the reflections of a looming response in the opposing contrast detector are of great interest but are beyond the scope of this paper. Clearly, the switches rely further on the nonlinear dynamics of the ELL network [90] and/or its feedback input [15], in order to control the coordinated and paradoxical contrast coding displayed by the electrosensory ON/OFF cells.

Importance of the receding response. The pyramidal cells of the ELL project to the torus semicircularis (TS), a mid-brain structure that projects to the optic tectum [19]. A subset of TS cells display strong directional selectivity for longitudinal motion and sparse representations of electrosensory signals emerge in this nucleus [20, 112]. Therefore, we hypothesize that there will be looming and receding specific cells in the midbrain (TS and/or tectum) that operate on both E and I channels to guide the tectal control of movement. Consistent with this hypothesis,

responses to looming stimuli have been described in the early stages of locust vision [105] and throughout the visual pathway of vertebrates [24, 92, 116, 120]. Responses to receding stimuli have been recorded in the optic tectum of barn owls [128] and there are pigeon midbrain neurons that are selective for either the expansion (looming) or contraction (receding) of illumination patterns on the retina [126]. Spare representations of motion appear in the posterior parietal cortex of rhesus monkeys, where a fraction of the motion sensitive neurons respond selectively to receding stimuli [120]. Neurons sensitive to looming and receding acoustic stimuli have also been reported in primate cortex [115]. All of these results confirm the intuitive idea that sparse representations of motion direction are important to higher levels of processing, not only in the electrosense, but in vision and audition as well.

Can sequences of patterned ON and OFF cell activity initiate representations of motion direction from dynamic contrast patterns? Does adaptive skew in the visual system necessitate ON/OFF switches when stimulus intensity changes from increasing to decreasing (or vice versa)? In the vertebrate retina, it has been noted that adaptation can reverse a RGC's directional selectivity [119]. Furthermore, it has been shown that longitudinal motion reversal produces burst discharge in RGCs, which is expected to reset downstream networks so that the motion patterns preceding the reversal event do not contaminate future estimates [122]. This interpretation extends nicely to the electrosense, where SFA in the electroreceptor afferents generates errors in an otherwise simple intensity-rate code and the system abandons its well-defined contrast channels. Schwartz et al. did not identify the cells as ON or OFF types, or address whether conventional contrast coding breaks down. Exploring this possibility may reveal deeper parallels between the electrosensory and visual systems. Interestingly, there exists a documented case of OFF cells in the salamander retina transiently responding ($\approx$ 100 ms) to positive contrast as if they were ON cells [107] but a switch from ON to OFF was not observed. In the electrosense, we have shown that contrast relabeling occurs from OFF to ON, as well as from ON to OFF, where the relabeled lines can persist on the order of seconds. This raises the possibility that, in addition to burst spiking acting as a salient cue, coordinated ON/OFF cell activity may also be involved in the sustained encoding of visual information

over longer timescales. In support of this idea, it has recently been proposed that olfactory cortex pyramidal neurons can read out sequential patterns of activation across a population of their mitral/tufted cell afferent inputs [108]. Therefore, monitoring sequences of activation across distinct neuron populations may be a common neural strategy to extract additional information about a stimulus that is not contained directly within the spiking responses of the individual cell types.

Decoding looming and receding motion. An unexpected result of our experiments was the apparent disconnect between the response of ELL pyramidal cells and the afferent inputs (Fig 3, 4). Looming responses are consistent with contrast coding definitions, behaving in accordance with the afferent input and intrinsic pyramidal cell dynamics. However, there is significant deviation from these mechanisms during receding motion. At the population level, these responses to receding motion are monotonically decreasing functions of distance and encode changes in object location in a way that is compatible with looming responses, even though the afferent input is no longer concordant with the physical stimulus and the electrical contrast is the opposite sign. Our results demonstrate that a decoder cannot exclusively rely on the instantaneous firing rates of either E or I cells to encode bidirectional motion. Although the suppression of a pyramidal cell's firing rate signals motion reversal, it does not provide an invertible mapping of the receding stimulus' position and could not provide unambiguous estimates of object location. Instead, a distance-rate code is distributed over both cell types, implying that E and I cell outputs cannot be mapped into distinct channels for encoding object location. As a result, the electrosensory ON/OFF cells can no longer be used to unequivocally signal electrical contrast information. In other words, the classic notion of labeled line contrast coding is inadequate; a downstream decoder must combine ON and OFF cell responses in a more flexible manner.

It has been previously suggested that veridical encoding of contrast information is too restrictive to permit visual constancy in a complex environment [22]. We have shown that maintaining perceptual constancy during contextual changes is even a problem for the relatively

simple electrosense and is expected to be accomplished by a putative decoder that monitors patterns of activity across distinct population subsets. Given the similarities between low level electrosensory and visual processing, it should prove interesting to explore cooperative ON and OFF cell coding under different conditions of optic flow [106], where moving contrast edges are created by expanding and contracting illumination patterns that shift across the retina. The design of neural prosthetics and brain/machine interfaces should benefit from the discovery of neural circuits responsible for extracting semantic information (like motion direction) from temporal activity patterns that are distributed over heterogeneous neuron populations.

2.3 Balanced ionotropic receptor dynamics support signal estimation via voltage-dependent membrane noise

Marcoux CM, Clarke SE, Nesse WH, Longtin A, Maler L.* (2016). Journal of Neurophysiology, 115(1): 530-545.

Contributions: C.M. Marcoux designed and carried out all in vitro experiments and analysis and participated in writing the manuscript. S.E. Clarke carried out the in vivo recordings and analysis, wrote the code for the in vitro data analysis and participated in writing the manuscript. A. Longtin carried out computational analyses and participated in writing the manuscript. L. Maler participated in the design of all experiments and analyses, supervised all experiments and analyses, and participated in writing the manuscript. *L. Maler is the corresponding author.

Significance: Although a second author publication, my involvement in this paper was significant. I have included an excerpt of Marcoux et al. here, which both highlights my data and analysis contributions and introduces an important statistical feature of pyramidal cell spike trains, considered in more detail in Section 2.4. The reader is not required, but is encouraged to browse over the excellent in vitro work of Curtis Marcoux (see Appendix).

Baseline EA discharge is not completely random but exhibits negative interspike interval (ISI) serial correlations (SCs) - i.e. a long ISI is followed by a shorter one and vice versa [52,57,170]. One might expect that these strong negative ISI serial correlations would be relayed to the ON (or OFF) cells as negative SCs of evoked EPSP amplitudes. Marcoux et al. first demonstrate that slow NMDA receptor (NMDA-R)-mediated excitatory postsynaptic potentials (EPSPs) are able to summate over many inter-spike intervals of the primary electrosensory afferents, effectively eliminating their baseline ISI correlations from the pyramidal cell input. Together with a dynamic balance of NMDA-R and GABA-A-R currents, this permits stimulus-evoked

changes in EA spiking to be transmitted efficiently to target electrosensory lobe (ELL) pyramidal cells for low-frequency signals. Interestingly, AMPA-R activity is depressed and appears to play a negligible role in the generation of action potentials. Instead, cell-intrinsic voltage-dependent membrane noise (blips) drives a significant proportion of pyramidal cell spikes.

The biophysical and synaptic mechanisms uncovered by Marcoux et al. convert bottom-up sensory input encoded by the membrane potential of the ON and OFF cells into a base renewal spike train, that is, a point process with no intrinsic ISI correlations. The benefit of this statistical feature is that sense input can modulate the ISI intervals and downstream neurons can unambiguously attribute changes in firing rate to the changing sense input, avoiding conflation of stimulus history or intrinsic temporal properties of the coding cell. The base renewal spiking response driven by the noisy blips is supplemented by an apparent 'replacement' process, in which dendero-somatic nonlinearities and top-down control through active dendrites intermittently replace a single spike with multiple spikes (e.g. a doublet or triplet burst event). The data included below shows that the majority of spontaneous ON and OFF cell spike trains retain the renewal property and that the inter-spike interval distributions largely fall into the same two classes observed for the blips in ON and OFF cell membrane potential; these noise based transients were reported in the first in vitro study of ELL [163].

Reprint Permission: "APS grants permission for free use of our articles (in whole or in part) in educational materials, provided there is no charge or fee for those materials, and/or those materials are not directly or indirectly commercially supported."

Results Excerpt

Elimination of electroreceptor afferent inter-spike interval serial correlations by slow NMDA-R mediated EPSPs. It has previously been shown that the baseline activity of EAs exhibit a negative ISI correlation at lag 1, indicative of sensitivity to the timing of the last two action potentials [170]. The effect of synaptic transmission on such correlations has not been well studied. A theoretical analysis did demonstrate that presynaptic depression can suppress positive ISI correlations in incoming spike trains, resulting in much less correlated ISIs impacting the post-synaptic receptors [148]. Recent theoretical work has also shown that correlations in input currents (but not ISIs per se) can be transferred to output ISIs [171]; but little is known about input-to-output transfer of ISI correlations. If an input spike strongly influences spiking probability, then one might intuitively expect that ISI correlations are transferred, but the situation is less clear when many spikes from different neurons are required to fire the cell, and when there is noise, which are both the situation of interest here. Our results below therefore advance our knowledge on ISI correlation transfer and also raise interesting questions in this context.

The baseline activity of target ELL pyramidal cells is effectively a renewal process with minimal or no ISI correlations (shown below in the in vivo section). The elimination of ISI correlations might be achieved at many levels of the ELL circuitry or via intrinsic properties of the pyramidal cells. In the absence of spiking and thus network feedback, our goal was to understand whether EA-to-CMS pyramidal cell synaptic dynamics can, by itself, remove the EA correlation structure. An earlier study established that blocking AMPA-R mediated transmission with CNQX also blocks NMDA transmission [135]. Therefore, we assume that AMPA transmission is crucial in sufficiently depolarizing pyramidal cell basal dendrites to unblock NMDA-R channels, and is required for transmitting electrosensory signals from EAs to pyramidal cells. For experiments examining the mechanisms of decorrelation and signal transmission, we consequently tested the role of NMDA and GABA-A receptors by first studying

the intact system and then systematically eliminating the NMDA and GABA-A receptor components.

Voltage-dependent membrane noise triggers spiking. Previous studies of cortical [129, 130] and ELL pyramidal cells [138] have shown that spiking is evoked by rapid depolarization of the membrane potential, i.e. by steep increases that can be localized in time using the first or second temporal derivative. It is often assumed that AMPA-R mediated currents provide the necessary rapid depolarization to elicit spiking. In an ELL slice, the rising phase of a single EA evoked EPSP (mostly AMPA-R) will evoke a spike [32,111]. Electroreceptor afferents normally discharge continuously at a high rate [52] and under these conditions the AMPA-R mediated component of the EPSP is slightly depressed [111]. We therefore hypothesize that, in vivo, it is the NMDA-R and not AMPA-R component of the stimulus evoked EPSP that evokes most spiking in ON cells. Further, our experimental results and statistical analysis suggest that the response to slow increases in EOD amplitude are smooth and lack the rapid depolarizing events (i.e. no large second derivative) required to evoke spikes [138]. This prompted us to consider how the slow NMDA-R EPSPs could possibly drive spiking.

Early work in the ELL described the presence of membrane noise that increased in amplitude with depolarization [163]; this noise was attributed to voltage-gated ion channels likely selective for Na+, although a contribution by synaptic noise could not be excluded. Since these rapid membrane potential fluctuations were able to elicit spikes in pyramidal cells in vitro [163], we decided to investigate whether noise could compensate for the depressed AMPA-R component of the EA evoked EPSP and drive the fast upstrokes in membrane potential required for spiking in pyramidal cells.

We treated the ELL with CNQX and APV to block synaptic transmission onto ON cells and interneurons and therefore eliminated synaptic input as the source of rapid fluctuations in membrane potential. We then recorded from CMS pyramidal cells without any channel blockers (i.e. no QX-314 or cesium in the pipette) and applied depolarizing current steps; because synaptic transmission was blocked, we were not able to determine whether we were

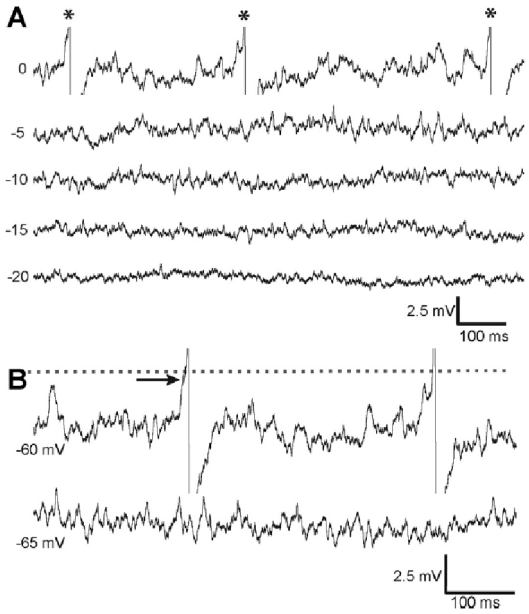

Figure 6 **Recordings of spontaneous pyramidal cell membrane potential at various holding potentials** Recordings were taken with extracellular CNQX and APV to block synaptic noise. A: Amplitude of membrane potential fluctuations increases dramatically with depolarization to spike threshold (around -65 mV, here normalized to 0). Near threshold, rapid large depolarization elicits spiking (*, spikes truncated). B: Blips elicit spikes (arrow) when they reach spike threshold (dashed line). Here we give the absolute membrane potentials for this particular neuron - the traces (top: -60 mV; bottom: -65 mV) are an expanded version of the normalized top traces of A (0, -5).

recording from ON or OFF cells. As previously described [163], the pyramidal cell membrane potential was noisy and the amplitude of the membrane potential fluctuations increased dramatically with depolarization (N = 5, Fig. 6A). Spike threshold varied across cells but was typically near -65mV. As the membrane potential approached spike threshold, the presence of rapid, large depolarizations (blips) became apparent and these blips were seen to co-occur with spiking (Fig. 6B). To investigate the membrane noise in more detail, we computed histograms of the membrane potential at different levels of depolarization. The membrane noise histograms were well fit by the Gaussian distribution at relatively hyperpolarized levels (Fig. 7A). However, at more depolarized levels (near threshold) the distribution has a higher variance (Fig. 7B, C) and becomes both more peaked (kurtotic) and positively skewed to the right (Fig. 7B, D). The positive skew is due to an increase in the occurrence of the large blips. When we included voltage-gated ion channel blockers in the pipette, the variance was low and independent of membrane potential (Fig. 7C inset, N = 1) conclusively identifying the noise

as intrinsic rather than a result of synaptic conductances.

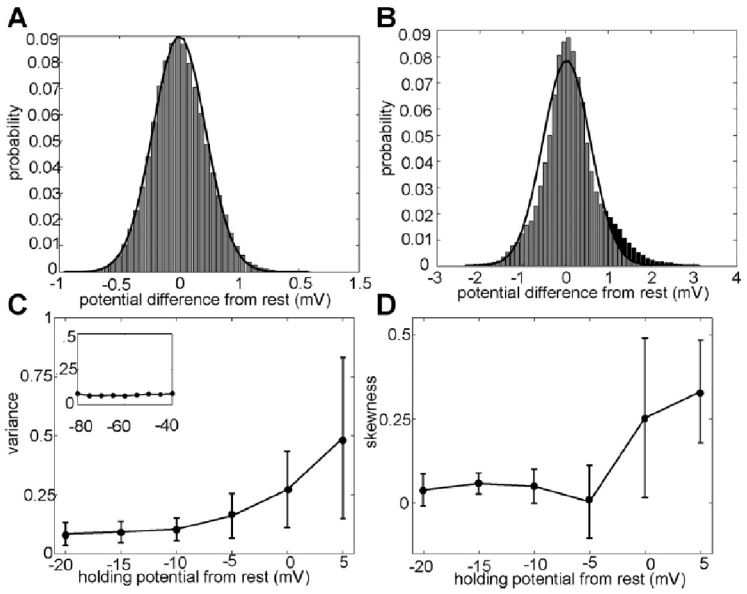

Figure 7 **Probability distribution, variance and skew of CMS pyramidal cell membrane fluctuation** Recordings were made with extracellular CNQX and APV to block synaptic noise. The resting membrane potential was simply the neuron's mean potential without any current injection. In the following panels, we normalized each recording by subtracting this mean potential so as to display more clearly the effect of injecting de- or hyper-polarizing current. A: When hyperpolarized, pyramidal cells membrane noise histogram (gray) is well fit by a Gaussian distribution (black curve overlay). B: Near threshold, the distribution is more peaked (kurtotic) and positively skewed than the best fit Gaussian distribution. The skew in the distribution (black) is likely a result of an increased frequency of rapid depolarizations (blips). C, D: Holding potentials are normalized to spike threshold, with 0 representing spike threshold. C: Variance of noise distribution increases with depolarization. Inset: When voltage gated ion channels were blocked, variance was reduced and became independent of membrane potential, demonstrating an intrinsic source of noise. D: Skew increases dramatically at potentials at or above spike-threshold.

We hypothesize that many stimulus-evoked spikes in ON cells are elicited by the voltage-dependent blips, which would ride on top of the summating NMDA-R component of the PSPs evoked by the EAs. To investigate this possibility, we turned to the centrolateral segment (CLS) of the ELL and repeated the noise experiments described above (N = 5). We switched to the CLS map because preliminary experiments had shown that the blip events (right tail of the distribution shown in Fig. 7B for the CMS map) were far more prominent, allowing us to determine blip occurrence with greater fidelity and temporal accuracy. The overall membrane noise characteristics were otherwise identical to the CMS map: CLS pyramidal cells display fluctuations whose variance and skewness increase with depolarization of the membrane

potential (data not shown).

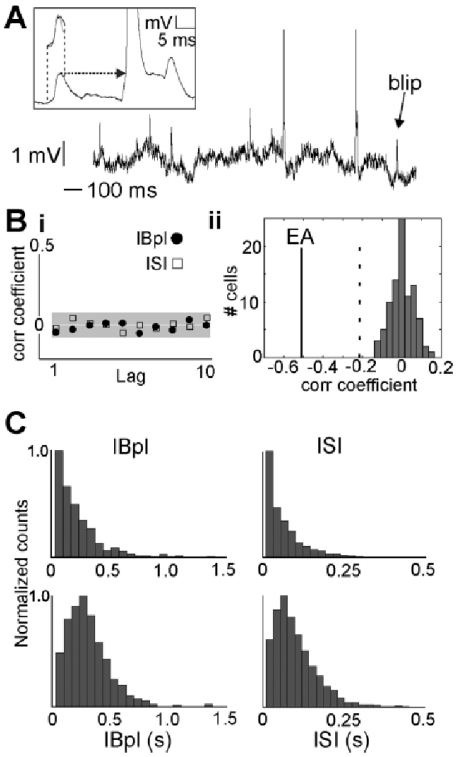

Figure 8 **Statistical structure of blips and of pyramidal cell spiking to which they contribute** A: An example membrane potential trace from the spontaneous activity of an E type pyramidal cell of the CLS map, showing many clear blips and two action potentials (truncated). The inset shows that the peak of a blip (start of arrow) is at the same height as the inflection point (arrow) for an action potential, suggesting that blips may trigger spikes. The thin dashed vertical lines enclose the blip waveform (gray) with a superimposed waveform of the AMPA-R component of an EA evoked EPSP (black). The onsets of the two waveforms are nearly identical suggesting these blips might trigger spikes as effectively as the rising phase (AMPA-R) of EA evoked EPSP. Bi: The interblip intervals (IBpI, black circles) are not serially correlated and are therefore a renewal point process (left); this lack of correlation is also seen in the ISI sequence derived from the spiking output of the ELL pyramidal cells (ISI, open squares). Bii: A histogram of serial ISI correlations from a larger (N =91) sample of CLS ON and OFF cells (firing rates between 5 and 35 spikes/s). Correlations are mostly within ± 0.1 with an average near 0. We also illustrate the strong mean negative serial correlations of EAs (black line, -0.52) and the highest correlation observed (dashed line, -0.23); note that there is no overlap between EA and ON/OFF cell correlations. C: We found two patterns of IBpIs (left), which are both reflected in the ISI statistics of individual ELL pyramidal cell neurons from the centrolateral map (right). This strongly suggests that blips directly drive a portion of spikes in ELL pyramidal cells.

Figure 8A shows an example membrane potential trace from a CLS neuron, demonstrating clear blips and the occasional spike. The figure inset shows that an action potential may trigger directly off the peak of a blip (indicated by the dashed arrow). Furthermore, the blip waveform has an onset slope nearly identical to the AMPA-R component of an EPSP (shown

in gray, overlaying the excised blip), suggesting that these noisy fluctuations are sufficient to trigger spikes when they occur near the action potential threshold. Using the same derivative criteria as was used above to identify spikes, we isolated the times at which blips occurred and computed inter-blip interval statistics including the serial correlation coefficients of inter-blip intervals (IBpI) and the IBpI histogram. The IBpIs had means ranging between 0.39 s (SD = 0.23) and 0.22 s (SD = 0.25) for the 3 CLS cells where blips could be cleanly extracted. The IBpI showed no serial correlation (Fig. 8Bi, black circles) indicating that the blips originate from a renewal process. We found the IbpI distributions were consistent with the renewal process being either a Poisson (Fig. 8C; left, top) or a more general gamma process (Fig. 8C; left, bottom), depending on the neuron. To determine whether the statistical patterns of blip generation might influence the statistical patterns of pyramidal cell spiking, in vivo extracellular recordings were obtained from CLS pyramidal neurons in the absence of a stimulus (5 ON cells and 5 OFF cells). Examination of the data showed that there were no significant differences between ON and OFF cells and the data was therefore pooled. The mean ISIs of the 10 cells ranged between 0.13 s (SD = 0.13) and 0.039 s (SD = 0.025). The mean ISIs are significantly smaller than the mean IBpIs, presumably due to the cells being driven more strongly by the EAs and feedback in vivo, rather than by intracellular current injection in vitro. As illustrated in Fig. 8Bi (open squares), this small sample suggests many in vivo ISIs are not significantly correlated at any lag demonstrating that some ON and OFF cell spiking follows a renewal process. Because there are some apparently contradictory results in the literature concerning ELL pyramidal cell serial ISI correlations (see Discussion), we also examined the distribution of baseline ISI serial correlations in a much larger sample of previously recorded CLS ON and OFF cells [140]. We had a sample of 50 ON cells (firing rates of 6.3 - 35.4 spikes/s) and 41 OFF cells (firing rates of 5 - 30.7 spikes/s). Preliminary analysis showed that their serial ISI correlations were not significantly different in the two populations and so the data were pooled for a sample of N = 91 cells. As illustrated in Fig. 8Bii, the ISI correlations are all low (mean 0.003; $\pm$ 0.059), and include both small positive as well as negative correlations ranging between -0.1 and +0.1. In contrast, we also illustrate the EA serial ISI correlations taken from

[170]. These have a mean of -0.52 ±0.14 (black line under EA) and a range of -0.23 to -0.82. The lower value (-0.82) is off the scale of the figure, and a dashed line indicates the maximum correlation (-0.23) observed. It is clear that, in going from EAs to pyramidal cells, there is a massive reduction in ISI correlations, and that the ON and OFF cell serial correlations are, for the cells with firing rates < 40 spikes/s, near zero.

The in vivo ISI histograms qualitatively match the two classes of IBpI histograms observed in our in vitro experiments (Fig. 8C, left vs right). We hypothesize that the blip voltage-dependence generates an optimal noise level for the encoding and transmission of sub- and peri-threshold low-frequency signals by ON cells, that is, blips are the basis for ON cell stochastic resonance. Further, we hypothesize that blips form a basis for a renewal point process, which is conserved in the spiking output of the ELL pyramidal cells, even in vivo when the ON or OFF cell functions as part of the entire network. Together with the decorrelation of EPSP peaks by the natural mixture of synaptic currents, the renewal blip-process ensures an efficient encoding of stimulus amplitude modulations centrally, including for signals that lie below or in the vicinity of the spiking threshold.

Conclusion: Spike train correlations in the ELL network.

In the absence of stimulation, we've seen that the bulk of sampled ON and OFF cells have no significant serial correlation among successive ISIs, but that many units possess small but significant positive or negative correlations. This is consistent with studies of retinal ganglion cells and cortical pyramidal neurons, where both renewal and non-renewal spike train statistics are reported. Since stochastic fluctuations in membrane potential drive spikes, bottom-up input to the pyramidal cells is apparently converted into a base renewal point process, which is then further transformed into an output spike train by the cumulative action of the spike generating mechanism, slow channel conductances, cell intrinsic adaptation and the influence of feedback acting through the apical dendrites. Under static conditions spike-rate adaptation is expected to be a contributor to negative ISI correlations (as described in Section 2.2). I suspect that depolarization caused by somato-dendritic nonlinearities and feedback may offset

the hyperpolarizing drift of spike-frequency adaptation [258]. Under this interpretation, units displaying slight positive and negative correlations may result from temporary or purposeful imbalances in the relative strengths of adaptive hyperpolarization and feedback induced depolarization. The situation is more complicated during stimulation, where non-stationary input recruits dynamic effects from adaptation and powerful time-limited feedback (demonstrated in Section 2.5). In the following Section (2.4), we will see that beyond stimulus induced correlations, the temporal dynamics of spike generation typically remain renewal during looming and receding motion, which permits instantaneous rate coding without contamination by strong intrinsic ISI correlations.

As an afterthought, in a population of rate coding neurons it may be beneficial to have the majority of units retain no correlation in their respective spike trains but also have smaller subsets of units that display positive correlations and subsets that display negative correlations. This division mainly preserves the desired statistical properties for rate coding at the population level, while also conferring the benefits associated with positive and negative correlation: while renewal spiking allows for idealized instantaneous rate coding for low frequency signals [174, 204], neurons with a negative ISI correlation maximize signal detection [57] and units with positive correlations act as a selective band-pass filter, preferentially encoding frequency information at approximately one half of the average rate of the process [174]. In the latter case, this would be a putative benefit to the initial detection of a beat frequency (5-10 Hz) produced by another fish (see Introduction; Figure I). This introduces the potential to combine three different correlation based coding strategies among single neurons of the population, provided these neuron outputs are correctly segregated and interpreted downstream. The idea of small subsets of neurons performing niche coding roles within a population has been previously emphasized [175]. At the population level, correlation based strategies such as sets of neurons switching between synchronized and desynchronized modes of activity adds a further layer of coding capacity [5, 133].

2.4 The neural dynamics of sensory focus

Clarke SE*, Longtin, A, Maler, L. Nature Communications 6, 8764 (2015).

Contributions: S.E.C. and L.M. designed the experiments and methods of data analysis; S.E.C. performed theory, experiments and data analysis; S.E.C., L.M. and A.L. wrote the paper. *S.E.C is the corresponding author.

Significance: The distributed representation of motion by ON and OFF cells in the electrosensory system has important consequences for active sensing. In the following article, a method was developed to assess the coding fidelity of non-Poisson spiking neurons, which was then applied to show that the responses of ON and OFF cells convey an optimal estimate of object location at 1.4 cm. This critical distance occurs at the transition between tonic and burst modes of ON/OFF cell spiking. Remarkably, during tracking behaviour, an electric fish maintains this specific distance from an object that swings back and forth along its transverse body axis. In agreement with the behaviour, we found that the optimal distance is independent of the object's speed, contrast, direction and size, illustrating the efficacy of this computation for flexible spatial processing. To our knowledge, this is the first demonstration that an active sensing behaviour directly optimizes neural coding with a direct connection made to the control of burst spiking dynamics.

Abstract

Coordinated sensory and motor system activity leads to efficient localization behaviors; but what neural dynamics enable object tracking and what are the underlying coding principles? We show that optimized distance estimation from motion sensitive neurons underlies object tracking performance in weakly electric fish. First, a relationship is presented for determining the distance that maximizes the Fisher Information of a neuron's response to object motion. When applied to our data, the theory correctly predicts the distance chosen by an electric fish engaged in a tracking behavior, which is associated with a bifurcation between tonic and burst modes of spiking. Although object distance, size and velocity alter the neural response, the location of the Fisher Information maximum remains invariant, demonstrating that the circuitry must actively adapt to maintain 'focus' during relative motion.

Introduction

Neural systems that actively engage and track moving objects are faced with two major challenges: determining motion parameters and directing appropriate motor commands to maintain informative sensory input. Behavioral studies on tracking eye movements [176], fly navigation [28], electrosensory tracking [26,177] and bat echolocation [27] have all led to the hypothesis that active sensing can be directed in order to optimize re-afferent sensory processing. However, the conclusion that active sensing can be executed in a manner that directly benefits neural coding is premature, since it has not been shown that the sensory activity evoked by these motor outputs optimizes neural transmission and thus the resulting behavior. To assess whether precise tracking performance relies on optimized stimulus estimation, we apply Fisher's Information ([178]; I_F) to sequences of action potentials (spikes) recorded from the motion sensitive responses of electrosensory ON and OFF contrast coding neurons. By finding where I_F is maximal along the transverse distance axis (Fig. 1a), we seek to identify where a decoder of ON and OFF cell firing rates may, in theory, achieve the best possible estimation of changes in object position from the observed spiking activity. The I_F of a neuron whose spiking activity follows a Poisson distribution, with firing rate function λ, can be computed

directly as follows (Supplementary Note 2; see Appendix) [178],

$$I_F = \frac{\lambda'(x)^2}{\lambda(x)}\Delta t \tag{1}$$

This equation illustrates that the best possible estimate of a stimulus feature (x), over an interval of time (Δt), occurs when the square of the derivative of the firing rate with respect to x, divided by the firing rate, is maximal. In other words, stimulus-induced changes in firing rate are more readily estimated against lower levels of spiking activity. This estimation principle appears to be reflected in natural behavior: during echolocation, bats cast their echo-beams off-axis from a target so that the maximum spatial slope, not the peak intensity, of the beam is reflected back to the animal [27]. Despite a weaker signal input, the benefit of this strategy is that small changes in relative distance result in large changes in reflected echo intensity, with putative benefits for motion processing. In an obvious parallel with bats, gymnotiform weakly electric fish track objects at distances that cause relatively small perturbations to their endogenously generated electric field, but with relatively large spatial derivatives (evoking large λ') [53–55,109]. We propose that sensing objects at distances that cause weak signals is not simply a consequence of where the slope in the physical signal is maximal. To optimize estimation, a fine balance exists between sensing an object at a distance that evokes a relatively low firing rate in sensory neurons but where relative changes in object distance over time cause large changes in the neural response. Although the Poisson case is conceptually important and a working approximation under static conditions, we are interested in dynamic stimuli (looming/receding motion) and the assumptions underlying Eq. 1 may no longer suffice. Therefore, we first sought to examine the statistical nature of pyramidal cell spiking more closely. We show that ON and OFF cell spiking is not a Poisson process under spontaneous or stimulus-driven conditions and then move on to more accurately investigate the idea that optimal estimation in sensory neural networks enables observed tracking behaviors.

Results

ON and OFF cell responses to motion. In vivo extracellular recordings of ON and OFF contrast

coding neurons - located in the primary electrosensory lobe (ELL) of gymnotiform electric fish [19] - were obtained from immobilized Apteronotidae, while spherical objects were moved toward (looming) and away (receding) from the animal along the transverse body axis (Fig. 1a). Importantly, our stimulus is a mimic of the type of motion experienced by the electrosense during a behavioral tracking task, the electromotor response [53,109]. Brass and plastic spheres were used in our experiments to cast both positive and negative local contrast patterns onto the cutaneous electroreceptors (object contrast is defined by its electrical conductivity relative to the background water). The electroreceptor afferents (EAs) project topographically to ON and OFF cell pairs in the ELL, forming direct excitatory contact with ON cells and indirect contact with the OFF cells through an inhibitory interneuron [19]. As a result, ON cells are selective for increases in stimulus intensity over time and OFF cells are selective for decreases in stimulus intensity, due to the sign inversion. Therefore, motion reversal (switching from looming to receding) changes the sign of the temporal derivative of input intensity, evoking switches in the activity of downstream ON and OFF cells, an event marked by prominent burst spiking [140] (Fig. 1a). By combining ON and OFF cell outputs, a downstream decoder achieves a bidirectionally symmetric representation of motion. The reader should note that both ON and OFF cells generate looming and receding responses, depending on the sign of the stimulus contrast (only the plastic negative contrast case is presented in Fig. 1a; ON and OFF cell role reversal is also observed for brass). In previous work [140], we show that there is no significant difference between ON and OFF cell responses for looming and receding motion. Therefore, we pooled the data in this paper into looming (ON cell, brass; OFF cell, plastic) and receding (OFF cell, brass; ON cell, plastic) responses. The instantaneous firing rates of individual cell responses were averaged to form ON/OFF cell population firing rates as a function of distance for our eight different stimulus conditions.

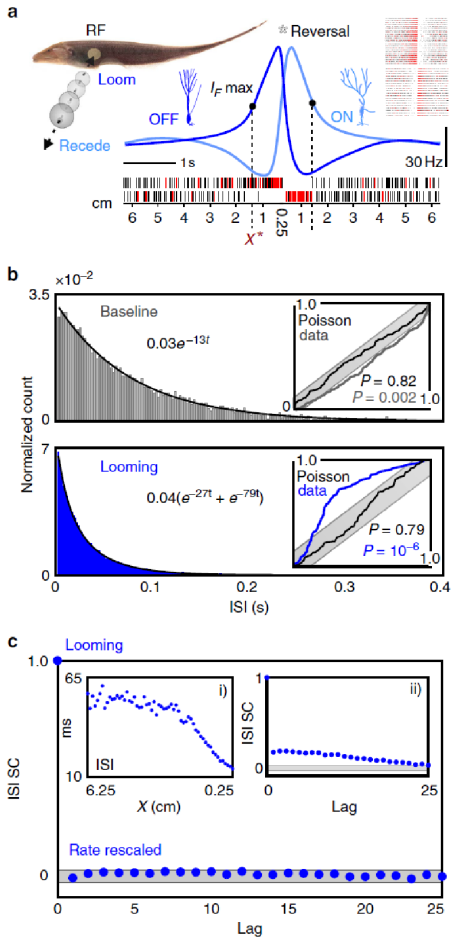

Figure 1 **Motion sensitive ON and OFF cell spiking is not Poisson but is memoryless** a) Recordings were taken from ON and OFF cells during looming and receding motion. The firing rate responses of an ON/OFF cell pair are shown in response to 2 cm/s motion of a negative contrast stimulus (plastic sphere, diameter $d = 1.21$ cm) in their joint receptive field. Examples of the ON and OFF cell spike trains are also shown below the firing rate curves and in the raster plots (upper right), where black lines indicate tonic spiking (inter-spike interval, ISI >10 ms) and red lines indicate burst discharge (3 < ISI ≤10 ms). Upon motion reversal, prominent bursting marks a dramatic switch in the cells' activity; the cell responding to looming motion ceases to discharge, while the opposing cell class is disinhibited and encodes receding motion. The transition from tonic to bursting (looming) and bursting to tonic (receding) closely align with the special distance (x^*), where I_F will be shown to be maximal. b) ISI histograms for a population of ON and OFF cells in the absence of a stimulus (baseline) and in response to looming. The best fit exponential(s) for the range of observed ISIs is shown in black. Insets Application of the time-rescaling theorem [179] removes the stimulus induced trend from the spiking response, confirming that individual pyramidal cell spiking is not Poisson distributed during stimulation. When the cumulative density of the time-rescaled ISI distribution (ordinate) is plotted against the cumulative density of a uniform distribution (U(0, 1); abscissa), the data curve (blue) significantly deviates from what is expected for a Poisson process (the result for a simulated Poisson process of the same duration is shown in black; grey shading denotes 95% confidence intervals; p-values obtained from a 99% confidence level two-way KS-test). Three second sequences of baseline ISIs also deviate significantly from a Poisson process. c) Each ISI is labeled by the spatial position of the object during looming, which yields an averaged non-stationary ISI sequence as a function of object distance, shown in inset (i). Inset (ii) shows that spatiotemporal stimulus correlations are mapped into temporal ISI serial correlations (SC; the correlation coefficient between two ISIs as a function of the lag, or the index number of the recorded sequence). However, after rescaling the ISI sequences, the average serial correlation function demonstrates that spiking can be treated as a renewal process during motion. The grey bands represent 95% confidence intervals associated with the averaged SC function.

ON and OFF cell spike train statistics The dynamical transitions between quiescent, tonic and burst spiking states (Fig. 1a, raster plot) impose statistical structure onto the inter-spike interval (ISI) distributions (Fig. 1b). Although the pooled ISI probability densities of ON and OFF cell populations can be described by exponential distributions (with dead time < 3 ms for the absolute refractory period), an individual neuron's ISI statistics are not Poisson distributed (Fig. 1b insets; Supplementary Note 1). In particular, during motion processing there is strong departure from a Poisson process, serving as an immediate caveat for application of Eq. 1 to our data. Below we present a generalized formula for I_F that is inclusive of the spiking distributions characteristic of ON and OFF cells. In response to looming and receding motion, the average serial correlation of ON and OFF cell ISIs shows that the spiking statistics are strongly non-renewal, that is, the spatiotemporal contrast patterns caused by moving objects produce temporal correlations between successive spikes (Fig. 1c and Supplementary Fig. 1c). To rigorously demonstrate that individual ON and OFF cell spiking is non-Poisson during motion processing, we need to distinguish the intrinsic temporal dynamics of spike generation from those induced by our spatiotemporal stimulus. To this end, we applied the time-rescaling theorem [179], also used in Fig. 1b (insets), to effectively remove the dependence of the ISIs on the distance of the object (Supplementary Note 1). After removing the stimulus-induced trend in the ISIs, no significant correlation remains, indicative of memoryless (renewal) spiking dynamics over the course of stimulation (see Supplementary Fig. 1b, c for receding motion). In other words, the motion-sensitive responses of ON and OFF cells depend only on the current stimulus value and the timing of the last spike, an important feature of instantaneous rate coding. Therefore, we generalize Eq. 1 to locate the I_F maxima of neurons with renewal spiking statistics, free of the restrictive assumption that the observed spiking is described by a Poisson distribution. We expect this result will be relevant for other rate coding systems with irregular, bursty spiking, such as retinal ON and OFF ganglion cells [180], hippocampal CA1 neurons [181] and cortical pyramidal neurons [182].

Stimulus estimation and Fisher's Information An instantaneous population firing rate , which

depends on object position (x), was determined by averaging individual firing rates obtained from both ON and OFF cells in response to 2 cm/s looming motion. This function was then substituted into our formula for locating potential I_F maxima (see derivation in Supplementary Note 2):

$$i_F = \frac{\lambda_x(x,t)^2}{\lambda(x,t)}(1 - \Delta t \cdot \lambda(x,t)) \tag{2}$$

where $\lambda_x \equiv \frac{\partial}{\partial x}\lambda$ and $\Delta t = 10$ ms, a short decoding time window. After repeating this procedure for three more natural looming speeds (1, 3 and 4 cm/s), the mean distance and standard deviation for the prominent I_F maximum was determined to be 1.37 ± 0.01 cm from the fish's body (Fig. 2a; Supplementary Fig. 2; see Methods for the number of repeats and replicates associated with each case). In this vicinity, the variance associated with the estimation of object distance from the observed spiking activity can achieve its lowest possible value [178], giving the best possible encoding. For comparison's sake, I_F was also computed directly using the Poisson formula, resulting in poor identification of a maximum (Supplementary Fig. 2). According to W. Heiligenberg's classic behavioral result [53], the electromotor response (data reprinted in Fig. 2b), gymnotiform electric fish track sinusoidally moving rods optimally (gain near 1 and phase near 0) while maintaining an average distance of 1.34 cm from the nearest rod. Given the striking agreement between the predicted position at which I_F is maximal and the position at which the animal best tracks the object, we suggest that the object distance which maximizes the I_F of a neuron's tuned response is the neural basis of a sensory focal point.

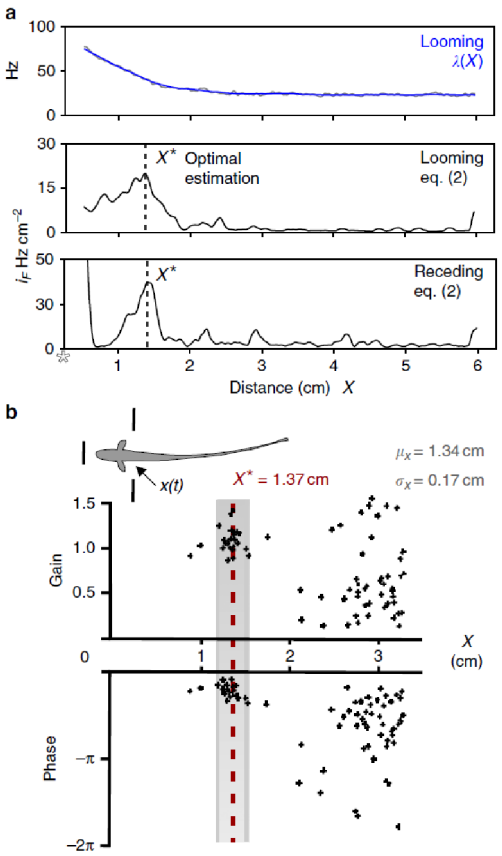

Figure 2 **Precise motion tracking aligns with optimal distance estimation** a) *Top* In response to the 2 cm/s looming stimulus ($d = 1.21$ cm), the average firing rate of an ON/OFF cell population is plotted against object distance (light grey). The firing rate was then smoothed with a 250 ms moving average filter (blue) to remove small fluctuations, while preserving the stimulus-induced trend. *Middle* The nonparametric I_F measure (i_F; Eq. [2]) is computed from the firing rate and plotted as a function of distance from the leading edge of the stimulus to the skin ($x(t)$). For 2 cm/s motion, this equation is maximal at $x = 1.37$ cm, as marked by the grey dashed line, indicating that this is the point where I_F is maximal. Repetition of this procedure for speeds of 1, 3 and 4 cm/s, yielded highly similar results with a mean and standard deviation of 1.37 ± 0.01 cm, denoted as x^* throughout. *Bottom* The theory predicts a local I_F maximum at 1.39 cm for the receding firing rates obtained under continuous motion conditions. The star at the origin indicates motion reversal, and the global maximum in i_F (< 0.5 cm) is due to sudden, sharp transitions from quiescence to high frequency bursting in the ON and OFF cells. b) The averaged value x^* is plotted as a red dashed line over the behavioral electromotor response data of Heiligenberg ([53]; reprinted with permission from the Journal of Comparative Physiology). The average gain (1.06 ± 0.14) and phase (-0.68 ± 0.26) were determined for the two data point clusters associated with excellent tracking performance, which occurred at a distance of 1.37 ± 0.11 cm and 1.31 ± 0.13 cm (see Methods). The composite mean and standard deviation of the two clusters (1.34 ± 0.17 cm) is presented as grey shading, showing remarkable agreement with our predicted location for optimal estimation. Note that the other behavioral data points correspond to the fish resting nearly equidistant between the rods (6 cm separation).

ON and OFF cells are sensitive encoders of object speed, reflected in both the peak of $\lambda(x, t)$ and its slope (Fig. 3a). Despite these strong speed dependencies, the position of maximal I_F was found to be speed invariant over the range of 1 to 4 cm/s, using Eq. 1. However, when applied

to the even slower speed of 0.5 cm/s, representative of the electromotor response behavior, we encountered a methodological issue: the weaker spiking evoked by very slow changes in object position created much more response variability, requiring far greater numbers of trials to obtain sufficiently smooth firing rates. This experimental roadblock to identifying a clear I_F maximum from a noisy Eq. 1 inspired us to investigate what aspect of ON and OFF cell spiking activity reflects maximal I_F in vivo, as well as how the electrosensory circuits might decode the responses in order to produce tracking behaviors for very slow speeds.

Neuron bursting and invariant sensory focus Both modeling and experimental studies of pyramidal cells have shown that input signal intensity controls a bifurcation between tonic and burst modes of spiking [42]. Since burst spiking is strongly dependent on input signal slope [183], is known to be important for feature extraction [39] and becomes prominent near the focal point (Fig. 1a), we sought to understand how bursting directly contributes to stimulus estimation. In particular, Eq. 1 shows that the relationship $1-\Delta t\cdot\lambda(x,t)$ scales the Poisson I_F relationship, suggesting that high-frequency burst spiking (large λ) is important for controlling the spike-likelihood within a small coding window (Δt). When a neuron is in the tonic spiking mode, this scale factor, $1-\Delta t\cdot\lambda(x,t)$, is close to one because the chance of observing a spike in the next $\Delta t \leq 10$ ms is low. However, when the cell sharply transitions to the bursting state, there is a dramatic increase in the spike-likelihood and the scale factor drops nearly to 0. Therefore, bursting activity is expected to sharpen local I_F maxima and enhance focal point acuity (even for very slow motion). To investigate this idea, the number of burst spikes ($3 < \text{ISI} \leq 10$ ms) divided by the total number of spikes (tonic and burst) was determined within 30 consecutive 2 mm intervals along the distance axis (6 cm trajectory) to compute burst fraction (BF) as a function of object distance (Fig. 3b; Supplementary Note 3). We found a clear increase in the relative proportion of burst spiking in the 25^{th} interval, 1.25 to 1.45 cm, for looming speeds of 0.5 to 4 cm/s, occurring very near a data-driven burst fraction threshold of 0.3 (Fig. 3c). Within the intervals spanning the BF threshold, there is a notable reduction in BF variance. From 1.25 cm onward, dramatic, speed dependent increases in BF are evoked (Fig. 3C). Note that the 0.3 threshold is a robust measure of burst activation as it sits more

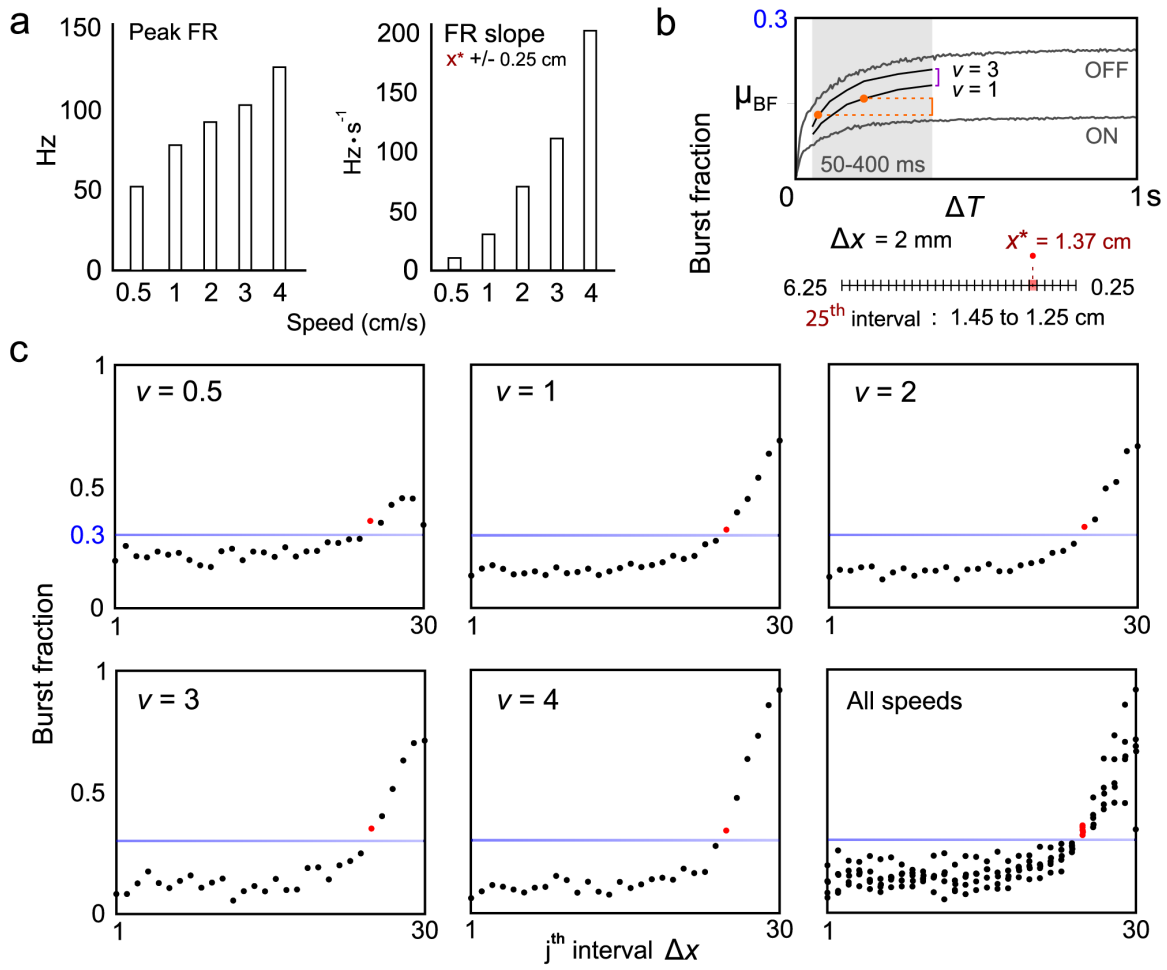

Figure 3 **ON and OFF cell responses are speed dependent but sensory focus is speed-invariant**. a) The peak firing rate and the slope, measured from the line of best fit to the firing rate around the focal point (x^*), are strongly sensitive to an object's looming speed. b) Burst fraction (BF; number of burst spikes divided by the total number of burst and tonic spikes) was used as a means of measuring how activation of bursting relates to the theoretically identified focal point. The 6 cm distance axis was partitioned into 30 successive 2 mm bins (Δx), each from which BF could be computed. Note the 25^{th} interval, which marks the range of distance 1.25 to 1.45 cm and contains x^*. Depending on the movement speed and the corresponding duration of time (ΔT) associated with Δx = 2 mm (50 to 400 ms, for our range of speeds 0.5-4 cm/s) the BF may be underestimated, as shown for the example ON and OFF cells (grey). When comparing between stimulus conditions, we need to be aware of this drift. First, we determined the BF from the first 2 cm of approach where the stimulus has no detectable effect. For example, the are 200 ms and 67 ms for the v = 1 and 3 cm/s data sets respectively (black), which largely determines an offset between the two stimulus conditions (orange). Additional variability occurs from the different composition of ON and OFF cell responses between the different stimulus condition data sets, which is reflected in an offset of their average BF (purple; diminishing as). Next, when examining our BF measure, data sets were aligned to the mean of the entire population (i.e. data from all stimulus conditions) for their respective time window associated with the interval Δx = 2 mm (Supplementary Note 3). This allows for a fair comparison using our simple BF threshold (0.3; $\pm$ 0.0005 shaded in blue). c) Averaged population burst fractions in response to looming stimuli are shown for the 0.5 to 4 cm/s cases. For each condition, the 25^{th} interval containing the focal point, marked as a red dot, is found where the proportion of bursting is starting to rise noticeably, lying just above the threshold but before the rapid divergence in BF. The plot showing all speeds illustrates two interesting facts: variance in the population BF response is squashed near the threshold and, from the 25^{th} bin onward BF intensity and slope reflect motion speed.

than 3 standard deviations away from the closely related burst probability of ON and OFF cells under spontaneous conditions (previously reported as ON: 0.25 ± 0.014; OFF: 0.22 ± 0.016) [35].

The match between the BF measure, our theoretical I_F maximum and the electromotor response behavior is remarkable, particularly because the size of our stimulus is smaller than the object used by Heiligenberg for the data presented in Fig. 2b (d = 1.21 cm versus d = 2 cm). To illustrate the impact of object size and electrical contrast, input intensity curves were generated for our main object size (d = 1.21 cm), and a significantly smaller object (d = 0.64 cm) using an empirical model (Fig. 4a) [55]. The intensity of the contrast sensed at the receptive field of ON and OFF cells scales with the cube of a spherical object's radius. Furthermore, due to their distinct electrical conductivities relative to the surrounding water, a negative plastic stimulus produces a contrast intensity that is half of the intensity produced by the same sized, positive brass stimulus [55,140]. These observations suggest that the location where I_F attains a local maximum is also intensity invariant, consistent with recorded behavioral performance for a range of object sizes [53]. To test this hypothesis directly, we presented 2 cm/s looming motion using the smaller stimulus (d = 0.64 cm), which is a lower bound for object size and electromotor response performance [53]. At the location of the I_F maximum (x^*= 1.37 cm), the signal intensity for the smaller sphere is 23% that of the larger sphere. Yet, when using our BF measure we found that the focal point was still located in the 1.25-1.45 cm range (Fig. 4b, left; Supplementary Table 1). Despite a bidirectional physical symmetry with the traces of Fig. 4a, receding stimuli evoke a skew in the EAs firing rate responses compared to the looming responses, which is caused by directionally selective spike-rate adaptation [140]. This asymmetric EA response causes an apparent disconnect between the feedforward sensory input, pronounced burst spiking and switches in ON and OFF cell coding [140]. Yet, the location of the I_F maximum is preserved in the population (Fig. 2a, bottom; Fig. 4b, right), provided continuous motion occurs, as in the electromotor response protocol. Interestingly, if long pauses (looming, 7 second pause, receding, and then 10 second pause) are inserted there is no longer a notable reduction of the receding burst response. These pauses create a

static object distance and are therefore unnatural for tracking behaviors; in reality continuously varying relative motion is experienced by the network. Under the pause circumstances the I_F maximum is now found at 1.72 cm according to the theoretical approach (Eq. 1). The BF measure also shifts further from the body to the 1.45-1.65 cm distance interval (Fig. 4b, right), which strongly supports the idea that burst onset is a major determinant of the focal point location (Supplementary Fig. 3).

Motion direction- and size- invariance are particularly surprising features of the focal point. An additional population coding perspective is provided for in Fig. 4c (left) for our 2 cm/s velocity cases (default sized looming, default size receding and small looming), which shows that the maximum probability for a neuron in the population to transition to bursting occurs near the 25^{th} interval, (1.25, 1.45) cm. This peak corresponds to the cumulative probability that approximately one half of the neurons in the stimulated population have transitioned into the bursting state Fig. 4c (right) and could be viewed as a tipping point between two population activity states. Remarkably, these population distributions are preserved for both directions of motion and for markedly different stimulus intensities. The close agreement between the focal point location predicted by Fisher Information and burst fraction (Fig. 4d; Supplementary Table 1) is even more convincing in light of these burst-probability distributions.

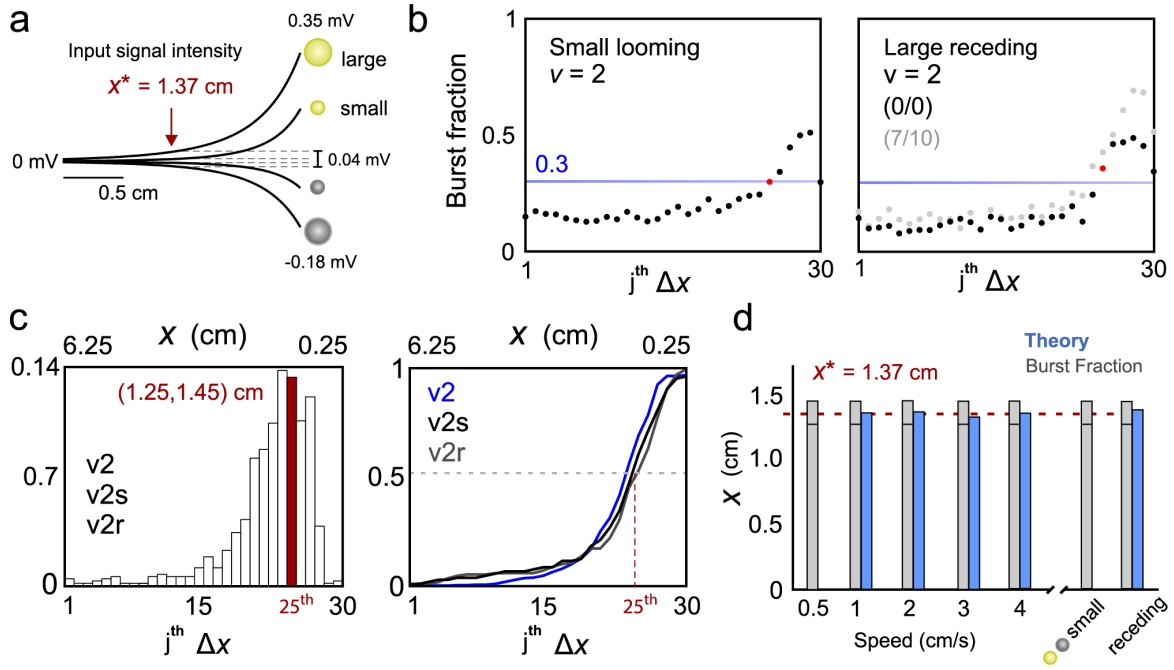

Figure 4 **ON and OFF cell responses are intensity dependent but the focal point is invariant** a) Model traces of the electric potential experienced on the skin of the fish for the final 2 cm of looming (or first 2 cm of receding), caused by brass (yellow) and plastic (grey) spheres with small ($d = 0.64$ cm) and large ($d = 1.21$ cm) diameters [55]. At x^* the small spheres create 23% of the stimulus intensity caused by the large spheres of the same material. Furthermore, a plastic sphere generates a signal that is approximately half the intensity of the same-sized brass sphere in absolute value. b) *Left* To test whether the focal point is size invariant, looming motion was presented to ON and OFF cells at 2 cm/s with the smaller spheres. Despite weaker signal intensity, the BF measure, plotted against distance, indicates that the focal point resides in the (1.25 to 1.45) cm interval. *Right* In agreement with the receding data in Fig. 2a, we see a crossing of the BF threshold between the 24^{th} and 25^{th} interval; thus the focal point is invariant to direction for continuous motion (no pauses; 0/0). This point is strengthened by the observation that long pauses (looming, 7 second pause, receding, 10 second pause; 7/10) result in more pronounced bursting in the system and that the focal point shifts to 1.45 to 1.65 cm according to the BF measure. c) The left panel shows the probability distribution, conditioned on object distance, that a cell in the population will transition to bursting (BF > 0.3) and remain in that state. The process was repeated for 2 cm/s looming (v2), continuous receding (v2r) and the small sphere (v2s), which are pooled together in the histogram – the distribution maximum occurs near the (1.25, 1.45) cm interval. The right panel shows the corresponding cumulative likelihood of bursting in the population, that is, the fraction of cells in the population that have transitioned to bursting. Despite different input intensities, approximately half of the population is activated around the focal point for each case. d) A summary of the two methods for identifying sensory focus. The capped tops of the grey bars denote (1.25, 1.45) cm. Although methodological limitations prevented successful application of the theory for weaker responses, the BF measure is shown to be a predictor of the distance at which I_F is maximal.

Discussion

We have demonstrated that the accuracy of the information conveyed by ON and OFF cells about the location of a transversely moving object is maximal between 1.3 and 1.4 cm from the fish's skin. This location is independent of the nature of the object (positive or negative contrast), its direction of motion, its speed and its size. Importantly, this location is precisely the one chosen by an electric fish as it tracks a transversely moving object in a classic behavioral paradigm. The methods we used to compute the location of the I_F maximum are sophisticated, and, at first, it was not clear how a neural network could actually implement a focal point. ON and OFF cells burst in response to transverse motion and we discovered that a burst detector could, in principle, accurately read out the theoretically defined optimal location. Detailed studies have elucidated the ON/OFF cell burst mechanism [41, 47, 49] and identified numerous potential modulators of bursting [45, 50]. As discussed below, these may be the cellular and network bases by which the burst mechanism is controlled in order to give rise to an invariant focal point.

The fact that a stable I_F maximum was maintained for both ON and OFF cell types under many stimulus conditions implies that the ELL network must actively adapt to the electrosensory input in order to dynamically control gain and burst onset in the ON and OFF cell population. This is a unique example of Barlow's efficient coding hypothesis [184], which holds that sensory systems should transmit information optimally by adapting to natural stimuli. However, the manner by which electrosensory networks adapt to different objects and control focal point stability is unknown. The observed speed invariance of the I_F maximum to looming motion may follow directly from two phenomena: a special computation performed by the EAs and the intrinsic bursting properties of ON and OFF cells. First, a scale-free (power law) form of spike-rate adaptation transforms EA firing rates in order to accurately encode changes in looming object distance, regardless of the stimulus timescales (i.e. looming speed) [104]. Second, both modelling and experimental studies of ELL pyramidal cells have shown that feedforward input intensity controls a saddle-node bifurcation between tonic and burst modes of spiking [42]. As such, object distance will be directly encoded by the EA firing rates,

independent of the object's looming speed [104] and could trigger a burst bifurcation in the downstream ON and OFF cells at a specific position, defined by the biophysical characteristics of the network.

Although the EAs are able to remove speed-dependent effects from their firing rates, the magnitude of their responses is strongly sensitive to different object sizes [104]. Therefore, assuming a hard-wired network response, it is reasonable to expect that the smaller object would trigger bursting much closer to the sensory surface, whereas larger objects would cause bursting to occur at distances further from the skin. However, this is not the case. The observed invariance of the I_F maximum to object size firmly demonstrates that the burst onset can't simply trigger off of the feedforward input. As a further example, our analysis pooled ON cell responses to looming brass spheres with OFF cell responses to looming plastic spheres since they are indistinguishable [140]. Likewise, receding responses of ON cells to plastic and OFF cells to brass were pooled. This simple fact is actually surprising given the stimulus intensity of a brass object is twice greater than the same sized object made of plastic (Fig. 4a). Clearly multiplicative [50] and divisive [185] gain control must be implemented by the network to influence bursting and stabilize the focal point. An understanding of such flexible gain control for dynamic stimuli is an exciting challenge for future work. Note that adjusting the overall gain based on object size and conductivity would allow for effective operation of the hypothesized speed invariance mechanism described above.

Receding motion further challenges our understanding of how burst spiking is controlled in the network. Despite the fact that the feedforward EA response to looming is considerably different than the receding response, downstream ON and OFF cell receding firing rates are nearly mirror-symmetrical versions of the looming response [140] and the focal point is preserved for continuous motion. In this scenario, the dynamical states are visited in the reverse order, but with the same result, illustrating that dynamical transitions optimize signal estimation regardless of their temporal sequence (burst to quiescence or vice versa). Further modelling and experiments on balanced excitatory and inhibitory feedback pathways will be required to directly connect dynamic physiological control of the tonic-burst spiking bifurcation to both

the observed behavioural responses and the optimized stimulus estimation. A clue to potential mechanisms may lie in the robustness of the spiking activity patterns of single neurons in response to concerted changes of multiple conductances induced by neuromodulators [186]. The invariant location of the I_F maximum would presumably require coordinated changes in synaptic conductances of the ELL network in order to control the location of the burst bifurcation in the face of varying electrosensory input. The ON and OFF cells project to the midbrain (torus semicircularis; TS) where there is an explosion in the number of cell types, indicative of early feature extraction [19]. Previously, directionally selective cells have been identified in the TS that are highly sensitive to longitudinal motion; however, further work is required to characterize TS cells that are selective for the transverse looming and receding motion. It has previously been suggested that the burst and tonic spikes of electrosensory ON and OFF cell spike trains can be segregated by facilitating and depressing synapses respectively [194]; both forms of plasticity have been observed in TS neurons [188, 189]. Therefore, we propose that midbrain networks can processes tonic and burst spiking in parallel to compute BF and identify the location of optimized distance estimation.

Extensive neuroanatomical studies [19] have demonstrated that a strong projection from TS to the tectum is the only route from the electrosensory periphery to the motor system. The electromotor response behavior presumably uses this pathway during active sensing, where stimulation of the EAs leads to motor outputs that simultaneously influence the re-afferent sensory processing. We hypothesize that sensory focus is not an open-loop, cascade-like computation but rather a closed sensorimotor loop that arises during active sensing behavior - the fish finds a location that maximizes the information from its electrosensory input and then uses this optimal input to guide subsequent motor outputs. The simultaneous activity of sensory and motor systems during tracking behavior is expected to preserve the relative distance as follows. The animal should adjust its position such that the object distance triggers bursting in approximately half of the stimulated population (Fig. 4c). On the cusp of transitions between different dynamical states, a downstream decoder can optimally estimate object position based on the evoked spiking activity of ON and OFF pyramidal cell populations. In this region of

space, better estimates of object distance are expected to permit more accurate estimates of speed, which are reflected in the temporal slope of the pyramidal cell firing rates (Fig. 3a). For a given object contrast, increases and decreases in signal intensity indicate changes in the relative distance and are expected to dictate appropriate orienting behaviors. Upon changes in motion direction, the prompt bursting of either the ON or OFF cell populations appears very well suited to guide compensatory motor commands in order to maintain object focus.

Methods

Surgical procedure Surgery was performed on adult male and female gymnotiform fish, Apteronotus leptorhynchus (imported from natural habitats in South America), to expose the caudal cerebellum overlying the electrosensory lobe (ELL). All surgical and experimental procedures were reviewed and approved by the Animal Care Committee at the University of Ottawa. Immediately following surgery, fish were immobilized with an injection of the paralytic pancuronium bromide (0.2% w/v), which has no effect on the neurogenic discharge of the electric organ that produces the fish's electric field (EOD) - the basis of the electrosense. The animal was then transferred into a large tank of water (27°C; electrical conductivity between 100 to 150 μS/cm) and a custom holder was used to stabilize the head during recordings. The tails were gently tethered in position with thread to avoid any potential displacement of the body due to the small hydro-mechanical effects caused by looming/receding motion. The fish were monitored for signs of stress and allowed time to acclimatize before commencing stimulation protocols.

Neurophysiology Extracellular recordings were taken from pyramidal cells of the centrolateral map of the ELL [19]. This map was chosen because its neurons respond strongly to object motion and have fairly large, easy-to-locate receptive fields (RFs) [29]. Recordings were obtained from cells whose RFs were located 30 to 65% along the rostral-caudal body axis of the animal, as this region provides the flattest body surface and EOD isopotentials with low curvature that lay perpendicular to the looming/receding stimulus trajectories. Likewise, since the body

curves away from the 'sensory plane' on the belly and back, distance is harder to control for, so only cells whose RFs were in the 25 to 75% range on the dorsal ventral axis were used. These restrictions were to ensure a consistent electric image that was not warped by body geometry or the field boundary effects occurring at the interface of tank water and air. Importantly, this range of the body surface includes the location where the gymnotiform fish Eigenmannia virescens align themselves during the electromotor response behavior [53, 109]. After finding a cell's RF center using a local stimulus dipole, we classified it as ON or OFF based on its response to step increases and decreases in the local field potential. We then mapped out the RF centers, which yielded spatial spreads consistent with anatomical estimates for the centrolateral map [29]. The baseline firing rates of the recorded ON and OFF pyramidal cells (5.4 - 25.9 Hz; $N_E = 15$, $N_I = 16$) demonstrate that they are the superficial and intermediate types [19]. In some cases, we were able to simultaneously record from ON/OFF cell pairs and directly compare their differential responses to object motion. A particularly nice example of one such pair is displayed in Fig. 1a. Using our total population of 31 cells (Supplementary Fig. 1a), we computed a representative standard deviation as $\sigma = 17.06{*}0.95 = 16.21$ Hz, in order to determine a sample size (n) as

$$\begin{aligned} n &\geq \left(\frac{z * \cdot \sigma}{W}\right)^2 \\ &= \left(\frac{2.58 \cdot 16.21}{5}\right)^2 \\ &= 69.4 \end{aligned}$$

for a 99% confidence level ($z^* = 2.58$) on a confidence interval width (W) of $\pm$ 5 Hz. From this simple calculation, we see that we need at least 70 trials. However, when choosing a sample size for estimating mean firing rates in a population of neurons by averaging repeated trials, we need to consider the following. It is not clear that the use of the Z-statistic, which is

related to the normal distribution, is correct since we are sampling different classes of ON and OFF cells whose spiking statistics are inhomogeneous and whose sampling cannot be treated as independent and identically distributed. There are a number of other complicating factors in determining our sample size, including the statistically nonstationary responses of ELL pyramidal cells to motion and the fact that there are two sources of variance: the variance of single cell's response to repeated trials, as well as the variance in the population spiking statistics. In the above calculation, we chose to use spike train statistics in the absence of a stimulus - although the variance grows larger when the stimulus is present, there are also more spikes present, which, when averaged, yield smoother firing rate estimates compared to baseline levels. The degree of smoothing is further influenced by the length of the smoothing kernel (although it was chosen to be a minimal 10 ms in the work presented here). Without a well-defined formula to compute an exact required sample size, we turned to practicality, averaging enough trials to get sufficiently smooth firing rates in order to readily discern the stimulus-induced response and address our hypotheses. We well exceeded the calculated population size for all of our data conditions, with the exception of 0.5 cm/s, which takes 24 seconds to do a single trial, greatly diminishing the amount of data that can be collected. Our largest sample, N = 463, yields 99% confidence on an interval of ± 1.94 Hz. The number of replicates (N_1) and repeats (N_2) for each of our stimulus conditions are listed here and were used for both the theory approach in Fig.2 and the BF measures of Figs. 3 and 4. For the large looming sphere: 0.5 cm/s, $N_1 = 9$, $N_2 = 73$; 1 cm/s, $N_1 = 23$, $N_2 = 255$; 2 cm/s, $N_1 = 31$, $N_2 = 463$; 3 cm/s, $N_1 = 13$, $N_2 = 120$; 4 cm/s, $N_1 = 15$, $N_2 = 166$. For the large receding sphere (2 cm/s): continuous (0/0), $N_1 = 14$, $N_2 = 168$; discontinuous (7/10), $N_1 = 13$, $N_2 = 147$. Finally, the small looming sphere (2 cm/s): $N_1 = 8$, $N_2 = 104$. According to cell type, a plastic or brass sphere was connected to an electromechanical positioner, which was pre-programmed for the appropriate motion sequence and initiated by outputs from our data acquisition software (Spike2 v7.03; Cambridge Electronic Designs). The selected sphere was aligned with the cell's RF center along the transverse (lateral) body axis and placed at the initial position, $x_0 = 0.25$ cm from the skin. Note that mal-alignment with a degree of ± 0.05 cm error was unavoidable

when setting x_0 by using 0.1 cm gradations to measure the position of the sphere's leading edge relative to the fish's body. Slight mal-alignment of the sphere's center with the RF center is another small, but unavoidable source of error. For our large sphere, $d = 1.21$ cm, the effect of mal-alignment on the electric image is negligible since the sphere easily saturated the receptive field. The sphere was then withdrawn and motion was initiated a few moments later. Stimulation consisted of consecutive repetitions of looming and receding sequences at a speed of 2 cm/s, chosen as an intermediate value from studies of gymnotiform locomotion [53,54,109]. This stimulation protocol was then repeated with a sphere creating an electric image with the opposite contrast, as well as for varying speeds (0.5 to 4 cm/s). Acceleration at the beginning and end of constant velocity looming/receding motion profiles was set to 150 cm/s^2, so periods of non-uniform velocity were negligible (< 0.05 cm in all cases). For 13 of the 31 pyramidal cells used in this study, the same loom/recede sequence was repeated with a seven second pause at the skin before receding to the initial position and a ten second pause before the next trial (as performed in a previous study [140]). Typically 10 trials were obtained per cell, but for a few cells (2 cm/s looming, large sphere) it was as many as 25. Population-averaged firing rates were computed by convolving the individually recorded spike trains with a minimal, 10 ms exponential kernel and then averaging across all trials and all cells to obtain smooth response curves for each stimulus condition. The example firing rate curves displayed in Fig. 1a were generated using a smoothing technique employed in previous work [140] (see reference within), but this technique was not used for the analysis since the algorithm assumes spiking can be treated as a Poisson process. Note that convolution of the spike train with a smoothing kernel results in a sharp rounding down of the firing rate at the very ends of the file, where the recorded spiking abruptly stops. As can be seen in Fig. 2, as well as Supplementary Figs. 2 and 3, we routinely clip 0.25 cm from one (receding) or both (looming) edges of the recordings to avoid this false curvature which causes large spurious jumps in Equations 1 and 2. The firing rates were then further smoothed with a short-duration moving average filter of (250 ms), as shown in Fig. 2a (top). Notice the smooth curve (blue) is still a very strong representation of the underlying firing rate. The curves resulting from Eqs. 1 and 2 were then smoothed once

more with a 100 ms moving average filter, enabling us to identify very clear maxima.

We collected data with two conventional sphere sizes, used previously by Chen et al. [55] in detailed models of the electrosensory image: our default sphere, an intermediate size from Heiligenberg's studies with a diameter (d) of 1.21 cm, and a substantially smaller sphere ($d =$ 0.64 cm), which was used as an object size control. Heiligenberg ([53], Fig. 10 within) showed that strong gain in the electromotor response performance begins to deteriorate for $d \approx 0.8$ cm and significantly so for object diameters less than 0.6 cm, thus the small stimulus is expected to represent a meaningful lower bound for network processing during motion tracking. The smaller sphere creates very localized changes in the electric potential; in many cases it seemed we were on the edge of the receptive field, partially stimulating the surround as evidenced by the occasional total lack of response, only to see it appear again. For this reason, we only used data in which a clear, strong response was observed, omitting cases in which the firing rate was inconsistent from trial to trial and dropped dramatically on some trials. In general, data trials were only excluded when external noise was present in a recording or if a cell showed pathological signs of activity, such as hyper-excitability or lack of response to the stimulus. This may occur due to cell fatigue, damage or general anoxic stress. All data analysis was performed using custom Matlab scripts, which can be made available to those interested upon request to the corresponding author. Application of the time rescaling theorem in particular is the most relevant; the remaining code is straight forward or intended to interact with our specific recording software.

Estimation of tracking distance from behavioural data Heiligenberg's original electromotor response data [53], presented in Fig. 2b of the main text, was imported into Matlab ® to identify the positions of the individual data points in the image relative to the axes; this allowed us to compute sample statistics for the obvious clusters, which were not provided explicitly in his paper. This was accomplished with open source code that can be found on the Matlab Central website (ReversePlot © 2009, Jordi Palacin. All rights reserved.) For the top half of the plot (gain versus distance), this method yielded a mean and standard deviation of 1.06 ± 0.14 cm for the gain, occurring at distance of 1.37 ± 0.11 cm. Repeating the analysis for

the bottom half of the plot, we found a phase of -0.68 ± 0.26 radians, occurring at a distance of 1.31 ± 0.13 cm. The average of these two mean distances and their corresponding composite standard deviation is 1.34 ± 0.17 cm, which is overlaid as grey shading onto the behavioral data. It is important to note that the electromotor response data sets were obtained using the weakly electric gymnotiform fish Eigenmannia virescens. Like the closely related gymnotiform Apteronotus leptorhynchus, they produce a continuous, high frequency EOD and have nearly identical electrosensory afferents and hindbrain circuitry [30]. Unfortunately, their electric organ is myogenic and the pancuronium bromide injections used for immobilization blocks the electric organ discharge. A mimic EOD can be generated by mounting an electric dipole onto the animal, with one end in the mouth and the other looped around the tail. Although this is suitable for studying broad global stimuli relating to social interactions with conspecifics, the resulting EODs are highly artificial and do not reflect the local spatial aspects of the field in vivo. Despite being useful as a behavioral species, Eigenmannia is not well suited to our neurophysiology protocols.

2.5 Feedback synthesizes neural codes for motion

Clarke SE*, Maler L. (2017). Current Biology, 27(9): 1356-1361.

Contributions: S.E.C and L.M designed the experiments, which were carried out by S.E.C. S.E.C performed data analysis. S.E.C. and L.M. designed the figures and wrote the paper. *S.E.C. is corresponding author.

Significance: Perception is an enduring problem in science since it relies on complex internal processes to impose meaning on raw sensory input. Neural feedback is central to this function and is typically described as a modulatory top-down influence on bottom-up input from an animal's senses.

"In more general terms, it remains unclear in any sensory system whether top-down projections innervating sensory areas merely modulate perception or are fundamentally involved in perception." - Manita et al. (2015).

In corticothalamic networks, top-down control of bursting was originally hypothesized by Francis Crick to act as a sensory searchlight for primate visual spatial attention, and, by extension, hearing and touch. Feedback in electrosensory neural networks was hypothesized to do the same. We've now identified a minimal computational unit - a time-limited positive feedback loop - that greatly expands the concept of a searchlight by linking it not only to burst modulation, but to the complete synthesis of neural responses to motion. Our experiments on looming motion show that feedback modulates bottom-up responses and establishs an important burst bifurcation linked to optimal motion coding. However, our exciting and thought provoking observation is that the neural code for motion away from the body is entirely synthesized by feedback, producing a directionally invariant representation of motion. By generating a neural code at the earliest stages of sensation, a bottle-neck for signal transmission to higher sensory

and motor areas, the electrosensory system closes the sensory-motor loop and is hypothesized to exert flexible control over its emerging perception of motion.

Introduction

In senses as diverse as vision, hearing, touch and the electrosense, sensory neurons receive bottom-up input from the environment, as well as top-down input from feedback loops involving higher brain regions [195–198]. Through connectivity with local inhibitory interneurons, these feedback loops can exert both positive and negative control over fundamental aspects of neural coding including bursting [39, 199] and synchronous population activity [200, 201]. Here we show that a prominent midbrain feedback loop synthesizes a neural code for motion reversal in the hindbrain electrosensory ON and OFF type pyramidal cells. This top-down mechanism generates an accurate bidirectional encoding of object position, despite the inability of the electrosensory afferents to generate a consistent bottom-up representation [5,140]. The net positive activity of this midbrain feedback is additionally regulated through a hindbrain feedback loop, which reduces stimulus-induced bursting and also dampens the ON and OFF cell responses to interfering sensory input [16]. We demonstrate that synthesis of motion representations and cancellation of distracting signals are mediated simultaneously by feedback, satisfying an accepted definition of spatial attention [202]. The balance of excitatory and inhibitory feedback establishes a 'focal distance for optimized neural coding, whose connection to a classic motion tracking behaviour provides new insight into the computational roles of feedback and active dendrites in spatial localization [13, 203].

Weakly electric fish use a self-generated electric field to track moving objects [17,53,54,109]. In one particular behaviour, the electromotor response [53,109], fish track swinging plastic rods at a fixed distance from their body. As the fish attempts to maintain this position, a sensory focus that optimizes motion estimation [204], the relative distance between the fish and the rod is constantly changing and causes spatially localized increases and decreases in the fishs electric field relative to the background (sensory contrast). These local motion signals are relayed by cutaneous electroreceptor afferents (EAs) that form excitatory topographic projections onto deep and superficial ON and OFF type pyramidal cell pairs, located in columns of the hindbrain electrosensory lobe (ELL; Figure 1) [5, 19]. The ON and OFF cell populations are a bottle-neck for bottom-up sensory contrast information and project topographically to

the torus semicircularis (TS), a midbrain structure in the ascending electrosensory pathway that projects to the optic tectum and thalamus [19].

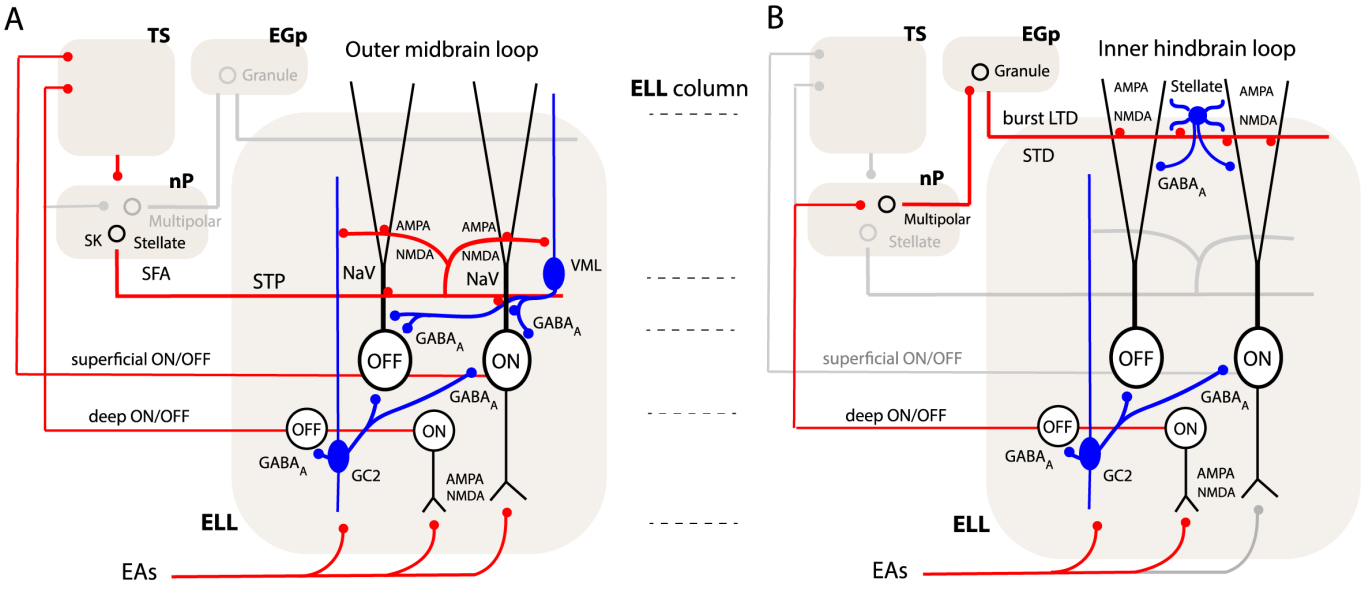

Figure 1 **Electrosensory feedback loops**. (A) Electrosensory signals are transmitted by electroreceptor afferents (EAs) that terminate topographically onto columns of the electrosensory lobe (ELL). The EAs form glutamatergic synapses on the basal dendrites of deep and superficial ON type pyramidal cells, as well as local GC2 interneurons, which, through ionotropic GABAergic synapses (blue), invert the EA signal for the deep and superficial OFF cells of the same ELL column. An outer loop is formed by excitatory (glutamatergic, red) topographic projections of both deep and superficial ON/OFF cells to the midbrain torus semicircularis (TS). There are many cell types in TS, some of which project back topographically to the stellate cells of nP, which, in turn project back topographically onto the AMPA/NMDA rich proximal apical dendrites of the superficial ON/OFF cells. This loop provides strong short-term potentiating (STP) excitatory control over the burst generating mechanism through interactions with the back propagation of action potentials, supported by sodium channels (NaV) in the proximal dendritic arbor. This excitation is time-limited through the hyperpolarizing action of SK channels on the nP stellate cells causing spike-frequency adaptation (SFA). The net positive feedback is also regulated by the subtractive inhibition of the GC2 interneurons and the divisive inhibition from VML interneurons [50]; both interneuron types receive positive feedback of the outer loop and drive GABA-A receptors on the soma and dendrites of superficial ON/OFF cells. (B) An inner hindbrain loop originates from the deep cells that emit collaterals to nP (superficial cells do not project directly to nP [16]). A different type of nP neuron, the multipolar cell, then projects to granule cells of the caudal cerebellum (EGp). Next, these granule cells project parallel fibers that terminate back on the distal apical dendrites of superficial ON/OFF cells. Burst induced long term depression (LTD) [210] and short term depression (STD) [13, 208] at the parallel fiber to pyramidal cell synapses enable flexible control over the excitatory input to AMPA/NMDA rich distal dendrites. The inner loop is crudely topographic compared to the outer loop, providing diffuse feedback to the superficial cells.

In addition to the bottom-up EA input, two prominent feedback pathways terminate on

the extensive apical dendrites of the superficial ON/OFF cells. First, the TS modulates its own superficial ON/OFF cell input through a topographic projection to a hindbrain nucleus (n. praeminentialis, nP) [13,15], where it drives stellate cells (Figure 1A). The stellate cells feedback with precise topography onto the proximal apical dendrites of the ELL superficial ON/OFF cells [13, 20, 39]. Since this feedback pathway engages the midbrain, we label it the 'outer loop. The outer loop also drives local ELL inhibitory interneurons [13] but previous in vivo [205] and in vitro [37] studies show that it is strongly net excitatory when activated. A second distinct loop remains confined to the hindbrain (Figure 1B) and is termed the 'inner loop. The inner loop originates from the deep ON/OFF cells, which directly excite the nP multipolar cells projecting diffusely to the cerebellum (EGp), whose granule cells provide excitatory input to the distal apical dendrites of superficial ON/OFF cells [13, 206]. The inner loop also engages local inhibitory interneurons [13]; during stimulation, this loop is net inhibitory due to potent disynaptic inhibition [205, 207, 208]. Both the inner and outer loops exert control over bursting, imparting strongly nonlinear receptive field (RF) properties to the superficial ON/OFF cells [13, 20, 90]. Unlike the superficial cells, the non-bursty deep ON/OFF cells have stunted dendrites, receive little feedback and are nearly linear encoders of sensory contrast [16, 90].

Results

Motion stimuli were presented to immobilized A. leptorhynchus while recording extracellularly from superficial ON and OFF type pyramidal cells in vivo. After mapping the RF, a brass or plastic sphere was aligned with the recorded cells RF center midpoint [91] and then withdrawn to an initial position of 6.25 cm from the body; sequences of loom-recede stimuli were presented at 2 cm/s with motion reversal occurring at 0.25 cm, either immediately or after a brief pause (Figure 2A; see Supplemental Experimental Procedures). Motion along this body axis is experienced during the electromotor response (Figure 2A, inset) [53]. Despite the directional symmetry in the electrosensory contrast, an asymmetry develops in the EAs after motion reversal due to spike frequency adaptation (Figure 2A) [5,140]. The superficial ON cells encode looming motion for positive contrast signals (brass) and superficial OFF cells encode

looming for negative contrast signals (plastic) [5, 140]. Both cell types rapidly increase their firing rate as their preferred stimulus approaches the body and their firing rate is suppressed by the 'non-preferred looming stimulus (Figure 2B). Upon motion reversal, there is a dramatic switch in burst activity between cell types: ON cells encode the receding motion of negative contrast signals, while OFF cells encode receding for positive signals [5, 140]. Example spike trains from an ON/OFF cell pair switch are shown for the brass sphere (Figure 2B, bottom), including the decreased firing rate responses, which signal context but ambiguously encode distance. Given that ON and OFF cell responses to looming and receding are indistinguishable [140], we pooled their looming and receding spike trains into separate groups to determine firing rates in each direction of motion (Figure 2B). Aside from an average delay of 142 ms until bursting onset, the receding firing rate is a reflection of the looming response, generating a directionally invariant neural code for object motion around the sensory focus (Figure 2B inset; x*) [204].

Spike trains were decomposed into burst spikes (red; inter-spike interval $\leq$ 10 ms) and tonic spikes (black; $>$ 10 ms) and population averaged firing rates for both modes of spiking are plotted against distance (Figure 2C). The skew from the bottom-up EA input is reflected in the tonic spike firing rates of the superficial cell receding response, which are qualitatively similar to the deep ON/OFF cell firing rates (Figure 2C, insets). The superficial burst firing rates surpass the tonic rates near the location of the sensory focus (x* = 1.4 cm) [204]. This specific distance occurs at a bifurcation between tonic and burst modes of spiking [140, 204]. In the following, we locate this point using the burst fraction (BF), that is, the number of burst spikes divided by the total number of spikes, determined as a discrete function of distance in 2 mm intervals along the distance axis (BF; see also Figure S1 and Supplemental Experimental Procedures) [140, 204].

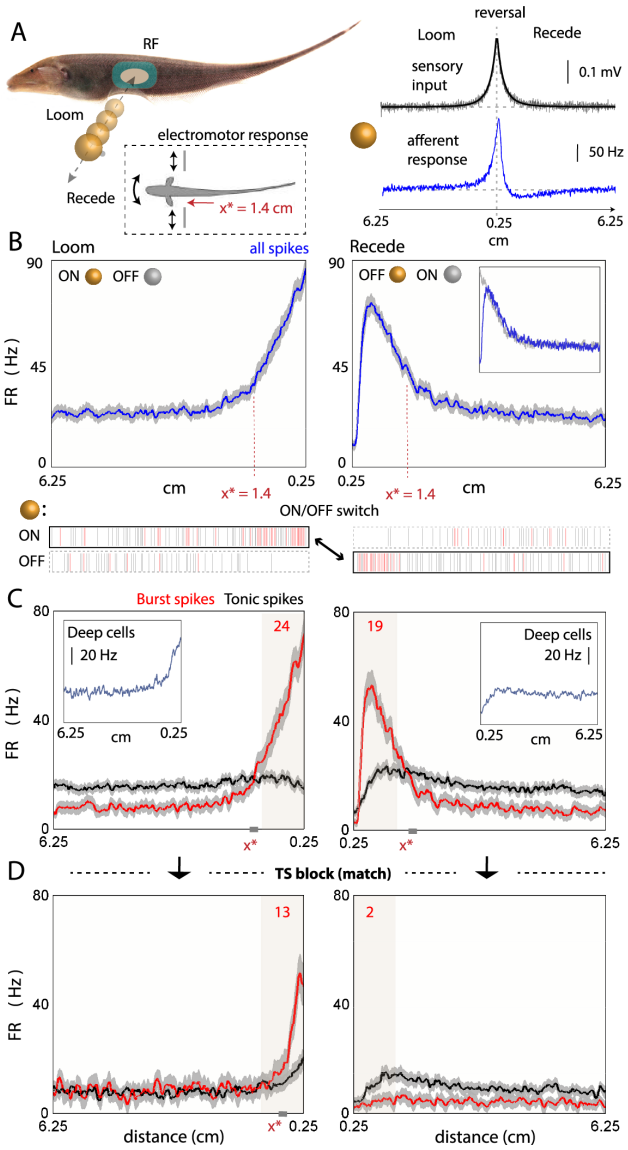

Figure 2 **Feedback synthesizes a code for motion**. (A) Motion stimuli were presented to immobilized fish during in vivo extracellular recordings from superficial ON/OFF pyramidal cells. A looming object increases (brass; shown) or decreases (plastic; not shown) the electrical contrast (black) and the EAs encode the changing object distance by respectively increasing or decreasing their firing rates (blue). Upon motion reversal, EA adaptation generates an asymmetry in the relayed EA input and the firing rate drops below baseline near 1 cm, falsely indicative of negative contrast for a positive contrast object. The same skew occurs for the receding plastic sphere [5, 140]. Inset: In the electromotor response [53], fish maintain a constant distance (x*) to a swinging bar. (B) During looming of brass or plastic spheres, the ON or OFF type neurons respectively increase their firing rate, while spiking is suppressed in the opposing cell pair [5, 140]. Population averaged firing rates (FR; blue) were determined from all cells and plotted over the sample means standard error (grey). Example spike trains from an ON/OFF cell pair switch are provided. While the ON cell increases burst spikes (red) relative to tonic spikes (black) during looming, spiking is suppressed in the corresponding OFF cell. Upon motion reversal, a rapid switch is evoked: the previously suppressed OFF cell begins to burst and the ON cell is now suppressed [5,140]. The distance x* = 1.4 cm marks a transition between burst and tonic modes of spiking, a 'sensory focus where motion estimation is optimal (see Figure S1) [204]. (C) The data was decomposed into tonic and burst spikes and plotted as separate firing rates. The average number of burst spikes (red numbers) were counted in the distance interval [0.25, 1.25] cm (beige). The insets show the responses of deep ON/OFF cells, which receive little feedback. (D) Bilateral TS circuitry was inactivated. Looming: bursting is significantly reduced. x* shifts to the distance interval [0.65, 0.85] cm. Receding: the burst response is abolished. The motion responses of superficial pyramidal cells (see Figure S1) now resemble the skewed bottom-up input from the EAs and deep cells.

A relative increase of 0.15 in the BF from baseline, crossing a simple threshold of 0.3, marks the interval [1.25, 1.45] cm for looming and, due to a mix of pause and continuous motion data, identifies [1.45, 1.65] cm for receding motion. Although pausing between looming and receding alleviates cell fatigue, the burst response doesnt adapt over repeated trials, whereas under continuous motion conditions it adapts and the interval [1.25, 1.45] cm is properly identified (see Figure S1). As a main comparative statistic between our experimental conditions, burst spikes were also counted for each trial over a one cm interval near the fishs body, where they are most prominent. These burst count distributions were compared between each experimental condition and the normal data using the two-way Kolmogorov-Smirnov test, $\alpha = 0.01$, whose null hypothesis (H_0) states that two empirical data sets are drawn from the same continuous distribution. A complete list of sample sizes and associated statistics is found in the Supplemental Experimental Procedures.

To investigate the role of feedback, glutamatergic transmission within a small region of TS was blocked with bilateral pressure injections of CNQX (10 μM) and AP5 (100 μM). Anatomical data [43] was used as a guide to match the topography of the TS injection to the ON/OFF cells RF location (see Supplemental Experimental Procedures). A putative topographic match between the inactivated TS circuitry and the recorded cells RF resulted in elimination of the receding response (reject H_0, p = 4 x 10^{-106}) and a much weaker looming response (reject H_0, p = 2 x 10^{-16}); Figure 2D). Top-down activity entirely synthesizes the burst responses to receding motion, whereas it enhances an existing bottom-up burst code for looming motion. The estimated focal point shifts toward the body for looming (Figures 2D and S1B) and is undefined for receding since burst spiking is abolished. Post-injection, the superficial responses resemble the deep ON/OFF cells (Figure 2B, insets; see also Figure S1) [20].

Neuroanatomical data suggests that the inner loop might be modulated by TS [43]; thus, it remained uncertain whether TS synthesizes receding responses through the outer feedback loop or the inner loop. Therefore, we inactivated inner loop feedback with a bilateral block of the cerebellar (EGp) projections, which leaves the outer loop completely intact.

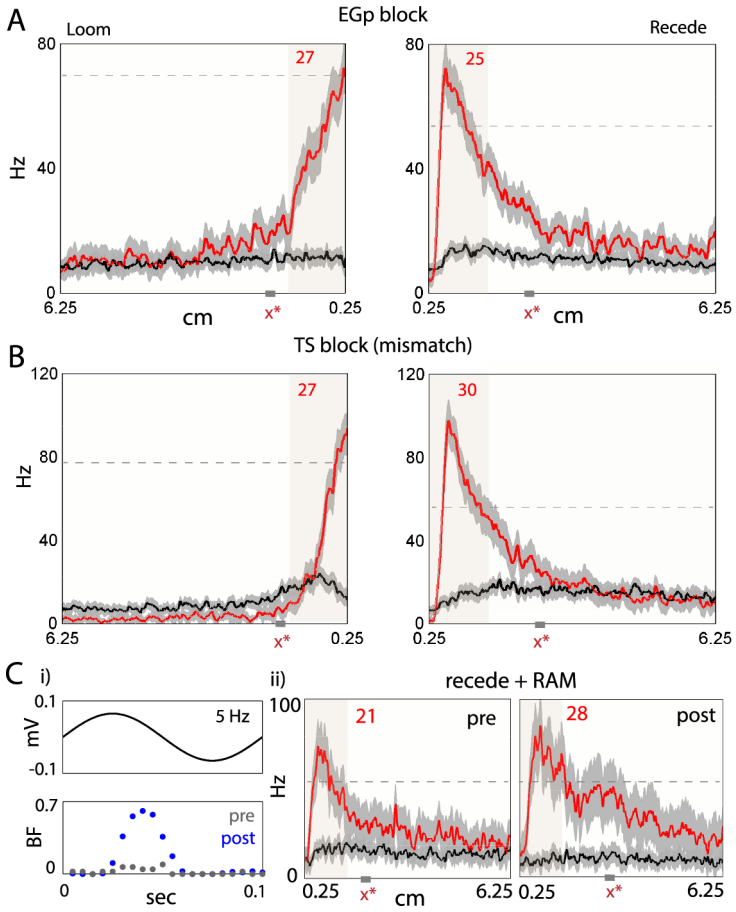

Figure 3 **Receding response synthesis during noise cancellation** . (A) Blocking the inner loop (EGp) leads to an enhancement of ON/OFF cell motion responses. For comparison, the dashed line marks the normal peak burst firing rates from Figure 2C. This data serves as an important control, proving that the outer loop is responsible for receding response synthesis. The focal point shifts slightly outward for looming, x* ϵ [1.45, 1.65] cm, and significantly outward for receding, x* ϵ [2.25, 2.45] cm (see also Figure S1). (B) A TS injection that is topographically mismatched with the recorded cells RF leads to strongly enhanced motion responses. The estimated focal point shifts out even further, x* ϵ [2.45, 2.65] cm. (C) When driven by spatially diffuse stimuli, signal cancellation operates via cerebellum (EGp). i) Under normal conditions, the burst response to a global sinusoidal stimulus is cancelled (grey) as expected; after TS injection, cancellation is eliminated and the cell responds strongly to the global stimulus (blue). ii) A strong 0-6 Hz random amplitude modulation (RAM) was played to the animal during motion: under normal conditions (left), the cancellation mechanism damps the response to the distraction, permitting the local receding response to be correctly synthesized. The estimated focal point lies in the [1.45, 1.65] cm interval. After TS mismatch block (right) the cells respond strongly to the RAM, which contaminates motion coding and shifts the estimated focal point substantially, x* ϵ [3.05, 3.25] cm (see also Figure S1 and S3).

Blocking the EGp output signal significantly increases the looming (reject H_0, p = 3 x 10^{-8}) and receding (reject H_0, p = 4 x 10^{-13}) motion responses in ON/OFF cells and shifts the focal point outward (Figure 3A, see also Figure S1). This is the complete opposite effect from the TS block (Figure 2D). Since the inner loop is net negative during motion (Figure 3A), we

conclude that positive feedback from TS and the outer loop is solely responsible for creation of the receding response, while the net negative action of the inner loop helps to stabilize the net positive action of the outer loop and balance the network around the sensory focus (x*).

The outer loop is precisely topographic at each stage of transmission; therefore, we hypothesize that blocking TS circuitry that is topographically matched to the superficial ON/OFF cells RF explains the abolished receding burst response. In support of the hypothesis, we repeated our motion protocol at sites more than one cm rostral or caudal to the RF center midpoint, aligned with, or just past the edge of the mapped RF center [91]. This hypothesized TS injection mismatch produced the opposite effect from the matched TS block (Figure 2D): very large increases in burst spiking and firing rate for both looming (reject H_0, p = 6 x 10^{-3}) and receding motion (reject H_0, p = 4 x 10^{-20}; Figure 3B). Although the focal point for looming remains the same, the focal point for receding shifts outward from the body (Figures 3B and S1). For the receding response, these increases in bursting are qualitatively similar but significantly larger than those produced by the EGp block (reject H_0, p = 8 x 10^{-8}), suggesting that negative mismatched TS modulation acts through both inner and outer loops. In further support of a topographic relationship between feedback and the pyramidal cells RF, if an apparent mismatch was obtained first, we could move the injection pipettes more rostral or caudal in TS and re-inject to eliminate the receding response. We further confirmed that our results extend to motion parallel to the body, where the spheres reverse at the RF center midpoint of ON/OFF cells (see Figure S2) [140]. The transition in all three dimensions between net positive feedback with a suspected topographic match, versus net negative feedback with mismatched topography is consistent with an earlier suggestion that the outer loop implements a spatial attention mechanism [13].

During natural motion, A. leptorhynchus continuously bends its tail, causing spatially diffuse amplitude modulations (AMs) of the electric field. These AMs are encoded by the EAs and deep cells but not by their target ON/OFF superficial cells [16,209]. Since the inner loop is responsible for cancelling interfering AMs [210], we wondered whether concomitant regulation

of outer and inner loops via the TS projection to nP is required during natural motion processing. Figure 3C shows an example superficial cells cancellation of a typical sinusoidal AM response under normal conditions. After mismatched TS injections, a strong bursting response to the AM is unmasked in agreement with EGp blocks [16, 210]; this result shows that TS has control over the inner loops cancellation circuitry. Can cancellation of a distracting AM occur simultaneously with the synthesis of the ON/OFF cell receding responses? To address this, we investigated the ON/OFF cell responses to receding motion in the presence of a strong random AM (RAM) that mimics tail bending (see Figure S3 and Supplemental Experimental Procedures). Under normal conditions, cancellation largely buffers the RAM, and the receding burst response maintains its form (Figure 3C; cannot reject H_0, p = 0.02), although burst spikes occur proportionally more than tonic spikes overall. After mismatched TS injections, cancellation is poor and there is a large increase in bursting evoked by the RAM stimulus that degrades the neural code (reject H_0, p = 8 x 10^{-9}; Figure 3C). For a TS match, the receding response vanishes again (see Figure S3). We conclude that TS coordinates the activity of the outer and inner loops to generate meaningful neural codes for spatially localized motion, even in the presence of noisy background distractions.

Discussion

The cellular and molecular components underlying the synthesis of neural codes for motion have been characterized. The outer loop stellate cells in nP respond to motion signals with high frequency bursts [15]. These bursts of stellate cell activity induce strong potentiation of synaptic feedback inputs onto the proximal apical dendrites of ON and OFF pyramidal cells [37, 205] and evoke summating NMDA-R postsynaptic potentials [13]. This amplifies the input and evokes superficial cell burst discharge through interactions with a backpropagation mechanism mediated by NaV channels (Figure 1A; [13, 211]). During motion, the TS drives inner and outer loop circuitry, balancing excitation and inhibition around the sensory focus, as evidenced by shifts of x* toward the body when net positive feedback is blocked (Figures 2D, S1) and away from the body when negative feedback is blocked (Figures 3A, B and S1).

Negative feedback is likely mediated by rapid SK channel spike-frequency adaptation in the outer loop nP stellate cells [13,15,212]. Additional negative regulation is provided by local ELL interneurons that receive outer and inner loop feedback and generate adaptation in ON/OFF cells [13]. Theories of sensory processing state that top-down projections modulate bottom-up, stimulus driven neural representations by regulation of receptive field tuning, bursting and population synchrony [13,195–197,199,200,203,213,214]. In mammalian sensory systems, cortical feedback loops dominate bottom-up sensory input to thalamus and either positively or negatively control bursting depending on whether the inactivated circuitry is topographically matched or mismatched to the spatial RF centre of thalamic relay neurons [195, 197, 201]. In the visual system and the electrosense, this organization is thought to implement a spatial attention mechanism or 'sensory searchlight [13, 203]. Our findings are important for theories of top-down processing and spatial attention in three distinct ways: first, that topographic feedback not only amplifies but must completely synthesize complete neural representations of motion; second, extends our understanding of gain amplification in the context of sensory focus and dynamic control of excitability and bursting [204]; and, third, illustrates how distinct computations can be coordinated simultaneously by feedback, operating within distinct dendritic compartments of bursty pyramidal cells. We note these results satisfy a broadly accepted definition of spatial attention: the enhanced processing of a targeted sense input with a coordinated reduction of distracting input [202]. Very recently, it has been demonstrated that top-down cortical projections are essential to complete the perception of touch [214–216]. In particular, Takahashi et al. [216] demonstrate that, in order for the feedback projections to modulate perception, they had to terminate on active apical dendrites of cortical pyramidal cells and generate burst discharge; additionally, the excitatory feedback was balanced by local cortical inhibition. This is consistent with our results, suggesting that equivalent algorithms for top-down control via active dendrites are utilized for representations of touch in mammalian cortex and representations of motion in the electrosensory system. Although there are clear differences (e.g. the cellular basis of bursting [13, 216], the striking algorithmic similarities

across distinct species and sensory modalities support Marrs idea of natural selection for neural computation [5], where evolutionary pressures for highly functional sensory coding select for similar computational principles from the available biophysical substrates.

Chapter 3

Discussion

3.1 Results summary

This thesis began by examining the response of electroreceptor afferents to looming motion (Section 2.1). There are two key results of this paper: first, spike-rate adaptation transforms looming motion signals such that the output firing rates are invariant to speed, providing unambiguous estimates of changing object distance; second, scale-free adaptation that approximates a power law with exponent -1 is critical for this function. However, since the presence of long adaptive time-scales interacts strongly with the low frequency looming motion signals, motion reversal generates an asymmetrical EA receding response (asymmetrical distance tuning curve), despite the symmetrical looming and receding electrosensory input. This is shown is Section 2.2, along with the observation that a symmetrical receding response is generated in the previously suppressed member of the ON and OFF cell pair during looming. In addition to restoring a bidirectionally symmetric representation of motion, this important coding strategy provides vector information by tracking the sequence of ON and OFF cell activation, allowing it to deduce object class (conductive versus non-conductive) and interpret scalar estimates of position and speed found in the firing rates. It appears highly likely that this ON/OFF switch is a key component of an active sensing behaviour (described further below), and that optimized estimation of motion parameters guide the animal to a specific distance when tracking a

moving object. This special point, described in Section 2.4, is intimately related to the bifurcation between quiescent, tonic and burst modes of spiking and has been described here as a *sensory focus*. We hypothesize that this focus is a fundamental feature of sensorimotor control and serves to optimize both stimulus encoding and behavioural output. The speed invariance of the sensory focus may be explained by the speed-invariant EA responses, but the directional invariance, contrast invariance and size invariance cannot be explained by bottom-up processing nor by intrinsic cell nonlinearities. The final major result of this thesis is described in Section 2.5: whereas top-down control from midbrain to hindbrain, acting via compartmentalized feedback to ON and OFF cell apical dendrites, amplifies the burst response to looming, it completely synthesizes the burst response to receding motion. Presumably feedback is responsible for the flexibility necessary to maintain a multi-feature invariant sensory focus by scaling the pyramidal cell excitability in response to a variable environment.

3.2 A proposed sensorimotor algorithm for motion tracking

Admittedly, our work has only a correlative connection to motion tracking behaviour, simply relying on the striking connection between in vivo neural dynamics and the results of a classic behavioural paradigm. Future studies establishing a causal link between the concept of sensory focus and observed animal behaviours will require in vivo wireless recordings during unrestrained active sensing. Nevertheless, it is relatively straight-forward to imagine how a sensory focus operates within a natural context, as briefly described in the Discussion of Section 2.4. When implementing sensory focus, first the animal approaches the object, resulting is a gradual quasilinear increase in the firing rate of the stimulated ON or OFF pyramidal cell population. As the object moves past the focal point, there is a strong, nonlinear ignition of bursting in the specific ON or OFF pyramidal cell population, which could hypothetically drive tectum to move the animal back from the object; this action creates a condition of motion reversal and would trigger a suppression of the activated neuron population while igniting a burst response in the opposing population. This signal could in turn drive the tectum to

initiate movement toward the object. Operating around a sensory focus may be a highly useful strategy, as small deviations of the object from the sensory focus point results in strong pyramidal cell switches that encode the change in direction, establishing a behavioral context in which to interpret the scaler firing rates. In this way, optimized estimates of direction, distance and speed are contained in the activated ON or OFF cell population firing rates. Downstream midbrain networks can hypothetically decode this motion vector and initiate appropriate motor commands to ensure that the object is held in the sensory focus. This 'push-pull' form of active sensing involves stabilization within a sensorimotor loop, in which neural coding and motor outputs simultaneously influence each other to optimize both stimulus estimation and motion tracking performance. The apparent heavy reciprocal connectivity between TS and tectum suggest a fascinating interplay of motor signals and sensory coding in freely moving animals, which may be used to further influence the top-down control of sensory processing. Based on Section 2.4 and 2.5, surely feedback is also involved in regulating sensory focus invariances to stimulus size and various conductivity level intensities (e.g. discrepancy between brass and plastic). A noisy and changing environment and real-time motor system outputs necessitate flexibility to successfully implement the proposed algorithm for sensorimotor control.

3.3 Feedback, sensory perception and cognition

As described in the introduction, one might expect that the foundations of sensory contrast coding related to encoding signal amplitude, along with its spatial and temporal derivatives could generalize to other species. In fact, power law spike-frequency adaptation operates in many sensory systems and performs a similar 'temporal whitening' operation in rodent neocortical pyramidal cells [104]. Furthermore, the retinal ganglion ON and OFF cells show the same algorithmic selectivity for increases and decreases in sensory contrast and distributed contrast coding has also been demonstrated in mammals (Section 2.2, [5, 140]; Appendix 1). The fact that ON and OFF cell types are found in diverse regions such as auditory, somatosensory and visual mammalian cortex, as well as the hindbrain of an electric fish and the eyes of both

vertebrate and invertebrate species, reflects their fundamental role in neural coding [5]. Finally, feedback is central to both simple and advanced neural systems. Low level electrosensory processing uses a feedback network architecture similar to that identified by Takahashi et al. [216]: in both systems, positive feedback amplifies dendrite-mediated bursting and is regulated by precisely controlled negative feedback from a variety of local interneurons. Since electrosensory ON/OFF cells form a bottle-neck for ascending electrosensory information, it appears that electrosensation and perception is also a closed-loop phenomena [217]. As mentioned in Section 2.5, the strong connection between our results and rodent somatosensory perception suggests that nested feedback control of bursty pyramidal cells is also very relevant to sensory cortical dynamics, providing evidence that our work will continue to show deep computational analogies with higher vertebrate circuitry.

A classic interpretation of perception is based on a hierarchical, bottom-up organization of information flow in neural networks, where low level regions mediate simple sensory processing, while perception emerges at higher cortical levels. However, the results in the electrosense and rodent somatosensory system suggest perception is a consequence of dynamically matched top-down positive and negative feedback, with bottom-up inputs; these various streams are organized into nested loops that simultaneously incorporate both 'low' and 'high' level brain regions. Perception [198, 221], social memory [222] and reward based choice decisions [223] all rely on cortical positive feedback loops and it is hypothesized that this feedback is an essential component of cognitive neural networks. It has even been suggested that consciousness is generated by positive feedback loops that span multiple cortical regions [224, 225]. In fact, two generic features of electrosensory feedback described in Section 2.5, response synthesis and cancellation, appear consistent with observations from the cognitive sciences. Specifically, Moutard et al. [218] summarize evidence for a slow rise in activity before an ignition of bursting in cortical sensory responses, which is reminiscent of the quasilinear increase in ON or OFF cell firing rates as an object first approaches the body, before reaching the location of the burst bifurcation found at the sensory focus. If a focus-like algorithm was operational in the cognitive

domain as well, the slow increase in intensity of an abstract representation would be bound in the global workspace by ignition of bursting and maintenance of optimized information transfer over the long range loops between distinct brain regions. The brain could conceivably operate and stabilize sensory-cognitive loops in a similar push-pull manner as sensory-motor loops while the dynamics of the mental state are perturbed over time by inputs from various brain regions and sensory modalities. Such an operation would necessarily rely on strong excitatory feedback to pyramidal neurons and allow for an active sampling of various features of the mental state.The role of negative feedback in spatial attention and perception suggests it may be important for the cognitive domain as well [219]. Although Ramaswami's review [219] has a glaring omission of relevant and well-known literature [210, 220], it confirms that the dynamics underlying negative image formation likely has great generality and plays an integral role in cortical dynamics and higher cognition. Together, the evidence for net excitatory and net inhibitory feedback loops in cortical dynamics and their striking similarity to electrosensory dynamics, suggest that a conserved spatial attention circuit has been coopted and repurposed in more advanced neural systems.

3.4 Concluding remarks

The goal of neuromorphic engineering is to understand how synapses, neurons, circuits and overall brain connectivity represent information, perform desirable computations, learn and adapt to a changing environment. I believe relatively simple sensorimotor systems, such as the electrosense, can provide a powerful research tool for those interested in abstracting complex cortical computations into dynamically equivalent circuit descriptions. This approach aims to emulate high level neural systems by contributing to a 'neural toolbox' which is based on the idea that a substantial component of cognition bears the imprint of classical dynamics and spatiotemporal processing. Characterization of these sensory computations is expected to be essential in the neurotechnology revolution by enhancing existing brain-machine interface technologies with neuromimetic computing.

Appendix A

Supporting Articles

A.1 Contrast coding in the electrosensory system: parallels with visual computation

Clarke SE, Longtin A, Maler L. (2015). Nature Reviews Neuroscience 16: 733-744.

Abstract

To identify and interact with moving objects, including other members of the same species, an animal's nervous system must correctly interpret patterns of contrast in the physical signals (such as light or sound) that it receives from the environment. In weakly electric fish, the motion of objects in the environment and social interactions with other fish create complex patterns of contrast in the electric fields that they produce and detect. These contrast patterns can extend widely over space and time and represent a multitude of relevant features, as is also true for other sensory systems. Mounting evidence suggests that the computational

principles underlying contrast coding in electrosensory neural networks are conserved elements of spatiotemporal processing that show strong parallels with the vertebrate visual system.

Box 1 **Characteristics of first- and second-order sensory stimuli**. Characteristics of first- and second-order sensory stimuli Electrosensory In the absence of stimuli, the electrosensory system of a weakly electric fish creates a baseline electric field (zeroth-order contrast) generated by a high-frequency electric organ discharge (EOD; see the figure, part a). This signal acts as a stable carrier wave on which environmental signals produce contrast modulations. When two static fish are present, their EODs superimpose and a 'beat pattern' in the electric field arises. This pattern is an example of a first-order contrast or amplitude modulation (AM) of the carrier. When the two fish move relative to each other, the amplitude of their combined EOD changes, causing a second-order modulation of beat pattern that is referred to as the stimulus envelope (Env). Visual For comparison's sake, zeroth-order visual contrast can be defined as a spatially homogeneous luminance that saturates the receptive field of ganglion cells (see the figure, part b). First-order visual contrast typically introduces edges and borders within an inhomogeneous pattern of illumination intensity. When extracted, such features can be combined to form representations of contours and outlines. In vision research, this first-order pattern is often referred to as the carrier. Natural images involve further modulations of this pattern, resulting in a second-order contrast (also known as a contrast modulation or a luminance envelope). The bottom panel of part b shows an example of a static, low-frequency spatial contrast modulation (shadows of tall grass and people) of the first-order contrast pattern (fence). A spatiotemporal envelope results if these second-order contrast modulations change over time.

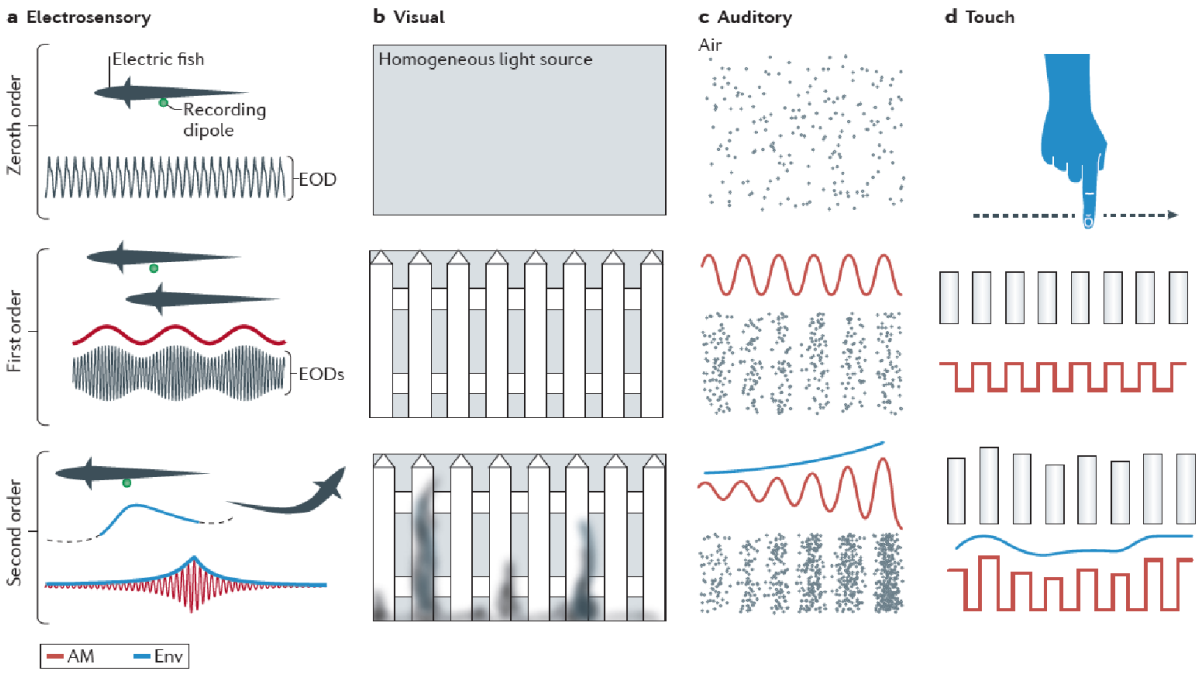

Auditory In the absence of all stimuli and in a controlled setting, ambient background air forms a noisy, stationary and spatially homogenous pressure condition (see the figure, part c). When a pure tone is emitted from a source, first-order contrast is generated as a sinusoidal modulation of the spatial distribution of air molecules. Again, this first-order modulation is referred to as a carrier. Superposing constant amplitude pure tones generates a more complex AM. Over time, both the amplitude and frequency that are emitted from the source can change to generate second-order contrast (a stimulus envelope). Mechanosensory First- and second-order contrast are also important to haptic senses. Imagine running a finger over a surface, making contact with a surface and breaking contact at regular intervals (see the figure, part d; approximation shown as a square wave). The pressure on the fingertip sensors is a first-order spatiotemporal contrast pattern. Second-order modulations may arise if the surface is uneven, with a lower-frequency envelope that results in variable pressure; alternatively, more or less finger pressure may be applied over time. For all types of stimuli, alternative assignments of zeroth-, first- and second-order stimuli have been used, depending on the history of a field.

Body

A common problem faced by many organisms is the need to identify and estimate the location and trajectory of moving objects, conspecifics and other animals. This is achieved by interpreting patterns of sensory contrast that is, relative differences in the level of a physical signal (such as light, pressure or an electric field) across space and time. These patterns are projected from the three-dimensional environment in which they arise onto a lower-dimensional array of sensory receptors and may overlap to create emergent or higher-order contrast patterns (BOX 1). For instance, the three-dimensional characteristics of a visual object such as its size, shape, orientation and distance from the observer create spatial contrast patterns on the retina, which is a two-dimensional sheet made of photoreceptors. Unequivocally identifying which of the many possible combinations of stimulus features cause a specific pattern of contrast is a challenging problem that does not have a unique solution, especially because one or more of these features can change over time [22]. As a result, nervous systems have evolved strategies to increase their capacity to generate useful sparse representations of objects from ambiguous sensory contrast patterns.

The problem of translating sensory contrast into perception is common to all the senses

(BOX 1). In this Review we focus on the principles of contrast coding in gymnotiform weakly electric fish. The electrosense involves a two-dimensional sensing surface and combines features of the more familiar senses of vision, hearing and touch. Although the early stages of processing in electrosensory and visual systems have substantially different biophysics, the emerging picture of sensory contrast coding suggests that the neural algorithms and computations involved in multiscale spatiotemporal processing are remarkably conserved between these senses. Here, we make comparisons between the electrosense and the vertebrate visual system at the biophysical, algorithmic and computational levels of analysis. Based on Marr's tri-level hypothesis [226], the framework that we adopt defines the computational level as the abstract operations that are performed to solve specific coding problems. This perspective embodies the idea that common selective pressures on organismal behaviour (such as the requirement for motion processing) can lead to the development of equivalent algorithms and computations in distinct sensory modalities, although the biophysical implementations of these strategies may be substantially different.

Categories of electrosensory contrast. The basis of the electrosense in gymnotiform fish is a constant high-frequency electric organ discharge (EOD) in the range of approximately 700 to 1,000 Hz, which stimulates electroreceptors distributed over the fish's body surface. This self-generated electric field typically has a steady amplitude, acting as a carrier wave that is modulated by social interactions, locomotion, prey capture and the fish's own body movements [19]. Importantly, the high-frequency EOD carrier (which provides zeroth-order contrast; see BOX 1) exceeds the temporal coding capacity of the electrosensory system's primary and secondary contrast coding neurons (electroreceptor afferents (EAs) and pyramidal ON and OFF cells in the electrosensory lobe) owing to the filtering properties of the intervening slow chemical synapses. Thus, only the modulations of the carrier are relayed past the first stage of electrosensory processing. This makes it possible to compare contrast coding in the electrosensory system with that of non-carrier-based senses such as vision, in which first-order contrast is instead defined relative to background illumination levels (BOX 1).

Both motion and social interactions modulate the EOD, producing two classes of temporal signal modulations: first-order amplitude modulations (AMs) of the electric field carrier and second-order modulations of the AMs, which are caused by a combination of social signals and motion. The first-order contrast modulations are historically referred to as AMs and the second-order modulations as envelopes (BOX 1).

First-order contrast: amplitude modulations. Objects with an electrical conductivity that is greater (such as other organisms and aquatic foliage) or less (such as rocks and wood) than that of the ambient water cause spatially localized increases or decreases, respectively, in the amplitude of the electric field relative to the background intensity caused by the ongoing EOD [55, 227]. This results in regions of positive and negative local to background spatial contrast (FIG. 1a). In analogy with vision, these first-order spatial contrast patterns are often described as 'bright' and 'dark' electric images. In natural settings, contrast can be detected over time as well as space. For example, as fish swim, they move relative to objects in the environment, which results in local, low-frequency (<23 Hz) AMs of the EOD carrier wave [17,117] (FIG. 1b). Similarly, when two fish are in close proximity, their EODs summate to produce a sinusoidal AM of the EOD carrier with a beat frequency that is equal to the frequency difference between their respective EODs (BOX 1; FIG. 1c). In the latter case, AM frequencies of >20 Hz are most commonly observed [228]. This 'social' AM is another type of first-order modulation of the EOD; however, unlike the AMs that are involved in object localization, social AMs stimulate electroreceptors over the entire body surface. In social situations, fish also communicate by transiently shifting their EOD frequency, resulting in fast AMs of the carrier (FIG. 1d).

Second-order contrast: envelopes. During social interactions, electric fish move relative to each other, and the amplitude of the first-order social AM is itself modulated. This envelope is presumed to be the dominant signal guiding navigation as well as the stereotyped motor patterns associated with aggressive interactions and courtship behaviours. Second-order visual features (known as contrast modulations), such as coarse texture, are typically spatially diffuse

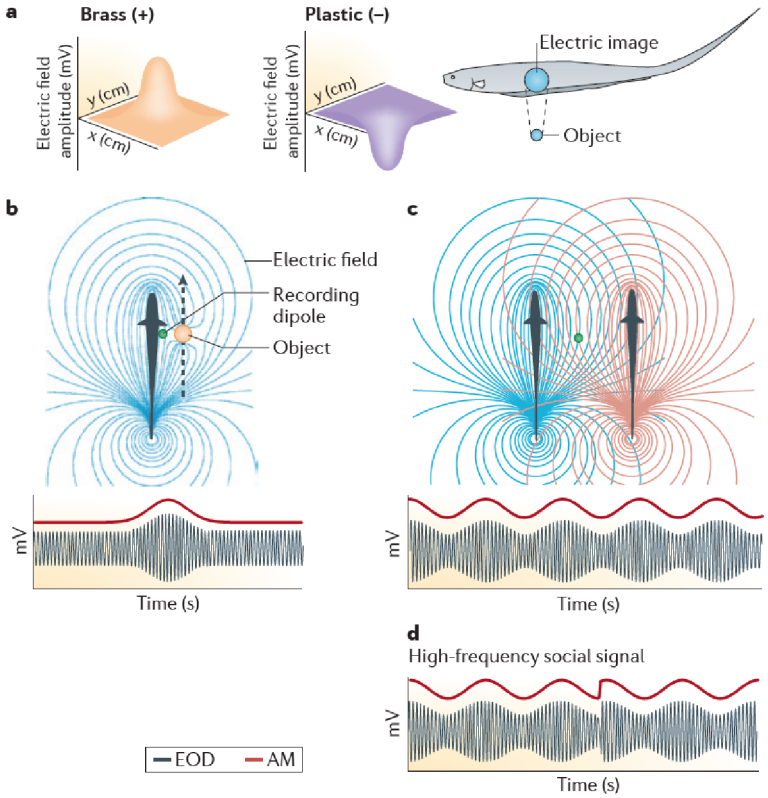

Figure 1 **Natural electrosensory signals**. a) The formation of static electric images. Conductive objects, such as those made of brass, cause a localized increase in the amplitude of the electric field relative to its background levels (driven by the electric organ discharge (EOD)). By contrast, non-conductive objects, such as plastic, cause a localized decrease in the amplitude of the electric field. Thus, these two object classes create either positive or negative local to background, or spatial, contrast. There is no focusing mechanism and so the electric image spreads across the skin in a roughly Gaussian manner. b) The formation of a dynamic electric image. The green dot indicates the location of a small recording dipole, which measures the amplitude of the electric potential experienced across the skin. As the fish swims by an object (a conductive sphere in this illustration), the EOD is locally increased above its baseline amplitude. The movement of the sphere through the electric field thus causes a low-frequency amplitude modulation (AM) that, in turn, excites the primary electrosensory neurons. c) The effects of EOD summation when two fish are in close proximity. The summation of the EODs of the two fish results in a global sinusoidal AM (beat), the frequency of which equals the difference of the EOD frequencies. d) A high-frequency communication signal that results from a purposeful frequency modulation of the EOD. This creates another type of AM, which occurs on timescales shorter than the typical beat period shown in part c. The top panels of parts b and c are reproduced with permission from [19], Elsevier.

(that is, they have a large spatial extent and low spatial frequency) [229] compared with first-order contrast, and this is also the case for electrosensory envelopes. In general, these combined first- and second-order features span many spatial and temporal scales in diverse sensory modalities (BOX 1). Their analysis in the context of motion provides insights into multi-scale neural coding.

Contrast coding by electroreceptor afferents. The first stage of electrosensory processing occurs in the cutaneous EAs (also known in the field as P units), which detect stimulus-induced contrast in the EOD amplitude. EA discharge is phase locked to the high-frequency EOD but skips a variable number of EOD cycles, resulting in a baseline discharge of approximately 100 to 400 spikes per second [52].

A defining characteristic of the response of EAs assessed in vivo is spike frequency adaptation, a phenomenon in which negative feedback causes the EA firing rate to decay to a lower steady-state, in the presence of a sustained step increase in EOD amplitude. Likewise, presentation of a negative step stimulus decreases the EA firing rate, which eventually results in a slow rise to a higher steady-state level. These processes also operate in EAs during natural dynamic stimulation and have been studied over both short (<0.025 s) [59,60,64,170] and long (0.025 s to >1 s) timescales [59, 104, 166]. Although the biophysical basis of EA adaptation is not currently known [104], we have gained a firm understanding of the algorithmic details of the adaptation and the resulting neural computations that it enables.

Natural stimuli typically fall into one of two categories according to the timescale over which they generate AMs in the EOD: fast (high-frequency communication signals, >23 Hz) [60, 133] or slow (low-frequency signals that typically occur during navigation and prey capture, < 20 Hz) [17,117]. It is thought that each of these categories evokes a specific algorithmic form of adaptation in EAs that enables the fish to extract behaviourally relevant features from temporal sensory contrast patterns. Both forms of adaptation are likely to be present in all EAs, although their relative proportions may vary [60, 64, 104, 166].

Segregating high- and low-frequency signal contrast. It is thought that some EAs use exponential spike rate adaptation to enable them to selectively process the high-frequency contrasts associated with communication signals [60]. Exponential spike rate adaptation exerts a negative effect on a neuron's firing rate by hyperpolarizing the cell in response to stimulus input.

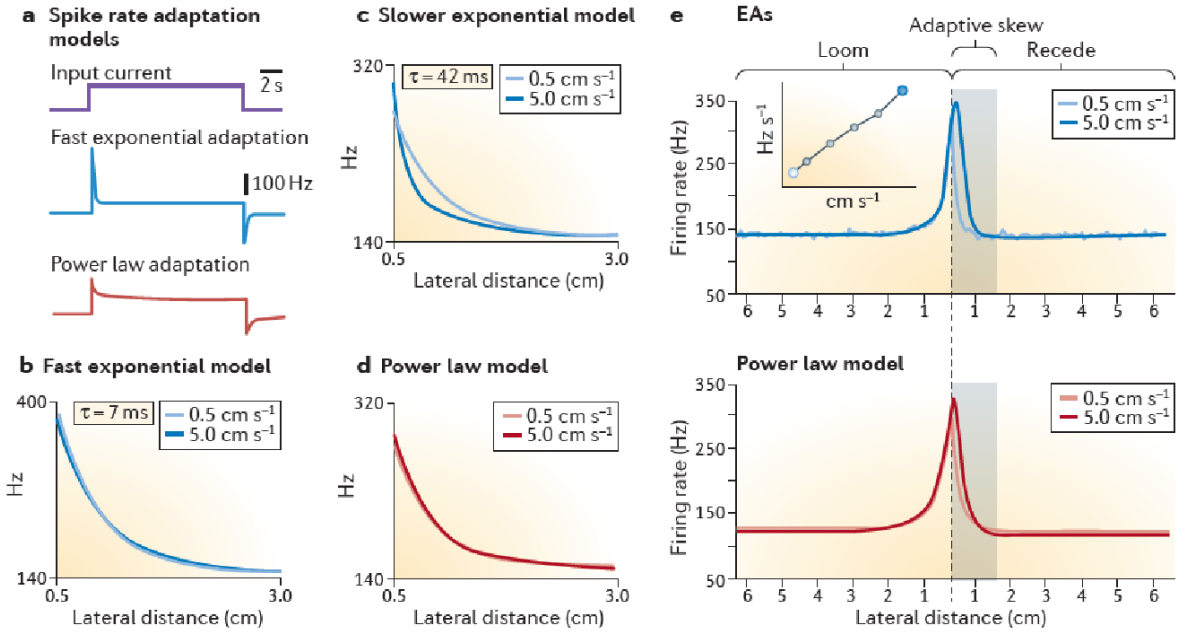

Figure 2 **Role of adaptation in the electroreceptor afferent response to object motion.** Schematic showing the role of adaptation in the electroreceptor afferent (EA) response to looming and receding stimuli. a) The firing rate responses predicted by two simple spike rate adaptation models. A model of fast exponential adaptation reveals a peaked response to stimulus onset, followed by a rapid decay to an equilibrated state. A model of power law adaptation [104] instead shows a much more gradual relaxation to a steady state, demonstrating longer timescales of adaptation. In both cases, removal of the stimulus causes a sharp drop in the firing rate and a rebound to the spontaneous firing rate. b) A fast exponential model (with an adaptive time constant $\tau = 7$ ms determined from in vivo responses to step changes of electric organ discharge (EOD) amplitude [60] does not differentially filter the response of the EA to an object drawing closer to the neurons' receptive field at different speeds (0.5 cm/s versus 5 cm/s) because the fast timescales associated with the adaptive process are not evoked by low-frequency motion stimuli. c) If we choose a longer timescale, such as $\tau = 42$ ms (similar to that used for a closely related model of EA adaptation and social contrast [60]), adaptation is again seen; however, because of the exponential adaptation model's temporal selectivity, there is now a differential response to various speeds of looming object approach. d) The power law adaptation model is, in agreement with in vivo data [59], not bound to any particular adaptive time scale and effectively reproduces the observed speed invariant responses. e) Data recorded in vivo from EAs in response to looming motion confirm the speed invariance of their firing rate responses, as predicted by the power law adaptation model. Information on the looming object's speed can be recovered by measuring the temporal derivative of the firing rate (inset panel). Both the in vivo data and the power law model show that motion reversal introduces a skew in the firing rate response (denoted by grey shading) as the object withdraws back to the initial position. As a result, the EAs no longer signal the correct sign of spatial contrast for a portion of object withdrawal.

A typical biophysical source of such hyperpolarization is the efflux of K^+ ions through $Ca2^+$-induced K^+ channel opening. However, at the algorithmic level, the result is the same no matter what the source of hyperpolarization: the magnitude of the inhibitory current is increased in an incremental manner by each action potential and decays exponentially in time after each

spike, according to an associated fixed timescale (with a time constant, τ). In response to a constant stimulus, the decay in firing rate can be well-described by an exponential time course (FIG. 2a). EA neurons have been shown to act as high-pass filters; computational analyses suggest that this is due to exponential spike rate adaptation and results in a cutoff frequency of 23 Hz below which the response to the signal is attenuated [60, 64]. Indeed, it has been shown that the low-frequency AMs that occur during navigation (<20 Hz) [17] and prey capture (1-23 Hz) [117] result in an asynchronous response from the EA neuron population because of the low gain of the firing rate responses to these signals [133, 139, 166]. Conversely, the high-frequency social AMs that lie above the cutoff for the fast exponential adaptive processes induce a transient synchronization of the EA population that results in the amplified transmission of a communication signal [133].

The computational level goal of this proposed mechanism is clear: the natural stimulus frequency range is partitioned into two distinct bandwidths that are associated with different behavioural contexts, controlling a switch in the population response (synchronous versus asynchronous) that could be easily distinguished by downstream neurons [20, 21, 133].

Coding low-frequency signal contrast. Although the exponential adaptation model described above can successfully explain the EA response to social AMs [60], it fails to capture an important in vivo observation: the adaptation in response to sustained steps up or down in EOD amplitude (positive or negative contrast) is just not fast, but is also drawn out over much longer timescales [59]. These longer timescales are more similar to those occurring with low-frequency AM and envelope signals associated with both object and conspecific motion (BOX 1; FIG. 1).

Does exponential adaptation also contribute to the processing of such low-frequency signals? If we select a time constant of $\tau = 42$ ms (as was used for a closely related adaptation model [60]), we can see that an exponential model that correctly mimics the EA response to fast communication signals (FIG. 1d) incorrectly generates different responses to objects moving at speeds of 0.5 and 5 cm/s (FIG. 2c). This is expected as exponential adaptation is known to filter inputs according to their rate of change, provided the frequencies that are present in the

stimulus have evoked such adaptation. Indeed, as shown in FIG. 2b, looming motion stimuli would not trigger fast exponential adaptation processes with very small τ values (however, these shorter time constants are even further away from the long timescales observed in vivo). This fact, in addition to the close agreement between the upper bound for natural motion frequencies (approximately 23 Hz) and the frequency cutoff of fast exponential adaptation, suggests that the partitioning of social information into a distinct high-frequency band by fast exponential adaptation acts to reduce its impact on low-frequency motion processing. However, the long timescales of adaptation observed in vivo are most certainly evoked by moving stimuli and will affect the EA neural response.

In response to a constant step stimulus, the long timescales of adaptation observed in all EAs are well-characterized by a power law relationship [104]. Like exponential adaptation, power law adaptation in EAs exerts a negative effect on firing rate; however, the magnitude of this negative effect on the hyperpolarizing current is proportional to the reciprocal of the time elapsed since the last spike (that is, there is an exponent of -1). Thus, unlike exponential adaptation processes, power law adaptation is not bound to any specific timescale [64]; instead, it implements a flexible coding algorithm, the timescales of which are influenced by those present in the stimulus: that is, if an object is moving faster, the algorithm will use shorter timescales. The importance of this multi-timescale adaptation in processing the slow AMs (<20 Hz) that are characteristic of motion signals has recently been demonstrated [104]: EAs were shown to directly map stimulus intensity into their firing rate, independent of its rate of change (FIG. 2d). This has important implications for processing looming motion: the change in the position of an object as it moves towards the animal can be determined with high fidelity from the firing rate, regardless of whether its motion occurs over long (0.5 cm/s or short (5 cm/s) timescales. Although speed-dependent effects are removed from the firing rate, a linear encoding of speed can be obtained by computing the temporal derivative of the EA response (FIG. 2e). In addition to speed invariance, the firing rates of the EAs do not change in response to positive and negative acceleration [104] provided the acceleration does not cause motion reversal. In this case, if a looming stimulus suddenly reverses direction and moves away from the fish's

body, then the speed invariance is temporarily lost and a significant skew is introduced into the EA firing rate [140] (FIG. 2e). At first, this seems counter-productive: adaptation exists to preserve the relationship between distance and firing rate for a looming stimulus, but it also introduces ambiguity into this relationship. However, the inherent directionality introduced by spike rate adaptation is an important innovation for spatial processing, as discussed below.

Comparison with retinal adaptation. Adaptation is a nearly ubiquitous feature of neural processing, and the retina is no exception. Indeed, adaptation over both short and long timescales occurs at low levels of visual processing [67, 230]. Although there seems to be no unanimous description of the functional form of this retinal adaptation, multi-exponential and power law models have been proposed to capture the effects of adaptation on long timescales [67]. In support of the proposal that power law adaptation takes place in the retina, changes in stimulus statistics, such as changes in the variance of stimulus intensity fluctuations, have been shown to elicit adaptation over several different timescales in vivo [67]. This suggests potentially deeper algorithmic parallels between low-level electrosensory and visual processing.

Studies in both insects and mammals [230] show that adaptation is key to visual processing, but how it relates to natural motion is less clear. If a power law is the best algorithmic description of retinal adaptation for the low frequencies associated with natural motion, it will be important to determine the exponent. Finally, we need to determine the associated computational level benefits for spatiotemporal processing in the visual system. It is worth noting that the observed invariance to looming speed in the electrosensory system requires that power law adaptation in this system uses an exponent of -1; however, different adaptive power law exponents arise in many diverse systems and probably provide distinct coding benefits [66,169]. Intriguingly, an equivalent speed invariant computation, known as lag normalization, acts in the ON and OFF retinal ganglion cell circuitry [93]. It is unknown whether lag normalization uses power law-based algorithms to achieve stimulus representations that are not influenced by speed, but the similarity between the systems at the computational level suggests a deeper connection. We expect that studies of the electrosensory system will provide fresh insights into

the role of adaptation in early visual processing.

Contrast coding by ON and OFF cells. As nearly linear encoders, EAs faithfully relay changes in the transdermal potential via topographic projections to three maps within the initial medullary electrosensory processing region: the electrosensory lobe (ELL; see FIG. 3a). The unique processing abilities of these three distinct maps have been previously reviewed [19–21]. Importantly, each ELL map contains two classes of nonlinear output pyramidal neurons: the ON and OFF cells (also known as E and I cells in the electrosensory literature). ON and OFF cells exhibit complex dynamics, including rapid stimulus-driven transitions (bifurcations) between tonic and bursting spiking states [20]. These tonic to burst spiking transitions (and vice versa) are crucial for the encoding of natural motion patterns, as discussed below.

Anatomical and in vitro physiological studies have shown that ON cells receive direct excitatory, glutamatergic input from the EAs onto AMPA and NMDA receptor-rich synapses [13], and in vivo recordings have shown that ON cells strongly discharge in response to increased EOD amplitude at the centre of their receptive field (RF) [231]. The EAs also project indirectly to OFF cells via GABAergic interneurons, implementing a signal inversion and generating a mechanism to encode decreases in EOD amplitude. The ON and OFF cells are found in pairs, arranged in topographic columns with overlapping RFs [29] (FIG. 3b). Under static conditions, ON and OFF cells compute local spatial contrast defined relative to the background: that is, they compare the intensity of the electric field at their RF centres to the mean intensity over a larger extent of the sensory surface (background). ON cells are excited when the intensity at their RF centre is greater than the background, and the reverse is true for OFF cells. The hard-wired circuitry, neurotransmitters and synaptic biophysics of these cells that have been identified are consistent with the idea that ON cells encode positive contrast and OFF cells encode negative contrast under simple stimulus conditions, as first suggested by early in vivo studies [231]. These findings also suggest that electrosensory ON and OFF cells form the basis of a 'labelled line' code that signals spatial distributions of positive and negative local to background contrast.

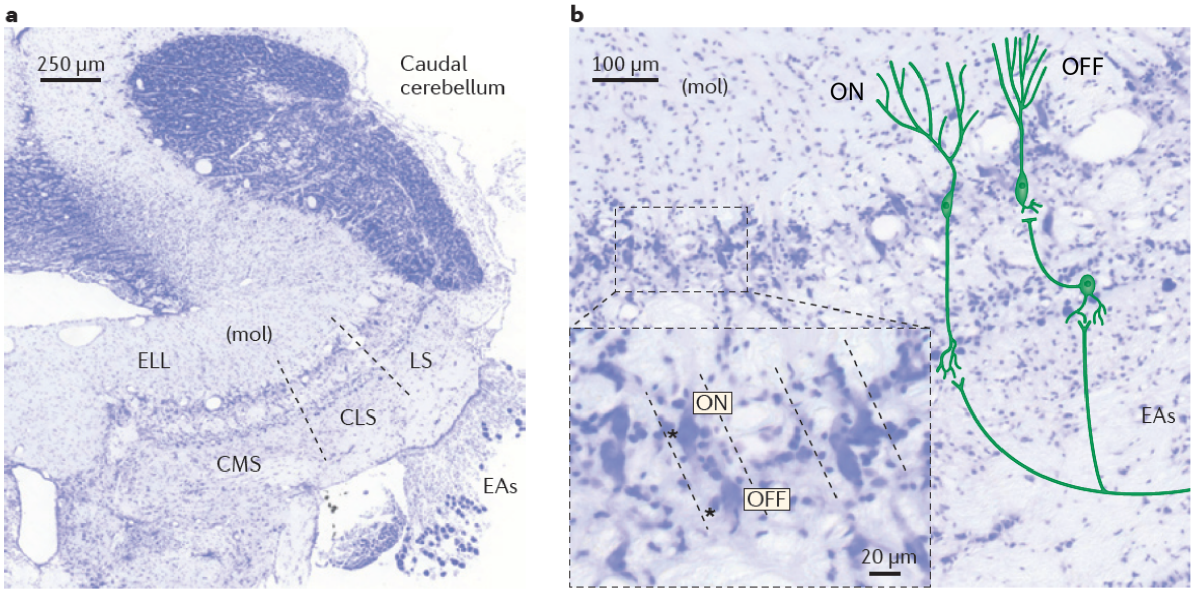

Figure 3 **Electrosensory lobe circuitry**. a) A coronal section of the electrosensory lobe (ELL) and the overlying caudal cerebellum Nissl stained to show cell bodies of the ON and OFF ELL pyramidal neurons and local interneurons. The ELL contains three topographic maps: the central-medial segment (CMS) and central-lateral segment (CLS) are primarily concerned with processing electrolocation information, whereas the lateral segment (LS) specializes in processing communication signals. Electroreceptor afferent (EAs) ganglion cell bodies are seen near the entry of the EAs into the ELL. The ELL molecular layer (mol) receives feedback input from the caudal cerebellum that is not discussed in this Review (see [19]). b) Each map, including the CLS, shown here at higher magnification, contains two classes of nonlinear output pyramidal neurons [90]: the ON and OFF cells. ON cells receive direct glutamatergic input from EAs, whereas OFF cells receive disynaptic input via GABAergic interneurons. The insert shows the ON cell (with basal dendrite) adjacent to the OFF cell (no basal dendrite), both marked by asterisks. The ON and OFF cells are found in pairs and organized into topographic columns (marked with dashed lines). The large apical dendrites of the ON and OFF cells extend into the molecular layer (mol).

There is a computational parallel between the secondary stages of sensory processing in the electrosensory system and those in the retina: the hardwired circuitry and biophysics that interconnect photoreceptors, bipolar and horizontal cells lead to the classic ON and OFF types of bipolar and retinal ganglion cells, which respond to positive and negative contrast within their RF centres [232, 233]. There is an additional computational parallel: in both the ELL and retina, ON and OFF cells are inhibited by stimulation directly outside of their RF centres; for example, an ON cell is inhibited by increases in EOD (or light) intensity that occur just outside its RF centre. These opposing RF surrounds are an essential mechanism for eliminating stimulus 'blur' and thus enhancing the detection of high-frequency spatial contrast [91], allowing higher brain centres to assemble sharply defined object edges and contours. Although

the underlying biophysics is completely different, there seems to be a remarkable equivalence between low-level computations in electrosensory and visual processing.

Identifying and tracking conspecifics. Envelopes of the EOD can arise as a result of the static interference pattern of the EODs of three or more fish [78] or the relative movement of two or more fish [228, 234, 235]. Social interactions among groups of fish are typically associated with movement; thus, both forms of envelope can occur simultaneously, resulting in even greater complexity. How do the ON and OFF cells in the ELL extract distinct representations of AMs and envelopes despite these challenges?

Tracking conspecific motion with envelopes. When two or more fish are moving with respect to one another, the high-frequency AMs produced by their summat-ing EODs experience additional changes in amplitude, increasing as the fish move closer together and decreasing as they move further apart (FIG. 4a). This constitutes a low-frequency envelope of the AM (FIG. 4a,b) and is essential for encoding the relative motion of conspecifics. Measurements of the envelope signal have shown that natural motion (< 10 cm s^{-1}) induces signal correlations on the order of a second [235]; thus, on short timescales, a swimming conspecific causes fluctuations in the electric field that are similar to low-pass filtered white noise. Long-term recordings of the transdermal electrical potential of freely swimming fish [17] revealed that the envelope evolves on many timescales, and that its power spectrum is well fit by a power law model that spans short and long timescales.

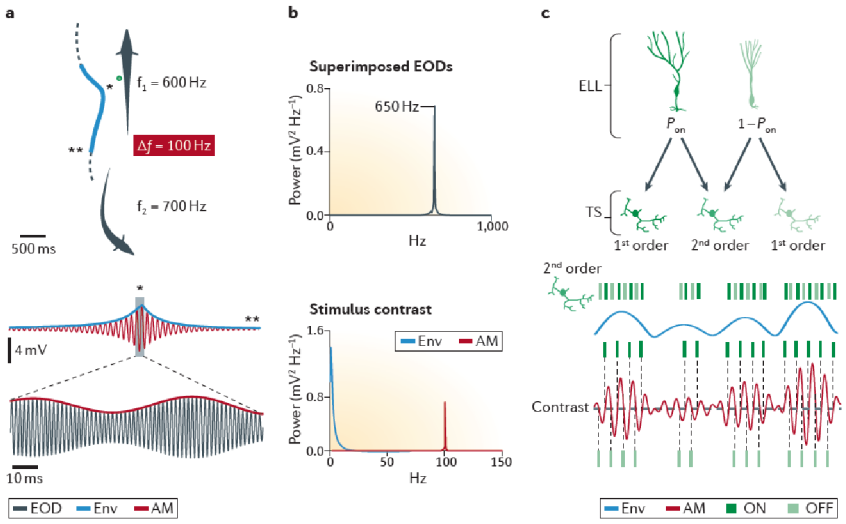

Figure 4 **Encoding and decoding conspecific motion using envelopes**. a) The image shows an example of an electric fish swimming past a stationary conspecific. Their example electric organ discharge (EOD) frequencies are $f_1 = 600$ Hz and $f_2 = 700$ Hz. A recording electrode (green dot) is placed next to the skin of fish # 1. In the absence of movement, the recording electrode would measure a beat amplitude modulation (AM), in which the average EOD carrier (the frequency of which is given by $\frac{f_1+f_2}{2}$ acquires a sinusoidal AM (red line) the frequency of which is the difference between the two EOD frequencies (100 Hz in this example). During relative motion the amplitude of the AM will change over time as the distance between the fish changes. This envelope (Env) is barely noticeable on the short timescale of the beat AM (bottom), but becomes more apparent on a longer timescale of movement (middle). b) The power spectral density of the combined EODs (top) and stimulus contrast (bottom) for the example shown in part a, illustrating their distinct frequency contents. c) Electroreceptor afferents project to electrosensory lobe (ELL) pyramidal neurons, which in turn project to the torus semicircularis (TS) in the midbrain. ELL outputs contain information about AMs, as well as envelope information from movement and/or social signals. Cells in TS can preserve the sign of the input, maintaining distinct ON and OFF channels (as shown for the right and left TS neurons), or combine the ON and OFF responses to encode envelopes (as show for the central TS neuron). Computational modelling predicts that the latter type of TS cells sparsely code for envelope signals by combining the spiking outputs of ELL ON and OFF cells in equal proportion; this also causes them to respond less to AMs because the streams arising from ON and OFF cells effectively cancel out. Note how the combined ON and OFF spikes (green bars) track the stimulus envelope. P_{ON}, the fraction of activated ON cells in ELL; $1 - P_{ON}$, the fraction of activated OFF cells in ELL.

Recent studies have provided direct behavioural evidence that electric fish can detect envelope signals [234, 236, 237]. Eigenmannia virescens (a gymnotiform wave-type electric fish) exhibits a form of avoidance response that is measurable in terms of the envelope. In this social envelope response (SER), the fish increases its baseline EOD frequency to shift the power in the envelope to higher frequencies, thus reducing the background noise that would otherwise impede the detection of low-frequency electrolocation targets [238]. A recent study [239] went

a step further by measuring the gain and phase of the SER. The gain versus frequency characteristic followed a power law over three orders of magnitude. This study demonstrated that the neural coding strategies used by weakly electric fish enable them to specifically perceive the detailed time course of the movement envelopes and use them to extract the identity of conspecifics and to direct their relative motion.

Envelope encoding and decoding mechanisms. Initial findings from single-unit recordings of EAs suggested that they did not respond to the envelope signal [78]. Subsequently, single EA responses to envelope signals were seen but only when there was strong sensory contrast [236, 240], limiting their use as a coding mechanism. Recently, a far more general envelope coding result was revealed: this study showed that the synchronized activity of EAs faithfully encodes envelope signals even when individual EAs fail to do so [241]. This mechanism, described below, operates in the linear range of EA coding and can be used to encode the full range of AM and envelope intensities occurring in natural settings. As outlined above, social beat frequency AMs (>20 Hz) induce synchronized discharge of EAs due to the properties of fast exponential adaptation and large signal contrast (depth of modulation). The low-frequency envelope, introduced by the relative motion of the two conspecifics, can increase and decrease the depth of modulation, the resulting EA firing rate and the extent of signal adaptation. Therefore, the response to the envelope is a modulation of the degree of EA synchrony.

A striking distinction emerges from this work: low-frequency AMs associated with electrolocation signals are encoded by modulations in EA firing rate, whereas low-frequency envelopes are encoded primarily by modulations of EA discharge synchrony. This result is a superb example of stimulus encoding through spike train synchrony. It has been shown that the same general principle applies to envelope coding mediated by primate vestibular afferents [241]. Given the immense differences between the origins of teleost EAs and primate vestibular afferents, we assume that the biophysical (and possibly algorithmic) mechanisms of envelope coding are different in these systems even though they implement the same final computation, a striking example of equivalent functionality at a computational level.

The ON and OFF cells in the ELL also encode envelope signals [78, 242]. The basic algorithm used by these cells is equivalent to that used in AM radio transmission: half-wave rectification followed by low-pass filtering [238]. Input from hundreds of EAs converge on a unique GABAergic interneuron, the ovoid cell, which is found in the ELL. Each EA has a discharge rate that is greater than 100 spikes per second [52], but ovoid cell discharge is fewer than 100 spikes per second [132]. Thus, each individual EA evoked excitatory postsynaptic potential in an ovoid cell must be weak, making them more likely to respond to synchronized EA input [78, 243]. Ovoid cells therefore extract the envelope by responding preferentially to modulations of EA synchrony. The ovoid cell spike threshold then acts as a half-wave rectifier to produce an output spike train that is highly correlated with the envelope [78, 244]. Finally, ovoid cell-mediated inhibition of the ON and (indirectly) the OFF cells occurs via slow G protein-mediated GABAB receptors that implement low-pass filtering. This eliminates the ovoid cell's response to the high-frequency AMs and imposes its envelope response onto the ON and OFF cells [238].

ON and OFF cells themselves are non-selective for contrast; that is, they encode both AMs and envelope modulations. The final step for selective envelope detection occurs in the ON and OFF cell midbrain target: the torus semicircularis (TS). A subset of TS cells responds to the envelope by summing their ON and OFF cell input [242]. The responses of ON and OFF cells to low-frequency AMs are out of phase, owing to the algorithmic sign inversion of the EA input that occurs in OFF cells. When the fish are stationary, the summed response of ON and OFF cells is an approximately constant firing rate: ON cells respond during the upstroke and top of the sinusoidal AM, and OFF cells respond to the down stroke and the bottom of the AM. When the fish are moving, the amplitude of the AMs themselves is now modulated, forming the motion envelope. When this envelope is strong (when the fish are in close proximity; see FIG. 4a) both ON and OFF cells respond strongly. When the envelope magnitude is low, the ON and OFF cells are nearly silent. Therefore, the summed response of the ON and OFF cells is far greater at the envelope peak than at its trough. There are specific cells in the TS that combine the ON and OFF signals, and others that respond to either ON or OFF channels

exclusively (FIG. 4c). In this way, a nearly complete separation of encoding is obtained at the level of the midbrain: one set of TS cells responds sparsely to the fish moving with respect to its environment (AMs), whereas another set responds to the fish moving with respect to other fish (envelopes). As discussed below, this is one example of the flexible coding that is made possible by combining the output of ON and OFF cells.

Envelopes in the visual system. Envelopes are also common in the visual system, where they are typically referred to as contrast modulations or second-order stimuli. Taking the classic visual grating as an example of a first-order modulation, second-order contrast (envelopes) occurs when the contrast of the visual grating is itself modulated over a greater spatial extent [245, 246]. These contrast modulations may be caused by an inherent spatial feature of the object, such as its texture, or may be induced by movement of a first-order contrast pattern. Behavioural studies have shown that zebrafish can detect envelope motion stimuli [245], and it has been speculated that envelope extraction in this species occurs at the level of the retina. Envelopes are also extracted by the mammalian visual system, including that of humans [247], although this seems to occur at a much higher level in the secondary visual cortex (V2) [248]. It has been speculated that V2 also extracts envelope signals using a mechanism that is formally equivalent to half-wave rectification followed by low-pass filtering, although alternative algorithms have been suggested [248, 249]. Given the presence of neurons in the primary visual cortex (V1) that are responsive to ON and OFF stimuli, it would be inter-esting to investigate whether envelopes in V2 are also obtained by summation of the ON and OFF channels within V1.

Encoding object motion reversal. Work on early visual system physiology was so compelling that it has influenced the interpretation of results for decades: the idea that the electrosense and vision both package positive and negative spatial contrast information into distinct ON and OFF labelled lines has been firmly entrenched in the published literature. However, it is now apparent that in the case of natural dynamic stimuli the roles of ON and OFF cells change

dramatically, and temporal changes in contrast dominate over the sign of spatial contrast.

Comparing looming and receding motion (FIG. 5a) for both positive (brass sphere) and negative (plastic sphere) local to background contrast reveals ambiguity in the meaning of changes in the electrical contrast over time. At the shared RF centre of an ON and OFF cell pair, a looming brass sphere and a receding plastic sphere both cause a relative increase in the electrical contrast; however, brass stimuli generate local to background positive spatial contrast patterns, whereas the patterns generated by plastic stimuli are negative (FIG. 5b). Likewise, the looming plastic and receding brass spheres both cause temporal decreases in local contrast, whereas the spatial contrasts are always negative for plastic spheres and positive for brass spheres. Therefore, under looming and receding conditions, labelled lines should be broken: either the cells respond conventionally to the sign of the local to background contrast and encode both positive and negative changes in local contrast over time, or they identify temporal contrast changes with the conventional sign but under local to background contrast conditions that directly violate the classic definitions of ON and OFF cells.

Many features, such as object size, distance and orientation, affect spatial patterns of contrast and can generate ambiguous sensory images [22, 250]. This problem becomes even more acute when these variables change over time, as motion direction also needs to be encoded. Dynamic stimuli are a particular challenge as slow spike rate adaptation is a characteristic of many sensory neurons and will interact with the time course of a stimulus. Although the induced electrical contrast is symmetrical for looming and receding stimuli, it has been shown that motion reversal evokes a skewed EA firing rate [140] (FIGS 2e, 5b), adding another facet to the problem of ambiguity in intensity rate coding. Although these skewed responses might be assumed to be a problem for the system, the resulting directional selectivity establishes context and is a computational innovation that is also present for looming stimuli in locust vision [61], despite different biophysical and algorithmic implementations of spike rate adaptation. This skew is a general characteristic of all adaptive processes, and is also present in retinal ganglion cells [230].

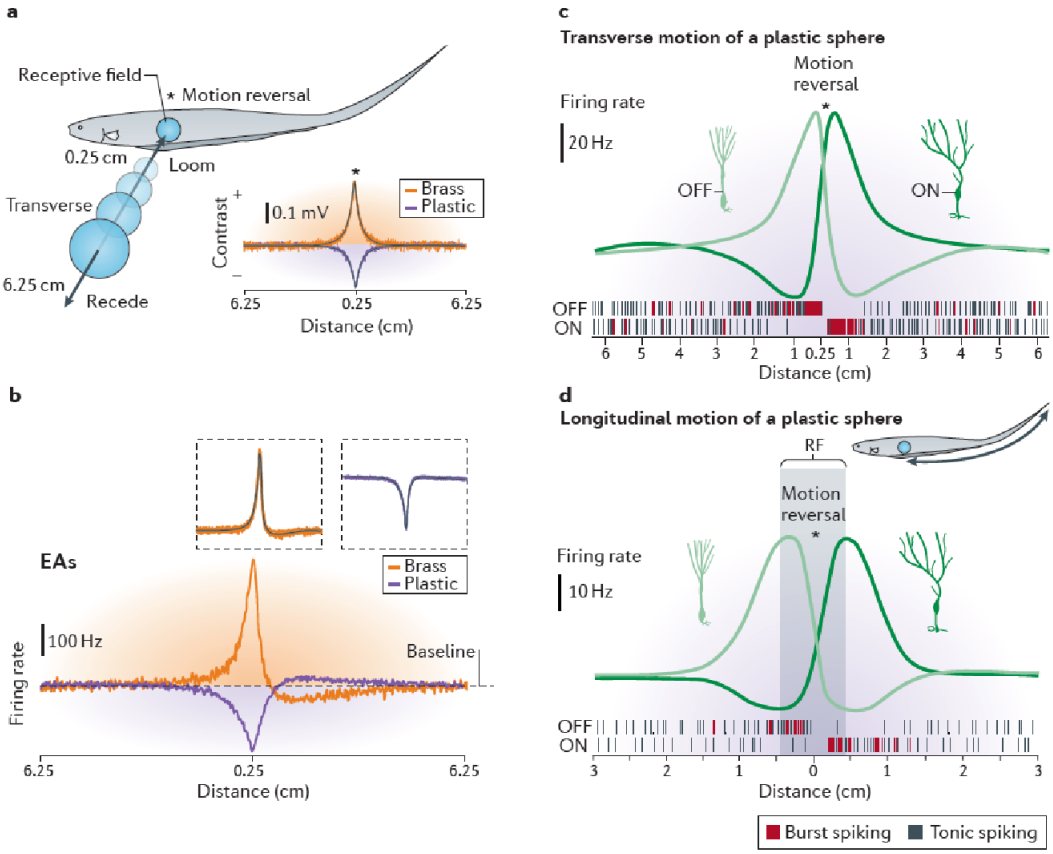

Figure 5 **Motion reversal and distributed contrast coding**. a) Looming and receding stimuli that follow trajectories perpendicular to the electrosensory surface (transverse) are shown. In the model shown [104, 140], motion along the transverse axis was set at 2 cm·s^{-1}, with a rapid period of acceleration (150 cm·s^{-2}). The spherical stimuli started 6.25 cm from the fish's body surface and reversed motion at 0.25 cm, before returning to the original position. Brass and plastic spheres were used to create positive and negative contrast stimuli, respectively[140]. Experimental data are shown in the graph in purple and orange and the predictions of a model5 are shown in grey. The plastic stimulus generates an electrical contrast that is half the amplitude of the brass stimulus, but otherwise the contrast intensities are reflections of each other and are symmetrical functions of distance regardless of the time course of motion. b) This symmetry is broken when the contrast intensity is encoded into the firing rates of the primary electroreceptor afferents (EAs), shown for an example cell. The insets show the predictions of the power law adaptation model (FIG. 2), superimposed onto many recorded EA responses; the complete overlap of model and data curves demonstrates that the model captures this skew in the population average. c) Changes in the firing rate of an ON and OFF cell pair in response to motion reversal along the transverse axis [140]. As expected, the OFF cell responds to the decreasing, negative local contrast caused by a looming plastic object and increases both its tonic and burst spiking rates. Upon motion reversal, it transitions from burst spiking to no spiking, despite the fact that the local to background contrast is still strongly negative. Surprisingly, the ON cell switches its polarity and transitions from silence to bursting under these negative contrast conditions, generating a receding response that mimics the OFF cell's looming response. The skew introduced in the EAs has been removed at this stage of electrosensory processing. d) Polarity switches are also observed for longitudinal motion reversal, shown for an ON/OFF cell pair in response to 2 cm/s looming motion of a plastic sphere, moving ±3 cm from the very centre of the receptive field (RF). Together these results indicate that ON and OFF cells are coding the sign of temporal contrast (regardless of spatial contrast) and that sequential activation of electrosensory ON and OFF cell subsets are combined to produce representations of motion in the three spatial dimensions.

Motion reversal switches ON/OFF cell polarity. Under motion reversal conditions, ON or OFF cells no longer respond to their 'preferred' sign of electrical contrast, despite a strong feedforward drive [140]. This is shown in FIG. 5c, in which ON and OFF cells can be seen to switch their polarity at the point of motion reversal [140]. Under negative contrast conditions (looming and receding plastic) the OFF cell encodes looming motion (and the resulting increase in negative contrast) with tonic and burst spikes; as expected, ON cell spiking is suppressed. However, upon motion reversal the OFF cell immediately transitions from high-frequency bursting to quiescence and the ON cell vigorously responds with bursts to the receding plastic despite the strong negative local to background contrast [140]. Although there is a noticeable skew in the feedforward input from the EAs for looming and receding motion, the receding responses of ON and OFF cells are nearly symmetrical versions of the looming responses. Hence, at this second stage of electrosensory processing, stimulus representations distributed over time and cell type can fix the skewed EA intensity rate code. The direction of motion is represented by the sequence of population activity. A polarity switch is also observed for looming and receding brass spheres, highlighting the fact that both ON and OFF cells respond to negative and positive contrast stimuli. We conclude that ON and OFF cells are highly selective for the temporal derivative of contrast and not for the spatial, local to background contrast as conventionally defined. From these results, it is clear that ON and OFF cell outputs must be combined simultaneously to encode three-dimensional motion and envelopes, and sequentially to encode motion reversal.

Longitudinal motion across the sensory surface of the fish Apteronotus leptorhynchus also triggers polarity switches and transitions from tonic to bursting states as shifting contrast patterns move into and then reverse in the RFs of electrosensory ON and OFF cells [140] (FIG. 5d). This type of motion is relevant to prey capture [117]. Longitudinal motion in the electrosense is especially important as it creates stimulus conditions that are analogous to the contrast patterns projected onto the retina during three-dimensional motion. Contrast patterns that shift across the sensory surface have leading and trailing edges that move coherently and are indicative of movement across the visual field. For example, a positive contrast stimulus

creates temporal contrast increases at its leading edge and relative contrast decreases at its trailing edge. As a result, ON cells would encode the leading edge and OFF cells would encode the trailing edge. If the stimulus were to reverse direction, then the roles would switch and the ON cells would encode the new leading edge, and the OFF cells would encode the new trailing edge. Looming and receding visual stimuli cause expansion and contraction of the visual image on the retina, respectively. Under these circumstances, motion reversal creates similar changes in the leading versus trailing edge and should also evoke ON and OFF cell switches. Furthermore, spike rate adaptation is prevalent in visual systems and thus adaptive skew will be generated upon motion reversal, presumably contributing to precise directional selectivity. Because of the deep analogies between vision and the electrosense, we have hypothesized that ON and OFF cell switches would also be an important coding innovation for visual systems [140].

Switches in retinal ON/OFF cell polarity. The first indication that contrast coding by retinal neurons also does not adhere to strict labelled lines was a curious switch in OFF retinal ganglion cell polarity when stimulation occurred outside the classic RF [107]. However, a connection to neural coding and the demonstration of an ON cell switching its polarity to encode negative contrast were not provided. Confirmation of the hypothesis that ON and OFF retinal ganglion cell polarity switches encode motion reversal has now been obtained in both salamander and mouse retinae [251], strongly suggesting that sequences of dynamical transitions between spiking states and switches in ON and OFF cell polarity are a general strategy for encoding spatiotemporal contrast patterns.

Local signal contrast is a relative measure, the sign of which is defined by the global signal background. For example, in the visual system a local increase in illumination (positive contrast) can be inverted to become a negative contrast stimulus by simply changing the background illumination to be brighter than the stimulus. It is easy to envision how this would occur naturally when tracking a moving object under patchy light conditions (in wooded areas on a sunny day, for example). Reversal in motion creates temporal contrast ambiguity, but

a static stimulus with a change in background illumination can also confuse the perceptual interpretation of visual contrast. A recent study has identified retinal ganglion ON and OFF cell switches in response to the level of adaptation to background illumination levels [252], providing evidence that this strategy may be well-suited to solve other types of ambi-guities in sensory systems that face rapidly changing environmental conditions.

Conclusions and perspective. The idea that ON and OFF cells decompose a sensory scene according to local to background contrast is experiencing a rapid overhaul. The old notion that labelled lines preserve the sign of spatial contrast en route to the cortex is now known to be incorrect, as decoding both AM and envelope stimulus features requires the flexible combination of ON and OFF cell responses at low levels of processing; either simultaneously for envelope coding or sequentially over time to track stimulus contrast levels and motion reversal. Demonstrations that rigid local to background contrast coding is an insufficient strategy for natural motion in the electrosensory and visual system have only recently been provided [140, 251]. Here, we have summarized evidence that ON and OFF cells in the electrosensory system are closely tuned to the temporal derivative of sensory contrast, but not bound to the sign of local to background contrast. Although strong anatomical and biophysical evidence exists for distinct ON and OFF contrast channels in the electrosense and vision, distributed contrast coding is a direct counter-example and requires refinement of overly simplistic definitions.

Distributed stimulus representations involving both simultaneous and sequential activation of distinct population subsets can greatly increase the representational capacity of a neural system. Whereas the firing rates of ON and OFF cells in the electrosensory system reflect scalar information, such as object speed, size and distance, the population activity toggles between ON and OFF subsets to encode vector information (direction). In the visual system of mice, convergence of bipolar ON and OFF cell inputs occurs in a class of W3 retinal ganglion cells (which are analogous to the local-edge detectors found in rabbits), enhancing local motion sensitivity down to the resolution of a RF [253]. Modelling studies of visual systems also show that systems combining ON and OFF cell inputs are more efficient at neural coding [233,254]. In

the electrosensory system a modelling study has demonstrated that TS cells, which combine ON and OFF cell input via a nonlinear mechanism, can extract a context invariant representation of important communication signals [255].

At Marr's computational level of analysis, the electrosense and vision seem to process sensory contrast patterns in an equivalent manner. Despite pronounced differences in the network biophysics, simultaneous and sequential ON and OFF cell population coding may be a common computational level strategy. Marr's theory suggests that optimizations of neural coding might have driven convergent evolution such that equivalent computations arise in distinct animal lineages and sensory modalities of different embryological origin. Therefore, it will be interesting to investigate the generality of distributed contrast coding in auditory [125, 256] and vibrissae [257] systems, as these senses also possess ON- and OFF-like neuron classes. As previously discussed [140,252] these results raise important questions about putative higher-level decoding circuits that must extract and interpret activity sequences of distinct neuron classes to deduce the proper stimulus context. Understanding how neural networks interpret and manipulate these population patterns is an essential step towards a more complete understanding of multiscale active sensory perception (Box 2).

Box 2 **Active sensing and optimal information transmission**. The distributed representation of motion by ON and OFF cells in the electrosensory system has important consequences for active sensing. During tracking behaviour, an electric fish maintains a specific distance (between 1.3 and 1.4 cm) from an object that moves back and forth along its transverse body axis (FIG. 5a). In a recent study [204], a new method, developed to assess the coding fidelity of non-Poisson spiking neurons, was applied to show that the responses of ON and OFF cells convey an optimal estimate of object location precisely within this range. This critical distance occurs at the transition between tonic and burst modes of ON/OFF cell spiking (FIG. 5c). Deviations of the object from this location result in suppression of the ON cell population and bursting of the OFF cell population, or vice versa, and this switch encodes the direction of motion. Accurate estimates of distance and speed are contained in the activated ON or OFF cell population firing rates. As such, downstream midbrain networks can decode the motion vector and initiate appropriate motor commands that ensure that the object is held in 'focus'. This form of active sensing involves a sensory-motor loop, in which neural coding and motor outputs simultaneously influence each other to optimize both stimulus estimation and motion tracking. Remarkably, the optimal distance is independent of the object's speed, contrast, direction and

size, illustrating the efficacy of this computation for spatial processing. To achieve these invariances, synaptic and intrinsic conductances in low-level electrosensory networks must be precisely balanced; however, the exact mechanisms that achieve this are not understood. This is the first demonstration that active sensing directly optimizes neural coding with a direct connection made to the control of spiking dynamics.

A.2 Balanced ionotropic receptor dynamics support signal estimation via voltage-dependent membrane noise

Marcoux, C.M., Clarke, S.E., Nesse, W.H., Longtin, A. and Maler, L.* Journal of Neurophysiology, 115(1): 530-545.

Abstract

Encoding behaviorally relevant stimuli in a noisy background is critical for animals to survive in their natural environment. We identify core biophysical and synaptic mechanisms that permit the encoding of low-frequency signals in pyramidal neurons of the weakly electric fish Apteronotus leptorhynchus, an animal that can accurately encode miniscule amplitude modulations of its self-generated electric field. We demonstrate that slow NMDA receptor (NMDA-R)-mediated excitatory postsynaptic potentials (EPSPs) are able to summate over many inter-spike intervals (ISIs) of the primary electrosensory afferents (EAs), effectively eliminating the baseline EA ISI correlations from the pyramidal cell input. Together with a dynamic balance of NMDA-R and GABA-A-R currents, this permits stimulus-evoked changes in EA spiking to be transmitted efficiently to target electrosensory lobe (ELL) pyramidal cells, for encoding low-frequency signals. Interestingly, AMPA-R activity is depressed and appears to play a negligible role in the generation of action potentials. Instead, we hypothesize that cell-intrinsic voltage-dependent membrane noise, which drives a significant proportion of pyramidal cell spikes, supports the encoding of perithreshold sensory input. Together, these mechanisms may be sufficient for the ELL to encode signals near the threshold of behavioral detection.

Introduction

Low-level sensory systems employ a balance of excitatory and inhibitory inputs to principal cells that, in turn, convey estimates of stimulus parameters (e.g. stimulus intensity) to higher level brain areas. The excitatory input may involve both AMPA and NMDA receptors, and the inhibitory input may involve both fast (GABA-A/glycine) and slow (GABA-B) channels. The effects of this specific balance of excitatory and inhibitory currents on stimulus encoding are currently unknown, as is the connection to the specific complement of receptor types. This scenario arises naturally in the electrosensory system of gymnotiform fish, animals which can encode a large range of stimulus intensities, extending down to barely detectable [58, 117]. We use the simplicity of electrosensory stimuli to show that the balance of excitatory (NMDA-R) and inhibitory (GABA-A) transmission, coupled with membrane noise, enables an accurate encoding of electrosensory signal amplitude.

Individual Apteronotus leptorhynchus emit a constant high frequency electric organ discharge (EOD, species range: 700-1000 Hz). The EOD generates an electric field around the fish sensed by $\approx$ 15,000 electroreceptors that drive electroreceptor afferents (EAs). The EOD drives EA discharge in a probabilistic manner with a mean frequency of 200 spikes/s [52]. Objects with conductivity greater (e.g. prey) or less (e.g. rocks) than the ambient water perturb the field to generate a spatially localized electric image - electrically bright or dark patches on the skin. Behavioral studies [117] have shown that the electrosense is essential for prey capture. Detection can occur with prey further than 3 cm from the fish's body [117], which translates to a < 1 μV increase over a baseline EOD amplitude of $\approx$ 1.3 mV [55,117]. In a prey detection time window of 200 ms, these ultra-weak stimuli cause the average EA to increase its discharge by $\approx$ 1 spike relative to a baseline of 40 spikes [52, 131, 166].

Baseline EA discharge is not completely random but exhibits negative interspike interval (ISI) serial correlations (SCs) - that is, a long ISI is followed by a shorter one and vice versa [52, 57, 170]. These SCs reduce EA spike count variability over the 200 ms detection window [57, 170] and can therefore improve the fish's ability to encode prey signals via a rate or spike count code [139]. Detailed calculations suggest that, even with this reduction in variability,

the small increase in spike count produced by the weakest prey signals is not sufficient for prey detection [52, 162]. Several more sophisticated detection models that utilize some form of temporal coding have been proposed. These theories all use stimulus-induced deviations from expected ISI correlations to improve signal encoding over the limits imposed by simple trial-based spike counts. The proposed mechanisms include temporal filtering plus integration of EA spike trains [147], or continuously computing conditional probabilities of successive ISIs via short-term plasticity [161]. It is, however, difficult to devise experimental tests of these theoretical mechanisms. Nesse et al. [167] demonstrated that, in theory, an encoding/decoding mechanism that matched pre- and post-synaptic kinetics could utilize the serial correlation between only two successive ISIs to encode weak signals. Our results below are a first step towards confirming this theory.

Glutamatergic EAs terminate in three topographic maps within the electrosensory lobe (ELL): the centromedial (CMS), centrolateral (CLS) and lateral (LS) segments [19]. The CMS and CLS are both strongly responsive to the spatially localized low-frequency signals associated with motion, while the LS is more specialized for processing spatially diffuse electrocommunication signals [19]. In all maps the EAs drive two classes of output pyramidal neurons [5,19,29,30] as illustrated in Figure 1. EAs terminate directly onto AMPA and NMDA receptor-rich ON-type pyramidal cells (previously described as E cells), and GABAergic interneurons [31–34]. These interneurons in turn inhibit the ON cells. ON cells typically detect conductive objects. OFF-type pyramidal cells (previously described as I cells) receive indirect EA input via the inhibitory interneurons and therefore typically respond to non-conductive objects [31–34].

In this study we use ELL slices to investigate the cellular mechanisms by which A. leptorhynchus can encode low-frequency prey signals. In order to get discernible synaptic responses in ON and OFF cells, we had to stimulate using pulse patterns derived from moderate to strong signals (> 3 μV, see Methods). Our results directly pertain to the cellular mechanisms by which such signals are encoded in the firing rate of EAs; they do not, however, directly address the mechanisms by which the weakest signals are detected. We focus on four

specific questions of EA and ELL ON cell physiology: 1) are EA negative ISI serial correlations transmitted to ON cells as negative SCs of evoked EPSP amplitudes? 2) What are the respective roles of AMPA- and NMDA-R components of the EA-evoked ON cell EPSPs in transmitting information about local low-frequency signals (e.g. prey)? 3) Is the disynaptic GABA-A mediated inhibition of ON cells essential for transmitting such information, or does it serve to simply prevent saturation of the ON cell excitatory EA input? 4) Can membrane noise aid in signal encoding, or is it merely an unavoidable contamination that limits encoding of low-frequency signals? We now elaborate on these individual questions.

1) We have previously shown that the AMPA-R component of the EA to ON cell synapses exhibits short-term presynaptic depression with rapid recovery [111]. As we discuss in detail below, this should lead to a negative SC of the AMPAR peaks at each EA to ON cell synaptic contact. These correlations might, over a short time scale (< 200 ms), interfere with the signal-induced modulations of synaptic release at this site, i.e. be a synaptic source of high-frequency noise. We hypothesize that the EA correlations are removed by postsynaptic dynamics and analyze this possibility in detail. As a second focus of this section, we note that the Nesse et al. analysis [167] shows that a matching of pre- and post-synaptic dynamics can eliminate the EA SCs. Although our data cannot prove this model, it could lend preliminary support to it; it could also disprove it if the SCs persist in the ON cell EPSP amplitudes.

2) In ELL slices, the AMPA-R component of the EA evoked EPSP (ON cell) can trigger spiking [32] suggesting that these receptors are important for signal encoding. This conclusion appears to be contradictory to the depression of the AMPA-R component of the evoked EPSPs when EAs are driven above their baseline frequency [111]. We hypothesize that the slow NMDA-R component of the evoked EPSP will then be critical for encoding slow signals (e.g. prey) and testing this idea.

3) EAs contact local GABAergic interneurons and evoke disynaptic IPSPs in ON cells [32, 33].

We consider two possible roles of this inhibition. First, it may merely prevent the high frequency excitatory EA input to the ON cells from saturating their response. Second, the disynaptic inhibition may be a critical component of signal encoding by ON cells. We address these hypotheses in two ways. First, we examine ON cell stimulus encoding in the absence of inhibition (pharmacological blockade). Second, we examine signal encoding in OFF cells. OFF cells are not directly contacted by EAs, but do receive disynaptic inhibition from the same GABAergic interneurons as ON cells. We therefore reason that, if OFF cells can encode low-frequency signals, it would support our second hypothesis: that inhibition is required for signal encoding in ON cells.

4) The first in vitro study of ELL reported that ON and OFF cells exhibited membrane noise [163]. This noise was voltage-dependent and might therefore be expected to increase with stimulus-evoked excitation of ON cells. This noise might first appear to be counterproductive for signal encoding. We therefore studied this noise in greater detail and, specifically, tried to connect it to the EA-evoked ON cell depolarization. Our data led us to hypothesize that the membrane noise may drive ON cell spiking via the conversion of subthreshold smooth NMDA-R-dependent synaptic input into spike trains [172]. This is an ingredient of the stochastic resonance (SR) signal enhancement effect [160, 164], here for low-frequency signals such as prey. Although it is not possible experimentally to vary noise levels alone to verify that SR is at play, our results show recruitment of noise near threshold, and thus point to noise-driven firing to assist the detection and encoding of stimuli. A major implication of our results on SR is that the responses of pyramidal cells with overlapping receptive fields should not be correlated, since their internal noise sources are likely independent. We explore this possibility in some detail (see Discussion).

Both the CMS and CLS are very sensitive to the electrosensory signals associated with prey [19]. Our in vitro analysis of how prey signal mimics are transmitted across the EA to ON cell synapses was, for technical reasons, confined to the CMS (see Methods). Our in vivo and

in vitro analysis of the contribution of noise to stimulus amplification was, again for technical reasons, done mainly in the CLS (see Methods).

Methods

In vitro recordings. The weakly electric fish, Apteronotus leptorhynchus (male and female, 10 - 15 cm in length) was used in these studies. Adult fish of both sexes were deeply anaesthetized in oxygenated water with 0.2% 3-aminobenzoic ethyl ester (Tricaine Methanesufonate, MS-222; Sigma) and transverse slices were prepared as previously described [151]. In brief, fish were transferred to a foam-lined holder and their gills were superfused with water containing the anesthetic, whereupon the ELL was removed. The ELL was then immersed in ice-cold artificial cerebrospinal fluid (ACSF; 124 mM NaCl, 3 mM KCl, 0.75 mM KH2PO$_4$, 2 mM $CaCl_2$, 1.5 mM $MgSO_4$, 24 mM $NaHCO_3$, and 10 mM D-glucose) containing 1 mM kynurenic acid and transferred to a vibratome (Technical Products International, St. Louis, MO), where 350 μm slices were taken from the transverse plane of the ELL [30]. The ELL slices were transferred to an interface slice chamber with flowing oxygenated ACSF for a minimum of one hour at room temperature before recordings began.

Stimulation and Recording procedures. Intracellular recordings were obtained from pyramidal cells of the centromedial segment (CMS) of the ELL using sharp microelectrodes (80 to 120 MΩ). We used the CMS because EA afferent fibers to this map are confined to compact narrow bundles [157]; we could usually place the bipolar stimulating electrodes over most of the extent of such bundles and thereby evoke strong, readily measured EPSPs. The greater dispersal of the EA afferent fibers in the CLS and LS maps made it far more difficult to find a stimulation site that evoked strong, consistent responses. We selected mainly ON-type pyramidal cells since they receive direct input from the EAs onto their basal dendrites and this greatly simplifies our analysis [30, 32, 34]. We identified ON cells by stimulating the EA afferents: ON cells exhibit short latency EPSPs in response to such stimulation while OFF cells exhibit IPSPs [32, 152]. In a few cases, in order to evaluate whether their inhibitory input contributed to stimulus

encoding by ON cells, we also recorded from OFF cells that are in receipt of the GABA-A receptor mediated disynaptic inhibition from the same interneurons as the ON cells [30, 32–34]. For studies of synaptic transmission between the EAs and downstream pyramidal cells, all active conductances were blocked by routinely filling the pipettes with cesium acetate, lidocaine N-ethyl bromide (QX-314, 100 mM in 3 M CsAc, Alomone Labs, Jerusalem, Israel), and tetraethylammonium (TEA, 50 μM, Sigma- Aldrich, St. Louis, MO) [111, 134]. As previously reported [111] cells stopped spiking in response to depolarizing current in < 5 minutes after impalement and experiments were commenced at this time. In this case, the ON cells effectively become passive reporters of the EA evoked synaptic potentials. In order to evaluate the role of NMDA-R in ON cell responses we bath applied 2-Amino-5-phosphonopentanoic acid (APV; 100 μM, Tocris, Bristol, UK) to block the NMDA-R mediated components of the electroreceptor afferent evoked EPSP [32, 111]. We first recorded the control response and then applied APV, while delivering single EA stimulating pulses every few seconds. Once the late phase of the EPSP had completely disappeared (at least 10 minutes) we initiated our stimulus protocols. For the APV experiments we therefore always compare the same cell for control and blockade conditions. Given the long times required for these interventions, we were not able to hold the cells long enough for washout. In some cases, we also included picrotoxin (PTX, 100 μM, Sigma- Aldrich, St. Louis, MO) in the recording pipette to block the disynaptic GABAergic input to all pyramidal cells. Again, we gave stimulating pulses to the EAs to determine when the evoked IPSP was fully blocked; as previously reported [111] the IPSP was eliminated in $<$ 9 minutes and experiments were then initiated. In this case, we could not record a true control response to EA stimulation because blockade was gradual.

Membrane potentials were recorded with an Axoclamp 900A (Molecular Devices, Sunnyvale, California) and the experiments were controlled with a Power 1401 data acquisition interface and associated Spike 2 software (Cambridge Electronic Design, Cambridge, UK). The voltage signal was amplified, low-pass filtered at 10 kHz, digitized at 20 kHz, and analyzed off-line using custom Matlab routines (MathWorks, Natick, Massachusetts). EPSP amplitude was defined as the difference in the average membrane potential just prior to the occurrence of the stimulus

artefact and the subsequent EPSP maximum. EPSP latency was measured as the time delay between the occurrence of the artefact and the subsequent EPSP maximum.

Pulse stimulation of the EA fibers was accomplished with a gold tipped bipolar tungsten electrode, positioned in the deep fiber layer (DFL) of the ELL [32,111]. The stimulus electrode was placed along the EA tract at least 300 μm from the recording site and the stimulus intensity was adjusted to prevent direct stimulation of the impaled pyramidal cells. The square wave pulse (20 μs, 1-80 V) stimulus was delivered through a signal isolation unit (model DS2, Digitimer, Welwyn Garden City, UK). Stimulus intensity (50 - 80 V) was set to evoke 70% of the maximal EPSP amplitude to facilitate the detection of the starting point of EPSPs with short latencies ($\approx$ 1 ms). Electroreceptor afferents run in a tight bundle to reach the CMS [157] and, since our bipolar stimulating electrode straddled the entire afferent tract, we likely stimulated a large fraction of the $\approx$ 25 EAs that converge onto a single ON type pyramidal cell [29]. Peak EPSP values ranged from <1 mV to 9 mV with the highest value presumably representing stimulation of nearly all of the innervating EAs. We only accepted cases where the evoked EPSP was greater than 0.5 mV and we confirmed that the stimulus artefacts did not change during the course of a recording. Stimulus artefacts were removed from the membrane potential data offline using custom scripts in Matlab (MathWorks, Natick, Massachusetts). Using the known stimulus pulse sequence, artefact peaks were localized and the membrane potential was removed for at most 1 ms preceding, and 2 ms following the timing of the peak. Cubic spline interpolation was then used to replace the $\leq$ 3 ms of excised recorded membrane potential. The peaks of the evoked EPSPs were identified by locating a local maximum in the membrane potential between successive stimulus artefact peaks and starting 2 ms after the peak to avoid contamination with the interpolated membrane potential. The amplitude was then measured as the difference between the value of the membrane potential at the EPSP peak and the membrane potential 1 ms before the occurrence of the stimulus artefact that drove the EPSP; this is the last value of the membrane potential that occurs before the artefact contaminates the signal. Two stimulation patterns were used in this study, both derived from in vivo recordings

of electroreceptor afferent activity [52]. We chose electroreceptor afferent recordings with moderate mean frequencies of 115 spikes/s and 128 spikes/s because higher frequency EAs often produced very short inter-pulse intervals (IPIs < 3 ms); in these cases, the stimulus artefact of the second pulse obscured the peak of the EPSP evoked by the first pulse. We used both the baseline discharge and evoked responses of these EAs as stimuli. In the case of baseline discharge, the EAs are driven by the constant amplitude of the fish's electric organ discharge (EOD) and variation in the spike train IPIs are due to the internal dynamics of the receptor and its afferent fiber. We also used pulse trains derived from one of the EA's spiking responses to 0-4 Hz random amplitude modulations (RAMs) of the fish's EOD [52]. Low-frequency amplitude modulations are typical of electrolocation, and are commonly experienced during navigation and prey capture [117]. In order to average across recordings from many pyramidal cells, we used a single short stretch of stimulus lasting one second and included both strong (≈ 80 μV) and moderate (< 5 μV) amplitude modulations. In preliminary tests we found that stimulation for >2 s resulted in clear run down of the evoked EPSPs. We therefore chose to use a minimal stimulus duration of 1 s to avoid the artefactual reduction of EPSPs towards the end of the stimulus period. We compared the evoked pyramidal cell membrane potential fluctuations to the external sensory stimulus using a correlation measure as done in previous in vivo studies [16, 137]. Although these stimulus pulse patterns were derived from in vivo recordings of EAs, our stimulation method causes synchronous activation of all EAs, whereas in vivo such low-frequency stimuli would evoke increased but uncorrelated discharge across the EA population contributing to the receptive field of the recorded neuron [29,133]. The effect of this difference is analyzed further below. To characterize the intrinsic pyramidal cell noise, we recorded ON cells from both the CMS and CLS maps [19]. The recording pipette was filled with 2 M potassium acetate only. In these cases we bath applied 6-cyano-7-nitroquinoxaline-2,3-dione (CNQX, 1 mM, Tocris, Bristol, UK) and APV to block all synaptic input to pyramidal cells [32]. We again used single EA stimulating pulses and initiated recording when we could not record any synaptic response (at least 10 minutes). In these cases, we could not perform a control case because membrane fluctuations before complete synaptic blockade could result

from either membrane or synaptic noise. After drug application, any remaining membrane fluctuations could then be attributed to cell-intrinsic sources. Studies examining the intrinsic membrane fluctuations (noise) of ELL pyramidal cells used two-second holding currents to maintain the impaled cell at various membrane potentials (see Results below). We started by applying sufficient holding current to bring the cell above spike threshold. For the cell in Fig. 6 spike threshold was at ≈ -65 mV, consistent with the pyramidal cell threshold in CMS (approximately -63 to -67 mV) [165]. For the illustrated cell, we first depolarized by 5 mV to -60 mV (Fig. 6B) to induce strong membrane noise and robust spiking (Fig. 6A, B); in order to compare levels of depolarization (above spike threshold) across cells; this suprathreshold level of depolarization was set to 0 as in Fig. 6A. From the above threshold membrane potential, we then stepped the injected current so as to produce -5 mV hyperpolarizations, bringing the cell down to -20 mV below the initial holding potential. Therefore, different holding currents were used for each cell to preserve this relative relationship to spike threshold.

In vivo recordings. Fish were anesthetized and the caudal cerebellum, overlying the ELL, was exposed. After stopping general anesthesia, a local anesthetic was applied to the wound margins. Fish were immobilized with a size-dependent dose of pancuronium bromide, injected intramuscularly, and were respirated with a constant flow of aerated water for the duration of the experiment. The fish were transferred into a large tank of 27°C water with the electrical conductivity kept between 100-120 μS/cm, and a custom holder was used to stabilize the head during long-term recordings. Fish were given time to acclimatize before data acquisition and were monitored closely for signs of stress. Single unit extracellular recordings were obtained from the CLS map of the ELL for direct comparison of pyramidal cell spiking to the in vitro data described above. One reason the CLS map was preferred for these studies is that the receptive fields of CLS pyramidal cells are much larger than those of CMS and therefore much easier to localize [29]. Pyramidal cells with receptive fields near the fish's dorsum (at the water's edge) were excluded from the analysis due to their proximity to the air-water interface, where boundary effects warp the electric field. Once a suitable cell was located and its firing

rate and type (ON or OFF) verified with local steps in the electric potential, long sections of baseline activity were recorded and used to compute ISI serial correlations. The serial ISI correlation coefficients for lag j ($SC(j)$) are defined as

$$SC(j) = \frac{< I_{i+j} I_j > - < I_j >^2}{Var(I)}$$

where $< \cdot >$ represents the average value and $Var(I)$ the variance of the ISIs. An average serial correlation was determined for 5 ON and 5 OFF cells from 3 different fish. Analysis was performed using custom Matlab scripts. All procedures were reviewed and approved by the Animal Care Committee at the University of Ottawa and follows Society for Neuroscience guidelines.

Results

Elimination of electroreceptor afferent inter-spike interval serial correlations by slow NMDA-R mediated EPSPs. It has previously been shown that the baseline activity of EAs exhibit a negative ISI correlation at lag 1, indicative of sensitivity to the timing of the last two action potentials [170]. The effect of synaptic transmission on such correlations has not been well studied. A theoretical analysis did demonstrate that presynaptic depression can suppress positive ISI correlations in incoming spike trains, resulting in much less correlated ISIs impacting the post-synaptic receptors [148]. Recent theoretical work has also shown that correlations in input currents (but not ISIs per se) can be transferred to output ISIs [171]; but little is known about input-to-output transfer of ISI correlations. If an input spike strongly influences spiking probability, then one might intuitively expect that ISI correlations are transferred, but the situation is less clear when many spikes from different neurons are required to fire the cell, and when there is noise, which are both the situation of interest here. Our results below therefore advance our knowledge on ISI correlation transfer and also raise interesting questions in this

context.

The baseline activity of target ELL pyramidal cells is effectively a renewal process with minimal or no ISI correlations (shown below in the in vivo section). The elimination of ISI correlations might be achieved at many levels of the ELL circuitry or via intrinsic properties of the pyramidal cells. In the absence of spiking and thus network feedback, our goal was to understand whether EA-to-CMS pyramidal cell synaptic dynamics can, by itself, remove the EA correlation structure. An earlier study established that blocking AMPA-R mediated transmission with CNQX also blocks NMDA transmission [135]. Therefore, we assume that AMPA transmission is crucial in sufficiently depolarizing pyramidal cell basal dendrites to unblock NMDA-R channels, and is required for transmitting electrosensory signals from EAs to pyramidal cells. For experiments examining the mechanisms of decorrelation and signal transmission, we consequently tested the role of NMDA and GABA-A receptors by first studying the intact system and then systematically eliminating the NMDA and GABA-A receptor components.

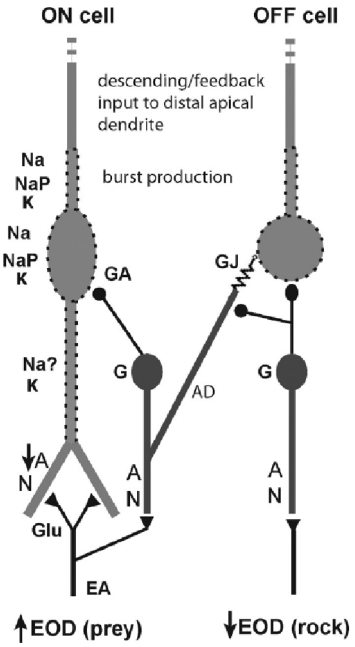

Figure 1 **Summary diagram of the ELL circuitry that generates the ON and OFF cell responses**. ON cells receive direct glutamatergic (Glu) synaptic input from EA afferents onto their basal dendrites; glutamate excites the ON cell via AMPA (A) and NMDA (N) receptors. The AMPA component of the EA evoked EPSP shows strong short term depression (down arrow beside the 'A'). The EAs also contact local GABAergic interneurons (G) that, in turn, synapse on the ON cell somata utilizing GABA-A receptors (GA). The net effect of this arrangement is that increases in EOD intensity within the receptive field of the ON cell due to a conductive object, e.g. prey, will depolarize the ON cell and elicit increased spiking. Immunocytochemistry and physiological studies have shown that the soma and proximal apical dendrite of the ON cell express both fast (Na) and persistent (NaP) Na+ channels as well as K+ (Kv3) channels. The basal dendrite of the ON cell also expresses Na+ channels (immunocytochemistry) but it is not known whether these are the fast or persistent variety or both (hence Na?). The OFF cell receives input from EAs only disynaptically via the same GABAergic interneuron; this inhibitory input generates the OFF cell receptive field center. Excitation of the OFF cell is via gap junction (GJ) input from ascending dendrites (AD) of the same interneurons; these, however, emanate from distant cells and therefore represent more distant body regions (receptive field surround). The GABAergic interneurons that inhibit the OFF cell also inhibit the ascending dendrites. The net effect of this circuitry is that a decrease in EOD intensity due to, e.g. a rock, will reduce the direct inhibition of the OFF cell and, via the ascending dendrite and gap junction synapses, also permit excitation from distant regions of the fish's skin. The OFF cell will therefore invert the electrosensory input and give a spiking response to non-conductive objects. The OFF cell also expresses the same Na+ and K+ channels as the ON cell. The circuitry illustrated in this figure was first demonstrated by L. Maler [30, 34].

ELL ON cells receive direct electroreceptor afferent input onto their basal dendrites (Fig. 1) [32]. With intrinsic conductances pharmacologically blocked (see Methods) but AMPA, NMDA and GABA receptors intact, stimulation of electroreceptor afferent with a natural baseline discharge pattern induced rapid summation of evoked potentials to a plateau level (Fig. 2A, left). This is consistent with a previous study showing that temporal summation

results in a plateaued potential when using a 200 Hz stimulus train [111]. Stimulating the EAs with these high-frequency stimulus trains evokes a complex sequence of IPSPs and EPSPs in the pyramidal cells, which vary greatly in amplitude (Fig. 2A, right). In some recordings it is possible to distinguish between the NMDA and AMPA-R components of the pyramidal cell EPSP (Fig. 2A). As previously shown [32, 111], the AMPA-R component appears as a rapidly rising, short latency response that can decay before full activation of the NMDA-R, which has a longer latency and slower rate of rise. This produces a prominent notch in the evoked EPSP. It is important to note that the magnitude of the fast AMPA-R component of the EPSP is always far smaller than the slower NMDA-R component.

Electroreceptor afferent evoked EPSPs vary in amplitude depending on the previous ISI length. After short ISIs, the NMDA-R component of the EPSPs summates and typically generates EPSPs with near equal or larger amplitudes (Fig. 2A, right). This result stands at odds with our previous study using fixed frequency or random stimulation [111] where, in the presence of NMDA and GABA-A receptor antagonists, strong and fast presynaptic depression of the EA-evoked EPSP was observed following short ISI stimulus pulses. To resolve this issue, we repeated our earlier study by first blocking NMDA receptors alone with APV. We note that this drug application does not merely block NMDA-R transmission at the electroreceptor afferent to ON cell synapse; ELL granular interneurons also express NMDA receptors [150] and so this treatment will likely reduce disynaptic GABA-A inhibition as well as block NMDA-R transmission onto ON cells (Fig. 1). Under these conditions, we observed minimal temporal summation (Fig. 2B, left), and short ISIs often resulted in prominent depression of the evoked EPSP (Fig. 2B, right). This is not surprising since there is no longer the slow NMDA-R component capable of temporal summation, thus unmasking the previously characterized depressing AMPA-R component.

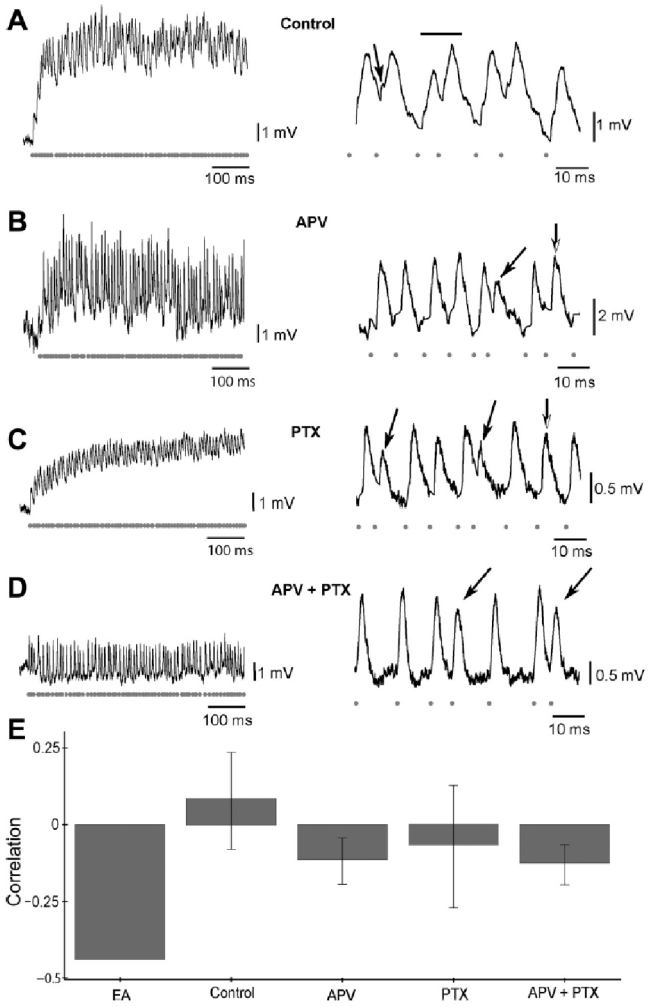

Figure 2 **Basilar pyramidal cell response to EA fiber stimulation with a natural baseline discharge pattern**. Intrinsic conductances are removed by intracellular blockade. A: Characteristic response to stimulation with AMPA, NMDA and GABA-A receptors intact. Stimulation results in plateauing temporal summation (left). Closer examination of the evoked response reveals a complex sequence of EPSPs and IPSPs (right). Note that the fast AMPA-R component of the EPSP (arrow) can be distinguished from the slower NDMD-R component. Short ISIs evoke EPSPs of equal or increasing (bar) amplitude. B: EPSPs in the presence of APV. Minimal temporal summation is seen with NMDA-R blocked (left). Short ISIs result in depression (first arrow), although this is not always the case (second half-arrow) (right). C: blocking GABA-A with picrotoxin while leaving NMDA-R intact results in strong temporal summation to a plateau potential (left). Short ISIs resulted in depressing EPSPs (first two arrows), although longer ISIs occasionally had the same result (half-arrow right). D: Blocking both NMDA and GABA-A receptors once again eliminated temporal summation. Short ISIs result in prominent depression (arrows). E: Serial correlations between the heights of successive EPSP peaks evoked by EA stimulation sequence obtained from a natural baseline EA discharge pattern. The EA ISIs had a negative serial correlation coefficient of -0.44. Two tailed t-tests were performed to determine if the mean serial correlations differed significantly from 0. Blocking intrinsic conductances (control) eliminated the negative serial correlation (0.083, SD = 0.16, N = 10, p = 0.13). Negative correlation re-appeared in the absence of NMDA-R (APV; -0.11, SD = 0.075, N = 6, p = 0.0046) or with both NMDA-R and GABA-A blocked (-0.12, SD = 0.066, N = 5, p = 0.013). Absence of GABA-A alone did not have a significant effect (PTX; -0.065, SD = 0.19, N = 5, p = 0.50). Both cases in which NMDA-R was blocked (APV, APV+PTX) had mean correlation coefficients that differ significantly from control (one-way ANOVA, p = 0.0188; Tukey post hoc). All conditions had significantly reduced negative amplitude correlations compared to ISI correlations from in vivo EAs.

We next blocked GABA-A receptors with intracellular PTX but left NMDA-R mediated transmission intact (Fig. 2C, left). Again, we observed strong temporal summation of EPSPs to a plateau potential and the EPSPs evoked after shorter ISIs were smaller; now, however, longer ISIs could also produce this effect (Fig. 2C, right). It appears that, with inhibition blocked, the NMDA-R component of the EPSPs can summate to a plateau potential and the peaks represent the combined AMPA-R and NMDA-R components. With both NMDA and GABA-A receptors blocked, temporal summation of successive EPSPs did not occur and no summation to a plateau potential was observed. As seen in Fig. 2D (left), short ISIs result in prominent depression that, as previously shown [111], recovers after only a single longer ISI. Therefore, the temporal summation of EPSPs evoked by short EA ISIs is due to slow NMDA receptor currents, which effectively counteract the fast EA presynaptic short-term depression. Note that the dynamics of disynaptic inhibition (currently unknown) may complicate this effect.

We next computed the serial correlations at lag 1 between successive peak amplitudes of the evoked EPSPs. Two-tailed t test were performed to determine if the mean serial correlations differed significantly from zero. The original EAs had negative ISI serial correlations (-0.44) but in the control case (AMPA, NMDA and GABA receptors intact) these negative ISI correlations were not reflected in any significant correlations between successive EPSP peak amplitudes (Fig. 2E, correlation = 0.083, SD = 0.16, N = 10, p = 0.13, two-tailed t-test). Blocking either NMDA (correlation = -0.11, SD = 0.075, N = 6, p = 0.0046, two-tailed t-test) or both NMDA and GABA-A receptors (correlation = -0.12, SD = 0.066, N = 5, p = 0.013, two-tailed t test) resulted in the reappearance of negative serial correlations in the peak amplitudes, while blocking inhibition with PTX application alone did not have a significant effect (correlation = -0.065, SD = 0.19, N = 5, p = 0.5037, two-tailed t test). Indeed, the correlation coefficient for the control condition differs significantly from both cases in which NMDA is blocked (p = 0.0188, one way ANOVA with Tukey post-hoc comparisons) but not when inhibition alone is blocked. For the APV and APV+PTX cases, the small AMPA-R mediated EPSP peaks merely reflect the depression due to a lack of NMDA-R mediated temporal summation [111].

On average, the unmasked depression results in higher peaks being followed by smaller ones, and vice-versa, constituting an expression of the negative ISI correlations at the level of synaptic responses. The absence of a significant effect in the case of blockade of inhibition by PTX is presumably due to the residual NMDA-R dependent temporal summation that masks the AMPA-R depression. Note that in all cases, the serial EPSP peak correlation did not reach in vivo SC values for the afferent ISIs.

We conclude that, under control conditions, the postsynaptic dynamics of combined direct excitatory plus disynaptic inhibitory electroreceptor afferent input onto E cell dendrites is matched to the EA ISI structure, in the sense that serial correlations between successive EPSP peak amplitudes are eliminated. These uncorrelated peak amplitudes are left to represent the stimulus, consistent with the Nesse et al. coding scheme [167], although it does not prove it. The NMDA-R mediated component of the EPSP is most important for this effect because its time course extends over several ISIs and the resulting temporal summation produces a positive correlation that counterbalances the negative correlation imparted by short term depression of the AMPA-R component.

Signal encoding by pyramidal cells with excitation plus inhibition. An in vivo study [16] has shown that the EA input to an ON cell (summed EPSPs/IPSPs) can faithfully reconstruct a low-frequency stimulus presented within its receptive field. Larger functional networks [20] were active in these experiments and might conceivably contribute to the observed stimulus reconstruction. Here, we aimed to determine the synaptic requirements for this reconstruction in the absence of these networks. In order to estimate reconstruction accuracy, we used a spike sequence, recorded from an EA in response to a random amplitude modulation (RAM) stimulus (Fig. 3A, see Methods) to drive the EAs of E cells. We used stimulus-evoked responses from the same EAs that were also used for our analysis of the ON cell response to baseline EA discharge. We then computed the cross-correlation coefficient between the evoked membrane potential and the original RAM stimulus. Again, we blocked voltage-dependent conductances to study the synaptic potentials in isolation in the E cells. Despite the fact that our stimulation

protocol induced non-physiological synchronous EA input, the ON cell membrane potential was still able to reconstruct moderate amplitude signals in vitro (Fig. 3B), provided both NMDA and GABA-A receptors were not blocked. The membrane potential clearly followed even the small modulations of the original stimulus.

Signal reconstruction is significantly impaired with NMDA-R blocked by APV but with inhibition intact; in particular, the response to the small modulations is now absent, although the response to the large dip in the RAM (trough) is still evident (Fig. 3C). At the maxima of the amplitude modulations, pyramidal cells are receiving increased excitatory input; however, with NMDA receptors blocked, there is no temporal summation and the AMPA-R mediated EPSPs become depressed. This is due to fast AMPA receptor mediated short-term depression [111] acting in concert with the GABA-A disynaptic inhibition as described above. It is not surprising that temporal summation of EPSPs is required to encode a low-frequency signal and that slow NMDA-R mediated synaptic currents are responsible for this encoding. Therefore, with NMDA-R currents intact, we expected efficient and possibly better than the control signal coding in the absence of GABA-A inhibition. Surprisingly, upon blocking inhibition with PTX, pyramidal cell encoding of amplitude modulations was almost completely eliminated (Fig. 3D). It appears that, in the absence of inhibition, the NMDA-R mediated EPSPs summate to a saturated plateau potential and can no longer encode the variations in electroreceptor afferent input. When both NMDA- and GABA-A receptors were blocked there was no modulation at all in response to the EA stimulation. AMPA receptors alone are not capable of encoding even strong sensory input (Fig. 3E).

As summarized in Fig. 3F, good stimulus reconstruction was only obtained when both NMDA and GABA-A receptors were intact (RAM-response cross-correlation = 0.53, SD = 0.091, N = 10). The mean cross correlation in the APV (cross-correlation = 0.10, SD = 0.19, N = 5), PTX (cross-correlation = 0.18, SD = 0.10, N = 6) and APV+PTX (cross-correlation = -0.14, SD = 0.22, N = 5) cases were significantly different from control (one way ANOVA, $p < 0.001$; Tukey post hoc). Two-tailed t-test revealed that the control

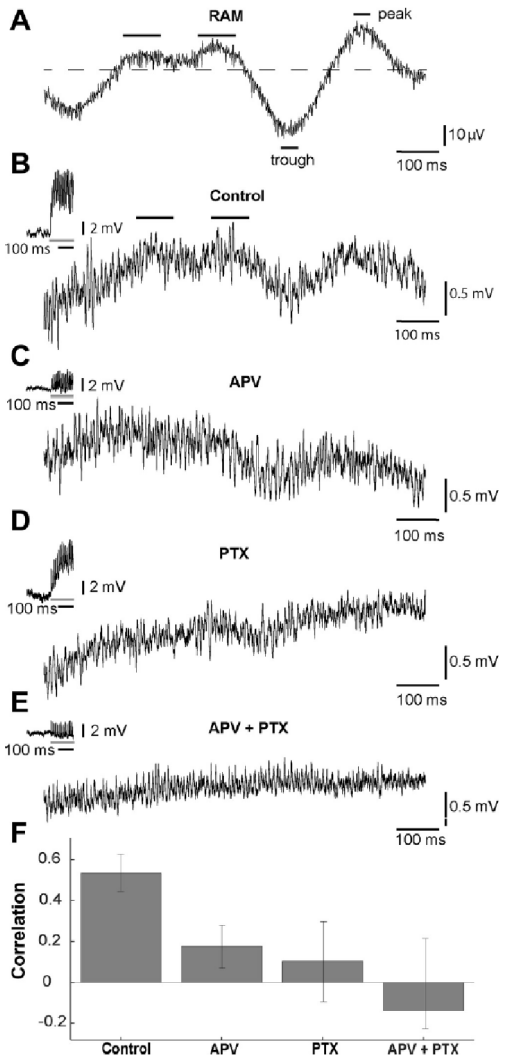

Figure 3 **Stimulus reconstruction from pyramidal cell voltage traces**. Pyramidal cell membrane fluctuations were evoked by stimulation of EAs with in vivo derived EA spiking responses to RAMs. A: RAM stimulus from which electroreceptor afferent spiking responses were obtained. Two left bars indicate weak stimulus fluctuations (bumps) mentioned in the text. "Peak" and "trough" bars indicate stimulus regions further analyzed in Figure 5. B-D: In each case, 10 pyramidal cell responses to electroreceptor afferent input were averaged. Insets: pyramidal cell responses at stimulus onset (gray bar). B: Inset: stimulation leads to temporal summation to a plateau potential; main figure is taken from the steady state response. With intrinsic conductances blocked and AMPA, NMDA and GABA receptors intact, membrane fluctuations can reconstruct even weak amplitude modulations (bars). C: Inset: in the presence of APV, no plateau potential is observed. In the absence of NMDA-R (APV), there is no temporal summation (inset) and signal reconstruction is impaired. D: Inset: in the presence of PTX, temporal summation to a plateau potential is observed. With GABA-A receptor mediated inhibition blocked, weak signal reconstruction is eliminated even though both AMPA-R and NMDA-R are intact. This suggests that, in the absence of inhibition, NMDA-R mediated EPSPs summate to a plateau potential and are no longer able to encode changes in the afferent input. E: Inset: in the presence of APV and PTX, no plateau potential is observed. AMPA receptors alone are not capable of encoding even strong sensory input. F: Mean cross-correlation between evoked pyramidal cell membrane potential fluctuations and the RAM stimulus (± SD). The stimulus was well reconstructed with NMDA-R and AMPA-R intact (cross-correlation 0.53 SD = 0.091, N = 10). Cross-correlation was significantly reduced in APV (0.10, SD = 0.19, N = 5), PTX (0.18, SD = 0.10, N =6) and APV+PTX (-0.14, SD = 0.22, N = 5) cases. All conditions have means significantly different from control (one-way ANOVA, $p < 0.001$). Two-tailed t-tests revealed that the control ($p < 0.001$) and APV ($p = 0.008$) conditions were significantly different from 0, while PTX ($p = 0.3038$) and APV+PTX ($p = 0.2322$) were not.

Two-tailed t-test revealed that the control ($p < 0.001$) and APV ($p = 0.008$) conditions were significantly different from 0, while PTX ($p = 0.30$, two-tailed t test) and APV+PTX ($p = 0.23$, two-tailed t-test) were not. We conclude that the relative proportions of excitation and inhibition in the in vitro control case are required to encode electrosensory signals by ON cells. The NMDA-component of the evoked EPSP must summate to permit an encoding of the slow time scale of the input RAM (0-4 Hz). By itself, NMDA summation will result in a saturated response that no longer follows the stimulus fluctuations. Fast disynaptic inhibition [32, 111] is required to prevent saturation and keep the NMDA-R excitation within its dynamic range.

In order to get a deeper appreciation of these effects, we examined the ON cell responses to the regions in Fig. 3, designated as "trough" and "peak," of the low frequency stimulus (Fig. 4). It is noteworthy that, in all treatment conditions, the EPSP peaks evoked at the local stimulus trough are larger than those evoked at the local peak. This is simply due to the fact that the decrease in stimulus intensity during a trough (below the baseline EOD amplitude) causes a reduction in EA discharge [52] and this in turn results in longer than average EA ISIs. These long ISIs do not cause depression at EA synapses [111]. In contrast, the shortened ISIs in the EAs during a stimulus peak cause strong depression and therefore reduced EPSP peak amplitudes.

In the control case (Fig. 4A), the EPSPs during a stimulus trough are large with clear AMPA- and NMDA-R mediated EPSPs, cleanly separated by strong hyperpolarizing events that are likely caused by disynaptic GABA-A inhibition. Although the peak EPSPs are large ($\approx$5 mV), they occur while the cell is hyperpolarized (Fig. 4A, left) and these EPSPs rarely trigger spikes in response to sensory input that falls below the baseline EOD amplitude [16]. During the peak response, much smaller fluctuations of the membrane potential ($\approx$1 mV) are observed riding on the slow NMDA-R mediated depolarization (Fig. 4A, right). Similar results are obtained after application of the drugs (Fig. 4B-D), the notable differences being that the EPSPs at the peak are more prominent than for the no drug condition and that blocking inhibition with PTX application (with or without APV) application results in less variability in EPSP amplitude at both the peak and the trough.

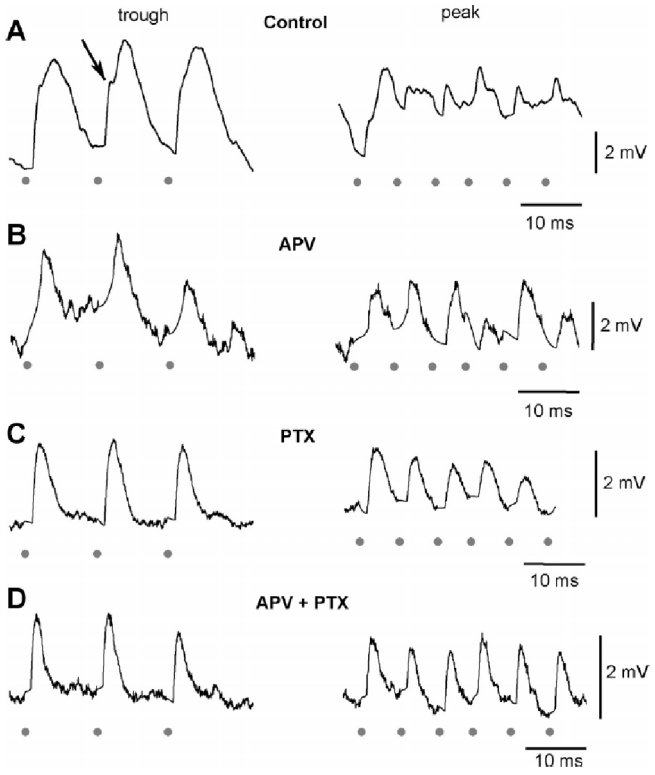

Figure 4 **Pyramidal cell responses evoked from stimulation of electroreceptor afferents using in vivo derived electroreceptor afferent spiking responses to RAMs**. The peak and trough were the sections of the response defined by the named bars in Fig.3. Individual EPSPs at the peak (left) and trough (right) of the RAM signal were examined. A, left: When intrinsic conductances are blocked, EPSPs have distinct AMPA-R (arrow) and NMDA-R mediated components. A, right: At stimulus peak, small membrane potential fluctuations are seen riding on the top of the slow NMDA depolarizations. B, C, D: Under all conditions, EPSPs at the stimulus trough are larger in amplitude than those evoked at the stimulus peak.

Two important issues are raised by these results. First, it is not clear whether the disynaptic GABA-A receptor-mediated inhibition is merely acting as a tonic inhibition that prevents NMDA-R mediated saturation of the responses to the RAM stimulus, or if it plays a more active role in stimulus coding. Secondly, it is not clear to what extent the remaining potential fluctuations in peak response are due to the artificial synchronous stimulation of the EAs. We deal in turn with these issues in the following sections.

Fast disynaptic inhibition can encode slow signals. Since the absence of disynaptic inhibition prevented signal reconstruction (Fig. 3D), we wanted to determine whether GABA-mediated

synaptic transmission contributed to the coding of these signals or simply prevented the NMDA-R component of the summating EPSPs from saturating. This was achieved by examining the RAM-stimulus evoked response of OFF cells (see Fig. 1 for OFF cell circuitry), which receive only inhibitory GABA-A input from their receptive field center and are excited by spatially averaged surround input, generated by gap junction input from granular cell dendrites [30, 32, 34, 91]. The OFF cells, as expected, inverted the response to the RAM signal (Fig. 5). Remarkably, they were able to accurately follow even the small amplitude modulations (Fig. 5). A stimulus-response cross-correlation value of -0.64 (SD = 0.17, N = 5) was attained and, although sign inverted, its absolute value was not significantly different from that obtained for E cells (p = 0.53). Blocking inhibition with PTX abolished the OFF cell's response to EA stimulation as expected from a previous study [32, 152]. The cell's membrane potential simply randomly drifted up and down, and the negative correlation between the OFF cell response and the RAM signal (cross correlation 0.057, N = 1) was eliminated, demonstrating that its response did indeed arise from disynaptic GABA-A mediated inhibition. The same GABAergic interneurons send projections to both ON and OFF cells [33]. Since these projections convey information sufficient for stimulus encoding in the OFF cells, we conclude that they also convey the same information to the ON cells. These results demonstrate that the ability of an ON cell's membrane potential to encode RAM signals is likely due to the dynamic balance of NDMA-R mediated excitation and GABA-A mediated disynaptic inhibition.

Computational analyses suggest that asynchronous in vivo synaptic potentials are smoother than those evoked by synchronous in vitro stimulation and are unlikely to evoke spikes. An unavoidable caveat of our in vitro stimulation protocol is the synchronous activation of multiple EAs that would otherwise fire asynchronously in vivo. EAs are probabilistic encoders, each firing at a given phase of the EOD waveform but skipping an intermittent number of EOD cycles [52]. In vivo, populations of EAs that converge onto a pyramidal cell (25 for CMS map) [29] will fire independently when driven by low frequency stimuli [133]. Under baseline

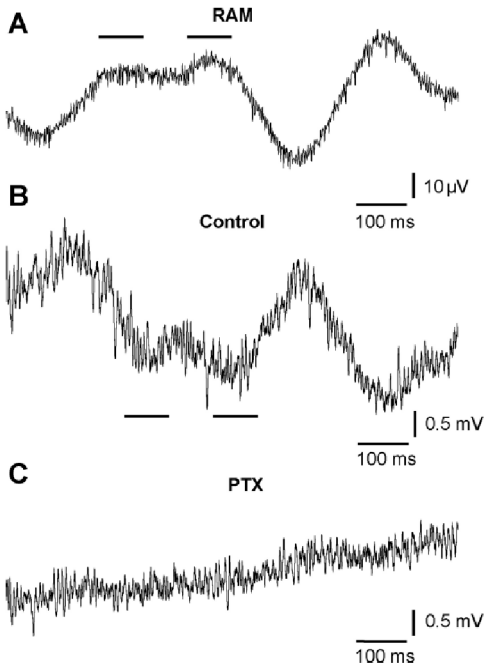

Figure 5 **Electroreceptor afferent evoked response of OFF cells to the RAM stimulus**. A: RAM stimulus from which electroreceptor afferent spiking response was obtained. B, C: In each case, 10 pyramidal cell responses to electroreceptor afferent input were averaged. B: Membrane fluctuations of OFF cells inverted the RAM signal (cross correlation = -0.64, SD = 0.17, N = 5). C: Application of PTX completely eliminated the inverse correlation (cross correlation 0.057, N =1), demonstrating that the response arose from GABA-A mediated inhibition.

conditions or when driven by low frequency prey mimic signals, various subsets of the EA population will discharge in every single cycle of the high frequency EOD, but will not all discharge synchronously. However, for our in vitro experiments, the strong pulses used to reliably stimulate the EA fibers in slice are derived from one EA spiking response to a RAM stimulus (Figs. 3, 4 and 5). As a result the stimulated population is entrained to the activity patterns of our exemplar unit (see Methods), firing synchronously within a given EOD cycle and producing an absence of spikes in many others. For example, in Fig. 4 (control, right, peak response) the stimulus pulses skip 2 to 4 EOD cycles. The strong stimulus likely evokes a response in most or all of the 25 EA afferents contacting the ON cell and generates a maximal response. The stimulus used for the in vivo recording that generated this EA spike train would result in a peak EA probability of discharge of 0.33 [52]. Therefore, in vivo, we would expect that 8 (one third) of the EA afferents discharged on each EOD cycle and evoked a weaker (one third of maximum in vitro) EPSP. Intuitively, one would expect the asynchronous case

to generate smoother summed synaptic potential because of the 'filling in' of each EOD cycle with smaller EPSPs and the temporal summation of evoked responses. We lack a detailed understanding of EA-evoked disynaptic inhibition in ELL, and cannot therefore directly model the effect of natural synaptic input on the smoothness of the summed ON cell response. Below, we provide a simple approximate statistical analysis of the heights of the EPSPs that illustrates the magnitude of our hypothesized smoothing effect. We assume that 25 EAs converge onto the CMS ON cell [29] and, during the peak stimulus response (Figs. 3, 4), have a mean discharge probability = 0.33. In the artificial in vitro case, with stimulation by the one EA exemplar, on each EOD cycle the input is 0 or 25 EAs. This is a discrete density with 0 having a probability of 2/3 and 25 a probability of 1/3. The first moment (i.e. mean) of this density is

$$\mu_1 = \sum xP(x) = 0 \cdot 2/3 + 25 \cdot 1/3 = 8.33$$

and the second moment (variance) is

$$\mu_2 = \sum x^2 P(x) = (25^2)/3 = 208.3.$$

The variance of the EPSP height can then be calculated as $\sigma^2 = \mu_2 - \mu_1^2 = 138.94$. In the natural case, on each EOD cycle a fraction of the 25 EAs will independently discharge. This is a binomial density, $n = 25$ and $P = 0.33$. The mean will again be $nP = 0.33 \cdot 25 = 8.33$ EAs discharging. The variance of the number of EAs that fire in each cycle is $nP(1 - P) = 5.53$. The variance of the artificial experimental case is therefore ≈ 25 times greater than the natural case. In order to estimate the evoked response it would be necessary to convolve the EA inputs with a kernel representing the dynamic response of the ON cell to excitatory (AMPA + NMDA receptors) and disynaptic inhibitory input; as mentioned above, this is not possible given our current state of knowledge. Assuming that the variance of the evoked summed EPSP/IPSP response is similar to that of the driving input, we would expect that the standard deviation of the membrane potential at the peak response (Figure 4) would decrease from an estimated 1.8 mV to 0.36 mV. Effectively, the membrane potential would be smooth and without the

rapid > 2 mV depolarizations that trigger spikes in vivo [16, 138]. In light of this, an obvious question arises: how are pyramidal cell spikes triggered off of this smooth depolarizing response.

Voltage-dependent membrane noise triggers spiking. Previous studies of cortical [129, 130] and ELL pyramidal cells [138] have shown that spiking is evoked by rapid depolarization of the membrane potential, i.e. by steep increases that can be localized in time using the first or second temporal derivative. It is often assumed that AMPA-R mediated currents provide the necessary rapid depolarization to elicit spiking. In an ELL slice, the rising phase of a single EA evoked EPSP (mostly AMPA-R) will evoke a spike [32,111]. Electroreceptor afferents normally discharge continuously at a high rate [52] and under these conditions the AMPA-R mediated component of the EPSP is slightly depressed [111]. We therefore hypothesize that, in vivo, it is the NMDA-R and not AMPA-R component of the stimulus evoked EPSP that evokes most spiking in ON cells. Further, our experimental results and statistical analysis suggest that the response to slow increases in EOD amplitude are smooth and lack the rapid depolarizing events (i.e. no large second derivative) required to evoke spikes [138]. This prompted us to consider how the slow NMDA-R EPSPs could possibly drive spiking. Early work in the ELL described the presence of membrane noise that increased in amplitude with depolarization [163]; this noise was attributed to voltage-gated ion channels likely selective for Na^+, although a contribution by synaptic noise could not be excluded. Since these rapid membrane potential fluctuations were able to elicit spikes in pyramidal cells in vitro [163], we decided to investigate whether noise could compensate for the depressed AMPA-R component of the EA evoked EPSP and drive the fast upstrokes in membrane potential required for spiking in pyramidal cells.

We treated the ELL with CNQX and APV to block synaptic transmission onto ON cells and interneurons and therefore eliminated synaptic input as the source of rapid fluctuations in membrane potential. We then recorded from CMS pyramidal cells without any channel

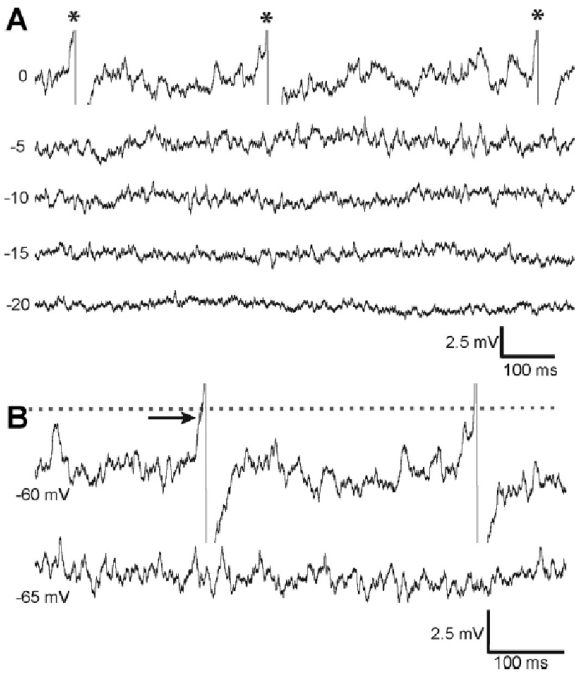

Figure 6 **Recordings of spontaneous pyramidal cell membrane potential at various holding potentials**. Recordings were taken with extracellular CNQX and APV to block synaptic noise. A: Amplitude of membrane potential fluctuations increases dramatically with depolarization to spike threshold (around -65 mV, here normalized to 0). Near threshold, rapid large depolarization elicits spiking (*, spikes truncated). B: Blips elicit spikes (arrow) when they reach spike threshold (dashed line). Here we give the absolute membrane potentials for this particular neuron - the traces (top: -60 mV; bottom: -65 mV) are an expanded version of the normalized top traces of A (0, -5).

blockers (i.e. no QX-314 or cesium in the pipette) and applied depolarizing current steps; because synaptic transmission was blocked, we were not able to determine whether we were recording from ON or OFF cells. As previously described [163], the pyramidal cell membrane potential was noisy and the amplitude of the membrane potential fluctuations increased dramatically with depolarization (N =5, Fig. 6A). Spike threshold varied across cells but was typically near -65mV. As the membrane potential approached spike threshold, the presence of rapid, large depolarizations (blips) became apparent and these blips were seen to co-occur with spiking (Fig. 6B). To investigate the membrane noise in more detail, we computed histograms of the membrane potential at different levels of depolarization. The membrane noise histograms were well fit by the Gaussian distribution at relatively hyperpolarized levels (Fig. 7A). However, at more depolarized levels (near threshold) the distribution has a higher variance (Fig. 7B, C) and becomes both more peaked (kurtotic) and positively skewed to the right (Fig. 7B, D). The positive skew is due to an increase in the occurrence of the large blips.

When we included voltage-gated ion channel blockers in the pipette, the variance was low and independent of membrane potential (Fig. 7C inset, N =1) conclusively identifying the noise as intrinsic rather than a result of synaptic conductances.

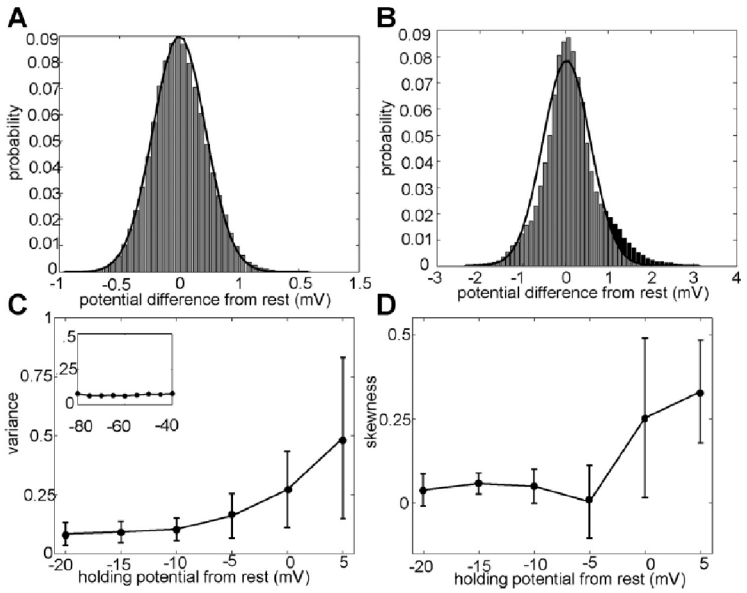

Figure 7 **Probability distribution, variance and skew of CMS pyramidal cell membrane fluctuations**. Recordings were made with extracellular CNQX and APV to block synaptic noise. The resting membrane potential was simply the neuron's mean potential without any current injection. In the following panels, we normalized each recording by subtracting this mean potential so as to display more clearly the effect of injecting de- or hyper-polarizing current. A: When hyperpolarized, pyramidal cell's membrane noise histogram (gray) is well fit by a Gaussian distribution (black curve overlay). B: Near threshold, the distribution is more peaked (kurtotic) and positively skewed than the best fit Gaussian distribution. The skew in the distribution (black) is likely a result of an increased frequency of rapid depolarizations (blips). C, D: Holding potentials are normalized to spike threshold, with 0 representing spike threshold. C: Variance of noise distribution increases with depolarization. Inset: When voltage gated ion channels were blocked, variance was reduced and became independent of membrane potential, demonstrating an intrinsic source of noise. D: Skew increases dramatically at potentials at or above spike-threshold.

We hypothesize that many stimulus-evoked spikes in ON cells are elicited by the voltage-dependent blips, which would ride on top of the summating NMDA-R component of the PSPs evoked by the EAs. To investigate this possibility, we turned to the centrolateral segment (CLS) of the ELL and repeated the noise experiments described above (N = 5). We switched to the CLS map because preliminary experiments had shown that the blip events (right tail of the distribution shown in Fig. 7B for the CMS map) were far more prominent, allowing us to determine blip occurrence with greater fidelity and temporal accuracy. The overall membrane

noise characteristics were otherwise identical to the CMS map: CLS pyramidal cells display fluctuations whose variance and skewness increase with depolarization of the membrane potential (data not shown).

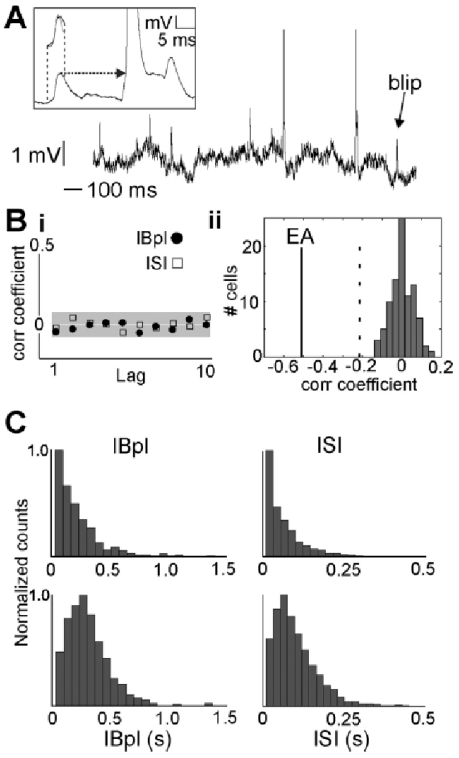

Figure 8 **Statistical structure of blips and of pyramidal cell spiking to which they contribute**. A: An example membrane potential trace from the spontaneous activity of an E type pyramidal cell of the CLS map, showing many clear blips and two action potentials (truncated). The inset shows that the peak of a blip (start of arrow) is at the same height as the inflection point (arrow) for an action potential, suggesting that blips may trigger spikes. The thin dashed vertical lines enclose the blip waveform (gray) with a superimposed waveform of the AMPA-R component of an EA evoked EPSP (black). The onsets of the two waveforms are nearly identical suggesting these blips might trigger spikes as effectively as the rising phase (AMPA-R) of EA evoked EPSP. Bi: The interblip intervals (IBpI, black circles) are not serially correlated and are therefore a renewal point process (left); this lack of correlation is also seen in the ISI sequence derived from the spiking output of the ELL pyramidal cells (ISI, open squares). Bii: A histogram of serial ISI correlations from a larger (N = 91) sample of CLS ON and OFF cells (firing rates between 5 and 35 spikes/s). Correlations are mostly within ± 0.1 with an average near 0. We also illustrate the strong mean negative serial correlations of EAs (black line, -0.52) and the highest correlation observed (dashed line, -0.23); note that there is no overlap between EA and ON/OFF cell correlations. C: We found two patterns of IBpIs (left), which are both reflected in the ISI statistics of individual ELL pyramidal cell neurons from the centrolateral map (right). This strongly suggests that blips directly drive a portion of spikes in ELL pyramidal cells.

Figure 8A shows an example membrane potential trace from a CLS neuron, demonstrating

clear blips and the occasional spike. The figure inset shows that an action potential may trigger directly off the peak of a blip (indicated by the dashed arrow). Furthermore, the blip waveform has an onset slope nearly identical to the AMPA-R component of an EPSP (shown in gray, overlaying the excised blip), suggesting that these noisy fluctuations are sufficient to trigger spikes when they occur near the action potential threshold. Using the same derivative criteria as was used above to identify spikes, we isolated the times at which blips occurred and computed inter-blip interval statistics including the serial correlation coefficients of inter-blip intervals (IBpI) and the IBpI histogram. The IBpIs had means ranging between 0.39 s (SD = 0.23) and 0.22 s (SD = 0.25) for the 3 CLS cells where blips could be cleanly extracted. The IBpI showed no serial correlation (Fig. 8Bi, black circles) indicating that the blips originate from a renewal process. We found the IbpI distributions were consistent with the renewal process being either a Poisson (Fig. 8C; left, top) or a more general gamma process (Fig. 8C; left, bottom), depending on the neuron. To determine whether the statistical patterns of blip generation might influence the statistical patterns of pyramidal cell spiking, in vivo extracellular recordings were obtained from CLS pyramidal neurons in the absence of a stimulus (5 ON cells and 5 OFF cells). Examination of the data showed that there were no significant differences between ON and OFF cells and the data was therefore pooled. The mean ISIs of the 10 cells ranged between 0.13 s (SD = 0.13) and 0.039 s (SD = 0.025). The mean ISIs are significantly smaller than the mean IBpIs, presumably due to the cells being driven more strongly by the EAs and feedback in vivo, rather than by intracellular current injection in vitro. As illustrated in Fig. 8Bi (open squares), this small sample suggests many in vivo ISIs are not significantly correlated at any lag demonstrating that some ON and OFF cell spiking follows a renewal process. Because there are some apparently contradictory results in the literature concerning ELL pyramidal cell serial ISI correlations (see Discussion), we also examined the distribution of baseline ISI serial correlations in a much larger sample of previously recorded CLS ON and OFF cells [140]. We had a sample of 50 ON cells (firing rates of 6.3 - 35.4 spikes/s) and 41 OFF cells (firing rates of 5 - 30.7 spikes/s). Preliminary analysis showed that their serial ISI correlations were not significantly different in the two populations and so the data were

pooled for a sample of N = 91 cells. As illustrated in Fig.8Bii, the ISI correlations are all low (mean 0.003; ±0.059), and include both small positive as well as negative correlations ranging between -0.1 and +0.1. In contrast, we also illustrate the EA serial ISI correlations taken from [170]. These have a mean of -0.52 ±0.14 (black line under EA) and a range of -0.23 to -0.82. The lower value (-0.82) is off the scale of the figure, and a dashed line indicates the maximum correlation (-0.23) observed. It is clear that, in going from EAs to pyramidal cells, there is a massive reduction in ISI correlations, and that the ON and OFF cell serial correlations are, for the cells with firing rates < 40 spikes/s, near zero.

The in vivo ISI histograms qualitatively match the two classes of IBpI histograms observed in our in vitro experiments (Fig. 8C, left vs right). We hypothesize that the blip voltage-dependence generates an optimal noise level for the encoding and transmission of sub- and peri-threshold low-frequency signals by ON cells, that is, blips are the basis for ON cell stochastic resonance. Further, we hypothesize that blips form a basis for a renewal point process, which is conserved in the spiking output of the ELL pyramidal cells, even in vivo when the ON or OFF cell functions as part of the entire network. Together with the decorrelation of EPSP peaks by the natural mixture of synaptic currents, the renewal blip-process ensures an efficient encoding of stimulus amplitude modulations centrally, including for signals that lie below or in the vicinity of the spiking threshold.

Discussion

Our in vitro study reveals how excitatory and inhibitory synaptic transmission to ON pyramidal cells and their intrinsic noise combine to encode electrosensory signals transmitted by the EAs.

Elimination of EA ISI correlations. The EA ISI correlations are not transmitted to serial correlations of EPSPs peaks because of the NMDA-R component of the EPSPs; the AMPA-R component, on its own, will transmit the correlation (Fig. 2E). This is expected because the AMPA-R EPSP component shows a rapidly recovering depression after short ISIs [111].

Therefore a short ISI will evoke a depressed second AMPA-R EPSP; the following longer ISI (due to the negative ISI correlation at lag 1) will evoke a larger AMPA-R EPSP. A sequence of a long ISI followed by a short ISI will, by the same reasoning, evoke a large, followed by a small, AMPA-R EPSP. In this manner, AMPA-R transmission will, on its own, preserve the ISI negative serial correlations in the EA as negative correlations of the EPSP peak amplitude (AMPA-R component).

The EA synapses onto ON cells utilize NMDA-Rs [134, 150] with long evoked EPSPs [32] (>100 ms), greatly exceeding the mean baseline EA ISIs ($\approx$ 5 ms) [52]. The NMDAR evoked EPSP time scale is better matched to the low firing rates (mostly $<$ 20 Hz or $>$ 50 ms and $\approx$ 10 EA ISIs) of our sample of ON/OFF cells; again the long ON cell ISIs would be expected to reduce or eliminate the effect of EA ISI correlations. We hypothesize that temporal summation of EPSPs over many ISIs due to NMDA-R effectively eliminates EA negative ISI correlations.

An earlier study [138] showed, in a small sample, that ON and OFF cells with a low firing rate ($<$ 20 Hz) showed minimal serial ISI correlations, consistent with our observations on a much larger sample (Fig. 8Bii). These authors did show that pyramidal cells with a higher firing rate ($>$ 40 Hz; in our sample all rates were $<$ 40 Hz) did show negative serial ISI correlations (-0.1 to -0.3). Chacron et al. [138] attributed it to an intrinsic mechanism (threshold fatigue) and not to the EA input and this result is therefore also consistent with our analyses. We hypothesize that the negatively correlated fluctuations in AMPA-R potential amplitudes constitute high-frequency synaptic noise that might potentially corrupt the low firing rate ON cell response to low-frequency prey signals. The NMDA-R component therefore eliminates this noise source and also matches the ON cell response to the low-frequency input associated with e.g., prey signals.

Theoretical analyses [167] predict that the negatively correlated EA ISIs are caused by quasi-independent peaks of the adaptation variable intrinsic to an EA. Further, the quasi-independence of the adaptation variable could be recovered postsynaptically provided that the synaptic kinetics were matched to those of the EA adaptation process. This representation in terms of independent variables could, in theory, implement an efficient encoding strategy. The

elimination of postsynaptic negative serial correlations is a signature of such matching and is thus at least consistent with the theory [167]. A similar effect has been observed at the single neuron level in cortex although it is implemented by an entirely different biophysical mechanism [169]. Their analysis strongly suggested that power law spike frequency adaptation performs temporal whitening of inputs. We have provided a direct example of temporal decorrelation (whitening) at the synaptic level, here implemented by the combined activity of NMDA and AMPA receptor currents.

Electrosensory signal encoding. Behavioral experiments have shown that A. leptorhynchus can detect weak prey signals (<1 μV) [58, 117]. Our results suggest that the dynamic balance between NMDA-R-mediated temporal summation and GABA-A mediated inhibition is needed to encode these signals. Blockade of NMDA-R activity eliminates this coding. The importance of NMDA-R transmission is made clear by examining EA synaptic responses during the peaks of the RAMs. The short ISIs induce presynaptic depression of the EPSP AMPA-R component [111] making it unlikely that they will trigger many spikes in vivo. We hypothesize that the AMPA-R component merely permits activation of the NMDA-R, but does not contribute to signal encoding in our CMS ON cell population.

The NMDA-R component of the EPSP does not depress. This is likely due to two factors: temporal summation of these long EPSPs may mask depression and the relative affinity (half-maximal effective concentration, EC_{50}) of glutamate for the AMPA-R (EC_{50}: 500 μM) versus NMDA-R (EC_{50}: < 2 μM) [144]. EA afferents are glutamatergic [173]. Glutamate concentrations at the synaptic cleft reach ≈ 1 mM [141] with extrasynaptic concentrations reaching 190 μM [145]. We hypothesize that the EA presynaptic depression is due to a reduction of the cleft glutamate concentration below that required for AMPA-R activation, but still adequate to activate NMDA-Rs. The longer time course and positive voltage dependence of the summating NMDA-R EPSP can then effectively encode and amplify low frequency signals extending over many EA ISIs. The sensitivity to prey signals inferred from our study is likely higher in vivo. Our in vitro stimulation, based on the response of a few EAs, resulted in the synchronous

activation of pyramidal cells. In vivo encoding in ELL would arise via asynchronous responses of heterogenous EAs, and better follow small stimulus fluctuations. For practical reasons (see Methods), our synaptic analysis was confined to the CMS. ON-type pyramidal cells in the CMS receive about 25 EA inputs while those in the CLS receive about 100 inputs [29]. CLS ON cells are thus more sensitive to prey mimics in their receptive fields [19–21], although both maps are equally sensitive to moving prey mimics [154].

Role of GABA-A mediated inhibition in signal detection. Blockade of GABA-A transmission alone prevents both ON- and OFF- cells from encoding signals. This might be due to prevention of NMDA-R EPSPs saturation. Saturation does not, however, account for the excellent OFF cells responses to stimuli in their receptive field center relayed by disynaptic GABA-A synaptic input [32–34]. Because OFF cell circuitry is complex [33, 34] we offer no further speculation on the mechanism(s) by which OFF effectively encode signals (Fig. 1). We simply conclude that ON cell encoding of prey signals requires a balance of direct EA input and disynaptic inhibitory input. Detailed computational analyses will be required to understand the underlying dynamics.

Somatic amplification of signal input via voltage-dependent stochastic resonance. The ON cell response to stimulus evoked EA spike patterns was typically small (< 2 mV) and comparable to the responses seen in vivo [16]. These small depolarizations are not expected to reach spike threshold from the typical in vitro resting membrane potential [165]. Yet, in vivo, these small compound EPSPs do evoke a strong spiking response [16] suggesting that some amplification intervenes between synaptic response and spike output. We have shown that somatic persistent sodium channels amplify EPSPs arising in distal apical dendrites [134] and hypothesize that the same mechanism will amplify EA input to the ON cell basal dendrites.

We have discovered voltage-dependent membrane noise that is steeply activated near spike threshold [165]. The fluctuations have a sharply rising slope resembling that of AMPA-R EPSPs and trigger spiking. Although the precise nature of the underlying stochastic biophysical

dynamics is not known for ELL pyramidal neurons, similar voltage-dependent noise has been noted in other systems [153]. Our initial studies suggested that the ELL pyramidal cell noise was due to Na^+ channels [163], while a recent theoretical analysis has suggested that the stochastic closure of K^+ channels is the main contributor to membrane noise [168]. We have shown (Fig. 1) that both Na^+ and K^+ (Kv3) channels are distributed over the soma and proximal dendrites of ON and OFF cells (Fig. 1) [40, 143] and that both fast and persistent Na^+ channels are present on the soma and on proximal apical dendrites [40, 134]. The biophysical substrates for membrane noise are therefore available in ELL pyramidal cells. The origin of the blips is more difficult to determine. Turner et al. showed that the Na^+ channels on the somatic and dendritic membranes of ELL pyramidal cells were clustered in small "hot spots" [40]. An untested but interesting idea is that blips might in part be generated by the cooperative interactions of tightly co-localized Na^+ channels.

Whatever the source of the ON cell membrane noise, we hypothesize that it implements a voltage-dependent stochastic resonance effect (SRVD). Through this effect, noise due to blips would provide the crucial amplification step that transforms subthreshold/peri-threshold, input-evoked smooth synaptic responses into ON cell spiking output that correlates with the input. The higher parts of the input signal elicit more noise via the voltage dependence, allowing them to become encoded into spikes, albeit with some stochasticity. In the absence of a sensory input, this voltage-dependent noise underlies the stochastic firing of the ON cell, and as is usual for SR, noise would likely not benefit the encoding of large signals. It is not possible, at present, to experimentally confirm that ON cells use SR to encode low frequency signals. The key test, using intracellular QX-314 application to block noise, would also block spiking. There is, however, supporting evidence for our conjecture. We previously demonstrated that the ON cell membrane potential accurately followed a 4 Hz stimulus within its receptive field center [16]. Figure 4 of this paper shows that fast depolarizations ride on top of the slow 4 Hz modulation and drive spiking. We suspect, but cannot prove, that these fast fluctuations seen in vivo are due to the membrane noise that we analyzed in vitro; although clearly not conclusive, this data is at least consistent with our voltage-dependent SR theory.

There are three consequences of our hypothesis that SRVD drives spiking to weak low frequency signals. First, since spiking is driven by intrinsic noise rather than the rising phase of EPSPs, it should not be phase locked to the EOD. This is indeed observed for all CMS and CLS ON neurons [113] and strongly supports our hypothesis. We note that this is not simply due to all ELL target cells being unable to follow the high frequency discharge of EAs but, rather, a design feature of these ON cells. This conclusion is based on two exemplars. First, one class of ELL interneuron (ovoid cell) is very strongly phase locked to the EOD [132]. This is likely due to this cell type having little [150] or no [136] NMDA-R expression and therefore being driven by EA-evoked AMPA-R EPSPs. Second, a large subset of LS ON cells (precise identity unknown) is also phase locked to the EOD [113]; neither the mechanism nor the consequences for sensory coding are known in this case. Based on analogy with the ovoid cell we predict that, in this cell class, 1) EA evoked AMPA-R EPSPs will drive spiking, 2) that these cells will have minimal membrane noise and 3) they will be most responsive to high frequency AMs.

The second consequence is that, as shown above, pyramidal cell discharge will have renewal statistics in the absence of sensory input, with the same distribution as that of the IBpIs (gamma). Their baseline spike trains are now an ideal basis for inhomogeneous rate coding.

The third consequence is that the spiking response of ON cells receiving overlapping EA input should not display correlations due to common input, i.e. noise correlations. This exact result has been reported for CMS cells driven by random amplitude modulations (RAMs) of the EOD with a cutoff frequency of < 20 Hz [156], providing strong support for our hypothesis. A different study [159], recording from the CLS and LS and delivering electrosensory input (RAM, 120 Hz cut-off) to neighboring pyramidal cells' receptive fields, did find noise correlations. The correlations peaked at time delays near 100 ms consistent with common EA input driving spiking via slow (i.e. NMDA-R driven) excitatory input and noise, and not consistent with spiking driven directly by fast synaptic events (i.e. AMPA-R). Again, this result is supportive of our hypothesis. A separate study [38], recording from the CLS and LS neurons (RAM, 120 Hz cutoff), reached partially contradictory conclusions. Correlations were observed

upon stimulation within the neighboring ON cells' overlapping receptive field, but these were mostly signal (not 70 noise) correlations. This result is consistent with Krahe et al. [156] and Litwin-Kumar et al. [159] and supportive of our hypothesis. Chacron and Bastian [38] also reported that there were correlations of baseline spiking activity of neighboring ON (and OFF) cells over short time windows. This result is apparently not consistent with our hypothesis. However, baseline EA discharge will include long ISIs evoking a large (nondepressed) AMPA-R component.

We hypothesize that, at least for CLS and LS cells, baseline discharge can be weakly correlated because it is triggered by the AMPA-R component of the EPSP. Sensory stimulation, by shortening ISIs, causes depression of AMPA-R EPSPs; noise correlations are reduced because spiking is then evoked by membrane noise riding on slow NMDA-R EPSPs. We hypothesize that ON (and likely OFF) cell discharge in the CMS and CLS maps, in response to low frequency input confined to their receptive fields, will be generated by intrinsic noise (blips). The response of cells with overlapping receptive fields will therefore be uncorrelated. This, in turn, will enable averaging the independent responses by downstream neurons and therefore enhance the detection and estimation of the weakest, e.g., prey signals. Clearly further experiments are required to verify these hypotheses.

Our results also point to a role for noise in signal encoding - facilitating encoding in a voltage-dependent manner. Blips are the main feature of this membrane noise and enable spiking where it would not otherwise occur. Noise-assisted signal encoding as in the stochastic resonance effect [146,149,160] falls under the broader heading of stochastic facilitation [160,164]. It assumes that the stimulus evoked EPSPs are subthreshold, as expected for weak stimuli, or generally stimuli that sit below threshold due to net bias inputs from the circuitry. For our study, where signals are slow and aperiodic, SR is referred to as aperiodic stochastic resonance [142]. Noise-assisted stimulus encoding has been demonstrated in vitro in hippocampal cells with current injection [172]. Our study reveals that this effect is likely present here due to noisy blips arising near threshold. Due to the voltage-dependence of the rate of occurrence of these blips, and consequently of the noise variance (Figs. 7, 8C), the noise is amplified just where it is

needed, namely, when subthreshold activity reaches spiking threshold. Thus not only does our study show that spikes are associated with noise blips and thus noise assists stimulus encoding at the second stage of a sensory system, it also relies on the voltage-dependence of this noise.

Let us put this result in a broader context. A modeling study [56] predicted that EAs operate in the suprathreshold regime for baseline firing, meaning that firings would still occur in the absence of noise. The same goes for encoding of zero-mean amplitude modulations into a modulation of baseline activity. Thus noise in these receptors does not help the encoding of subthreshold stimuli, and SR is not at work; noise is nevertheless thought to help by linearizing the EA input-output firing rate function, smoothing over nonlinear phase locking effects [155].

Our results suggest that the next stage (ELL) is poised to detect any small modulations of baseline EA firing using noise. We cannot carry out the required classic experiment to prove that SR is at work, i.e. we cannot show that the input-output correlation of a pyramidal cell peaks for an intermediate noise level by adding and suppressing noise. The reason is that we cannot vary the noise level alone - at the very least, the noise level co-varies with the mean of the membrane potential, i.e. it is voltage dependent. Nevertheless, the fact that the noise increases right at the limit of detection of the signal suggests that the noise-induced firing helps encode the signal. In fact, upward excursions of the signal will recruit more blips, with the result that the (stochastic) rate of firing is modulated by the signal.

Hence, postsynaptically to the EAs, it appears that noise helps the encoding process, in contrast to the EA level where the signal appears to modulate an already suprathreshold baseline firing pattern. It is also clear that too much noise at the second stage will degrade the encoding, as in the SR effect. It is tempting to further investigate whether this suprathreshold-followed-by-subthreshold encoding is a more general design principle of sensory systems, and whether an optimal noise level associated with a voltage-dependent stochastic resonance is at play here and in other systems.

The ISI decorrelation process supported mainly by the NMDA-R synaptic component appears to combine with noise-induced firing to ensure a sensitive encoding of naturalistic stimuli. The true statistics of the input spikes from multiple EAs to ON cells is not fully known, and

the summed spike train may already have altered serial correlations compared to single EAs [158]. The interaction of the summed EA spike trains and postsynaptic dynamics remains a critical but challenging subject for future investigation.

Appendix B

Supplementary Information

B.1 SI for *Speed-invariant encoding of looming object distance requires power law spike-rate adaptation*

Detailed Experimental Procedures

Standard surgical procedures were similar to those previously described [96] and are recapitulated here. Fish were anesthetized by immersion in a solution of tricaine methanesulfonate and distilled water (0.2 % w/v). Surgery was performed to expose the caudal cerebellum overlying the electrosensory lateral line lobe (ELL), while the fish was being respirated with water containing the anaesthetic. After stopping general anaesthesia, a local anaesthetic (lidocaine) was applied to the wound margins. Fish were immobilized with a size dependent dose of pancuronium bromide (0.03% v/v), injected intramuscularly, and were then respirated with a constant flow of aerated water for the duration of the experiment. All surgical procedures were reviewed and approved by the Animal Care Committee at the University of Ottawa. The electric field produced by the fish is neurogenic and thus unaffected by the paralytic, leaving the electrosense completely intact. The fish were mounted into a large tank of 27°C water with conductivity kept in a range of 120 to 150 μS/cm, and a custom holder was used to stabilize the head and maintain long-term recordings. A covering of saline solution was maintained over the exposed brain surface to avoid desiccation and a reference electrode was placed in the saline

solution. Glass micropipettes (filled with 3M potassium acetate; resistance 90 to120 MΩ) were advanced through the cerebellum to take extracellular recordings from electroreceptor nerve afferents in the deepest layer of the ELL [29]. Neural recordings were amplified using an Axoclamp 2b (Molecular Devices Inc.), digitized at 20 kHz with a Power 1401 analogue to digital converter and collected in Spike2, version 7.03 (Cambridge Electronic Design). Firing rates for both electrophysiological data as well as the models, were computed by convolving binary spike trains with a 50 ms exponential kernel. A previous looming study estimated firing rates from the spiking responses of high frequency, primary sensory afferents using a 20 ms Gaussian kernel [23]. Since the choice of kernel width can be a bit arbitrary, we also tried an existing algorithm to choose an optimal kernel width for a Gaussian filter [97]. For all the cells tested, we found kernel widths between 40-80 ms (with one outlier of 109 ms). Based on these facts, we picked an intermediate value of 50 ms and used an exponential filter instead of a Gaussian to avoid non-causal contributions to firing rate. Averaged firing rates were then computed from repeated presentations of a looming signal and were taken over a small number of repetitions in all cases (10-20), a fraction of the lower bound for the minimum convergence numbers of electroreceptors onto downstream ELL targets [29]. All analysis was performed using custom scripts and MATLAB's built-in-functions (Mathworks). The simulation of the brass sphere's effect on a fish's electric field (Fig. 1A) was generated using COMSOL MULTIPHYSICS 4.3 ®.

Although the changes in transdermal potential have been studied as a function of lateral axis distance [55], these results were obtained from spheres moving parallel to the rostral-caudal axis at fixed lateral axis distances. Therefore, we mimicked the recording protocol of Chen et al. (2005), to observe the change in transdermal potential resulting from our looming brass sphere (0.635 cm radius) aligned with the dipole center, moving continuously along the lateral axis towards the fish's body. The voltage drop across the skin was recorded using a custom-made, shielded recording dipole attached to a thin flexible cable. The transdermal dipole itself consisted of two Teflon-coated silver wires (0.20 mm bare, 0.28 mm coated), which were 3 cm

in length. The Teflon® coating was scraped from the distal 1 mm, and the exposed silver tips were chloridized. One tip was implanted subcutaneously along the longitudinal axis of the fish, level with the lateral line. The other tip rested up against the outside of the fish, so that the dipole spanned the epidermal layers. This cable was connected to the aforementioned amplifier and the data was acquired through Spike2. Amplitude modulations of the oscillatory transdermal potential were extracted by bandpass-filtering the signal between ± 100 Hz of the fish's electric organ discharge frequency and then applying the Hilbert transform [55, 77, 78]. The brass sphere was attached to a rigid, thin plastic rod and mounted to the mobile platform of a Parker LP28 linear actuator, controlled by a Parker ViX 250 IM micro-stepping drive. The actuator was positioned on the wall of the recording tank and the stimulus hung down into the water. The platform was slid along the tank so that the sphere was aligned with the center of our transdermal dipole. Using the analogue control feature of the drive, a voltage pulse from Spike2 is issued, which initiates a controlled sequence of movements pre-programmed onto the drive. The choice for this mode of control is essential as it allowed us to track the sphere's position and match it to the recorded transdermal dipole data displayed in our recording software. As described below, we directly modulated the EOD amplitude with custom-made stimulus dipoles, in order to recreate the electrosensory signals generated by looming brass spheres at the receptive field center. The looming sphere will always saturate the tiny receptive fields of the electroreceptors directly beneath it [29], however locating the exact receptive field center during recordings can often be challenging. A global dipole signal will saturate the receptive field of every electroreceptor neuron, alleviating concerns about stimulus alignment with the receptive field center. Furthermore, recordings from the fine electroreceptor afferents are difficult to maintain during the perturbations caused by sphere movement and while trying to manually position the motor within a given electroreceptor's receptive field.

The mimic looming stimuli were initially presented through either global or local dipoles. Two graphite rods (diameter = 0.75 cm, length = 29 cm) served as our global dipoles, and flanked both sides of the fish's body. Local dipoles were made from stainless steel wire (diameter

= 76.2 m) with a tip separation of 2 mm. When stimulating locally the dipole center was placed directly into the receptive field center of the electroreceptor. We compared global to local dipole stimulation and saw no difference in the electroreceptor responses to looming stimuli. Since the receptive fields of the electroreceptors are so small, locating them with a local dipole and positioning it in the receptive field center is time consuming and occasionally inaccurate. Therefore, we used primarily global signals, alleviating worries about possible local dipole / receptive field misalignment. Using global signals ensures that we always stimulate the electroreceptor as if it was aligned with the exact center of the sphere.

Looming stimuli were generated using the empirically derived model of Chen et al. (2005), for the transdermal potential,

$$V_{tr} = 9.3\chi r^3 x^{-4.8}$$

where χ is the electrical contrast of the object relative to the surrounding tank water, r is the radius of the spherical object and x is the lateral distance to the fish midline. By adjusting the strength of the signal, we were able to simulate the movement of various sized spheres along the lateral axis (r = 0.32 to 0.96 cm). As shown in the main text, the invariance property is not specific to the exact form of the looming stimulus. This is important to the experimental design. Realistically, depending on the location of the looming object relative to the body of the fish, the signal may change its form slightly due to the inhomogeneous nature of the field (Fig. 1A). Additionally, warping of the looming signals may result because of electroreceptor location relative to the dipoles, or the electric field boundary effects present at the interface of the tank water and the air. Independence of the exact form of $s(x)$ assures us that these small variations in looming signal are inconsequential to our results. The fact that the speed-invariance property does not depend on the exact form of our stimulus is also important for generalization of the results to natural electrolocation, where different objects of various sizes, shapes and electrical contrasts will create variations of the signal used in our experiments.

Supplemental text and supporting arguments

A general dilemma for rate coding. The leaky-integrate-and-fire model (LIF) of neural spiking is very useful as a conceptual tool for exploring abstract questions about properties of neural transmission. Its dynamics are given by

$$\tau_m \frac{du}{dt} = -u + RI(t)$$

where u is the membrane potential, τ_m is the membrane time constant, R is the membrane resistance and $I(t)$ is an external input current. Each time the membrane potential reaches a given threshold, an action potential is fired and the membrane voltage is reset to zero. An LIF neuron can be considered as an ideal rate coder, because its firing rate is a linear function of constant stimulus input, creating an invertible mapping from the firing rate to the value of the stimulus. However, what about a dynamic stimulus that varies over some natural time course? By presenting looming stimuli over a range of approach speeds (0.5 to 5 cm/s) we illustrate that the firing rate of this generic neuron is not only influenced by stimulus intensity, but its temporal derivative as well (Fig. S1). We see that the firing rate no longer provides an unambiguous read-out of the stimulus features. This simple model possesses only one timescale - its membrane time constant - which is the product of the membrane resistance (dependent on the ion channels) and membrane capacitance (dependent on properties of the lipid bilayer). The time constant governs the rate at which the input current is transformed into a change in membrane potential and the subsequent generation of action potentials. Intrinsic timescales such as these are an unavoidable consequence of neural transmission, and leave a neuron's stimulus encoding vulnerable to corruption by the way a stimulus evolves in time. This problem of 'temporal constancy' represents a physiological limitation for rate coding.

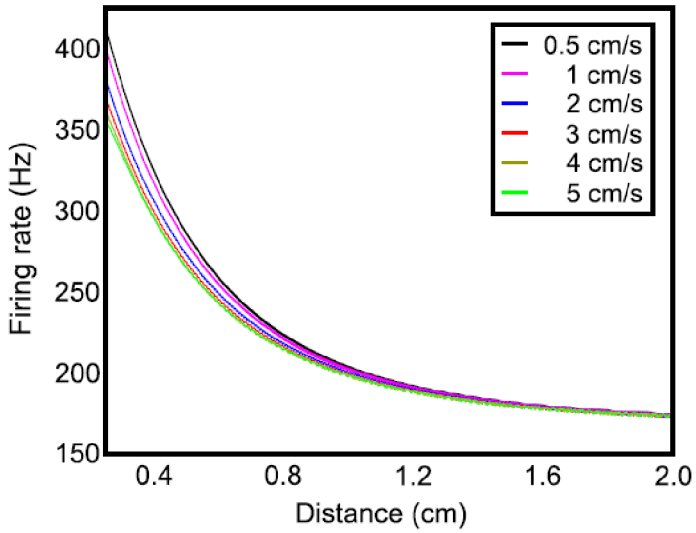

Figure S1 **Responses of a simple LIF neuron to the same looming stimulus for six different approach speeds** An encoding of object distance is warped by approach speed, creating an ambiguous representation of looming object distance in the output firing rate. This illustrates a common problem for a rate code: stimulus intensity and its temporal derivative both influence the firing rate of neurons.

Object size and electroreceptor P-value. To ensure that speed invariance was independent of the overall stimulus intensity, we simulated the movement of various sized spheres (r = 0.32 to 0.96 cm) along the lateral axis. We found speed-invariance for all object sizes tested. Figure S2A shows the change in transdermal potential created by two different sized brass spheres. Figure S2B provides an example of electroreceptor responses for all six speeds, to these two different signals. We also note that speed invariance is not related to individual characteristics of a given electroreceptor. More specifically, each electroreceptor has a P-value, defined as the probability of spiking on one cycle of the electric organ discharge which varies quasi-sinusoidally as a function of time, at frequencies between 600-1000 Hz. For every fish, the population of electroreceptors has a range of P values reflected in their spontaneous firing rates. The neurons shown in Fig. S2B have different P-values, and therefore different firing rates, yet both display speed invariance. This fact was confirmed for all 24 electroreceptor afferents that nearly spanned the entire range of P values [52].

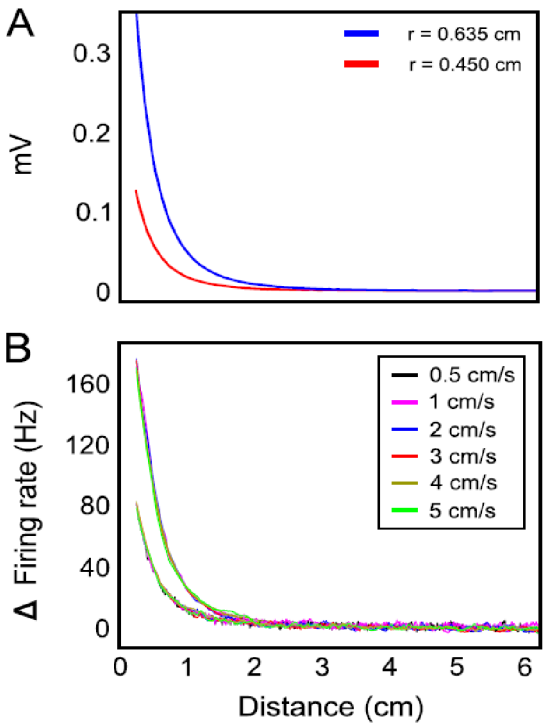

Figure S2 **Speed-invariant responses are independent of object size and electroreceptor P value** A) Model of the changes in the transdermal potential caused by two different-sized looming brass spheres. B) Change in electroreceptor firing rate in response to the two different-sized spheres for speeds of 0.5 to 5 cm/s. The looming signal for a sphere with a radius of 0.635 cm was used to drive an electroreceptor with a baseline discharge of 144.83 Hz, and the looming sphere with a radius of 0.450 cm was simulated for an electroreceptor with baseline firing rate of 108.61 Hz. This demonstrates that the speed-invariance property is independent of object size and does not correlate with electroreceptor P value or spontaneous firing rate.

Exponential adaptation model. Simulations of exponential adaptation were obtained using a previously existing model of electroreceptor activity [56]. The model's original adaptation time constant τ_w was 7.75 ms, which is well suited for high-frequency signals, but might be expected to perform poorly on low frequency electrolocation signals. Therefore, we determined what value of τ_w made the model as close to speed invariant as possible. For time constant increments of 10 ms, model responses to looming stimuli (0 to 0.5 cm/s) were determined and the maximum difference between all 6 curves was calculated as a function of distance. To achieve a scalar measure for each τ_w, these differences were then integrated over the range of distance considered. Finally, we divisively normalized our scalar measure to the largest value obtained for the range of time constants considered, giving us δ as a function of τ_w (Fig. S3A). The bias current and stimulus gain were adjusted to reproduce the observed electroreceptor

firing rates in response to looming stimuli, using 1 cm/s looming data to calibrate the model responses with the best possible adaptation time constant τ_w (420 ms). All other parameters were taken from [56]. Figure S3B shows the exact same plot as Fig. 3A of the main text, but for $\tau_w = 10$ ms. We note that no matter the value of the time constant, there will always be a conflated measure of distance and speed in the output of an exponentially adapting neuron.

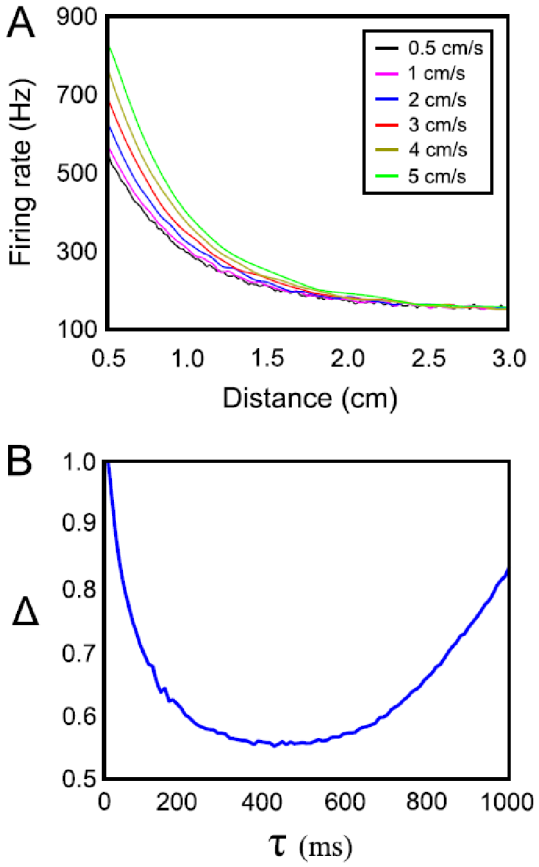

Figure S3 **Approach speed distorts a rate code for object distance** A) Looming responses were generated using a time constant of 10 ms as previously determined for the electroreceptor afferents. The responses show a clear dependence on both distance and approach speed. Large discrepancies in the firing rate occur for distances less than 2 cm, a range very important to the fish during hunting and tracking behavior. B) Maximum difference between model responses was determined across all looming speeds as a function of distance and was then integrated over distance to give a scalar measure of speed-induced discrepancy. This was repeated for a wide range of adaptation time constants to see where the exponential model performed best. The closest the model comes to achieving speed invariance is at 420 ms, which is not close at all (Fig. 3A).

In the main text we state that the exponential adaptation model produced firing rates that are non-separable functions of distance and speed. Let $F(x, v)$ be the rate coding surface for object distance and approach speed, generated by the model responses from Fig. 3A but with

the noise source removed to allow for smoother derivatives. We claim that this function cannot be written in the form $F(x, v) = G(x) \cdot H(v)$, where G and H are arbitrary functions. If this function were separable, the quotient of the partial derivative of F with respect to speed, and F itself, would be independent of lateral axis distance as follows:

$$\frac{F_v}{F} = \frac{G(x)H'(v)}{G(x)H'(v)} = \frac{H'(v)}{H(v)}$$

Figure S4 shows the function $\frac{F_v}{F}$ clearly demonstrating that the firing rate is a multiplicatively non-separable function of speed and distance. We also note that it is not additively separable either, since the mixed partial derivatives are non-zero.

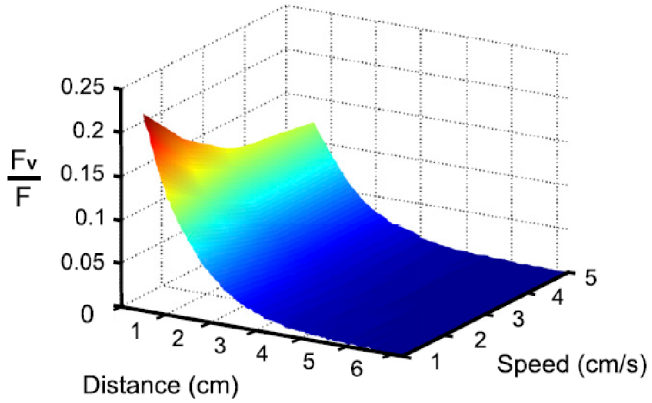

Figure S4 **Exponential model responses are non-separable functions of object distance and approach speed** The partial derivative of the model firing rate, with respect to speed (F_v), is divided by the firing rate (F) and plotted as a function of distance and speed. This plot demonstrates that the responses of Fig. 3A are non-separable functions of these looming stimulus features.

To better understand the dependence of exponentially adapting models on approach speed, consider an exponential spike-response kernel $\eta(t) \equiv e^{-\frac{t}{\tau}}$ in equation (1), where τ corresponds to a single, fixed timescale. In this case we obtain,

$$I_{net} = s(x) - \frac{e^{(\tau v)^{-1}}}{v} \int_{-\infty}^{x} \lambda\left(\frac{x^*}{v}\right) \cdot e^{x-x^*} dx^*$$

Therefore, we see that the faster the looming speed, the smaller the factor $\frac{e^{v^{-1}}}{v}$ becomes, which

reduces the strength of the hyperpolarizing adaptation current. For fixed timescale adaptation, a stimulus with a larger temporal derivative elicits a stronger response than a stimulus of equal intensity but smaller temporal derivative [63, 74]. Note that whether adaptation is subtractive or divisive [98], the adaptation response will always depend on the speed of motion filtered through a single timescale. This is reflected in the model responses of Fig. 3A, which actually implements a form of divisive adaptation; as in the subtractive case, the firing rate increases as a function of speed.

Power law adaptation model. Simulations of power law adaptation were obtained using equation (1), where $\eta(t) = \alpha(\beta + t)^{-1}$. The input current included zero-mean, Gaussian synaptic noise, whose strength was chosen to reproduce the variability seen in the averaged firing rate responses of the electroreceptor afferents. The bias current I_0, and the stimulus gain were adjusted to match the spontaneous and stimulus-induced firing rates respectively (Fig. 2A). The constant β (50 ms) was introduced by Drew and Abbott [64] to prevent $\eta(0)$ from diverging to infinity. This actually introduces a weak dependency of the net current on approach speed as follows:

$$I_{net} = s(x) - c \int_{-\infty}^{x} \frac{s(x^*)}{x - x^* + \beta v} dx^*$$

Looking closely at Fig. 3B, this dependency can be seen when the object is very near the fish's skin, but is otherwise imperceptible. In other words, the spike response kernel chosen by Drew and Abbott is a very suitable approximation to the t^{-1} kernel required for speed invariance.

Averaged percent error. The measure of rate coding error was averaged over data sets from 24 electroreceptor afferent recordings. Figure S5 shows the averaged percent error, as a function of distance, with the line of best fit (y = -0.00017x + 0.98) superimposed. The trend is very weak, suggesting that this error is independent of distance. For this reason we computed the averaged percent error across all speeds and distances, yielding the result of 0.98%.

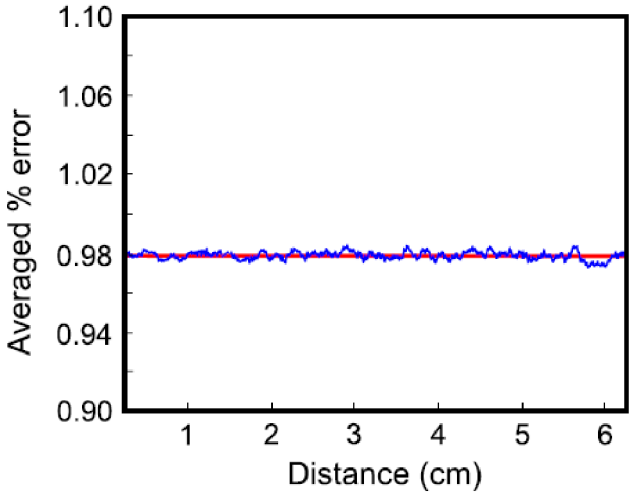

Figure S5 **The percent error in firing rate is independent of the stimulus** The percent error measure shown in Fig. 2C was computed for all 24 electroreceptors and averaged together to get a global error measure as a function of distance. The line of best fit ($y = 0.00017x + 0.98$) is shown in red.

Characteristic frequencies of looming signals. The frequency content of looming signals, simulating approach speeds of 0.5 to 5 cm/s, are shown in Fig. S6. Electroreceptor exponential adaptation has been shown to have a cut off frequency of 23 Hz [60]. At this frequency, a 5 cm/s looming object gives the highest normalized power: a mere 0.0069. Therefore, electrolocation signals will effectively not recruit any fast exponential adaptation, allowing power law adaptation to operate unencumbered in this low frequency signal range.

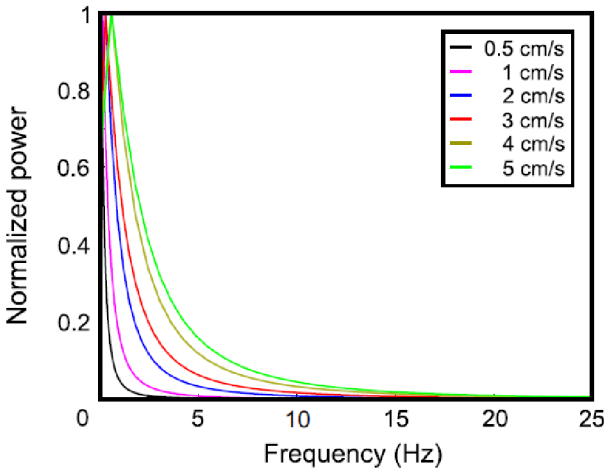

Figure S6 **Low-frequency content of electrolocation signals** The power spectra of looming signals, for speeds of 0.5 to 5 cm/s, were plotted with the power normalized to the largest value obtained for each speed. Electrolocation signals such as these have very little high-frequency content, and thus barely interact with fast exponential adaptation (which has a cut-off frequency of 23 Hz).

Power law adaptation and nonconstant speed invariance. To probe the abilities of power law adaptation further, we tested its ability to produce response invariance for non-constant approach speeds. Fig. S7A shows the responses of the Drew and Abbott model (14) (without noise) to four different looming stimuli: two accelerating and two decelerating. Next, we presented these same stimuli to electroreceptor afferents in vivo (n = 7), confirming that they exhibit an invariant distance-rate code for accelerating looming stimuli (Fig. S7B).

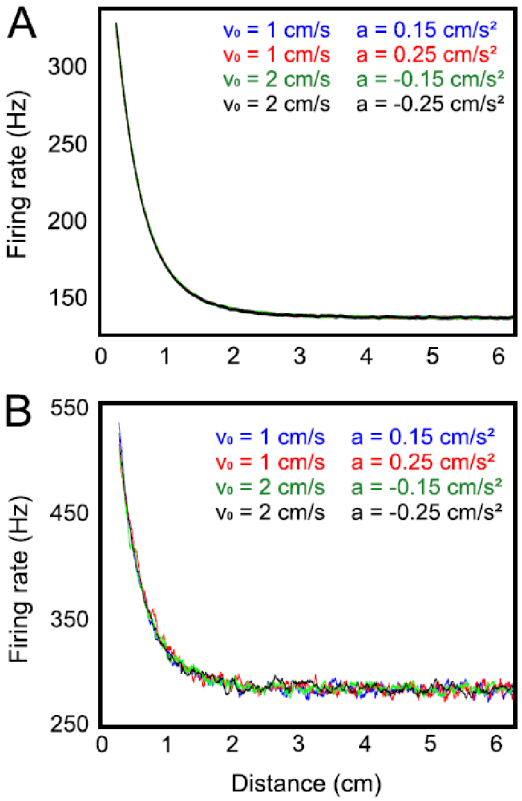

Figure S7 **Power law adaptation permits invariance to constant acceleration** A) Power law model responses to four different looming stimuli that accelerate or decelerate during approach. The time course of the object's position has no effect on the rate coding of object distance, given by $x_0 = 6.25 - v_0 t + \frac{1}{2}at^2$. B) Electroreceptor afferent responses to the same four stimuli demonstrate the ability to maintain a rate code for distance, unhampered by approach speed or acceleration.

Now, consider the lateral axis distance of an object as $x(t) = x_0 + \frac{1}{2}at^2$ such that $dx = at \cdot dt$ and $t = \left[\frac{2(x-x_0)}{a}\right]^{\frac{1}{2}}$, where we assume $x_0 = x(-\infty)$. The adaptation current becomes:

$$
\begin{aligned}
I_{net} &= s(x(t)) - \int_{-\infty}^{t} \eta(t-t^*)s(t^*)dt^* \\
&= s(x) - c\int_{0}^{x+x_0} \eta\Big(\frac{\sqrt{2x}-\sqrt{2x^*}}{\sqrt{a}}\Big)s(x^*)\Big(\frac{2x^*}{a}\Big)^{-\frac{1}{2}}dx^* \\
&= s(x) - \frac{c}{2}\int_{0}^{x} \frac{s(x^*)}{\sqrt{xx^*}-x^*}dx^*
\end{aligned}
$$

The argument of η and the integrand are both proportional to $a^{-\frac{1}{2}}$. By choosing $\eta \equiv t^1$, the adaptation integral depends only on distance and is in agreement with our electrophysiological data and simulations from the power law adaptation model. Again, it is clear that the only suitable choice for the spike response kernel is a power law with an exponent of 1.

Hodgkin-Huxley neurons display power law adaptation. Consistent with a previous report demonstrating that generic Hodgkin-Huxley neurons can account for power law adaptation [66], we find that they can also produce firing rate responses that are nearly invariant to looming speed (Fig. S7). Presumably this ability arises from the voltage dependant time constants associated with the dynamic gating variables which describe channel activation and inactivation. Through channel inactivation, it is likely that a variable threshold for action potential generation accounts for the adaptive effects on firing rate. These model results were obtained using standard parameters of the giant squid axon [99].

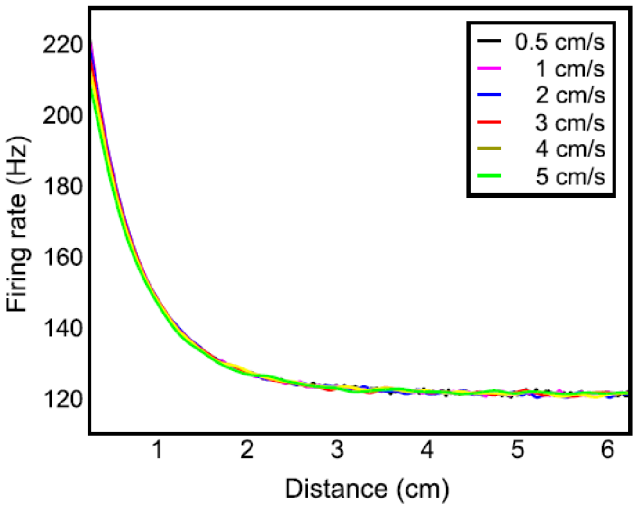

Figure S8 **Hodgkin-Huxley model nearly produces speed-invariance** Hodgkin-Huxley model neuron responses to looming stimuli display invariance to approach speed (0.5 to 5 cm/s) without any adaptation explicitly built into the model. This suggests that power law adaptation is a ubiquitous feature for low-frequency neural processing.

B.2 SI for *The neural dynamics of sensory focus*

Supplementary Note 1 ON/OFF cell spiking is memoryless during motion processing ON and OFF pyramidal cell spiking is highly irregular, which can be seen in the raster plots of Fig. 1a. Supplementary Fig. 1a shows a scatterplot of the coefficient of variation (CV) of each cell's ISIs as a function of their baseline firing rate. Note the mean of the population (0.95), with many cells having a CV near one. This suggests that the spiking of many ON and OFF cells might be reasonably described as a Poisson process (with dead time, that is, no spiking during the action potential refractory period < 3 ms). In the absence of a stimulus (or baseline conditions), histograms of inter-spike intervals (ISIs) recorded from the entire population (Supplementary Fig. 1a) were pooled for ON and OFF cells and are very nearly fit by exponential distributions on the range of observed ISI times, (0.003,0.62) seconds (Figs. 1a, Supplementary Fig. 1b). These facts suggest that treating the baseline spiking of a pyramidal cell population as a Poisson processes is reasonable.

However, the individual ON and OFF cells have a CV that ranges from as low as 0.5 to just over 1.5, indicating that spiking is non-Poisson for many ON and OFF pyramidal cells. Pyramidal cell ISIs may actually arise from a Gamma process [181] (with a scale parameter k that varies from cell to cell); this would account for the observed range of CVs, given by $(\sqrt{k} \cdot \mu_{ISI})^{-1}$, where μ_{ISI} is the ISI sample mean. Despite this fact, the best fits of Gamma distributions were unsatisfying. Furthermore, at baseline, the average serial correlation function between successive ISIs shows weak, yet significant negative correlations (Supplementary Fig. 1c), violating the renewal assumption that is implicit to both Poisson and Gamma processes. It thus appears that baseline pyramidal cell spiking in the ELL, as a whole, cannot be described by common parametric distributions. Therefore, we sought to use survival analysis [181] to develop a simple connection between our empirical firing rates and Fisher's information, as previously done for Poisson spiking neurons (Eq. 1) [178].

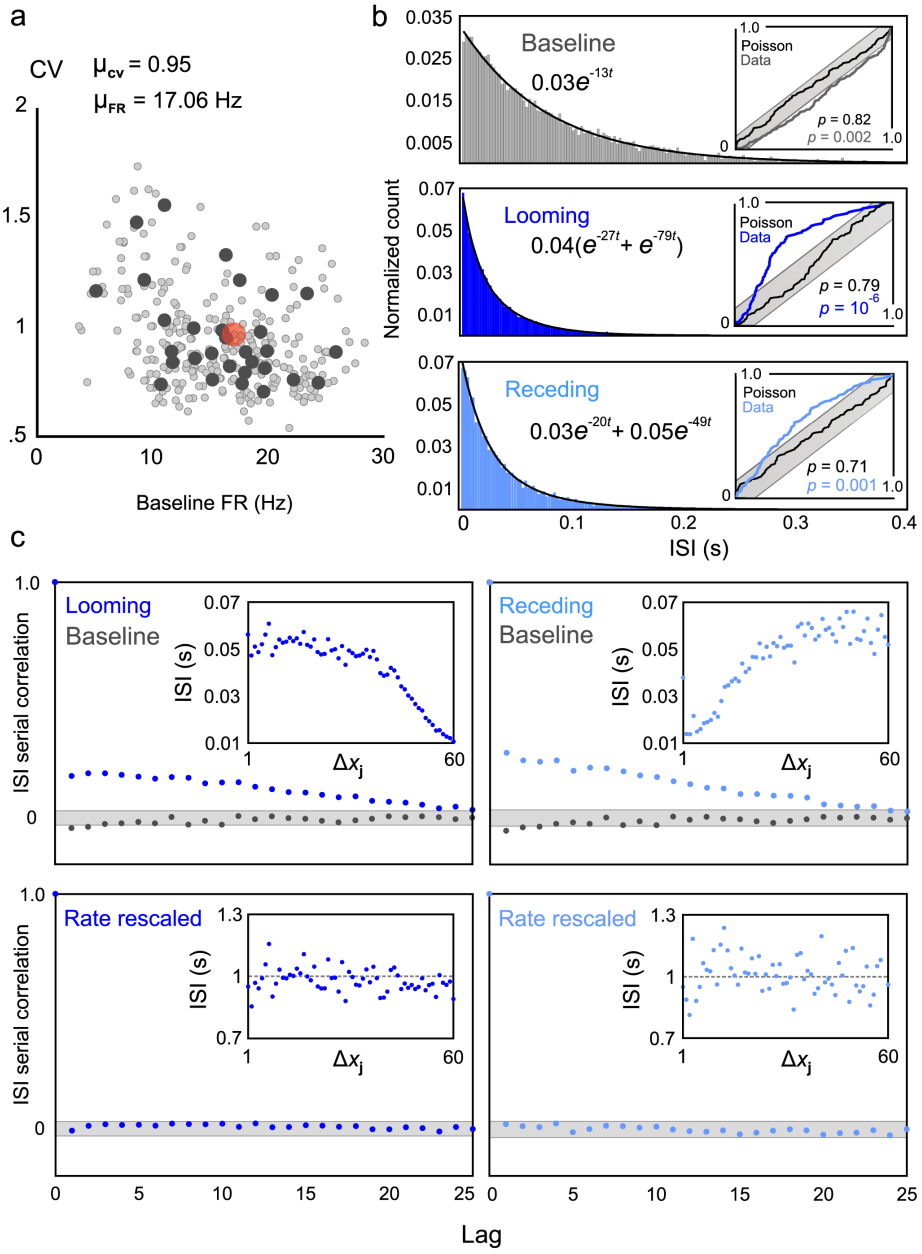

Supplementary Figure 1 **ON and OFF cell statistics during the absence and presence of a motion stimulus** a) Our population average CV (red dot) is plotted against baseline firing rate, along with the average CV values of individual ON and OFF cells used in this study (dark grey; N = 31) and an additional 200 values (light grey) determined from 6 second clips of spontaneous spiking, randomly sampled from the population. b) Best fit exponential (baseline) or sum of exponentials (looming and receding) are shown for the population ISI histograms, where the bin size was chosen to minimize a cost function between the sample histogram and the unknown underlying probability density [190]. Note that here, and in Fig. 1a, the fit neglected the absence of ISIs smaller than the 3 ms refractory period. The discrete time-rescaling theorem was applied to test whether the underlying spiking could be described as a Poisson process — clearly the null hypothesis is rejected (both visually and by the p-values associated with the 99% confidence level, two-way Kolmogorov-Smirnov test. In particular, receding data is included for comparison with the looming and baseline results shown here and in Fig. 1a. c) Our looming and receding stimuli impart strong, positive temporal correlations to the successive ISIs. The insets show the population averaged ISIs within 60 intervals ($\Delta x = 1$ mm) along the distance axis. This stimulus-induced trend is reflected in the ISI serial correlation (SC) functions. Many pyramidal cells show a weak negative correlation in the absence of stimulation, reflected in the population averaged SC (grey bands represent 95% confidence intervals in all plots). The rescaled ISIs during looming and receding motion can be treated as a renewal point process with unit rate.

During stimulus presentation, population ISI distributions show compound exponential behavior (Supplementary Fig. 1b). To demonstrate that individual pyramidal cell spiking is also non-Poisson during stimulation, we applied the discrete time-rescaling theorem [179, 191]. This technique effectively detrends the spiking response. Instead of using the stimulus dependent spike likelihood obtained from a model distribution of spiking (e.g. Poisson or Gamma) [179], we used the population averaged, stimulus induced instantaneous firing rate as a measure of the spike likelihood in a small interval of time. Through this population averaging of spike trains, intrinsic temporal correlations between spikes are removed. When analyzing the spike trains of individual cells, this population-derived conditional likelihood was used to transform the inhomogeneous point process (i.e. a process with time-varying instantaneous rate) into a homogenous point process with unit rate (Supplementary Fig. 1c, insets) [179,191]. Note, in the absence of the stimulus, six second long sequences of ISIs were transformed into a point process with unit rate for each cell using the reciprocal of the average ISI obtained from entire baseline recordings (typically 1-2 minutes). The same procedure, outlined below, was applied for the baseline data, simulated Poisson data, and our looming/receding data. The resulting time series allowed us to explore the statistical characteristics of pyramidal cell spiking.

Procedure The application of the continuous time rescaling theorem [191] has one major drawback for neural data: it relies on the assumption of truly instantaneous events. Since action potentials actually have a 1-2 ms time course, and since data collection/analysis discretizes time, false rejection of the null hypothesis (H_0: ON and OFF cell spiking is not significantly different than realizations of a Poisson point process) is inevitable. When applied to our data, we observed the exact same spurious rejection previously reported ([179]; see Fig. 1 within reference). To avoid potentially false conclusions that the neurons could not be described as a Poisson process, we applied the more recently published revised methods for discrete time [179]. The steps taken to obtain the rescaled ISIs are explicitly written out in Haslinger et al. ([179]see Section 2.4: Discrete Time Version of Time Rescaling Theorem, Procedure for Analytic Correction). After the rate-rescaling step, if the Poisson description of ON and OFF

cell spiking is valid, then our empirical ISIs (τ_k) are now exponentially distributed and arise from a homogenous point process with unit rate. Next, we followed the exact steps outlined in section 2.2 of the original time-rescaling paper [191]. Briefly the rescaled ISIs (τ_k) are further transformed as $z_k = 1 - e^{-\tau_k}$, which yields independent, uniform random variables on the interval (0, 1), assuming the Poisson process description is valid. Next, the z_k are sorted according to length, smallest to largest, and then plotted against the corresponding value of the cumulative distribution function for the uniform distribution, defined as $b_k = \frac{k-0.5}{n}$ for $k =$ 1 to n, where n is the total number of ISIs. If the process is indeed Poisson, then the n points should lie along the 45-degree line, contained within the confidence intervals constructed as $b_k \pm 1.36\sqrt{n}$, a suitable approximation of the distribution for the Kolmogorov-Smirnov (KS) statistic for a 95% confidence level ($\alpha = 0.05$). To generate actual p-values (included in Fig. 1b and Supplementary Fig. 1b) we performed a more stringent two-way KS test between our transformed ISIs and the uniform distribution (99% confidence, $\alpha = 0.01$). As an illustration of the method and for the sake of comparison, simulated realizations from a Poisson process (three seconds, the same duration as our in vivo recordings for $v = 2$ cm/s) were included (Fig. 1b, Supplementary Fig. 1b): in this case, the null hypothesis that spiking was Poisson could not be rejected. This is an important demonstration, since we are analyzing spiking over small intervals of time (on the order of a few seconds) and thus need to ensure that rejection of the null hypothesis obtained for baseline, looming and receding is not related to an under-sampling of the spiking process (previous studies [179, 191] used very long recording samples).

ISI serial correlation and renewal spiking The rescaled ISIs further permitted us to examine potential intrinsic temporal correlations (as observed under baseline conditions) of spike timing during stimulation by removing the confounding temporal correlations induced by our looming and receding stimuli (Supplementary Fig. 1c; top, insets). Importantly, the ON and OFF cell population average loses fine temporal information and is a reflection of the stimulus-induced spike likelihood only; thus, any potential history-dependent effects (i.e. memory) in the individual ISI sequences should remain intact after rescaling. The serial correlation was

computed for the rescaled ISIs of each stimulus trial and then averaged (Fig. 1c and Supplementary Fig. 1c, bottom). Note the insets, showing the rescaled ISIs with unit rate. The averaged serial correlation function indicates that ON and OFF cell spiking can be treated as a time-inhomogeneous renewal point process (memoryless). This indicates that, for an interval of time $\Delta_t = t - t_i$, the chance of observing a spike at time t_{i+1} depends simply on the current value of the stimulus and the timing t_i of the last spike. The renewal assumption is important to the derivation of a relationship to identify the stimulus value that maximizes the Fisher Information of non-Poisson rate coding neurons (Supplementary Note 2).

Supplementary Note 2 Application of Fisher Information to Spiking Neurons The Cramr-Rao bound, the reciprocal of the Fisher Information (I_F), is a lower bound on the variance of an observed random variable, in our case the timing of action potentials, conditioned on a stimulus feature (x) [178]. By finding where I_F is maximal along the transverse distance axis ($x \equiv x(t)$), we seek to identify where a decoder of ON and OFF cell firing rates may, in theory, achieve the best possible estimation of changes in object distance from the observed spiking activity.

The I_F of Poisson spiking neurons: The following is a well-known result, explained without proof in the classic text of Dayan and Abbott [178]. We provide a proof here since the Poisson case is important for understanding our subsequent extension to non-Poisson spiking neurons. Assume that the discrete probability density (f) of observing n spikes in a given interval of time (Δt) is conditional on the value of a stimulus feature (x) and follows the Poisson distribution:

$$f \equiv Pr[n|x;\Delta t] = \frac{(\lambda(x)\Delta t)^n}{n!} \cdot e^{-\lambda(x)\Delta t}$$

where the rate parameter λ is interpreted as the firing rate. The *score* of the likelihood, with

respect to the stimulus feature x, can be determined as follows:

$$\begin{aligned}\frac{\partial}{\partial x}\log f &= \frac{\partial}{\partial x}\big(-\lambda(x)\Delta t + n\cdot(\log\lambda(x)+\log\Delta t-\log n!)\big)\\ &= -\lambda'(x)\Delta t + n\cdot\frac{\lambda'(x)}{\lambda(x)}\\ &= \frac{\lambda'(x)}{\lambda(x)}\cdot\big(n-\lambda(x)\Delta t\big)\end{aligned}$$

where $\lambda' \equiv \frac{d}{dx}\lambda$. Starting with the alternative definition of I_F provided in Dayan and Abbott [178] and using $\lambda(x)\Delta t = \mu$, the mean of the Poisson process, we obtain:

$$\begin{aligned}I_F &= \langle\Big(\frac{\partial}{\partial x}\log f\Big)^2\rangle\\ &= \sum_{n=0}^{\infty} f\cdot\Big(\frac{\lambda'(x)}{\lambda(x)}\cdot\big(n-\lambda(x)\Delta t\big)\Big)^2\\ &= \Big(\frac{\lambda'(x)}{\lambda(x)}\Big)^2\sum_{n=0}^{\infty} f\cdot\big(n-\mu_x\big)^2\\ &= \Big(\frac{\lambda'(x)}{\lambda(x)}\Big)^2\cdot\sigma^2\end{aligned}$$

where σ^2 is the spike count variance over Δt. Since spiking is assumed to be Poisson here, its spike count variance is equal to its mean spike count in the interval Δt and we have an expression for I_F in terms of the firing rate and its spatial derivative:

$$\begin{aligned}I_F &= \Big(\frac{\lambda'(x)}{\lambda(x)}\Big)^2\cdot\mu\\ &= \Big(\frac{\lambda'(x)}{\lambda(x)}\Big)^2\cdot\lambda(x)\Delta t\\ &= \frac{\lambda'(x)^2}{\lambda(x)}\cdot\Delta t\end{aligned}$$

It's clear that a large change in the firing rate, starting from low frequency spiking, is a more reliable indicator of a stimulus feature than when the same rate of change occurs during high

levels of spiking activity. This expression allows for the direct calculation of the Poisson I_F, referred to in the main text and shown in Supplementary Fig. 2.

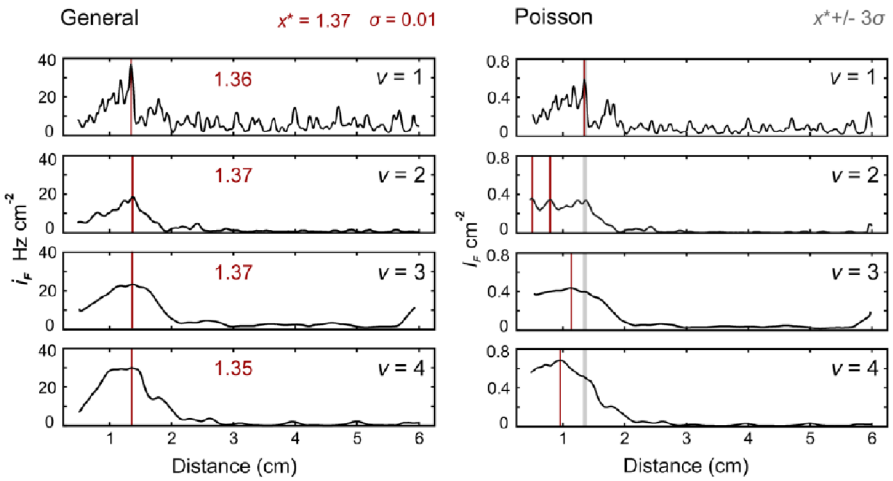

Supplementary Figure 2 **Identification of maximal I_F with a nonparametric versus Poisson relationship** The derived measure for locating the local I_F maxima (i_F, Eq. 1) was applied to the 1 to 4 cm/s looming population data, yielding a mean and standard deviation of 1.37 ± 0.01 cm, presented as x^* in the main text figures. The Poisson case (Eq. 1) is noticeably worse at identifying a consistent maximum; the grey shading in the Poisson panels show three standard deviations about x^*. A time interval of $\Delta t = 10$ ms was used for $v = 1$ and 2 cm/s, whereas $\Delta t = 8$ ms was used for $v = 3$ and 4 cm/s since the peak firing rates exceeded 100 Hz in these cases, causing Eq. 2 to become negative (Fig. 3a; Supplementary Note 2). The choice of 8 versus 10 ms has a negligible effect on the location of maximal I_F, where the spiking rates are still relatively low: the maximum shifts to and 1.39 cm for $v = 3$ cm/s and 1.37 cm for $v = 4$ cm/s. We chose to use the values for $\Delta t = 8$ ms, since it respects the conditions of the theory, while giving even tighter estimates. Importantly, this choice does not impact the paper's conclusions.

Assessing I_F extrema for general spiking statistics: The goal of the following is to generalize the applicability of I_F to electrophysiological data by ridding ourselves of the Poisson assumption, which is unsatisfactory in many important brain regions displaying irregular spike train statistics. In order to describe general, continuous spiking distributions, we turn to survivor analysis and the hazard rate [181]. The likelihood of observing the i^{th} action potential at time t is a continuous random variable with an event (spike) density function $f(t|x) \equiv Pr[t_i = t|x, t_{i-1}]$, conditioned on the time-dependent stimulus feature (object distance in our study). The associated cumulative distribution $F(t|x) \equiv Pr[t_i \in (t_{i-1}, t_{i-1} + t)|x, \{t_n\}_{n=1}^{i-1}]$ gives the probability that the next spike will have occurred by time $t > t_{i-1}$, for a given time course of x and any history-dependent effects in the spiking dynamics generated by the n previous spike times

$\{t_n\} \in (-\infty, t_{i-1}]$. The complement of $F(t|x)$, the 'survivor' function $S(t|x) = 1 - F(t|x)$, describes the probability that a spike will not have occurred by time t. The hazard rate, λ, is formally defined as the rate of spike occurrence in a small interval ($\Delta t \to 0$) and is written as $\lambda(x,t) = \frac{f(t|x)}{S(t|x)}$. This relationship can be well approximated over the short intervals of time (Δt) associated with synaptic transmission, relative to the much longer timescales of motion. When the probability distributions of ISIs are known, one can use the conditional intensity (the trial averaged instantaneous firing rate) to compute $f(t|x)$ directly and then, in turn, compute the hazard rate [181]. However, the underlying ISI statistics of neurons in vivo cannot be characterized by a closed form distribution (e.g. Poisson, Gamma or inverse Gaussian), limiting the applicability of this approach. Furthermore, when determining the conditional event density function we are posed with a serious challenge: smooth motion results in sampling ISIs around instantaneous values of object distance, making it impossible to obtain sufficient numbers of ISIs to properly characterize $f(t|x)$ as a continuous distribution. Note that if we were to leave the stimulus at a fixed position, in an attempt to gather large numbers of ISIs, spike-rate adaptation would largely impact the observed patterns of spiking activity and the resulting hazard would not be applicable to natural motion tracking. To circumnavigate this experimental difficulty, we average the ISIs obtained in many repeated trials as a function of distance, which is the population averaged instantaneous firing rate. In neural spike train analysis, the hazard function for a neuron becomes its theoretical instantaneous firing rate for infinitesimally small intervals [192]. Note that over very small time windows (Δt), the change in position of the stimulus is negligible, and the spiking statistics can be considered stationary with respect to stimulus-induced effects. In other words the timescales associated with spike generation far exceed those of our motion stimuli. This approximation of the hazard rate provides us with a simple and direct connection to our in vivo experiments. After rate-rescaling the ISIs to remove the stimulus-induced correlations, ON and OFF cell spiking can be characterized as a renewal process, that is, the discharge probability depends only on the current stimulus value and the timing of the last spike (t_{i-1}; Fig. 1c and Supplementary Fig. 1c). This implies that the aforementioned cumulative likelihood, determined over the entire history

$(-\infty, t_{i-1})$, is reduced to $F(t|x) \equiv Pr[t_i \in (t_{i-1}, t_{i-1} + t)|x, t_{i-1}]$. For some sufficiently short interval $\Delta t = t - t_{i-1}$, for which only one spike should occur, the cumulative density collapses to the likelihood of observing a single spike, allowing us to approximate it as $F(t|x) \approx \Delta t \cdot \lambda(x, t)$, provided Δt is sufficiently small such that $\Delta t \cdot \lambda(x, t) \leq 1 \ \ \forall \ x, t$. This approximation for small Δt implicitly satisfies the definition of the hazard rate defined in the previous paragraph and is used to simplify the following expression for I_F. Efron and Johnstone have demonstrated a direct connection between the hazard rate and I_F for arbitrary, real-valued probability distributions [193]. Letting λ_x denote the partial derivative of the hazard rate with respect to x, they showed that

$$I_F = \int_{-\infty}^{\infty} \Big[\frac{\lambda_x(x,t)}{\lambda(x,t)}\Big]^2 f(t|x)dt$$

Their expression holds for all regular conditional probability densities $f(t|x)$ on the real line, with corresponding well-defined hazard rates and existing partial derivatives. In order to characterize the ability of a system to encode a stimulus, up until a given moment in time, we assess I_F on the observation interval $(-\infty, t)$. Using the approximating relationship between the hazard rate and the survivor function, we see that

$$\begin{aligned} I_F(t) &= \int_{-\infty}^{t} \Big[\frac{\lambda_x(x,u)}{\lambda(x,u)}\Big]^2 \cdot f(u|x)du \\ &= \int_{-\infty}^{t} \frac{\lambda_x(x,u)^2}{\lambda(x,u)} S(u|x)du \\ &= \int_{-\infty}^{t} \frac{\lambda_x(x,u)^2}{\lambda(x,u)} \big(1 - F(u|x)\big)du \\ &\approx \int_{-\infty}^{t} \frac{\lambda_x(x,u)^2}{\lambda(x,u)} \big(1 - \Delta t \cdot \lambda(x,u)\big)du \end{aligned}$$

Provided Δt is sufficiently small as required above, the integrand of $I_F(t)$ is a strictly positive function $\forall \ x, t \in \mathbb{R}$ and unimodal, implying that the value of x for which the integrand is maximal is also where $I_F(t)$ is maximal. Simply put, when searching for the I_F maximum of a

neuron's tuning curve, we can locate a focal point by identifying the value of the stimulus for which the integrand achieves a maximal value — in our case, object distance along the transverse body axis [0.25, 6.25] cm. This expression contains the same important relationship found for Poisson spiking but is further modified by the approximated survivor function. Applying this formula for 1, 2, 3 and 4 cm/s motion yielded clear estimates of the focal point location. As a validation of the new formula, we compared these responses to the relationship for Poisson spiking neurons (Eq. 1). Supplementary Fig. 2 shows that the Poisson spiking assumption smears the estimate of I_F and makes it difficult to identify one clear maximum. The Poisson formula is relatively more sensitive to slope, which continues to grow rapidly after the onset of bursting and is speed dependent. For example, when applied to 2 cm/s looming data, Eq. 1 still recognizes a local maximum near 1.37 cm but the global maximum on $x \in [0.25, 6.25]$ now occurs at 0.81 cm.

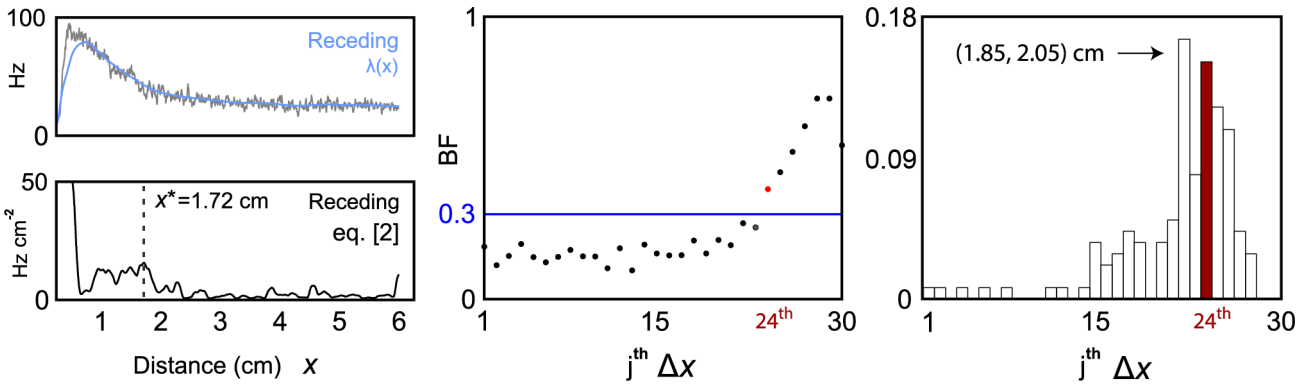

Supplementary Figure 3 **Discontinuous motion shifts the focal point for receding** When long pauses are inserted between looming and receding trials (looming, 7 second pause, receding 10 second pause, repeat) the theory (left) predicts a focal point at 1.72 cm for receding motion. This is reflected in the shifted burst fraction measure to the (1.45, 1.65) cm interval (center) and the probability of a neuron in the population transitioning to the burst state as a function of object distance (right). Notice that this probability distribution is highly reminiscent of Fig. 4c in the main text, except there is now another pronounced maximum in the 22^{nd} interval (1.85, 2.05) cm, reflecting the extra bursty responses not present in the continuous motion trials.

Supplementary Note 3 A simple threshold for burst fraction demarcates the focal point Bursts are often referred to as "informative" without precise meaning; here we explore their direct contribution to stimulus estimation. Both looming and receding motion are marked

by prominent burst spiking, which is noted to occur in the near vicinity of our theoretically identified I_F maximum (Fig. 1a). Thus, we sought to better pinpoint the onset of bursting relative to the focal point, and further test the idea that a downstream decoder could establish a focal point based on a simple bursting criteria. According to previous work [35] the baseline burst probabilities for ON and OFF cells have a mean and standard deviation of 0.25 ± 0.014 and 0.22 ± 0.012 respectively. We started by simply picking a threshold (0.3) significantly greater than these asymptotic estimates (see Fig. 3b) of ON/OFF cell burst fraction (BF). Our reasoning was as follows: first, a BF value of 0.3 infrequently occurs in the ON/OFF cell populations under baseline conditions (Fig. 4c); secondly, extensive bursting across a population of ON or OFF cells could be rapidly detected at this threshold value. With respect to the downstream circuitry, the exact choice of 0.3 is slightly arbitrary but it was inspired by an obvious trend in the data: the burst fraction shoots up after crossing through the focal point region [1.25, 1.45] cm. We looked for a refined BF threshold value that was compatible with our theoretical predictions for 1 to 4 cm/s (shown in Supplementary Fig. 2), described below.

Burst fraction In order to determine when bursting became significantly activated, individual spike trains were separated into tonic (ISI $>$ 10 ms) or burst ($3 <$ ISI $\leq$ 10 ms) spikes [140]. Burst fraction is computed as the number of burst spikes, divided by the total number of combined tonic and burst spikes. In previous work, BF was either determined in the absence of a stimulus or during presentation of stationary signals (e.g. sinusoidal EOD amplitude modulations), and thus the proportion of burst spikes was determined over the entire duration of a recording (on the order of seconds to minutes); for obvious reasons (see Fig. 3b) we refer to this as the asymptotic BF. The estimates of our population asymptotic BF were determined from entire baseline recordings for each cell (ΔT = 60-120 s) and yielded a mean and standard deviation of 0.15 ± 0.11 for ON cells and 0.22 ± 0.12 for OFF cells, consistent with in vitro measurements for the centrolateral map of the ELL [165] and reflecting a good representative sample of ELL pyramidal cells.

For non-stationary ON/OFF cell responses to motion, we are dealing with a BF conditioned

on a time-dependent stimulus; therefore we must count spikes within small intervals of distance (Δx). For our different experimental conditions, this resulted in different time windows (each one calculated as $\Delta T = x/|v|$, where v is object velocity). Figure 3b shows that the estimated baseline BF changes as a function of the time window. Not surprisingly, as $\Delta T \to 0$ the chance of observing a burst event (i.e. multiple spikes) becomes very unlikely and the BF rapidly becomes underestimated compared to the asymptotic estimates. Therefore, when choosing a spatial interval, there is a trade-off to consider. A small Δx gives great spatial resolution but moves ΔT into a range that grossly underestimates the BF. The other extreme is a large ΔT, such that even for the 4 cm/s looming stimulus the estimated BF is somewhat near its asymptotic value (Fig. 3b). This results in poor spatial resolution and quickly begins to defeat the purpose of our analysis — precisely determining the location of an I_F maxiumum. For Figures 3b, 3c and 4b in the main text, $\Delta x = 2$ mm was chosen as the minimal interval that, when divided by our top speed, gave an acceptable ΔT while maintaining good spatial resolution. As shown in Supplementary Table 1, $\Delta x = 2$ mm gave results that were very compatible with Eq. 2, whereas shorter intervals of 1 and 1.5 mm were less reliable. However, when in agreement with the theory, these shorter spatial intervals were useful as they allowed us to compute the intersection of the different Δx and obtain improved spatial resolution for the identification of the focal point.

BF I_F measure	$\Delta T_1 = 0.1/v$	$\Delta T_2 = 0.15/v$	$\Delta T_3 = 0.2/v$	$\bigcap_i \Delta x_i$	Theory
v = 0.5 cm/s	50/60	33/40	25/30	[1.33, 1.35]	-
v = 1 cm/s	50/60	34/40*	25/30	[1.25, 1.3]	1.36
v = 2 cm/s	51/60*	33/40	25/30	[1.3, 1.45]	1.37
v = 3 cm/s	52/60*	33/40	25/30	[1.3, 1.45]	1.37
v = 4 cm/s	49/60	34/40*	25/30	[1.35, 1.45]	1.35
Small (2 cm/s)	52/60*	34/40	25/30	[1.25, 1.3]	-
Recede 0/0 (2 cm/s)	50/60*	33/40	25/30	[1.3, 1.45]	1.39

Supplementary Table 1 **Assessing BF results for varying window lengths** To assess how window length impacted our findings, and to determine which window length was most congruent with the theory, BFs were computed as a function of object distance for three fixed spatial intervals ($\Delta x_1 = 1$ mm, $\Delta x_2 = 1.5$ mm and $\Delta x_3 = 2$ mm). Each entry in the table records the distance interval found just above the BF threshold (0.3) as a ratio of the total number of intervals in which the 6 cm trajectory is subdivided. To avoid underestimating the BF (Fig. 3b), and to account for some discrepancy between the population subsets used for each stimulus condition, the mean was measured for the first third (2 cm) of the approach, where the stimulus is undetectable, and then adjusted to match the mean population BF for its specific time window, $\Delta T = \Delta x/|v|$, determined from all 31 cells used in the study (Methods). Determining where the BF exceeds our threshold for these three different spatial intervals allowed us to compute their intersection and narrow down the predicted location of the I_F maxima (x^*) for each condition, for comparison with the theory. For the cases in which Eq. 2 was applied (1 to 4 cm/s looming and 2 cm/s receding), we found that the BF value lying just above the hard threshold of 0.3 contains the theoretically identified focal point consistently. The burst fraction intervals produced identical results for the 0.5 cm/s looming stimulus, which is in agreement with strong electromotor response behavior at slow speeds [53]. For the finer resolution (1 and 1.5 mm), the time windows grow shorter and underestimation appears to weaken the fidelity of our BF measure. In particular, the instances marked with a red star were omitted from the intersection operation as they generate the null set and stand at odds with the theory and behavior. Since 1 and 1.5 mm bins appear less reliable, we chose 2 mm as our distance interval for the BF analysis in Figs. 3 and 4 of the main text. In the case of the small sphere, both 1 and 1.5 mm predict that the sphere's focal point is actually a bit closer to the skin but still in the range [1.25, 1.35] cm (discrediting the 1 mm interval as per above), just like the $v = 1$ cm/s case. The results for the 1 and 1.5 mm interval may be due to chance, due to underestimation of the BF, to the potential under-stimulation due to more difficult RF alignment (see Methods), or to the limitations of using a hard threshold as opposed to more sophisticated synaptic decoding, hypothesized to occur in vivo. However, the result may also be meaningful since the $d = 0.64$ cm object is the absolute smallest size for which electromotor motion tracking was observed — gymnotiform fish appear uninterested in or unable to continuously track smaller inanimate objects. Therefore, the small object's focal point may be beginning to shift, accompanied by the diminishing behavioral response. Whether a I_F maximum is still important for even weaker stimuli is a question for future work.

Note that $\Delta x = 2$ mm is a reasonable spatial resolution given the standard deviation for the

position of optimal behavioral performance (1.7 mm; Fig. 2b). For each time window ΔT, used in our analysis, a population BF was computed for each of the populations associated with the eight different stimulus conditions, using the first (last) 2 cm of the looming (receding) stimuli, where there are no discernible stimulus effects. These different BF values were then averaged giving a population average BF and standard deviation as a function of the time window. This average value was used to align each stimulus condition's population BF, so that it could be accurately compared with the other cases. This counteracts the drift due to different windows of time associated with each stimulus condition and the fixed spatial interval, as well as any small discrepancies based on the slightly different, though largely overlapping, ON/OFF cell populations obtained for our various stimulus conditions. Our hard threshold of 0.3 was given a small buffer zone of $\pm$ 0.005 for cases, as in a few cases BF values were practically on 0.3. In a concerted effort not to overestimate the BF, we did not adjust the baseline mean of the stimulus condition if it was a standard deviation (ranging from 0.02-0.04 as a function of ΔT) below the population mean from all conditions for that particular time window. This is important because the dependence of the BF estimate on the time window is further influenced by the stimulus distance and the degree of burst activation. In the more activated state, BF is less susceptible to underestimation. This can result in inflated values of the BF near the focal point. The burst fraction plots for the different stimulus conditions are presented in Figs. 3c and 4b. Note that the 25^{th} BF interval spans from 1.25 to 1.45 cm along the distance axis. We found that the 25^{th} interval is consistently just above the threshold and that, from the 25^{th} interval onward, there are substantial speed-dependent increases in the BF. From the figures it is clear that bursting activity is increasing and is detectable in the 25^{th} interval, where the majority of the activated population transitions to the burst state (Fig. 4c). Based on our improved Fisher Information criterion, this is where we find x^*, indicating that optimal estimation is achieved if the animal can maintain a distance near the location of a bifurcation to bursting in the population, where approximately half the units have transitioned to bursting (Fig. 4c).

Our simple burst criterion is used as a means of assessing the relationship between bursting

and optimal stimulus estimation, in addition to extending our analysis to stimulus conditions that cause significantly weaker firing rates (slower speeds or smaller spheres), where the theoretical analysis becomes less practical. This BF threshold of 0.3 was chosen based on our particular sample of the ON/OFF cell population under study and the choice of the burst fraction interval. In reality, we expect that downstream synapses in the midbrain are adapted to baseline burst statistics for a given decoding timescale (Δt) and that, unlike the hard-threshold used in our analysis, a soft dynamic threshold is more likely utilized in freely swimming fish. In addition to BF, encoding BF slope is also likely important. Stimulus intensity could be encoded as relative changes in BF, where the tonic and burst spikes are extracted by facilitating and depressing synaptic dynamics [188, 194]. However, these speculative ideas will require extensive further study and are beyond the scope of this paper.

B.3 SI for *Feedback synthesizes neural codes for motion*

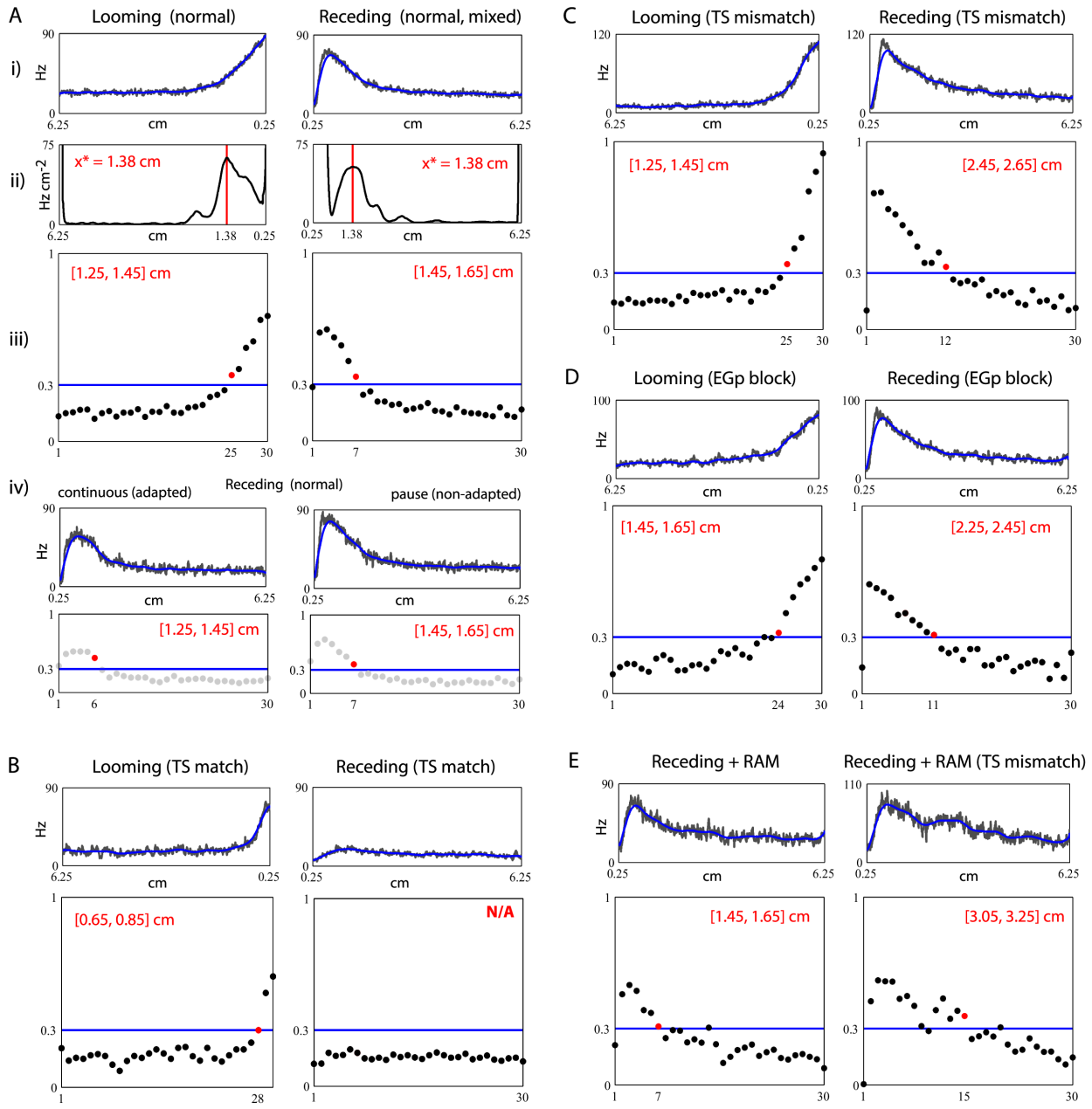

Supplemental Figure 1 **Top-down control of bursting shifts the sensory focus** Related to Figures 2 and 3. The population average firing rates for each condition are plotted in grey and the overlying blue curves are the smoothed firing rates. We applied our methods for determining the distance where Fisher Information (I_F) is maximal [204] which are fully described in the Analysis section of Supplemental Experimental Procedures. At this specific distance, the system can optimally decode object motion and is reflected in a motion tracking behaviour [53]. (A) Normal conditions: i) Looming and receding firing rates (data from Figure 2B, C), containing a mix of continuous and pause motion sequences. ii) Application of Equation 1 (see Supplemental Experimental Procedures), demonstrates that a local maximum in I_F occurs at the distance x* = 1.38 cm in both looming and receding cases. iii) Equation 1 can be difficult to use in practice because it relies on very large data sets to achieve sufficiently smooth estimates of neural tuning; this requirement was met for the normal data (sample sizes listed in Supplemental Experimental Procedures). We have shown that a

simple burst measure can identify x*, allowing us to estimate the focal point location for relatively smaller and more physiologically realistic data sets [204]. The 6 cm distance axis is broken into 30 intervals of 2 mm and the burst fraction (BF) is calculated in each interval to produce a discrete function of distance. The curves are then aligned to the population mean of the normal data (0.15) for comparison between the cases and measuring the relative change in BF. The estimated focal point is found in the first interval sitting above 0.3, a simple threshold that passes above the BF in the 24^{th} interval and below the 25^{th} interval, [1.24, 1.45] cm. For our looming responses, Equation 1 and the BF agree, predicting x* = 1.38 cm and the 25^{th} interval [1.25, 1.45] cm. Although Equation 1 predicts the same distance for receding (x* = 1.38 cm), the BF method predicts the [1.45, 1.65] cm interval instead. Although this is still close and could be attributed to chance, the slight discrepancy is expected since we used primarily pause motion sequences in this paper; the longer the pause between loom and recede, the less the system adapts to repeated stimulation and bursting remains very strong, causing the estimated focal point to shift slightly further from the skin [204]. iv) We illustrate this point by directly comparing the effect of continuous (adapted) versus paused (non-adapted) firing rates. The paused motion protocol (non-adapted burst count; 22 ± 11, N_1=13, N_2 =160) produces more bursts than continuous motion (adapted; 15 ± 10, N_1 =14, N_2 =168; reject H_0, p = 3 x 10^{-8}) and is not significantly different from looming burst counts (24 ± 13, N_1 = 36, N_2 = 507; cannot reject H_0, p = 0.2). Like our control data, the estimated focal point for non-adapted receding falls in the [1.45, 1.65] cm interval. However, the adapted response to continuous motion reduces overall bursting and the estimated sensory focus settles accordingly into the [1.25, 1.45] cm interval. In either case, both measures give close agreement for the location of sensory focus. In the following, we use the physiological BF as our comparative measure for examining the influence of feedback on control of the focal point location. (B) TS block, topographic match: For looming motion, the focal point shifts significantly toward the body, [0.65, 0.85] cm, since removing positive feedback causes significant reduction in burst spiking and the firing rate (Figure 2D). The BF measure is non-applicable for the totally abolished receding response. (C) TS block, topographic mismatch: The BF measure gives good agreement with the control looming case, [1.25, 1.45] cm. However, the focal point for receding shifts much further from the body, [2.45, 2.65] cm, consistent with prominent and sustained burst activity (Figure 3B). (D) EGp block: As noted in the main text, the results of EGp block mirror those of TS but are less exaggerated (Figure 3A). The BF estimates only a slight shift outward for looming, [1.45, 1.65] cm, but the receding response shows a significant shift to the [2.25, 2.45] cm interval. Taken together these results demonstrate that the bifurcation between burst and tonic modes of spiking, associated with the focal point, is established using balanced excitatory and inhibitory feedback through the outer and inner feedback loops. (E) A strong, diffuse RAM stimulus is presented (Figures 3C, S3; see Supplemental Experimental Procedures). Left: Cancellation of this global signal via the inner loop (EGp) occurs during synthesis of the receding response. Remarkably, the focal point is predicted to be in the [1.45, 1.65] cm interval, like the normal control data. In other words, despite the overall inflated proportion of burst spiking, the relative change in BF of 0.15 is preserved. Right: Removing TS activity prevents cancellation. The estimated focal point gets shifted even further from the skin to the [3.05, 3.25] cm interval. Note, the alignment procedure to the population mean of 0.15 was done for focal point comparison; in the RAM cases, the overall BF at all distances is driven much higher. We note that the offset alignment causes an underestimation of the actual peak BF values in the evoked response, but since we are interested in the relative change in BF this is not a problem. Ignoring alignment shifts the focal point even further from the body. Similarly, the matched receding BF in panel B is adjusted from near 0 to 0.15, but still does not even come close to the threshold of 0.3.

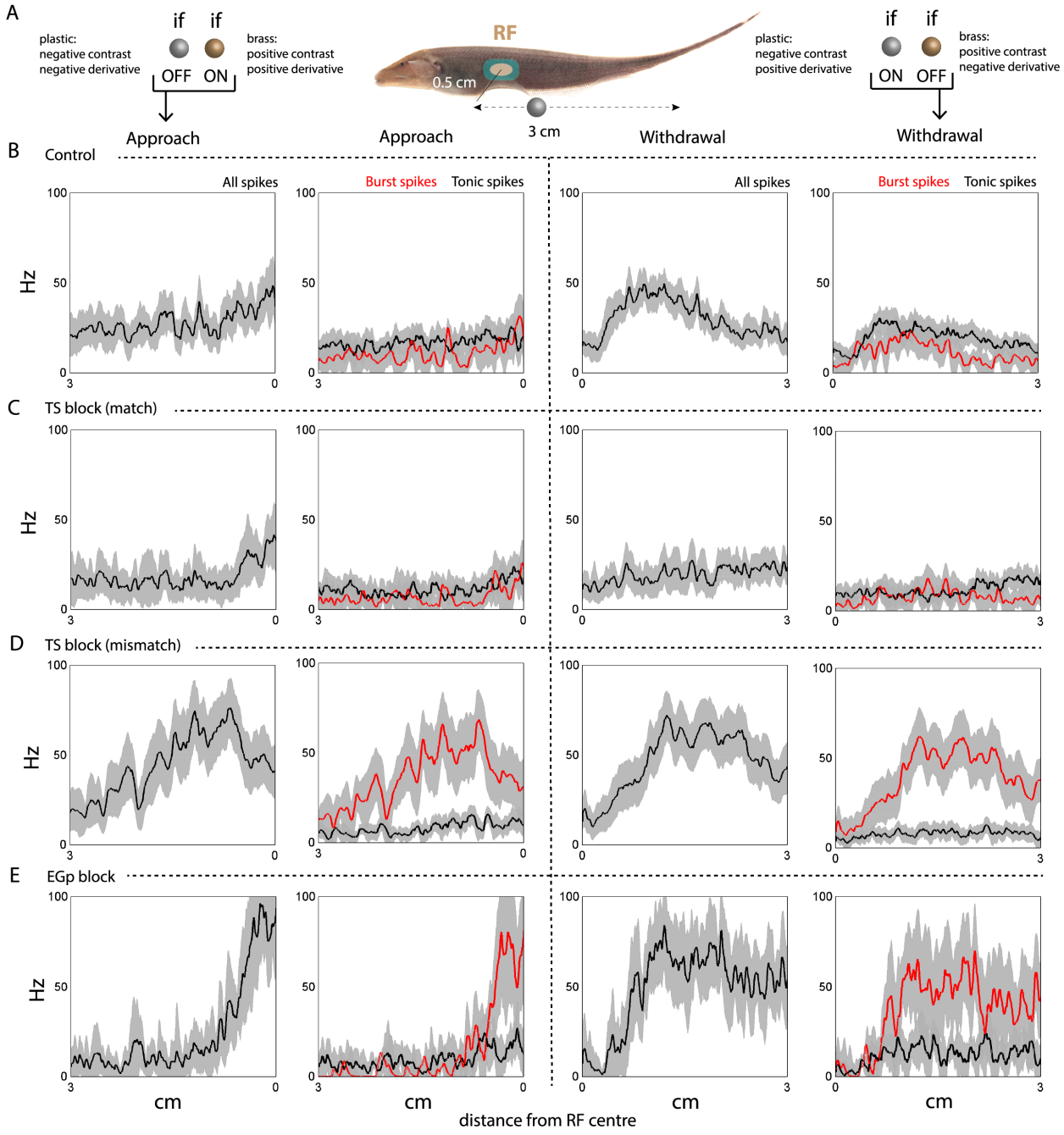

Supplemental Figure 2 **Modulation and synthesis of longitudinal motion responses** Related to Figures 2, 3 and associated text. ON and OFF cell switches in response to motion reversal in the plane orthogonal to the lateral axis, that is, moving across the body surface [140]. Here, approach is defined as the sphere moving into and through the RF surround to the RF center midpoint, while withdrawal is defined as the sphere reversing direction at the midpoint, leaving the RF center, then travelling back through and out of the RF surround. As for the lateral axis motion protocol in main text (see Supplemental Experimental Procedures), the approach stimuli were chosen to be appropriate to the cell identity: a brass sphere was used for an ON cell and a plastic sphere for an OFF cell. The withdrawal stimulus was opposite: a plastic sphere for an ON cell and a brass sphere for an OFF cell. (A) Using the same kinematic parameters, motion was repeated for 3 cm of travel parallel to the rostral-caudal body axis, at a fixed lateral distance of 0.5 cm. (B) Plots of the firing rate and the separated burst and tonic firing rates for approach (replicates, $N_1 = 3$ and repeats, $N_2 = 35$) and withdrawal ($N_1 = 4$, $N_2 = 60$) under normal conditions. Although the evoked responses are smaller for this protocol than the lateral axis, they show the same qualitative switch behaviour and bursting. These results have been previously reported and quantified [140]. (C) A matched TS block produced a reduction of the approach response ($N_1 = 2$, $N_2 = 30$) and elimination of the withdrawal response ($N_1 = 3$, $N_2 = 45$). (D) A mismatched TS block produced massive increases in burst spiking for

approach ($N_1 = 5$, $N_2 = 65$) and withdrawal ($N_1 = 5$, $N_2 = 68$) that demonstrate feedback to ELL must engage strong, local inhibitory control over responses to 3D motion. (E) Blocking EGp (inner loop), also results in large increases in burst spiking and firing rate for approach ($N_1 = 1$, $N_2 = 14$) and withdrawal ($N_2 = 1$, $N_2 = 15$), as expected and shown in previous work [258]. The fact that the EGp block of the inner loop enhances bursting and is entirely opposite to the TS matched injections, confirms that the outer loop must also synthesize a withdrawal response in this plane of motion.

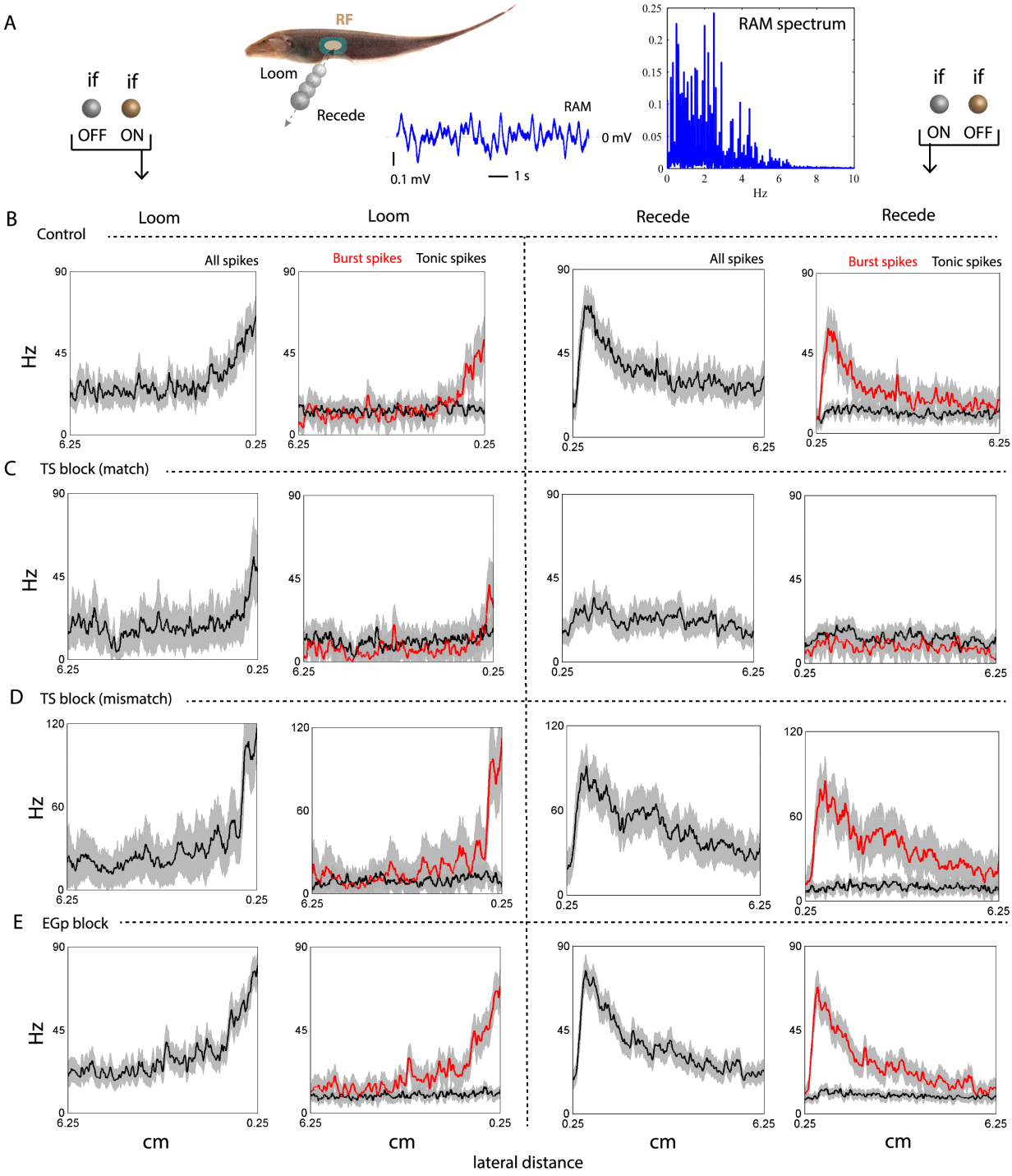

Supplemental Figure 3 **Effects of feedback on motion during a distracting signal** Related to Figure 3. (A) Looming and receding motion along the lateral axis, as presented in main text, was repeated in the presence of a strong, low-pass filtered random amplitude modulation (0-6 Hz RAM; 0.1 mV peak, compared to the peak brass sphere signal of 0.35 mV and minimum plastic signal of -0.18 mV). Sample sizes and comparative statistics for the normal condition and the TS block (mismatch) receding responses are summarized in the *Analysis* section of Supplemental Experimental Procedures with the other main text data sets. Weve included the supporting looming data sets here, as well as the matched TS block and EGp block receding data sets for completeness. (B) Despite the interfering RAM signal, looming ($N_1 = 5$, $N_2 = 68$) and receding responses appear relatively normal since cancellation functions to remove the response to the RAM signal [16, 210]. However, overall burst spiking and firing rates are increased. (C) TS matched blocks reduced the looming response

($N_1 = 2$, $N_2 = 30$) and receding ($N_1 = 3$, $N_2 = 45$) is drastically reduced. (D) The mismatched TS block shows the expected increases in response to both looming ($N_1 = 2$, $N_2 = 30$) and receding, and very poor cancellation of the RAM stimulus, resulting in large distortions of a veridical distance-rate code. Note the change of scale on the dependent axis. (E) Parallel with our main text findings, bilateral blocks of EGp generate stronger firing rates for looming ($N_1 = 9$, $N_2 = 210$) and receding ($N_1 = 13$, $N_2 = 285$) than normal, and bursting is clearly too strong as the RAM can no longer be cancelled.

Supplemental Experimental Procedures

Surgical procedure Surgery was performed under deep general anesthesia on adult male and female gymnotiform fish (Apteronotus leptorhynchus) to expose the caudal cerebellum overlying the hindbrain ELL, as well as the more rostral cerebellum overlying the midbrain TS [259]. A topological anaesthetic was applied to the exposure margins. Immediately following surgery, fish were immobilized with an injection of the paralytic pancuronium bromide (0.2% w/v) that has no effect on the discharge of the electric organ (EOD), which derives from neural tissue and forms the basis of the electrosense. The animal was then transferred into a large tank of water (27◦ C; electrical conductivity kept at approximately 150 μ S cm-1) and a custom holder was used to stabilize the head during recordings. The fishs tail was gently tethered in position with thread to avoid any potential displacement of the body due to small hydromechanical effects caused by looming/receding motion. All fish were monitored for signs of stress while positioning the recording and injection equipment and were allowed to acclimatize before commencing stimulation protocols. Aside from the initial handling, these procedures do not greatly stress the fish, whose parasympathetic response can be inferred from the return of healthy physiological markers such as skin tone and the absence of skin secretions [260]. All surgical and experimental procedures follow the guidelines of *The Society for Neuroscience* and were reviewed and approved by the Animal Care Committee at the University of Ottawa.

Recording and motion protocols Extracellular recordings were taken from the deep, intermediate and superficial ON and OFF pyramidal cells of the centrolateral map of the electrosensory lobe (ELL) [19]. Choice of sample size for our main experimental conditions are discussed below and the number of replicates (N_1) and repeats (N_2) for our different protocols and conditions are listed, along with their associated statistics. Both superficial and intermediate ON and OFF cells of the pyramidal cell layer receive strong feedback and their distinction loosely correlates with features such as firing rate, coefficient of variation, recording depth and the size of their apical dendrites. These cell classes produce the same responses to looming and receding stimuli and are affected in a similar manner by our feedback manipulations; therefore, we grouped them together in our analysis and refer to them as superficial cells for simplicity, distinguishing them from the deep pyramidal cells found at the bottom of the pyramidal cell layer. The deep cells receive very little feedback and produce a qualitatively different receding response. All data presented is for 'superficial ON/OFF cells unless otherwise noted (i.e. Figure 2C, insets). When using our sphere stimuli, we only recorded from cells with receptive fields in the mid-trunk region (30-65% along the rostral-caudal body axis) because of the large flat body surface and electromotor response behaviour (see Figure 2A). Furthermore, the surgical exposure lies above the water level, and, as a result, the air-water boundary effect and plastic mouth tube distort the electric field around the head. The presence of a recording electrode, reference electrode, muscle ground and multiple injection pipettes make it impossible to properly position the brass/plastic spheres (diameter of 1.21 cm) in the receptive field (RF) of cells corresponding to the head region. We mapped the RF center of each superficial pyramidal cell by presenting a local, 5 Hz sinusoidal amplitude modulation with a local stainless steel dipole (2 mm tip separation) [91]. The RFs were roughly oval-shaped and the strongest response was found at the ovoids center; this point is known as the RF center midpoint. Pyramidal cell

responses gradually declined from the midpoint outwards as expected from previous studies [29, 91]. The response was typically minimal at approximately 1 cm from the RF center midpoint in agreement with Bastian et al. [91], but with some variation due to the exact location of the RF center and the size of the fish [29]. At the edge location, there is a balance between electrosensory afferent input to the superficial cells and the surround inhibition due to local ELL inhibitory interneurons [91]. After finding a cells RF center midpoint, we generated step increases and decreases in the local EOD potential to classify the cell as ON or OFF respectively. In many cases, we were able to simultaneously record from ON/OFF cell pairs and directly compare their responses to object motion. Next, according to cell type, a plastic or brass sphere was connected to an electromechanical positioner, which was pre-programmed for the appropriate motion sequence and initiated by outputs from our data acquisition software (Spike2 v7.03; Cambridge Electronic Designs). The selected sphere was aligned with the cells RF centre midpoint along the transverse (lateral) body axis and the leading edge was placed at the initial position, $x_0 = 0.25$ cm from the skin. Note that misalignment with a $\pm$ 0.05 cm degree of error is unavoidable when setting x_0 by using 0.1 cm gradations to measure the position of the spheres leading edge relative to the fishs body. Potential misalignment of the spheres centre with the RF centre is another small, but unavoidable source of error; however, for our sphere size (d = 1.21 cm), the effect of misalignment on the electric image is expected to be negligible since the spheres electric image saturates the RF centers of the CLS map [19]. The sphere was then withdrawn and motion was initiated a few moments later. Stimulation consisted of repetitions of looming and receding sequences along the distance axis [0.25, 6.25] cm, at a speed of 2 cm s^{-1} and an acceleration of 150 cm s^{-2}. These values are within the observed behavioural range as the fish interacts with prey [54]. Motion signals cause strong burst discharge for all cells on each trial and we found that the many consecutive repetitions

could exhaust the cells and lead to reduced discharge or even cell death towards the end of long stimulation protocols that produce heavy bursting. Therefore, we primarily used a motion sequence with a 3 s pause at the skin between looming and receding and another 3 s pause before the next trial. This allowed us to be sure that strong, full receding responses are generated each time and that our main result on receding burst response reduction is not confounded by any adaptive responses to sustained/persistent stimulation, nor dependent on the exact time course between looming and the onset of receding motion. For all the motion protocols, 10 to 15 trials were obtained per cell. Despite our efforts to record from cells whose RF is in the mid-rostral region of the trunk, the bulk of the electrosensory circuitry is biased toward the head. When we inevitably obtained high quality recordings but could not align the motor correctly due to the experimental apparatus, we used a calibrated dipole mimic of the EOD perturbations created by motion at the RF center (brass mimic shown in Figure 2A), multiplied with the real-time EOD signal. Although this AM is an artificial motion stimulus, the model parameters have been carefully determined experimentally [55] and perfectly fit our previously recorded EOD data using the spherical stimulus [104]. The resulting ON/OFF cell responses to the dipole stimuli are very similar. When compared to our normal data sets, the mean burst counts for looming (25 ± 13; $N_1 = 9$, $N_2 = 28$) and receding (19 ± 12; $N_1 = 8$, $N_2 = 25$) mimics are not significantly different from our actual moving spheres according to the two-way KS test, $p = 0.66$ and $p = 0.17$, respectively. For receding motion, 7 of 21 TS matched cells and 2 of 14 TS mismatch cells were stimulated using dipoles; for looming motion, 1 of 36 normal cells, 4 of 9 TS matched cells, and 2 of 14 EGp block cells, were stimulated using the dipole mimic. The global amplitude modulations of the fishes EOD (random and sinusoidal; Figures 3C and S3) were delivered via two long graphite rods (0.5 cm diameter), mounted to the sides of the tank parallel with the fishs rostral-caudal body axis. The desired

amplitude modulation is multiplied with the recorded EOD signal and broadcast globally to activate receptors all over the body [91].

Blocking the feedback pathways Motion protocols were repeated after bilateral pressure injections (100 kPa for 75-100 ms) of CNQX (10 μM) plus AP5 (100 μM) into TS. The location of the TS injections were guided by an atlas of the Apteronotus brain [259], matched to mappings of the ELL to TS projections [43]. With the fish angled at 15 degrees, we inserted a glass pipette (40-60 μm tip) and pressure-injected the drugs at a few depths between 1000 and 1500 μm (2-3 puffs each). Previous studies have shown that these AMPA_R and NMDA_R antagonists are effective in Apteronotus [135, 261]. Our injection settings were calibrated using a low density agarose gel block (0.6%), which lies within an accepted range for mimicking neural tissue [262]. The observed spread from the point of injection had a radius of approximately 0.5 mm after a few minutes; given the length of TS is about 3 to 3.5 mm in diameter, our central blocks may have reached as much as a third of the TS cells, but the fully deactivated area is likely much smaller, as the drug concentration becomes more dilute further from the epicenter. Initially, we also used lidocaine (3% w/v); this was useful in that we were able to observe washout and see responses returning. However, because lidocaine significantly wears off after a few minutes, it is hard to obtain stable effects and requires many injections that cause unnecessary tissue damage. By comparison, injection of CNQX and AP5 caused long-term effects ($>$ hour). Although washout was rarely achieved, we were able to gather complete motion protocols and highly stable results. The CNQX/AP5 results were concordant with the initial results of the lidocaine injection and are used exclusively for our analyses. Inactivation of the ipsilateral EGp was carried out by lidocaine injections to the superficial nP fiber bundle as previously reported [263, 264]. These injections are administered directly into a dense white

matter bundle lying near the surface of the brain to completely inactivate the ipsilateral inner loop; injections were reapplied as needed in order to maintain the block of action potential propagation. Additionally, the contralateral EGp projection to the ELL was blocked via a 400-500 μm deep cut through the commissural fibers [265] using an ultra-fine razor blade, controlled by a micromanipulator. This combined approach yielded a complete bilateral block of inner loop (indirect) feedback.

Analysis All data analyses were performed using custom and default Matlab scripts. Data trials were only excluded when external noise was present in a recording or if a cell showed pathological signs of activity or recording degradation, which may occur due to cell fatigue, damage, anoxic stress or after multiple reinjections of drug. To compute firing rates for Figures 2, 3, S2 and S3, individual spike trains were convolved with a minimal 10 ms exponential filter (synaptic filtering timescales). The individual FRs were then averaged together to obtain the mean FR and were plotted over the populations standard error (grey shading). Spike sequences were classified as bursts if their inter-spike interval (ISI) was $\leq$ 10 ms [35, 44, 204, 266]. Spike trains were separated accordingly to compute tonic and burst firing rates (Figures 2, 3 and S2, S3) since burst spiking in particular is affected by the feedback blocks, while the tonic spiking appears to be mostly driven by the bottom-up signal from the electrosensory afferents. For this reason, we opted to simply count the burst spikes within the interval [0.25, 1.25] cm when comparing motion responses under the various experimental conditions. The means appear as red numbers in the beige shaded area of main text Figures 2C, D and 3A-C. For the control looming and receding cases, an instantaneous population firing rate $\lambda(x, t)$, conditioned on object position (x), was determined by averaging individual firing rates obtained from both ON and OFF cells in response to 2 cm/s motion. Looming and receding firing rates were

smoothed with two short duration moving average filters (175 ms span; Figure S1) to dampen noisy fluctuations in the mean firing rate and allowed us to cleanly estimate the distance from the skin at which Fisher Information (I_F) is locally maximal on the distance axis, [0.25, 6.25] cm, reflecting the potential for optimized estimation of motion parameters from a mid-brain decoder (see Figure S1) [204]. This function was then substituted into our formula to locate (I_F) maxima (for a short decoding window $\Delta t = 10$ ms [204]):

$$\frac{\lambda_x(x,t)^2}{\lambda(x,t)}(1 - \Delta t \cdot \lambda(x,t)) \tag{1}$$

The curves resulting from Equation 1 were then smoothed once more with a short 100 ms moving average filter. The optimized distance was also identified using the burst fraction (BF): quotient of the number of burst spikes and total number of spikes [204], sampled in intervals of 2 mm along the distance axis (6 cm = 30 intervals). Previously, we found that if we aligned the tails of the sampled BFs to the population average (0.15 for 2 cm/s motion and 2 mm, 100 ms intervals), for direct comparison between experimental conditions, the focal point could be predicted using a simple threshold of 0.3 (Figure S1) [204]. This reflects the importance of the relative change in BF to a hypothetical downstream decoder. Note, if there are no burst or tonic spikes, an ill-defined 0/0 BF arises, which is valued at 0 by convention, as it reflects the absence of burst activity. For baseline discharge (no stimulation), we binned recordings of varying duration, typically between 1-2 minutes, into 500 ms intervals and sampled the BF in each time-window to determine a mean and standard deviation for each cell. Sampling the burst fraction in time windows, as opposed to the standard use of the entire recording, is important since our injection can cause abnormal periods of silence lasting for many seconds - an extremely rare occurrence in our population of superficial ON/OFF cells with mean firing rates of approximately 9-22 Hz. Using the entire recording to count burst

and tonic spikes will not capture this event. Given the 2 cm/s motion protocol, 500 ms was chosen to be compatible with the spatial scale (1 cm) and the significant response events over the timescales of motion (note 1 cm was also chosen for burst count comparisons). The means of each cell were then averaged together and these population values were used to compare between the effects of different feedback blocks on spontaneous activity (listed below). All comparative statistics for BF (baseline) and burst count (motion) were assessed using the non-parametric, two-way Kolmogorov-Smirnov test, $\alpha = 0.01$, whose null hypothesis (H_0) states that two empirical data sets are drawn from the same continuous distribution, while making no underlying assumptions about the distribution itself (e.g. normality or equality of variance). The mean firing rates presented in Figures 2, 3, S1, S2 and S3 are plotted over their standard error (95% confidence intervals). To detect the hypothesized differences in the mean burst counts between our experimental conditions, we applied the following formula as a guide for sample size for our main conclusion (Figure 2C, D):

$$n = 1 + 2C \cdot \left(\frac{\sigma}{E}\right)^2$$

where C is dependent on values chosen for a specific significance level (α) and power (1-β) [267]. This simple formula, derived from the t-test, can be used to compute sample size when power, significance level, hypothesized difference in means (the effect), and standard deviation of the population means are specified. In our case, the continuous random variable is the mean burst spike count from each recorded neuron and the main hypothesized effect is a complete reduction of receding response burst spiking (18.7 $\pm$ 9.8 bursts to 0 bursts) after blocking feedback. For a significance level of 0.05 and a statistical power of 90%, 10.51 is the value of C [267], and an estimated minimum of 7 recorded neurons are required for replicates (N_1). For the main data presented in the paper (Figures 2C, D and 3A, B), we exceed this number.

With many repeats (N_2) per recording, our total spike train data sets provide a strong statistical sample. Our longitudinal motion (Figure S2) and motion/RAM (Figure S3) data sets are slightly smaller, as the effects were mostly anticipated from our main results (Figure 2C, D and 3A, B) and previously published work on EGp. Other data sets include the looming ($N_1 = 7$, $N_2 = 97$) and receding deep pyramidal cell responses ($N_1 = 11$, $N_2 = 184$) and the example cell cancellation ($N_1 = 1$; pre $N_2 = 44$, post $N_2 = 332$) to the 5 Hz sinusoidal amplitude modulation in Figure 3C (i), which is only intended to illustrate a well-known electrosensory cancellation result, setting up the motivation for Figure 3C (ii). We comprehensively list the sample sizes and associated comparative burst count statistics here for our different main text feedback block protocols.

Looming normal: 24 ± 13, $N_1 = 36$, $N_2 = 507$.

Looming EGp block: 27 ± 8, $N_1 = 14$, $N_2 = 210$. Looming burst counts during EGp block are significantly greater than normal (reject H_0, p = 3 x 10^{-8}).

Looming TS block (match): 13 ± 8, $N_1 = 9$, $N_2 = 132$. Looming burst counts during TS match are significantly less than normal (reject H_0, p = 2 x 10^{-16}) and EGp block (reject H_0, p = 3 x 10^{-31}).

Looming TS block (mismatch): 27 ± 11, $N_1 = 10$, $N_2 = 145$. Looming burst counts during TS mismatch are significantly greater than normal (reject H_0, p = 6 x 10^{-3}) and TS match (reject H_0, p = 4 x 10^{-20}), but not significantly different from the EGp block (cannot reject H_0, p = 0.08).

Receding normal: 19 ± 10, N_1 =33, N_2 =463.

Receding EGp block: 25 ± 10, N_1=20, N_2=285. Receding burst counts during EGp block are significantly greater than normal (reject H0, p = 4 x 10^{-13}).

Receding TS block (match): 2 ± 3, N_1=21, N_2=300. Receding burst counts during TS match are significantly less than normal (reject H_0, p = 4 x 10^{-106}) and EGp block (reject H_0, p = 3 x 10^{-117}).

Receding TS block (mismatch): 30 ± 11, N_1=14, N_2=16. Receding burst counts during TS mismatch are significantly greater than normal (reject H_0, p = 4 x 10^{-20}), TS match (reject H_0, p = 4 x 10^{-85}), and EGp block (reject H_0, p = 8 x 10^{-8}).

Receding normal + RAM: 21 ± 7, N_1 = 7, N_2 = 100. Receding burst counts for motion, in the presence of a strong global RAM are not significantly greater than normal (cannot reject H_0, p = 0.02).

Receding TS block (mismatch) + RAM: 28 ± 7, N_1=4, N_2=60. Receding burst counts during TS mismatch and strong global RAM are significantly greater than normal, both in the presence (reject H_0, p = 8 x 10^{-9}) and absence of the RAM stimulus (reject H_0, p = 6 x 10^{-12}).

Baseline BF (normal): 0.21 ± 0.07, N_1 = 18. Note the average population BF is higher than 0.15, since here we used 500 ms, whereas motion recordings used 100 ms bins. The monotonic

increasing and saturating relationship between the magnitude of the BF and the choice of time bin has been previously published [204].

Baseline BF EGp block: 0.04 ± 0.04 $N_1 = 20$. Burst fraction during baseline, sampled within 500 ms windows, is significantly reduced by the EGp block (reject H_0, p = 8.8 x 10^{-8}), as previously reported [258].

Baseline BF TS block (match + mismatch): 0.04 ± 0.04, $N_1 = 33$. After matched and mismatched TS block, there was a substantial decrease in BF to 0.04 ± 0.04 ($N_1 = 13$) and 0.06 ± 0.05 ($N_1 = 15$) respectively. The null hypothesis that the matched and mismatched BF estimates are drawn from the same continuous distribution could not be rejected (p = 0.052); therefore, the TS blocks were grouped together, along with 5 other TS block cases where motion was not performed. This combined TS block data shows a substantial reduction compared to normal (reject H_0, p = 1.5 x 10^{-9}) but is not significantly different from EGp blocks (cannot reject H_0, p = 0.99). The fact that the TS block accounts for the entire EGp block result strongly suggests that TS controls the inner loop circuitry to establish spontaneous levels of bursting.

Note: After a few rounds of recording and TS injections, some subsequently recorded cells display a high baseline burst fraction (0.53 ± 0.18). These values are well outside the expected range of the recorded pyramidal cells under normal conditions and have never been observed previously. Furthermore, they are completely opposite to the reduction in spontaneous bursting displayed by the bulk of our data, although we have no pre-injection comparison as this does not happen normally. Although the proportion of burst spikes in these cells are higher

than normal ($N_1 = 19$: reject H_0, p = 1.5 x 10^{-9}), there is also less tonic spiking and the average firing rates are not significantly different (cannot reject H_0, $\alpha = 0.05$, p = 0.54). When entrained by the stimulus, these cells produced the expected result for looming and receding motion and could be subsequently blocked. Therefore, if a cell displayed an unexpectedly high baseline BF it was not excluded from our motion data sets.

Code and data availability: Custom code, figure source data and associated materials can be made available to interested readers upon request to the corresponding author.

Bibliography

[1] Lamb TD, Collin SP, Pugh EN (2007) Evolution of the vertebrate eye: opsins, photoreceptors, retina and eye cup. Nat Rev Neurosci, 8(12): 960-976.

[2] Shinomiya K, Takemura SY, Rivlin PK, Plaza SM, Scheffer LK, Meinertzhagen IA (2015) A common evolutionary origin for the ON-and OFF-edge motion detection pathways of the Drosophila visual system. Front Neural Circuits, 9.

[3] Suzuki, H., Thiele, T. R., Faumont, S., Ezcurra, M., Lockery, S. R., Schafer, W. R. (2008) Functional asymmetry in Caenorhabditis elegans taste neurons and its computational role in chemotaxis. Nature, 454(7200), 114-117.

[4] Thiele TR, Faumont S, Lockery SR (2009) The neural network for chemotaxis to tastants in Caenorhabditis elegans is specialized for temporal differentiation. J Neurosci 29(38): 11904-11911.

[5] Clarke SE, Longtin A, Maler L. Contrast coding in the electrosensory system: parallels with visual computation. Nat Rev Neurosci 16: 733-744, 2015.

[6] New JG, Coombs S, McCormick CA, Oshel PE. (1996) Cytoarchitecture of the medial octavolateralis nucleus in the goldfish, Carassius auratus. Journal of Comparative Neurology, 366(3), 534-546.

[7] Modrell MS, Bemis WE, Northcutt RG, Davis MC, Baker CV. (2011) Electrosensory ampullary organs are lateral line placode-derived in bony fishes. Nat Comm, 2:496.

[8] McCreery DB (1977) Two types of electroreceptive lateral lemniscal neurons of the lateral line lobe of the catfish Ictalurus nebulosus; connections from the lateral line nerve and steady-state frequency response characteristics. J Comp Physiol A, 113(3): 317-339.

[9] MacIver MA, Schmitz L, Mugan U, Murphey TD, Mobley CD. (2017) Massive increase in visual range preceded the origin of terrestrial vertebrates. PNAS 114 (12): E2375-E2384.

[10] Pinker S (2010) The cognitive niche: Coevolution of intelligence, sociality, and language. PNAS 107(2): 8993-8999.

[11] Marcus G (2009) How Does the Mind Work? Insights from Biology. Top Cogn Sci, 1: 145-172

[12] Wagner A (2011) The molecular origins of evolutionary innovations. Trends in Genetics, 27(10): 397-410.

[13] Berman, N.J., and Maler, L. (1999). Neural architecture of the electrosensory lateral line lobe: adaptations for coincidence detection, a sensory searchlight and frequency-dependent adaptive filtering. J. Exp. Biol. 202, 1243-1253.

[14] Spruston N. (2008) Pyramidal neurons: dendritic structure and synaptic integration. Nature Reviews Neuroscience, 9(3), 206-221.

[15] Bratton B, Bastian J (1990) Descending control of electroreception. II. Properties of nucleus praeeminentialis neurons projecting directly to the electrosensory lateral line lobe. J. Neurosci. 10(4): 1241-1253.

[16] Bastian J, Chacron MJ, Maler L. Plastic and nonplastic pyramidal cells perform unique roles in a network capable of adaptive redundancy reduction. Neuron 41: 767-779, 2004.

[17] Fotowat H, Harrison RR, Krahe R (2013) Statistics of the electrosensory input in the freely swimming weakly electric fish Apteronotus leptorhynchus. J. Neurosci. 33(34): 13758-13772.

[18] Geisler WS (2008) Visual perception and the statistical properties of natural scenes. Annu Rev Psychol, 59: 167-192.

[19] Krahe R, Maler L (2014) Neural maps in the electrosensory system of weakly electric fish. Curr. Opin. Neurobiol. 24: 13-21.

[20] Chacron MJ, Longtin A, Maler L (2011) Efficient computation via sparse coding in electrosensory neural networks. Curr Opin Neurobiol 21: 752-760.

[21] Marsat G, Longtin A, Maler L. Cellular and circuit properties supporting different sensory coding strategies in electric fish and other systems. Curr Opin Neurobiol 22: 1-7, 2012.

[22] Purves D, Wojtach WT, Lotto RB (2011) Understanding vision in wholly empirical terms. Proc Natl Acad Sci USA 108: 15588-15595.

[23] Gabbiani F, Krapp HG, Laurent G (1999) Computation of object approach by a wide-field, motion-sensitive neuron. J Neurosci 19: 1122-1141.

[24] Sun HJ, Frost BJ (1998) Computation of different optical velocities of looming objects. Nat Neurosci 1(4): 296-303.

[25] Yang SCH, Wolpert DM, Lengyel M (2016) Theoretical perspectives on active sensing. Curr Opin Behav Sci 11: 100-108.

[26] Stamper, S.A., Roth, E., Cowan, N.J., Fortune, E.S. Active sensing via movement shapes spatiotemporal patterns of sensory feedback. J. Exp. Biol. 215, 1567-1574 (2012).

[27] Yovel, Y., Falk, B., Moss, C.F., Ulanovsky, N. Optimal localization by pointing off axis. Science 327, 701-704 (2010).

[28] Louis, M., Huber, T., Benton, R., Sakmar, T.P., Vosshall, L.B. Bilateral olfactory sensory input enhances chemotaxis behavior. Nat. Neurosci. 11, 187-199 (2007).

[29] Maler L (2009) Receptive field organization across multiple electrosensory maps. I. Columnar organization and estimation of receptive field size. J Comp Neurol 516(5): 376-393.

[30] Maler L. The posterior lateral line lobe of certain gymnotiform fish. Quantitative light microscopy. J Comp Neurol 183: 323-363, 1979.

[31] Bastian J (1981) Electrolocation. II. The effects of moving objects and other electrical stimuli on the activities of two categories of posterior lateral line lobe cells in Apteronotus albifrons. J. Comp. Physiol. A 144: 481-494.

[32] Berman NJ, Maler L (1998) Inhibition evoked from primary afferents in the electrosensory lateral line lobe of the weakly electric fish (Apteronotus leptorhynchus). J. Neurophysiol. 80(6): 3173-3196.

[33] Maler L, Mugnaini E (1994) Correlating gammaaminobutyric acidergic circuits and sensory function in the electrosensory lateral line lobe of a gymnotiform fish. J. Comp. Neurol. 345(2): 224-252.

[34] Maler L, Sas EK, Rogers J (1981) The cytology of the posterior lateral line lobe of highfrequency weakly electric fish (gymnotidae): Dendritic differentiation and synaptic specificity in a simple cortex. J. Comp. Neurol. 195(1): 87-139.

[35] Bastian, J., Nguyenkim, J. Dendritic modulation of burst-like firing in sensory neurons. J. Neurophysiol. 85, 10-22 (2001).

[36] Sproule MK, Chacron MJ (2017) Electrosensory neural responses to natural electrocommunication stimuli are distributed along a continuum. PloS One 12(4): e0175322.

[37] Oswald, A.M., Lewis, J.E., and Maler, L. (2002). Dynamically interacting processes underlie synaptic plasticity in a feedback pathway. J. Neurophysiol. 87, 2450-2463.

[38] Chacron MJ, Bastian JA. Population coding by electrosensory neurons. J Neurophysiol 99: 1825-1835, 2008.

[39] Krahe R, Gabbiani F (2004) Burst firing in sensory systems. Nat. Rev. Neurosci. 5(1): 13-23.

[40] Turner RW, Maler L, Deerinck T, Levinson SR, Ellisman MH. TTX sensitive dendritic sodium channels underlie oscillatory discharge in a vertebrate sensory neuron. J Neurosci 14: 6453-6471, 1994.

[41] Fernandez, F.R., Mehaffey, W.H., Turner, R.W. Dendritic Na+ current inactivation can increase cell excitability by delaying a somatic depolarizing after-potential. J. Neurophysiol. 94, 3836-3848 (2005).

[42] Doiron, B., Laing, C., Longtin, A., Maler, L. Ghostbursting: a novel neuronal burst mechanism. J. Comput. Neurosci. 12, 5-25 (2002).

[43] Carr, C.E., Maler, L., Heiligenberg, W., and Sas, E. (1981). Laminar organization of the afferent and efferent systems of the torus semicircularis of gymnotiform fish: Morphological substrates for parallel processing in the electrosensory system. J. Comp. Neurol. 203, 649-670.

[44] Oswald A-M, Chacron MJ, Doiron B, Bastian J, Maler L (2004) Parallel processing of sensory input by bursts and isolated spikes. J. Neurosci. 24(18): 4351-4362.

[45] Mehaffey, W.H., Fernandez, F.R., Maler, L. Turner, R.W. Regulation of burst dynamics improves differential encoding of stimulus frequency by spike train segregation. J. Neurophysiol. 98, 939-951 (2007).

[46] Noonan L, Doiron B, Laing C, Longtin A, Turner RW (2003) A dynamic dendritic refractory period regulates burst discharge in the electrosensory lobe of weakly electric fish. J. Neurosci. 23(4): 1524-1534.

[47] Laing, C.R., Doiron, B., Longtin, A., Noonan, L., Turner, R.W. Maler, L. Type I burst excitability. J. Comp. Neurosci. 14, 329-342 (2003).

[48] Laing CR, Longtin A. (2002). A two-variable model of somatic-dendritic interactions in a bursting neuron. Bulletin of Mathematical Biology 64(5): 829-860.

[49] Lemon, N., Turner, R.W. Conditional spike backpropagation generates burst discharge in a sensory neuron. J. Neurophysiol. 84, 1519-1530 (2000).

[50] Mehaffey, W.H., Doiron, B., Maler, L. Turner, R.W. Deterministic multiplicative gain control with active dendrites. J. Neurosci. 25, 9968-9977 (2005).

[51] Fairhall AL et al. (2006) Selectivity for multiple stimulus features in retinal ganglion cells. J Neurophysiol 96: 2724-2738.

[52] Gussin D, Benda J, Maler L (2007) Limits of linear rate coding of dynamic stimuli by electroreceptor afferents. J Neurophysiol 97: 2917-2929.

[53] Heiligenberg W (1973) Electrolocation of objects in the electric fish Eigenmannia (Rhamphichthyidae, Gymnotoidei). J Comp Physiol 87: 137-164.

[54] MacIver MA, Sharabash MA, Nelson ME (2001) Prey-capture behavior in Gymnotid electric fish: motion analysis and effects of water conductivity. J Exp Biol 204: 543-557.

[55] Chen L, House JL, Krahe R, Nelson ME (2005) Modeling signal and background components of electrosensory scenes. J Comp Physiol A 191: 331-345.

[56] Chacron MJ, Longtin A, St-Hilaire M, Maler L (2000) Suprathreshold stochastic firing dynamics with memory in P-type electroreceptors. Phys Rev Lett 85(7): 1576-1579.

[57] Chacron MJ, Longtin A, Maler L (2001) Negative interspike interval correlations increase the neuronal capacity for encoding time-dependent stimuli. J Neurosci 21: 5328-5343.

[58] Knudsen EI (1974) Behavioral thresholds to electric signals in high frequency electric fish. J Comp Phys 91: 333-353.

[59] Xu Z, Payne JR, Nelson ME (1996) Logarithmic time course of sensory adaptation in electrosensory afferent nerve fibers in a weakly electric fish. J Neurophysiol 76(3): 2020-2032.

[60] Benda J, Longtin A, Maler L (2005) Spike-frequency adaptation separates transient communication signals from background oscillations. J Neurosci 25: 2312-2321.

[61] Peron S, Gabbiani F (2009) Spike frequency adaptation mediates looming stimulus selectivity in a collision-detecting neuron. Nat Neurosci 12: 318-326.

[62] McCormick DA, Connors BW, Lighthall JW, Prince DA (1985) Comparative electrophysiology of pyramidal and sparsely spiny stellate neurons in the neocortex. J Neurophysiol 54: 782-806.

[63] Benda J, Herz AV (2003) A universal model for spike-frequency adaptation. Neural Comput 15: 2523-2564.

[64] Drew PJ, Abbott LF (2006) Models and properties of power-law adaptation in neural systems. J Neurophysiol 96: 826-833.

[65] Wang XJ, Liu Y, Sanchez-Vives M, McCormick D (2003) Adaptation and temporal decorrelation by single neurons in the primary visual cortex. J Neurophysiol 89: 3279-3293.

[66] French AS, Torkkeli PH (2008) The power law of sensory adaptation: simulation by a model of excitability in spider mechanoreceptor neurons. Ann Biomed Eng 36(1): 153-161.

[67] Wark B, Fairhall A, Rieke F (2009) Timescales of inference in visual adaptation. Neuron 61: 750-761.

[68] Lundstrom BN, Fairhall AL, Maravall M (2010) Multiple timescale encoding of slowly varying whisker stimulus envelope in cortical and thalamic neurons in vivo. J Neurosci 30(14): 5071-5077.

[69] Ulanovsky N, Las L, Farkas D, Nelken I (2004) Multiple time scales of adaptation in auditory cortex neurons. J Neurosci 24(46): 10440-10453.

[70] Zilany MSA, Carney, LH (2010) Power-law dynamics in an auditory-nerve model can account for neural adaptation to sound-level statistics. J Neurosci 30(31):10380-10390.

[71] Laughlin S (1989) The role of sensory adaptation in the retina. J Exp Biol 146: 39-62.

[72] Lindner B, Chacron MJ, Longtin A (2005) Integrate-and-fire neurons with threshold noise: a tractable model of how interspike interval correlations affect neuronal signal transmission. Phys Rev E 72: 021911.

[73] Sobel EC, Tank DW (1994) In Vivo Ca2 + Dynamics in a cricket auditory neuron: an example of chemical computation. Science 263: 823-826.

[74] Peron S, Gabbiani F (2009) Role of spike-frequency adaptation in shaping neuronal response to dynamic stimuli. Biol Cybern 100(6): 505-520.

[75] Lundstrom BN, Higgs MH, Spain WJ, Fairhall AL (2008) Fractional differentiation by neocortical pyramidal neurons. Nat Neurosci 11(11): 1335-1342.

[76] Tripp B, Eliasmith C (2010) Population models of temporal differentiation. Neural Comp 22(3): 621-659.

[77] Haykin S (2001) in Communication Systems (John Wiley & Sons, Inc.), pp 723-734.

[78] Middleton J, Longtin A, Benda J, Maler L (2006) The cellular basis for parallel neural transmission of a high-frequency stimulus and its low-frequency envelope. Proc Natl Acad Sci USA 103(39): 14596-14601.

[79] Kohn A (2007) Visual adaptation: Physiology, mechanisms, and functional benefits. J Neurophysiol 97: 3155-3164.

[80] Zeng J, Powers RK, Newkirk G, Yonkers M, Binder MD (2005) Contribution of persistent sodium currents to spike-frequency adaptation in rat hypoglossal motoneurons. J Neurophysiol 93: 1035-1041.

[81] Baccus SA, Meister M (2002) Fast and Slow Contrast Adaptation in Retinal Circuitry. Neuron 36, 909-919.

[82] Sokolove PG, Cooke IM (1971) Inhibition of impulse activity in a sensory neuron by an electrogenic pump. J Gen Physiol 57(2): 125-163.

[83] Chung S, Li X, Nelson S (2002) Short-term depression at thalamocortical synapses contributes to rapid adaptation of cortical sensory responses in vivo. Neuron 34: 437-446.

[84] Liebovitch LS, Fischbarg J, Koniarek JP (1987) Ion channel kinetics: a model based on fractal scaling rather than multistate Markov processes. Math Biosci 84: 37-68.

[85] Millhauser GL, Salpeter EE, Oswald RE (1988) Diffusion models of ion-channel gating and the origin of power-law distributions from single-channel recording. Proc Natl Acad Sci USA 85: 1503-1507.

[86] Toib A, Lyakhov V, Marom S (1998) Interaction between duration of activity and time course of recovery from slow inactivation in mammalian brain Na+ channels. J Neurosci 18: 1893-1903.

[87] Torkkeli PH, French AS (2002) Simulation of different firing patterns in paired spider mechanoreceptor neurons: the role of Na+ channel inactivation. J Neurophysiol 87: 1363-1368.

[88] Brenner N, Bialek W, de Ruyter van Steveninck R (2000) Adaptive rescaling maximizes information transmission. Neuron 26: 695-702.

[89] Panzeri S, Brunel N, Logothetis NK, Kayser C (2010) Sensory neural codes using multiplexed temporal scales. Trends Neurosci 33: 111-120.

[90] Chacron MJ (2006) Nonlinear information processing in a model sensory system. J Neurophysiol 95: 2933-2946.

[91] Bastian J, Chacron MJ, Maler L (2002) Receptive field organization determines pyramidal cell stimulus-encoding capability and spatial stimulus selectivity. J Neurosci 22(11): 4577-4590.

[92] Nakagawa H, Hongjian K (2010) Collision-sensitive neurons in the optic tectum of the bullfrog, Rana catesbeiana. J Neurophysiol 104: 2487-2499.

[93] Trenholm S, Schwab DJ, Balasubramanian V, Awatramani GB (2013) Lag normalization in an electrically coupled neural network. Nat Neurosci 16(2): 154-156.

[94] Baker CL, Mareschal I (2001) Processing of second-order stimuli in the visual cortex. Prog Brain Res 134: 1-21.

[95] Joris PX, Schreiner CE, Rees A (2004) Neural processing of amplitude-modulated sounds. Physiol Rev 84: 541-577.

[96] Marsat G, Proville RD, Maler L (2009) Transient signals trigger synchronous bursts in an identified population of neurons. J Neurophysiol 102: 714-723.

[97] Shimazaki H, Shinomoto S (2010) Kernel bandwidth optimization in spike rate estimation. J Comput Neurosci 29(1-2): 171-182.

[98] Benda J, Maler L, Longtin A (2010) Linear versus nonlinear signal transmission in neuron models with adaptation currents or dynamic thresholds. J Neurophysiol 104: 2806-2820.

[99] Hodgkin AL, Huxley AF (1952) A quantitative description of membrane current and its application to conduction and excitation in nerve. J Physiol (London) 117: 500-544.

[100] Bastian J, Courtright J (1991) Morphological correlates of pyramidal cell adaptation rate in the electrosensory lateral line lobe of weakly electric fish. J. Comp. Physiol. A 168(4): 393-407.

[101] Berry MJ, Brivanlou IH, Jordan TA, Meister M (1999) Anticipation of moving stimuli by the retina. Nature, 398(6725): 334-338.

[102] Caputi AA, Aguilera PA, Carolina-Pereira A, Rodrguez-Cattneo A (2013) On the haptic nature of the active electric sense of fish. Brain research. doi: 10.1016/j.brainres.2013.05.028.

[103] Chacron MJ, Toporikova N, Fortune ES (2009) Differences in the time course of short-term depression across receptive fields are correlated with directional selectivity in electrosensory neurons. J. Neurophysiol. 102(6): 3270-3279.

[104] Clarke SE, Naud R, Longtin A, Maler L (2013) Speed-invariant encoding of looming object distance requires power law spike rate adaptation. Proc. Natl. Acad. Sci. USA 110(33): 13624-13629.

[105] Fotowat H, Gabbiani F (2011) Collision detection as a model for sensory-motor integration. Annu. Rev. Neurosci. 34: 1-19.

[106] Frost BJ, Nakayama K (1983) Single visual neurons code opposing motion independent of direction. Science 220(4598): 744-745.

[107] Geffen MN, de Vries SEJ, Meister M (2007) Retinal ganglion cells can rapidly change polarity from off to on. PLoS Biol. 5(3): e65.

[108] Haddad R, Lanjuin A, Madisen L, Zeng H, Murthy VN, Uchida N (2013) Olfactory cortical neurons read out a relative time code in the olfactory bulb. Nat. Neurosci. 16(7): 949-957.

[109] Heiligenberg W (1973) Electromotor response in the electric fish Eigenmannia (Rhamphichthyidae, Gymnotoidei). Nature 243: 301-302.

[110] Joesch M, Schnell B, Raghu SV, Reiff RF, Borst A (2010) ON and OFF pathways in Drosophila motion vision. Nature 468(7321): 300-304.

[111] Khanbabaie R, Nesse WH, Longtin A, Maler L (2010) Kinetics of fast short-term depression are matched to spike train statistics to reduce noise. J. Neurophysiol. 103(6): 3337-3348.

[112] Khosravi-Hashemi N, Fortune ES, Chacron MJ (2011) Coding movement direction by burst firing in electrosensory neurons. J. Neurophysiol. 106(4): 1954-1968.

[113] Krahe R, Bastian J, Chacron MJ (2008) Temporal processing across multiple topographic maps in the electrosensory system. J. Neurophysiol. 100(2): 852-867.

[114] Lockery SR (2011) The computational worm: spatial orientation and its neuronal basis in C. elegans. Curr. Opin. Neurobiol. 21(5): 782-790.

[115] Maier JX, Ghazanfar AA (2007) Looming biases in monkey auditory cortex. J. Neurosci. 27(15): 4093-4100.

[116] Mnch TA, da Silveira RA, Siegert S, Viney TJ, Awatramani GB, Roska B (2009) Approach sensitivity in the retina processed by a multifunctional neural circuit. Nat. Neurosci. 12(10): 1308-1316.

[117] Nelson ME, MacIver MA (1999) Prey capture in the weakly electric fish Apteronotus albifrons: sensory acquisition strategies and electrosensory consequences. J. Exp. Biol. 202(10): 1195-1203.

[118] O'Keefe TC, Brewer MC, Dodson SI (1998) Swimming behavior of Daphnia: its role in determining predation risk. J. Plankton Res. 20(5): 973-984.

[119] Rivlin-Etzion M, Wei W, Feller MB (2012) Visual stimulation reverses the directional preference of direction-selective retinal ganglion cells. Neuron 76(3): 518-525.

[120] Sakata H, Shibutani H, Kawano K (1983) Functional properties of visual tracking neurons in posterior parietal association cortex of the monkey. J. Neurophysiol. 49(6): 1364-1380.

[121] Schiller, PH (1992) The ON and OFF channels of the visual system. Trends Neurosci. 15(3): 86-92.

[122] Schwartz G, Taylor S, Fisher C, Harris R, Berry MJ (2007) Synchronized firing among retinal ganglion cells signals motion reversal. Neuron 55(6): 958-969.

[123] Shumway CA, Maler L (1989) GABAergic inhibition shapes temporal and spatial response properties of pyramidal cells in the electrosensory lateral line lobe of gymnotiform fish. J. Comp. Physiol. A 164(3): 391-407.

[124] Snyder JB, Nelson ME, Burdick JW, MacIver MA (2007) Omnidirectional sensory and motor volumes in electric fish. PLoS Biol. 5(11): 2671-2683.

[125] Tian B, Kumierek P, Rauschecker JP (2013) Analogues of simple and complex cells in rhesus monkey auditory cortex. Proc. Natl. Acad. Sci. USA 110(19): 7892-7897.

[126] Wang YC, Jiang S, Frost BJ (1993) Visual processing in pigeon nucleus rotundus: luminance, color, motion, and looming subdivisions. Visual Neurosci. 10(1): 21-30.

[127] Wang D, Maler L (1997) In vitro plasticity of the direct feedback pathway in the electrosensory system of Apteronotus leptorhynchus. J. Neurophysiol. 78(4): 1882-1889.

[128] Zahar Y, Wagner H, Gutfreund Y (2012) Responses of tectal neurons to contrasting stimuli: an electrophysiological study in the barn owl. PloS One 7(6): e39559.

[129] Azouz R, Gray CM. Dynamic spike threshold reveals a mechanism for synaptic coincidence detection in cortical neurons in vivo. Proc Natl Acad Sci USA 97: 8110-8115, 2000.

[130] Azouz R, Gray CM. Adaptive coincidence detection and dynamic gain control in visual cortical neurons in vivo. Neuron 37: 513-523, 2003.

[131] Bastian J. Electrolocation I. How the electroreceptors of Apteronotus albifrons code for moving objects and other electrical stimuli. J Comp Physiol A 144: 465-479, 1981a.

[132] Bastian J, Courtwright J, Crawford J. Commissural neurons of the electrosensory lateral line lobe of Apteronotus leptorhynchus. Morphological and physiological characteristics. J Comp Physiol A 173: 257-274, 1993.

[133] Benda J, Longtin A, Maler L. A synchronization-desynchronization code for natural communication signals. Neuron 52: 347-358, 2006.

[134] Berman N, Dunn RJ, Maler L. Function of NMDA receptors and persistent sodium channels in a feedback pathway of the electrosensory system. J Neurophysiol 86: 1612-1621, 2001.

[135] Berman NJ, Plant J, Turner R, Maler L. Excitatory amino acid transmission at a feedback pathway in the electrosensory system. J Neurophysiol 78: 1869-1881, 1997.

[136] Bottai D, Dunn R, Ellis W, Maler L. N-methyl-D-aspartate receptor 1 mRNA distribution in the central nervous system of the weakly electric fish Apteronotus leptorhynchus. J Comp Neurol 389: 65-80, 1997.

[137] Chacron MJ, Doiron B, Maler L, Longtin A, Bastian J. Non-classical receptive field mediates switch in a sensory neuron's frequency tuning. Nature 423: 77-81, 2003.

[138] Chacron MJ, Lindner B, Longtin A. Threshold fatigue and information transfer. J Comput Neurosci 23: 301-311, 2007.

[139] Chacron MJ, Maler L, Bastian J. Electroreceptor neuron dynamics shape information transmission. Nat Neurosci 8: 673-678, 2005.

[140] Clarke SE, Longtin A, Maler L. A neural code for looming and receding motion is distributed over a population of electrosensory ON and OFF contrast cells. J Neurosci 34: 5583-5594, 2014.

[141] Clements JD, Lester RA, Tong G, Jahr CE, Westbrook GL. The time course of glutamate in the synaptic cleft. Science 258: 1498-1501, 1992.

[142] Collins JJ, Chow CC, Imhoff TT. Aperiodic stochastic resonance in excitable systems. Phys Rev E 52: R3321, 1995.

[143] Deng Q, Rashid AJ, Fernandez FR, Turner RW, Maler L, Dunn RJ. A C-terminal domain directs Kv3.3 channels to dendrites. J Neurosci 25: 11531-11541, 2005.

[144] Dingledine R, Borges K, Bowie D, Traynelis SF. The glutamate receptor ion channel. Pharmacol Rev 51: 7-51, 1999.

[145] Dzubay JA, Jahr CE. The concentration of synaptically released glutamate outside of the climbing fiber-Purkinje cell synaptic cleft. J Neurosci 19: 5265-5274, 1999.

[146] Gammaitoni L, Hnggi P, Jung P, Marchesoni F. Stochastic resonance. Rev Mod Phys 70: 223-287, 1998.

[147] Goense JB, Ratnam R. Continuous detection of weak sensory signals in afferent spike trains: the role of anti-correlated interspike intervals in detection performance. J Comp Physiol A 189: 741-759, 2003.

[148] Goldman MS, Maldonado P, Abbott LF. Redundancy reduction and sustained firing with stochastic depressing synapses. J Neurosci 22: 584-591, 2002.

[149] Hanggi P. Stochastic resonance in biology. How noise can enhance detection of weak signals and help improve biological information processing. ChemPhysChem 3: 285-290, 2002.

[150] Harvey-Girard E, Dunn RJ, Maler L. Regulated expression of N-methyl- D-aspartate receptors and associated proteins in teleost electrosensory system and telencephalon. J Comp Neurol 505: 644-668, 2007.

[151] Harvey-Girard E, Lewis J, Maler L. Burst-induced anti-Hebbian depression acts through short-term synaptic dynamics to cancel redundant sensory signals. J Neurosci 30: 6152-6169, 2010.

[152] Harvey-Girard E, Maler L. Dendritic SK channels convert NMDA-R dependent LTD to burst timing-dependent plasticity. J Neurophysiol 110: 2689-2703, 2013.

[153] Jacobson GA, Diba K, Yaron-Jakoubovitch A, Oz Y, Koch C, Segev I, Yarom Y. Subthreshold voltage noise of rat neocortical pyramidal neurones. J Physiol 564: 145-160, 2005.

[154] Khosravi-Hashemi N, Chacron MJ. Motion processing across multiple topographic maps in the electrosensory system. Physiol Rep 2: e00253, 2014.

[155] Knight B. Dynamics of encoding in a population of neurons. J Gen Physiol 59: 734-766, 1972.

[156] Krahe R, Kreiman G, Gabbiani F, Koch C, Metzner W. Stimulus encoding and feature extraction by multiple sensory neurons. J Neurosci 22: 2374- 2382, 2002.

[157] Lannoo MJ, Maler L, Tinner B. Ganglion cell arrangement and axonal trajectories in the anterior lateral line nerve of the weakly electric fish Apteronotus leptorhynchus (Gymnotiformes). J Comp Neurol 280: 331-342, 1989.

[158] Lindner B. Superposition of many independent spike trains is generally not a Poisson process. Phys Rev E Stat Nonlin Soft Matter Phys 73: 022901, 2006.

[159] Litwin-Kumar A, Chacron MJ, Doiron B. The spatial structure of stimuli shapes the timescale of correlations in population spiking activity. PLoS Comput Biol 8: e1002667, 2012.

[160] Longtin A. Stochastic resonance in neuron models. J Stat Phys 70: 309-327, 1993.

[161] Ludtke N, Nelson ME. Short-term synaptic plasticity can enhance weak signal detectability in nonrenewal spike trains. Neural Comput 18: 2879- 2916, 2006.

[162] Maler L. Receptive field organization across multiple electrosensory maps. II. Computational analysis of the effects of receptive field size on prey localization. J Comp Neurol 516: 394-422, 2009b.

[163] Mathieson WB, Maler L. Morphological and electrophysiological properties of a novel in vitro preparation: the electrosensory lateral line lobe brain slice. J Comp Physiol A 163: 489-506, 1988.

[164] McDonnell MD, Ward LM. The benefits of noise in neural systems: bridging theory and experiment. Nat Rev Neurosci 12: 415-426, 2011.

[165] Mehaffey WH, Maler L, Turner RW. Intrinsic frequency tuning in ELL pyramidal cells varies across electrosensory maps. J Neurophysiol 99: 2641-2655, 2008.

[166] Nelson ME, Xu Z, Payne JR. Characterization and modeling of P-type electrosensory afferent responses to amplitude modulations in a wave-type electric fish. J Comp Physiol A 181: 532-544, 1997.

[167] Nesse WH, Maler L, Longtin A. Biophysical information representation in temporally correlated spike trains. Proc Natl Acad Sci USA 107: 21973- 21978, 2010.

[168] O'Donnell C, van Rossum MC. Systematic analysis of the contributions of stochastic voltage gated channels to neuronal noise. Front Comput Neurosci 8: 105, 2014.

[169] Pozzorini C, Naud R, Mensi S, Gerstner W. Temporal whitening by power-law adaptation in neocortical neurons. Nat Neurosci 16: 942-948, 2013.

[170] Ratnam R, Nelson ME. Non-renewal statistics of electrosensory afferent spike trains: implications for the detection of weak sensory signals. J Neurosci 20: 6672-6683, 2000.

[171] Schwalger T, Droste F, Lindner B. Statistical structure of neural spiking under non-Poissonian or other non-white stimulation. J Comput Neurosci 39: 29-51, 2015.

[172] Stacey WC, Durand DM. Synaptic noise improves detection of subthreshold signals in hippocampal CA1 neurons. J Neurophysiol 86: 1104-1112, 2001.

[173] Wang D, Maler L. The immunocytochemical localization of glutamate in the electrosensory system of the gymnotiform fish, Apteronotus leptorhynchus. Brain Res 653: 215-222, 1994.

[174] Blankenburg S, Lindner B (2016) The effect of positive interspike interval correlations on neuronal information transmission. Math Biosci and Eng 13(3), 461-481.

[175] Buzski G, Mizuseki K (2014) The log-dynamic brain: how skewed distributions affect network operations. Nat Rev Neurosci 15(4): 264-278.

[176] Friston, K., Adams, R.A., Perrinet, L., Breakspear, M. Perceptions as hypotheses: saccades as experiments. Front. Psychol. 3, 1-20 (2012).

[177] Hofmann, V. et al., Motor patterns during active electrosensory acquisition. Front. Behav. Neurosci. 8, 1-13 (2014).

[178] Dayan, P., Abbott, L.F. Theoretical neuroscience: computational and mathematical modeling of neural systems (MIT Press, Cambridge, MA, 2001).

[179] Haslinger, R., Pipa, G., Brown, E. Discrete time rescaling theorem: determining goodness of fit for discrete time statistical models of neural spiking. Neural Comput. 22, 2477-2506 (2010).

[180] Pillow, J.W. Time-rescaling methods for the estimation and assessment of non-Poisson neural encoding models. Advances in Neural Information Processing Systems (NIPS) MIT Press. 1473-1481 (2009).

[181] Barbieri, R., Quirk, M.C., Frank, L.M., Wilson, M.A., Brown, E.N. Construction and analysis of non-Poisson stimulus-response models of neural spiking activity. J. Neurosci. Meth. 105, 25-37 (2001).

[182] Shadlen, M.N., Newsome, W.T. The variable discharge of cortical neurons: implications for connectivity, computation, and information coding. J. Neurosci. 18, 3870-3896 (1998).

[183] Kepecs, A., Wang, X.J., Lisman, J. Bursting neurons signal input slope. J. Neurosci. 22, 9053-9062 (2002).

[184] Rosenblith, W.A. Sensory Communication: Contributions. (MIT Press, Cambridge, MA, 1961).

[185] Mejias, J.F., Payeur, A., Selin, E., Maler, L., Longtin, A. Subtractive, divisive and non-monotonic gain control in feedforward nets linearized by noise and delays. Front. Comput. Neurosci. 8, 1-15 (2014).

[186] Goldman, M.S., Golowasch, J., Marder, E. Abbott, L.F. Global structure, robustness, and modulation of neuronal models. J. Neurosci. 21, 5229-5238 (2001).

[187] Middleton, J., Yu, N., Longtin, A. Maler, L. Routing the flow of sensory signals using plastic responses to bursts and isolated spikes: experiment and theory. J. Neurosci. 31, 2461-2473 (2011).

[188] Fortune, E.S. Rose, G.J. Short-term synaptic plasticity contributes to the temporal filtering of electrosensory information. J. Neurosci. 20, 7122-7130 (2000).

[189] Fortune, E.S. Rose, G.J. Short-term synaptic plasticity as a temporal filter. Trends Neurosci. 24, 381-385 (2001).

[190] Shimazaki, H., Shinomoto, S. A method for selecting the bin size of a time histogram. Neural Comput. 19, 1503-1527 (2007).

[191] Brown, E.N., Barbieri, R., Ventura, V., Kass, R.E., Frank, L.M. The time-rescaling theorem and its application to neural spike train data analysis. Neural Comput. 14, 325-346 (2002).

[192] Kass, R.E., Eden, U.T., Brown, E.N. Analysis of neural data (Springer-Verlag, New York, NY 2014).

[193] Efron, B., Johnstone, I.M. Fisher's information in terms of the hazard rate. Ann. Statist. 18, 38-62 (1990).

[194] Middleton, J., Yu, N., Longtin, A., Maler, L. Routing the flow of sensory signals using plastic responses to bursts and isolated spikes: experiment and theory. J. Neurosci. 31, 2461-2473 (2011).

[195] Wang, W., Jones, H.E., Andolina, I.M., Salt, T.E., and Sillito, A.M. (2006). Functional alignment of feedback effects from visual cortex to thalamus. Nat. Neurosci. 9, 1330-1336.

[196] Yan, W., and Suga, N. (1998). Corticofugal modulation of the midbrain frequency map in the bat auditory system. Nat. Neurosci. 1, 54-58.

[197] Temereanca, S., and Simons, D.J. (2004). Functional topography of corticothalamic feedback enhances thalamic spatial response tuning in the somatosensory whisker/barrel system. Neuron 41, 639-651.

[198] Albright, T.D. (2012). On the perception of probable things: neural substrates of associative memory, imagery, and perception. Neuron 74, 227-245.

[199] Sillito, A.M., Jones, H.E., Gerstein, G.L., and West, D.C. (1994). Feature-linked synchronization of thalamic relay cell firing induced by feedback from the visual cortex. Nature 369, 479-482.

[200] Sillito, A.M., and Jones, H.E. (2002). Corticothalamic interactions in the transfer of visual information. Phil. Trans. R. Soc. B 357, 1739-1752.

[201] Whitmire, Clarissa J., Waiblinger, C., Schwarz, C., and Stanley, Garrett B. (2016). Information Coding through Adaptive Gating of Synchronized Thalamic Bursting. Cell Reports 14, 795-807.

[202] Sridharan, D., Schwarz, J.S., and Knudsen, E.I. (2014). Selective attention in birds. Curr. Biol. 24, R510-513.

[203] Crick, F. (1984). Function of the thalamic reticular complex: the searchlight hypothesis. Proc. Natl. Acad. Sci. USA 81, 4586-4590.

[204] Clarke, SE, Longtin, A, Maler, L. The neural dynamics of sensory focus. Nat. Commun. 6, 8764 (2015).

[205] Bastian, J. (1998). Plasticity in an electrosensory system III: Contrasting properties of spatially segregated dendritic inputs. J. Neurophysiol. 79, 1839-1857.

[206] Bastian, J., and Bratton, B. (1990). Descending control of electroreception. I. Properties of nucleus praeeminentialis neurons projecting indirectly to the electrosensory lateral line lobe. J. Neurosci. 10, 1226-1240.

[207] Berman, N.J., and Maler, L. (1998c). Distal versus proximal inhibitory shaping of feedback excitation in the electrosensory lateral line lobe: implications for sensory filtering. J. Neurophysiol. 80, 3214-3232.

[208] Lewis, J.E., and Maler, L. (2002). Dynamics of electrosensory feedback: short-term plasticity and inhibition in a parallel fiber pathway. J. Neurophysiol. 88, 1695-1706.

[209] Bastian, J. (1995). Pyramidal-cell plasticity in weakly electric fish: a mechanism for attenuating responses to reafferent electrosensory inputs. J. Comp. Physiol. A 176, 63-73.

[210] Bol, K., Marsat, G., Harvey-Girard, E., Longtin, A., and Maler, L. (2011). Frequency-tuned cerebellar channels and burst-induced LTD lead to the cancellation of redundant sensory inputs. J. Neurosci. 31, 11028-11038.

[211] Turner, R.W., Lemon, N., Doiron, B., Rashid, A.J., Morales, E., Longtin, A., Maler, L., and Dunn, R.J. (2002). Oscillatory burst discharge generated through conditional back-propagation of dendritic spikes. J. Physiol. Paris 96, 517-530.

[212] Ellis, L.D., Maler, L., and Dunn, R.J. (2008). Differential distribution of SK channel subtypes in the brain of the weakly electric fish Apteronotus leptorhynchus. J. Comp. Neurol. 507, 1964-1978.

[213] Knudsen, E.I. (2007). Fundamental components of attention. Annu. Rev. Neurosci. 30, 57-78.

[214] Manita, S., Suzuki, T., Homma, C., Matsumoto, T., Odagawa, M., Yamada, K., Ota, K., Matsubara, C., Inutsuka, A., Sato, M., et al. (2015). A Top-Down Cortical Circuit for Accurate Sensory Perception. Neuron 86, 1304-1316.

[215] Kwon, S.E., Yang, H., Minamisawa, G., and O'Connor, D.H. (2016). Sensory and decision-related activity propagate in a cortical feedback loop during touch perception. Nat. Neurosci. 19, 1243-1249.

[216] Takahashi, N., Oertner, T.G., Hegemann, P., and Larkum, M.E. (2016). Active cortical dendrites modulate perception. Science 354, 1587-1590.

[217] Clarke, S. E., Maler, L. (2017). Feedback Synthesizes Neural Codes for Motion. Current Biology, 27(9), 1356-1361.

[218] Moutard, C., Dehaene, S., Malach, R. (2015). Spontaneous fluctuations and non-linear ignitions: two dynamic faces of cortical recurrent loops. Neuron 88(1), 194-206.

[219] Ramaswami, M. (2014). Network plasticity in adaptive filtering and behavioral habituation. Neuron 82(6), 1216-1229.

[220] Mejias, J. F., Marsat, G., Bol, K., Maler, L., Longtin, A. (2013). Learning contrast-invariant cancellation of redundant signals in neural systems. PLoS Comput Biol, 9(9), e1003180.

[221] Garrido MI, Kilner JM, Kiebel SJ, Friston KJ. (2007) Evoked brain responses are generated by feedback loops. Proc Natl Acad Sci USA, 104(52):20961-20966.

[222] Tanimizu T, Kenney JW, Okano E, Kadoma K, Frankland PW, Kida S. (2017) Functional connectivity of multiple brain regions required for the consolidation of social recognition memory. J Neurosci, 37(15):4103-4116.

[223] Hunt LT, Hayden BY. (2017) A distributed, hierarchical and recurrent framework for reward-based choice. Nat Rev Neurosci, 18(3):172-182.

[224] Edelman GM, Gally JA. (2013) Reentry: a key mechanism for integration of brain function. Front Integr Neurosci, 7:63.

[225] Koch C, Massimini M, Boly M, Tononi G. (2016) Neural correlates of consciousness: progress and problems. Nat Rev Neurosci, 17(5):307-21.

[226] Marr, D. Vision: A Computational Investigation into the Human Representation and Processing of Visual Information (MIT Press, 2010).

[227] Babineau, D., Lewis, J. E., Longtin, A. Spatial acuity and prey detection in weakly electric fish. PLoS Comput. Biol. 3, e38 (2007).

[228] Stamper, S. A. et al. Species differences in group size and electrosensory interference in weakly electric fishes: implications for electrosensory processing. Behav. Brain Res. 207, 368-376 (2010).

[229] Baker, C. L. Jr Central neural mechanisms for detecting second-order motion. Curr. Opin. Neurobiol. 9, 461-466 (1999).

[230] Wark, B., Lundstrom, B. N., Fairhall, A. Sensory adaptation. Curr. Opin. Neurobiol. 17, 423-429 (2007).

[231] Saunders, J., Bastian, J. The physiology and morphology of two classes of electrosensory neurons in the weakly electric fish Apteronotus Leptorhynchus. J. Comp. Physiol. A 154, 199-209 (1984).

[232] Schiller, P. H. The ON and OFF channels of the visual system. Res. Publ. Assoc. Res. Nerv. Ment. Dis. 67, 35-41 (1990).

[233] Lee, C. H. Neuroscience: the split view of motion. Nature 468, 178-179 (2010).

[234] Stamper, S. A., Fortune, E. S., Chacron, M. J. Perception and coding of envelopes in weakly electric fishes. J. Exp. Biol. 216, 2393-2402 (2013).

[235] Yu, N., Hupe, G., Garfinkle, C., Lewis, J. E., Longtin, A. Coding conspecific identity and motion in the electric sense. PLoS Comput. Biol. 8, e1002564 (2012).

[236] Metzen, M. G., Chacron, M. J. Neural heterogeneities determine response characteristics to second-, but not first-order stimulus features. J. Neurosci. 35, 3124-3138 (2015).

[237] Stamper, S. A., Madhav, M. S., Cowan, N. J., Fortune, E. S. Beyond the jamming avoidance response: weakly electric fish respond to the envelope of social electrosensory signals. J. Exp. Biol. 215, 4196-4207 (2012).

[238] Middleton, J. W., Harvey-Girard, E., Maler, L., Longtin, A. Envelope gating and noise shaping in populations of noisy neurons. Phys. Rev. E Stat. Nonlin. Soft Matter Phys. 75, 021918 (2007).

[239] Metzen, M. G., Chacron, M. J. Weakly electric fish display behavioral responses to envelopes naturally occurring during movement: implications for neural processing. J. Exp. Biol. 217, 1381-1391 (2014).

[240] Savard, M., Krahe, R., Chacron, M. J. Neural heterogeneities influence envelope and temporal coding at the sensory periphery. Neuroscience 172, 270-284 (2011).

[241] Metzen, M. G. et al. Coding of envelopes by correlated but not single-neuron activity requires neural variability. Proc. Natl Acad. Sci. USA 112, 4791-4796 (2015).

[242] McGillivray, P., Vonderschen, K., Fortune, E. S., Chacron, M. J. Parallel coding of first- and second-order stimulus attributes by midbrain electrosensory neurons. J. Neurosci. 32, 5510-5524 (2012).

[243] Middleton, J. W., Longtin, A., Benda, J., Maler, L. Postsynaptic receptive field size and spike threshold determine encoding of high frequency information via sensitivity to synchronous presynaptic activity. J. Neurophysiol. 101, 1160-1170 (2009).

[244] Longtin, A., Middleton, J. W., Cieniak, J., Maler, L. Neural dynamics of envelope coding. Math. Biosci. 214, 87-99 (2008).

[245] Orger, M. B., Smear, M. C., Anstis, S. M., Baier, H. Perception of Fourier and non-Fourier motion by larval zebrafish. Nat. Neurosci. 3, 1128-1133 (2000).

[246] Mareschal, I., Baker, C. L. Jr Cortical processing of second-order motion. Vis. Neurosci. 16, 527-540 (1999).

[247] Ramachandran, V. S., Rao, V. M., Vidyasagar, T. R. Apparent movement with subjective contours. Vision Res. 13, 1399-1401 (1973).

[248] Hallum, L. E., Movshon, J. A. Second-order selectivity of single units in macaque primary visual cortex (V1) and V2. J. Vision 11, 1198-1198 (2011).

[249] Tanaka, H., Ohzawa, I. Surround suppression of V1 neurons mediates orientation-based representation of high-order visual features. J. Neurophysiol. 101, 1444-1462 (2009).

[250] Lewis, J. E., Maler, L. Neuronal population codes and the perception of distance in weakly electric fish. J. Neurosci. 21, 2842-2850 (2001).

[251] Chen, E. Y., Chou, J., Park, J., Schwartz, G., Berry, M. J. The neural circuit mechanisms underlying the retinal response to motion reversal. J. Neurosci. 34, 15557-15575 (2014).

[252] Tikidji-Hamburyan, A. et al. Retinal output changes qualitatively with every change in ambient illuminance. Nat. Neurosci. 18, 66-74 (2015).

[253] Zhang, Y., Kim, I. J., Sanes, J. R., Meister, M. The most numerous ganglion cell type of the mouse retina is a selective feature detector. Proc. Natl Acad. Sci. USA 109, E2391-E2398 (2012).

[254] Gjorgjieva, J., Sompolinsky, H., Meister, M. Benefits of pathway splitting in sensory coding. J. Neurosci. 34, 12127-12144 (2014).

[255] Aumentado-Armstrong, T., Metzen, M. G., Sproule, M. K. J., Chacron, M. J. Electrosensory midbrain neurons display feature invariant responses to natural communication stimuli. PLoS Comput. Biol. 11, e1004430 (2015).

[256] Robin, D. A., Royer, F. L. Auditory temporal processing: two-tone flutter fusion and a model of temporal integration. J. Acoust. Soc. Am. 82, 1207-1217 (1987).

[257] Szwed, M., Bagdasarian, K., Ahissar, E. Encoding of vibrissal active touch. Neuron 40, 621-630 (2003).

[258] Bastian, J. (1986). Gain control in the electrosensory system. A role for descending projections to the lateral electrosensory lateral line lobe. J. Comp. Physiol. A 158, 505-515.

[259] Maler, L., Sas, E., Johnston, S., and Ellis, W. (1991). An atlas of the brain of the weakly electric fish Apteronotus Leptorhynchus. J. Chem. Neuroanat. 4, 1-38.

[260] Hitschfeld, E.M., Stamper, S.A., Vonderschen, K., Fortune, E.S., and Chacron, M.J. (2009). Effects of restraint and immobilization on electrosensory behaviors of weakly electric fish. Ilar J 50, 361-372.

[261] Harvey-Girard, E., and Dunn, R.J. (2003). Excitatory Amino Acid Receptors of the Electrosensory System: The NR1/NR2B N-Methyl-D-Aspartate Receptor. J. Neurophysiol. 89, 822-832.

[262] Pomfret, R., Miranpuri, G., and Sillay, K. (2013). The substitute brain and the potential of the gel model. Ann. Neurosci. 20, 118.

[263] Marsat, G., and Maler, L. (2012). Preparing for the unpredictable: adaptive feedback enhances the response to unexpected communication signals. J. Neurophysiol. 107, 1241-1246.

[264] Bastian, J. (1986). Gain control in the electrosensory system mediated by descending inputs to the electrosensory lateral line lobe. J. Neurosci. 6, 553-562.

[265] Sas, E., and Maler, L. (1987). The organization of afferent input to the caudal lobe of the cerebellum of the gymnotid fish Apteronotus leptorhynchus. Anat. Embryol. 177, 55-79.

[266] Oswald, A.M., Doiron, B., and Maler, L. (2007). Interval coding. I. Burst interspike intervals as indicators of stimulus intensity. J. Neurophysiol. 97, 2731-2743.

[267] Dell, R.B., Holleran, S., and Ramakrishnan, R. (2002). Sample Size Determination. Ilar Journal 43, 207-213.